Graduate School Form 30
Updated 1/15/2015

PURDUE UNIVERSITY
GRADUATE SCHOOL
Thesis/Dissertation Acceptance

This is to certify that the thesis/dissertation prepared

By Brian John Murphy

Entitled
PROFILING THE MOISTURE ENVIRONMENT OF DEVELOPING TROPICAL STORMS USING AIRBORNE RADIO OCCULTATION

For the degree of Doctor of Philosophy

Is approved by the final examining committee:

Michael Baldwin Chair	Shu-Hua Chen
Jennifer S. Haase	Wen-Yih Sun
James L. Garrison	

To the best of my knowledge and as understood by the student in the Thesis/Dissertation Agreement, Publication Delay, and Certification Disclaimer (Graduate School Form 32), this thesis/dissertation adheres to the provisions of Purdue University's "Policy of Integrity in Research" and the use of copyright material.

Approved by Major Professor(s): Jennifer S. Haase

Approved by: Indrajeet Chaubey 7/23/2015

Head of the Departmental Graduate Program Date

PROFILING THE MOISTURE ENVIRONMENT OF DEVELOPING TROPICAL STORMS USING AIRBORNE RADIO OCCULTATION

A Dissertation

Submitted to the Faculty

of

Purdue University

by

Brian J. Murphy

In Partial Fulfillment of the

Requirements for the Degree

of

Doctor of Philosophy

August 2015

Purdue University

West Lafayette, Indiana

ACKNOWLEDGEMENTS

I would like to deeply thank my major professor and advisor, Dr. Jennifer S. Haase and express my gratitude for her support and guidance. Dr. Haase is a superb mentor, always helping me to progress and greatly improve my work.

I would also like to give my special thanks to my co-advisor Professor Wen-Yih Sun whose door was always open to help and offer advice.

I would like to thank my advisory committee members, Professor James Garrison, Professor Shu-Hua Chen and Professor Michael Baldwin. I am very grateful and appreciative for all their help. I am very grateful for the involvement of Professor Garrison, who has monitored my research since I started and always offered his suggestions and insight. I am also sincerely thankful for the input of Professor Shu-Hua Chen who kindly shared her expertise and graciously hosted me at UC Davis for two visits.

Also great thanks to fellow students Kuo-Nung Wang, Xue Meng Chen and former fellow students Paytsar Muradyan and Ulvi Acikoz as well as collaborators Professor Feiqin Xie and his post-doc, Dr. Loknath Adikari. All provided a lot of help and fruitful discussions throughout my studies.

I would like to acknowledge the National Science Foundation and NASA which provided support as well as Purdue and the Earth, Atmospheric and Planetary Sciences

department for support through the Ross and Bilsland fellowships, an AMS travel grant and a two year teaching assistantship.

TABLE OF CONTENTS

Page

Page

LIST OF TABLES

Table Page

LIST OF FIGURES

Figure Page

Figure Page

Figure Page

Figure Page

Figure Page

Figure Page

Figure Page

Figure Page

Figure Page

Figure Page

Figure Page

Appendix Figure

Appendix Figure Page

Appendix Figure Page

Appendix Figure Page

LIST OF ABBREVIATIONS

ARO	Airborne Radio Occultation
CHAMP	CHAllenging Mini-satellite Payload
CL	Closed-Loop
CODE	Center for Orbit Determination in Europe
COSMIC	Constellation Observing System for Meteorology, Ionosphere, and Climate
DA	Data Assimilation
ECMWF	European Center for Medium Range Weather Forecasts
ERAI	European Re-Analysis Interim
FSI	Full Spectrum Inversion
GISMOS	GNSS Instrument System for Multistatic and Occultation Sensing
GNSS	Global Navigation Satellite System
GPS	Global Positioning System
GPS/MET	Global Positioning System/Meteorology
GRACE	GRAvity Recovery and Climate Experiment
GRAS	GNSS receiver for Atmospheric Sounding
GRS	GPS Recording System
GV	Gulfstream V
IGS	International GNSS Service

IMU	Inertial Measurement Unit
LEO	Low Earth Orbit
NASA	National Aeronautics and Space Administration
NHC	National Hurricane Center
NSF	National Science Foundation
NWP	Numerical Weather Prediction
OL	Open-Loop
PLL	Phase Locked Loop
PM	Phase Matching
PREDICT	PRE-Depression Investigation of Cloud Systems in the Tropics
PRN	Pseudo-Random Number
PSR	Purdue Software Receiver
RF	Research Flight
RO	Radio Occultation
SAC-C	Satelite de Aplicaciones Cientificas-C
SNR	Signal-to-Noise ration
TOGA	Tropical Ocean and Global Atmosphere
WRF	Weather Research and Forecast model

ABSTRACT

Murphy, Brian J. Ph.D., Purdue University, August 2015. Profiling the Moisture Environment of Developing Tropical Storms using Airborne Radio Occultation. Major Professor: Jennifer S. Haase.

An extensive airborne radio occultation (ARO) data set has been collected by the GNSS instrument system for multistatic and occultation sensing (GISMOS) during the PRE–Depression Investigation of Cloud systems (PREDICT) field experiment in 2010. ARO is a promising new technique in which GPS radio occultation measurements are made with an airborne receiver. ARO has the potential to provide spatially and temporally dense data sets over a mesoscale region to complement other observing systems such as dropsondes or meteorological satellites and to improve forecasts after assimilation of the ARO data into numerical weather prediction (NWP) models.

The PREDICT campaign was the first full scale deployment of GISMOS and a primary goal was to assess the accuracy of the ARO refractivity retrievals near developing tropical storms. Twenty–six research missions were flown which sampled eight storm systems. GISMOS collected data using both geodetic quality GPS receivers, to produce preliminary profiles of the upper troposphere, and a 10 MHz GPS recording system (GRS) used to sample and record the raw GPS signals throughout the lower troposphere. Radio (RF) signals recorded by the GRS are analyzed in post processing mode using a software receiver with an open loop (OL) technique. Both the refractivity

results from the geodetic receiver data and GRS data are compared to refractivity profiles calculated from data recorded by nearby radiosondes and dropsondes as well as profiles calculated from numerical weather prediction model output. All ARO retrievals were based on geometric ray optics.

Twenty-one refractivity profiles of the upper troposphere were obtained from setting occultations measured by the geodetic receivers. The geodetic receiver retrievals agreed within 2% of co-located dropsonde, radiosonde and model output, but on average did not extend below 6 km altitude and only one or two retrievals were obtained per flight. The conventional phase locked loop (PLL) tracking used by the geodetic receivers could not maintain signal lock in the lower troposphere where signal propagation through more complex moisture structure produces rapid fluctuations in amplitude and phase.

In the middle to lower troposphere, the open loop tracking technique used with the recorded raw GPS signals is more robust for extracting the carrier phase and amplitude measurements. A set of 46 refractivity profiles was obtained from the four research flights that sampled the pre-hurricane Karl system. Typically, 10 to 15 retrievals per flight were possible using open loop tracking, a great improvement over the conventional receivers. Phase measurements were possible with open loop tracking to lower altitudes, 2 km on average. The mean error of the open loop retrievals compared to dropsondes and model output was also about 2% in the 6 – 12 km altitude range. A bias was discovered between rising and setting occultations. Also, a negative bias was found that becomes significant at lower altitudes, likely due to multipath propagation. The full data set was analyzed using geometric optics retrieval methods, in order to examine the dependence of the bias on atmospheric characteristics. Radio holographic techniques

based on physical optics are being developed for ARO to retrieve refractivity in the presence of multipath. A test case comparing radio holographic retrieval results to a geometric optics retrieval shows the potential for significantly reducing this type of bias. Further analysis of the extensive geometric optics dataset is carried out, within the context of these biases below 6 km. Several examples of the type of analysis now possible with ARO are given, including radial profiles of thermodynamic variables

In the middle to lower troposphere, variations in refractivity are shown to be indicative of moisture variations. ARO refractivity profiles sampling different areas within the tropical wave showed characteristics that were consistent with horizontal moisture gradients present in the NWP model representation of the developing tropical storms. The use of the dense ARO data set for model validation is tested in comparisons with a high resolution Weather and Research Forecasting (WRF) model simulation and the European Center for Medium Range Weather Forecasting Interim Reanalysis (ERAI). Variation in refractivity of ARO profiles preceding the development of the pre-Karl system is consistent with increasing moisture near the storm center. These promising results demonstrate that the ARO refractivity retrievals should be an attractive option for assimilation into NWP models. The ARO data set produced in this thesis have been provided to project collaborators for future work assimilating them into WRF simulations of Hurricane Karl to assess improvements in forecast intensity.

CHAPTER 1. INTRODUCTION

1.1 Motivation

Hurricane genesis is the transition from a tropical disturbance to a tropical depression with organized convection and closed cyclonic wind circulation. The genesis process is known to depend on the degree of vertical instability needed to support deep convection and on mid-level moistening or drying, which modulates convective activity Because of the small fraction of systems which actually develop in favorable conditions, it is thought a pre-existing disturbance of sufficient strength, such as a easterly wave, is required for genesis [*Nolan*, 2007]. Given a sufficiently sized existing disturbance under favorable conditions, it is then important to distinguish which cases will develop. A recent hypothesis proposed that a co-moving closed circulation associated with atmospheric waves moving through the mean flow could be identified as a protected region favorable for tropical cyclone (TC) development [*Dunkerton et al.*, 2009]. A developing storm in this region would be protected from inhibiting factors such as dry air intrusion and vertical wind shear.

The Pre-Depression Investigation of Cloud Systems in the Tropics (PREDICT) experiment identified and investigated the areas of closed circulation co-moving with easterly as possibly favorable for tropical cyclone development. Primarily, dropsonde observations were made using a high altitude research aircraft. A receiver capable of

making radio occultation measurements was also deployed on the research aircraft. The objective of deploying the airborne radio occultation (ARO) capability during PREDICT was to determine the average moisture structure within the protected region of enhanced convection, and of the external environment outside the tropical wave to supplement the dropsonde point measurements. Global Positioning System (GPS) radio occultation (RO) is a remote sensing technique using GPS radio signals to obtain high resolution vertical profiles of atmospheric refractivity which can be directly related to atmospheric pressure, temperature and moisture. The ability of ARO to densely sample the environment on both sides of the flight track, obtaining a high vertical resolution integrated picture of the surrounding air masses, is complementary to dropsonde observations beneath the flight track, and to high spatial but low vertical resolution satellite soundings. Eventually data assimilation will be used to determine how well the resolution of mesoscale features can be improved over using dropsondes alone by incorporating the dense sampling of crossing rays of the airborne RO dataset, using the nonlocal assimilation operators that account for the effect of integrating over a long horizontal path length.

Since spaceborne GPS radio occultation has become operational, the data have shown a positive impact in global numerical weather prediction models in the 300 to 50 hPa range. A few recent examples of spaceborne radio occultation data assimilation into high-resolution models of tropical cyclones have shown that localized regions where the moisture increment is high relative to the first guess model have produced significant changes in low and mid-level circulations [*Kueh et al.*, 2009]. In a study of the 2006 hurricane Ernesto, assimilation of GPS RO profiles during the period of one half to two days before hurricane genesis resulted in an improvement of the forecast of hurricane

intensification [*Liu*, 2009]. This is attributed to the reduction of a dry bias in model initial conditions and the enhancement of the initial perturbation within the easterly wave. In addition, in this case the improvement was shown to be a result of assimilating only a few key RO profiles, by chance located nearby and upstream of the storm [*Huang et al.*, 2008; *Liu*, 2009]. Kunii et al. [2012] found assimilation of spaceborne RO soundings had a positive impact on a TC forecast from the formative stages and significantly improved the intensity forecast. Liu et al. [2012] demonstrated the importance of assimilating RO soundings which extend below 6 km altitude for the greatest positive impact on a TC forecast. While the results of these individual cases are promising, the number of cases where an RO profile happens to be located near a developing system is limited, so an insufficient number of cases have been investigated. Operationally, spaceborne RO data has improved long-term global numerical weather model simulations [*Cucurull et al.*, 2008]. However, RO data have only had limited overall impact on short-term weather simulations and forecasts [*Kueh et al.*, 2009]. One primary reasons for this is that typically, only a few RO soundings are available within a limited regional domain and short assimilation time window, given the current spaceborne instrument constellation.

This thesis lays the groundwork for assimilation tests of airborne radio occultation data for forecasting tropical storms by developing the optimal methodology for analyzing the GPS data, determining the practical capabilities of the system, and providing a first look at horizontal and temporal variations in atmospheric properties over the early stages of tropical cyclone development as determined by these observations. It seeks to answer the following questions:

1) Given the flight paths and instrument capabilities, what are the sampling characteristics of ARO, how do the commercial conventional components compare to research instrumentation, what techniques can be used to increase performance, and what are the implications for improvements and ease of use in future research deployments and a future operational system?
2) Given the challenges of observing from an aircraft platform, what new techniques are required to increase performance of the system in the presence of noise? What was the resulting improvement in sampling?
3) For the purpose of establishing reasonable description of observation errors required for future data assimilation, what is the accuracy of the retrieved profiles? Are these measures consistent, taking into consideration the different scales of independent measurements and models used for comparison? Are there limitations and what are the prospects for how accuracy can be improved?
4) Using observations from the system that would eventually become hurricane Karl, what are the expected and observed scales of temporal and spatial moisture variability evident directly in the refractivity profiles prior to any data assimilation and how is that evident in comparisons with high-versus low-resolution model fields over the course of tropical storm development? What is the observed contrast in refractivity in the larger scale environment compared with that near the storm center at different stages of development? What limitations are imposed on the interpretation because of biases and how might those change in the future with implementation of the radio holographic techniques?

1.2 Background

Global Positioning System GPS radio occultation (RO) is a remote sensing technique using Global Navigation Satellite System (GNSS) radio signals to obtain high resolution vertical profiles of atmospheric refractivity which can be directly related to atmospheric pressure, temperature and moisture. Refractivity, in N - units, is defined in terms of refractive index as shown in equation (1.1).

$$N = (n-1) \times 10^6 \tag{1.1}$$

Refractivity can be determined from analysis of the delay in transmissions by GNSS satellites due the neutral atmosphere. For spaceborne RO, a Low Earth Orbiting (LEO) satellite is used to receive the GPS signal (Figure 1.1). The refractivity can be used to determine atmospheric pressure, temperature and humidity using equation (1.2) [*Smith and Weintraub*, 1953].

$$N = k_1 \frac{p_d}{T} + k_2 \frac{e}{T} + k_3 \frac{e}{T^2} \tag{1.2}$$

where p_d is dry atmospheric pressure in hPa, e is water vapor pressure in hPa, and T is temperature in Kelvin.

The RO observable is the accumulated phase of the received GNSS signal carrier phase. The delay of the signal due to refractive bending of the ray path through the neutral atmosphere will result in additional accumulated excess phase compared to that of a signal following a straight line path from transmitter to receiver. A limb observation is

made of the GNSS satellite as it rises above or sets below the horizon of the spaceborne receiver as illustrated in Figure 1.1. The bending angle, α, of the ray path measures the deviation of the ray from its straight line path. The impact parameter, a, is the product of the refractive index, n_t, at the tangent point with the radial distance of the tangent point from the Earth center, r_t. Geometric optics can be used to determine the bending angle of the refracted signal using the Doppler frequency found from the time derivative of the excess phase due to atmospheric delay [*Kursinski et al.*, 1997; *Vorob'ev and Krasil'nikova*, 1994]. For a spherically symmetric atmosphere, the bending angle of the ray path is then directly related to refractivity through an Abel integral transform.

GPS RO has become a very useful remote sensing technique because it offers stable highly accurate measurements with global coverage and all weather visibility with insensitivity to rain and clouds [*Kursinski et al.*, 1997]. Since the proof of concept mission, GPS/MET launched in 1995 [*Ware et al.*, 1996], many applications have been developed for GPS RO such as assimilation into operational numerical weather prediction (NWP) models, planetary boundary layer studies, composite analysis of the thermodynamic structure of hurricanes, and the study of large scale atmospheric circulations [*Anthes*, 2011b; *Mannucci et al.*, 2014; *Vergados et al.*, 2013]. The global coverage of the first RO constellation of receiving satellites, the Constellation Observing System for Meteorology, Ionosphere and Climate (COSMIC)/ Formosa Satellite 3 (FORMOSAT-3) [*Anthes et al.*, 2008], averaged a global coverage of about 2000 soundings daily after the system became fully operational [*Yue et al.*, 2014]. The COSMIC mission greatly increased the number of available RO soundings, and while the global density of observations is roughly the same order of magnitude of daily global

radiosonde soundings [*Durre et al.*, 2006], it provides a much better distribution by providing soundings over the oceans and the southern hemisphere. However, even at its peak the COSMIC constellation of spaceborne receivers provided a temporal and spatial density of observations that was relatively sparse, about 4 daily over a 1000 x 1000 sq. km area when assuming roughly uniform global coverage. The coverage of spaceborne RO missions is also constrained by the orbital paths of the receiving satellites and individual storm systems within a limited area cannot be independently targeted by spaceborne RO, or be easily observed at the desired time.

The distribution and density of spaceborne RO soundings can be improved by optimizing LEO satellite orbital patterns [*Asgarimehr and Hossainali*, 2015] or deploying larger constellations of LEO satellites. For instance, the next generation 12 satellite COSMIC-2 constellation is expected to provide up to 12000 daily soundings when fully deployed [*Ho et al.*, 2013]. While larger and optimally placed spaceborne RO constellations will provide a greater density of global soundings, it will still not be possible to target a mesoscale size area for a dense sampling. Again, assuming uniform coverage, about one occultation per hour would be available over a 1000 x 1000 sq. km area from the new COSMIC-2 constellation.

Not long after the use of spaceborne receivers for GPS RO was established, it was suggested that a receiver for RO could be deployed inside the atmosphere on board an aircraft [*Healy et al.*, 2002; *Zuffada et al.*, 1999]. With an airborne GPS radio occultation (ARO) system, an aircraft can target a specific area and stay on station to make a dense sampling over a specific period of time. An aircraft can also fly multiple missions to return to a weather system of interest and capture the system evolution over time. Given

the promise of ARO, the GNSS Instrument System for Multistatic and Occultation Sensing (GISMOS) was developed with funding by the National Science Foundation [*Garrison et al.*, 2007]. GISMOS can receive and record GNSS signals and make both occultation and reflectometry measurements.

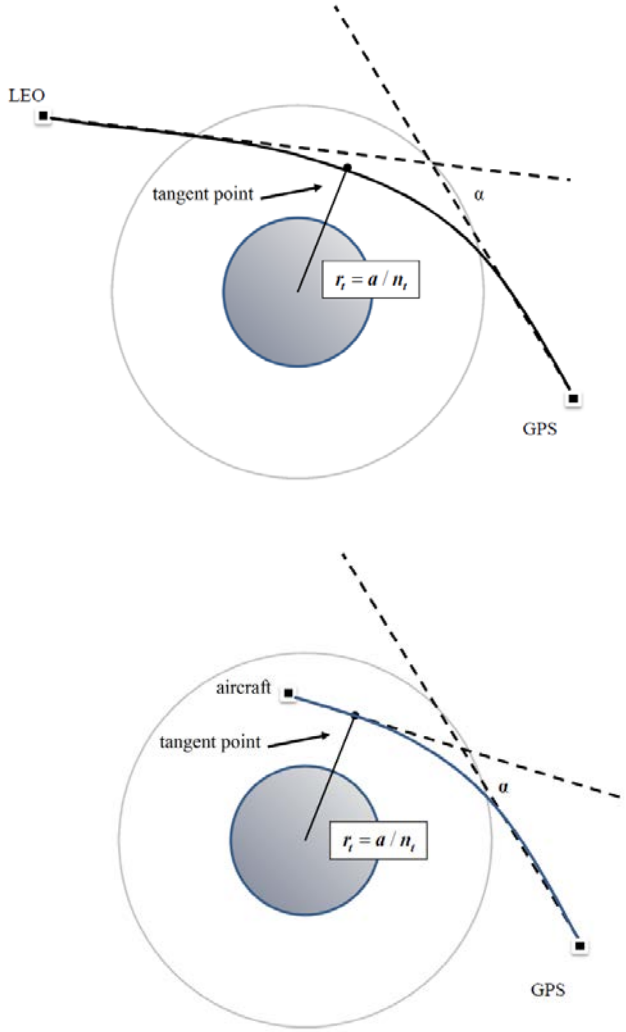

Figure 1.1 TOP: The spaceborne RO geometry with an LEO receiver that receives the signal from the GPS satellite. The angle, α, is a measure of the total bending of the signal ray path due to the Earth's atmosphere. The tangent point is the point of the ray path closest to the Earth's surface. The impact parameter, a ,is the radial distance of the tangent point from the center of the Earth, r_t , multiplied by the index of refraction, n_t , at the tangent point. BOTTOM: The airborne RO geometry with the receiver on an aircraft within the atmosphere.

The first full scale deployment of ARO for a science mission was during the PRE-Depression Investigation of Cloud systems in the Tropics (PREDICT) field experiment in 2010 and the work in this thesis is concerned with the analysis of data from this campaign. The test campaign for GISMOS was carried out in 2008 with flights over the southeastern United States and Gulf of Mexico [*Lulich*, 2010; *Muradyan*, 2012]. Muradyan [2012] established that a dense ARO dataset can be obtained at a rate of about 3 retrievals per hour of flight time, with the lowest profile extending below the aircraft to below 1 km altitude. The sensitivity of ARO to synoptic scale variations in atmospheric vertical structure was also demonstrated, illustrating the potential of the new technique.

1.3 Airborne Radio Occultation

The ARO geometry shown in Figure 1.1 has fundamental differences with the spaceborne technique because the receiver is inside the atmosphere and mounted on an aircraft. The part of the signal path geometry passing through the neutral atmosphere is not symmetric from transmitter to receiver as it is in the spaceborne case. The ARO sounding will only extend from the aircraft altitude to the surface and the retrieval technique will need to account for the unknown atmospheric structure above the airborne receiver [*Healy et al.*, 2002]. It is also necessary to know the atmospheric refractivity at the receiver altitude. In the case of a LEO satellite, which is outside the atmosphere, there will be no bending in the vicinity of the receiver and the index of refraction can be assumed to be unity at the satellite position. The aircraft will also need to be equipped with a high accuracy navigation system so that the receiver trajectory is precisely known. Even a relatively small error in aircraft velocity can result in a large error in retrieved

refractivity. A velocity measurement error above 5 mm/s will lead to errors in the retrieved refractivity of greater than 0.5 % [*Muradyan et al.*, 2010; *Xie et al.*, 2008].

As in spaceborne RO, the refractivity is calculated from the ray path bending angle profile as a function of tangent point height using an Abel integral transform, under the assumption of a spherically symmetric atmosphere. There are horizontal variations in the structure of the atmosphere sampled by the RO profiles, though. The bending is an integral of properties along the full extent of each ray path, and although the majority of bending occurs along the ray path in the vicinity of the tangent point, the properties may not be symmetric further from the tangent point. Also, because the aircraft moves much slower than the setting satellite, the tangent point location will move horizontally away from the aircraft as the satellite sets or rises relative to the receiver horizon. Therefore, a RO profile can be considered a slanted profile representative of averaged atmospheric properties over some horizontal scale length in the vicinity of the tangent point. The duration of a occultation observed by an airborne receiver is longer than for spaceborne RO, so the ARO tangent point drift is greater.

1.4 The GNSS Instrument System for Multistatic and Occultation Sensing (GISMOS)

As mentioned above, GISMOS has been developed to perform ARO measurements. For the work described in this thesis, GISMOS was installed on the National Science Foundation (NSF) Gulfstream-V (GV) research aircraft and deployed to the Caribbean for the PREDICT field experiment to study developing tropical storms in 2010. GISMOS included four Trimble NetRS geodetic quality dual frequency GPS receivers (Figure 1.2) and a 10 Mhz GPS recording system (GRS). The GRS sampled and

recorded both GPS L1 and L2 signals. The data were written to Small Computer System Interface (SCSI) disk drives in a JBOD ('just a bunch of disks') system. A Symmetricom ET6000 GPS frequency generator with a voltage controlled ovenized crystal oscillator provided a common timing signal for the NetRS receivers and the GRS.

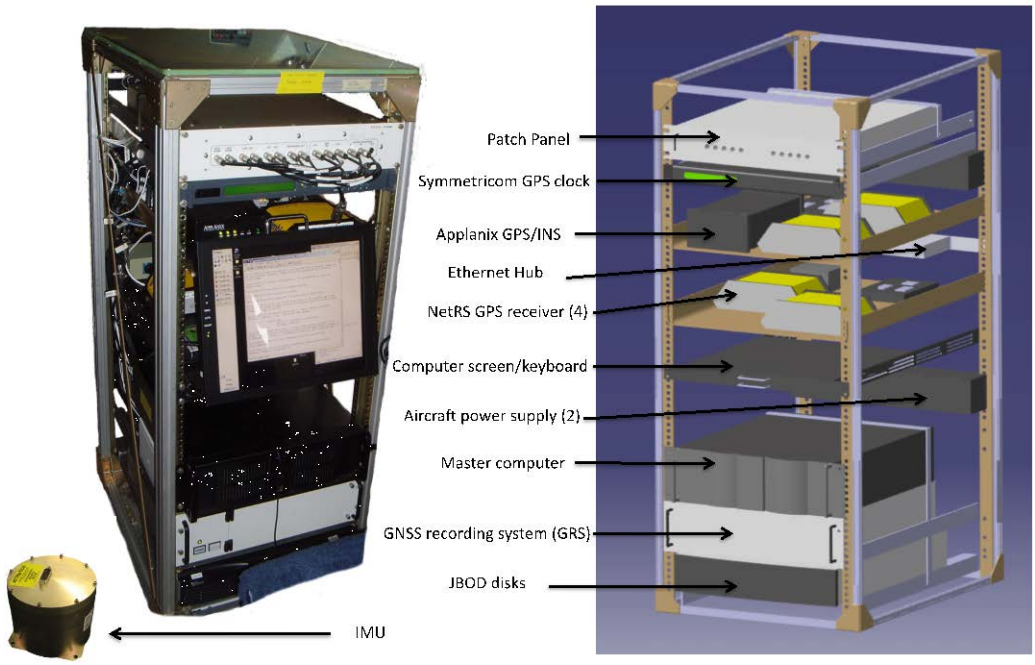

Figure 1.2 The GISMOS instrument rack. The NetRS receivers (yellow) were mounted below the patch panel on top. The GRS and JBOD were installed on the bottom of the rack.

GPS signals were received through seven possible antennas installed on the GV (Figure 1.3). A high gain antenna was installed on the interior of the aircraft window on each side of the GV with a narrow vertical gain pattern aligned to the horizon but wider azimuthal gain pattern to optimize SNR for occultations which are observed near the local horizon of the aircraft [*Lulich*, 2010]. Two isotropic lower gain avionics GPS antennas were also mounted on the exterior sides of the aircraft. Another avionics

antenna was placed on the top of the aircraft. Left and right circularly polarized antennas were mounted on the underside of the plane with a nadir view for making reflectometry measurements and were not used for the PREDICT campaign. A patch panel was used to route signals from the antennas to the receivers and three input channels of the GRS. For the PREDICT campaign, each side mounted avionics antenna was connected to a NetRS receiver. The signals from the high gain antennas were each split to the remaining two NetRS receivers and two GRS channels. The output from the top avionics antenna was routed to the third channel of the GRS.

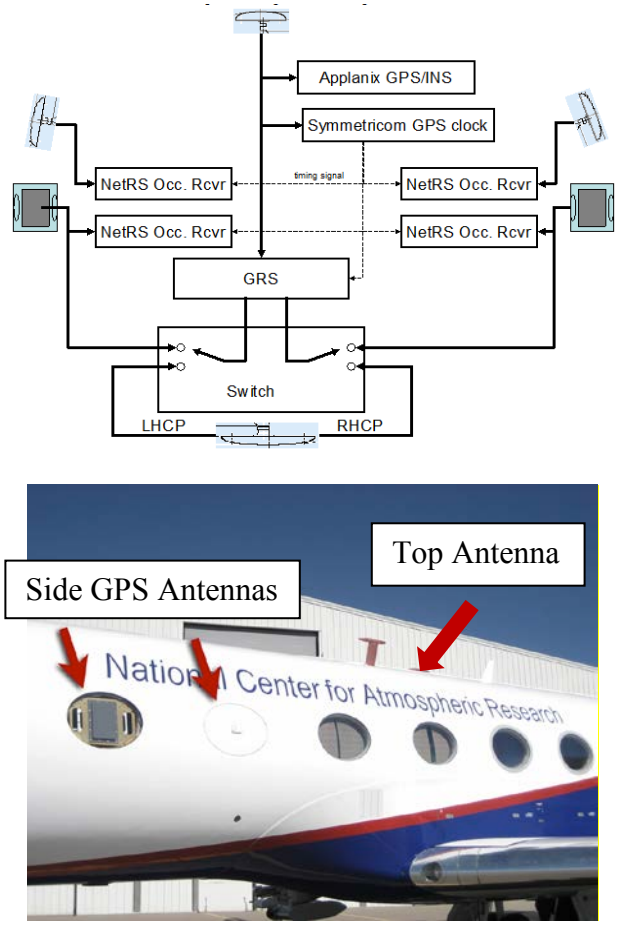

Figure 1.3 TOP: Schematic of GISMOS antennas and their connections. BOTTOM: GISMOS side looking antennas mounted in GV window ports.

For high accuracy navigation data, GISMOS contains an Applanix 510 GPS Position and Orientation System for airborne vehicles (POS-AV) with an integrated inertial measurement unit. The Applanix system provided precise trajectory information with velocity errors within 5 mm/s for each of the antennas locations for use in the ARO refractivity retrievals.

1.5 Tropical Cyclogenesis

The objective of PREDICT was to investigate the development of tropical disturbances before reaching tropical storm strength and collect data which could be used to evaluate new hypotheses on tropical storm development [*Montgomery et al.*, 2012]. The observed processes that occur from the stage of tropical disturbance to that of a tropical depression, which has a defined circulation and an ability to sustain itself by its interaction with a warm ocean, can be used as the basis of a physical definition of tropical cyclogenesis [*Montgomery et al.*, 2006; *Tory and Frank*, 2010]. However, these processes governing tropical cyclone formation are still not fully understood. There is general agreement on the necessary climatology for tropical cyclone formation, such as sea-surface temperatures in excess of 26.5 °C, even though the mechanisms which initiate genesis in an amenable environment are not as well established [*Tory and Frank*, 2010]. Because only a few disturbances develop into a tropical storm out of many occurring in the generally favorable climatologic conditions of tropical oceanic regions, it is necessary to distinguish those with the best likelihood of development [*Frank and Roundy*, 2006; *Nolan*, 2007].

Recently, it was postulated that the presence of a dynamically protected region of

convection and vorticity co-moving with a tropical wave could be an area favorable for cyclogenesis and indicate increased probability of development [*Dunkerton et al.*, 2009]. Within this region of closed streamlines, deep convection is more likely to reach the level of strength where it will independently intensify through interaction with an underlying warm ocean. Because of minimal flow across the streamlines enclosing the protected region, the system would be protected from inhibiting processes such as the lateral intrusion of dry air or strong vertical wind shear. Air within the protected region could be continually re-moistened via convection. A primary motivation for PREDICT was to test this hypothesis of cyclogenesis [*Montgomery et al.*, 2012].

One of the most important systems investigated during PREDICT was sampled by six GV missions over 10 – 14 September 2010 and eventually developed into hurricane Karl. The evolution of Karl and two other PREDICT cases were studied by Davis and Ahijevych [2012] using satellite observations, dropsondes and model operational analysis. The pre-Karl system exhibited a diurnal convective cycle in the region of co-moving closed circulation, with increasing precipitation levels over time. Its development into a tropical storm proceeded quickly after alignment of the low level and middle tropospheric circulations [*Davis and Ahijevych*, 2012]. Consistent with previous studies, they found the vortex alignment, middle-tropospheric moistening, an increase of the middle tropospheric cyclonic circulation and middle to upper level tropospheric warming as signals for imminent genesis of the pre-Karl system. GISMOS collected data during all six missions, providing a large ARO data set for this interesting case.

Because deep moist convection and high mid-level humidity are important conditions needed for the development of a tropical depression such as in the pre-Karl

case, knowledge of the moisture field in the environment of a developing system will be important. ARO provides a promising new tool to sample the developing storm environment. In the pre-Karl case, a dense ARO sampling across the convective environment is available over five days and it should be possible to resolve the high moisture regions near the storm location that may indicate strengthening storm activity and identify any trend in moisture levels near the storm center over the days preceding genesis. Therefore, the pre-Karl system was chosen as a case study to assess the sensitivity of ARO to moisture. A primary objective of this work was to determine the observed scales of temporal and spatial variability of moisture evident directly in the refractivity profiles, and how that variability is evident in comparisons with model fields over the course of storm development. In particular, the sensitivity of ARO refractivity soundings in the middle to upper troposphere to temporal and spatial moisture variations is necessary to confirm prior to any data assimilation efforts.

In order to accomplish this, it was necessary to implement a streamlined analysis process based on previous work done with ARO data [*Muradyan*, 2012; *Xie et al.*, 2008] adapting the use of the Purdue Software Receiver (PSR) [*Acikoz*, 2011; *Heckler and Garrison*, 2004; *Lulich*, 2010; *Ventre*, 2006] to obtain the best quality ARO refractivity soundings. After obtaining the ARO datasets, thorough comparisons were made of ARO with refractivity profiles calculated from both in situ data sets and numerical weather prediction (NWP) model output to provide statistics to validate the airborne technique and to assess ARO accuracy relative to the state of the art spaceborne RO so that realistic observation error estimates could be provided for the future data assimilation efforts.

A radio occultation sounding is not a vertical profile measurement, because the tangent point locations drift horizontally along a path that often exceeds 400 km in the airborne case. The lateral extent of the tangent point sampling must be considered in the analysis of the ARO moisture variability. The larger scale sampling of the ARO profiles can be seen as complementary to the point measurement profiles provided by the dropsondes deployed during PREDICT because they provide additional information from regions not sampled by dropsondes.

This dissertation describes the initial analyses and moisture sensitivity of the ARO data set collected during the PREDICT campaign outlined above. Chapter 2 describes the analysis and evaluation of the set of ARO retrievals obtained from the NetRS geodetic receiver data that demonstrate the proof of concept for the technique and provide a preliminary sampling of the upper troposphere. Chapter 3 reviews the open loop tracking technique using the data recorded by the GRS in order to fully sample the lower troposphere. Chapter 4 examines the ability of the ARO open loop soundings to describe the moisture environment of the pre-Karl system investigated during PREDICT. Chapter 5 summarizes the analysis of the PREDICT ARO data set, highlighting the major advantages provided by this new remote sensing technique.

CHAPTER 2. AIRBORNE GPS RADIO OCCULTATION PROFILES OBSERVED IN TROPICAL STORM ENVIRONMENTS

(An article published in the Journal of Geophysical Research: Atmospheres)

B. J. Murphy[1], J.S. Haase[2], P. Muradyan[1], J.L. Garrison[3], K.-N. Wang[3]

1. Dept. of Earth, Atmospheric and Planetary Sciences, Purdue University, West Lafayette, IN 47907
2. Scripps Institution of Oceanography, University of California, San Diego, La Jolla, CA 92093
3. Aeronautics and Astronautics Engineering, Purdue University, West Lafayette, IN 47907

Corresponding author: Brian Murphy

Dept. of Earth, Atmospheric and Planetary Sciences

Purdue University

550 Stadium Mall Drive

West Lafayette, IN 47907

ph. (765) 494-0659

email: bmurphy@purdue.ed

Key Points

Atmospheric refractivity profiles found using Airborne Radio Occultation (ARO)

This is the first utilization of ARO in a full scale science mission

ARO refractivity is generally within 2% of independent sounding measurements

ABSTRACT

Airborne GPS radio occultation (ARO) data have been collected during the 2010 PRE-Depression Investigation of Cloud systems in the Tropics (PREDICT) experiment. GPS signals received by the airborne GNSS Instrument System for Multi-static and Occultation Sensing (GISMOS) are used to retrieve vertical profiles of refractivity in the neutral atmosphere. The system includes a conventional geodetic GPS receiver component for straightforward validation of the analysis method in the mid to upper troposphere, and a high sample rate (10 MHz) GPS recorder for post processing complex signals that probe the lower troposphere. The results from the geodetic receivers are presented here. The retrieved ARO profiles consistently agree within ~2% of refractivity profiles calculated from the European Center for Medium-range Weather Forecasting (ECMWF) model interim reanalyses as well as from nearby dropsondes and radiosondes. Changes in refractivity obtained from ARO data over the five days leading to the genesis of tropical storm Karl are consistent with moistening in the vicinity of the storm center. An open loop tracking method was implemented in a test case to analyze GPS signals from the GISMOS 10 MHz recording system for comparison with geodetic receiver data. The open loop mode successfully tracked ~2 km deeper into the troposphere than the conventional receiver and can also track rising occultations, illustrating the benefit from the high rate recording system. Accurate refractivity retrievals are an important first step toward the future goal of assimilating moisture profiles to improve forecasting of developing storms using this new GPS occultation technique.

Keywords: radio occultation; airborne observations; dropsondes; tropical cyclone.

2.1 Introduction

Radio occultation (RO) is a remote sensing technique for measuring atmospheric properties using Global Navigation Satellite System (GNSS) signals. It provides high-resolution vertical soundings that have low sensitivity to clouds and precipitation, making them appealing for assimilation in numerical weather prediction (NWP) models [*Poli et al.*, 2010; *Poli et al.*, 2008; *Schreiner et al.*, 2007]. The RO technique measures the excess phase delay and Doppler shift of a GNSS radio signal which results from the atmospheric refraction of the signal along the path between the transmitting GNSS satellite and a receiver in Low Earth Orbit (LEO) [*Kursinski et al.*, 1997]. The airborne RO technique is an extension of the spaceborne technique, which we review below.

Atmospheric refractivity in the neutral atmosphere is related to temperature, air pressure and water vapor pressure by equation (2.1):

$$N = \frac{k_1 P}{T} + \frac{(k_2 - k_1)e}{T} + \frac{k_3 e}{T^2};\ N = (n-1)\times 10^6 \tag{2.1}$$

where N is refractivity in N-units, P is atmospheric pressure in hPa, e is water vapor pressure in hPa, T is temperature in Kelvin and n is the index of refraction [*Healy*, 2011; *Smith and Weintraub*, 1953]. The constant coefficients,

$k_1 = 77.6\ \text{hPa}^{-1};\ k_2 = 70.4\ \text{K hPa}^{-1};\ k_3 = 3.739\times 10^5\ \text{K}^2\ \text{hPa}^{-1}$, are derived from empirical data [*Bevis et al.*, 1994]. The refractive bending angle of the signal ray paths through the atmosphere can be determined from the excess Doppler and the positions and velocities

of the receiver and transmitter using geometric optics [*Fjeldbo et al.*, 1971; *Vorob'ev and Krasil'nikova*, 1994]. A vertical profile of refractivity is then calculated from the bending angles using an Abel transform [*Hajj et al.*, 2002; *Kursinski et al.*, 1997].

In the lower troposphere, multipath propagation occurs due to sharp gradients in refractivity principally due to large moisture variations. The superposition of signals with different Doppler frequencies corresponding to multiple ray paths interferes with the receiver tracking of the signal and retrieval of bending angle using geometric optics. Radio holographic methods have been developed to analyze signal phase and amplitude using Fourier operators, such as Full Spectrum Inversion (FSI), to determine the bending angle profile in the presence of multipath [*Gorbunov*, 2002; *Gorbunov and Lauritsen*, 2004; *Jensen et al.*, 2003; *Jensen et al.*, 2004].

Once the refractivity profile is determined, it can be used to infer temperature and humidity [*Hajj et al.*, 2002; *Healy and Eyre*, 2000; *Rodgers*, 1976]. When using a receiver in LEO, a vertical resolution of ~1.4 km in the stratosphere to less than 500 m near the Earth's surface can be achieved when using geometric optics, corresponding to the first Fresnel zone for GPS RO [*Healy and Eyre*, 2000; *Kursinski et al.*, 1997]. The resolution when using a radio holographic method is approximately 100 m in the lower troposphere with higher resolutions theoretically possible [*Gorbunov et al.*, 2004; *Jin*, 2013]. Vertical resolutions in the lower stratosphere estimated at 100 - 200 m have been obtained using the FSI method [*Tsuda et al.*, 2011].

The first GPS RO mission, the GPS/MET (Global Positioning System/Meteorology) experiment, was launched in 1995 and successfully demonstrated the GPS RO concept [*Ware et al.*, 1996]. Since the GPS/MET experiment, multiple

spaceborne programs have obtained radio occultation measurements using onboard GPS receivers, such as the German CHAllenging Minisatellite Payload (CHAMP) satellite [*Wickert et al.*, 2001], US-Taiwan co-operative Constellation Observing System for Meteorology Ionosphere and Climate (COSMIC) / Formosa Satellite 3 (FORMOSAT-3) [*Anthes et al.*, 2008], International Satelite de Aplicaciones Cientifico –C (SAC-C) [*Hajj et al.*, 2004], National Aeronautics and Space Administration (NASA) Gravity Recovery and Climate Experiment (GRACE) [*Anthes*, 2011a; *Wickert et al.*, 2009] and European Meteorological operational (Metop) [*von Engeln et al.*, 2011] satellites.

With the success of spaceborne systems, it was proposed that the RO technique be adopted for use with a receiver inside the Earth's atmosphere either stationed on a mountaintop [*Zuffada et al.*, 1999], or onboard an aircraft [*Healy et al.*, 2002; *Lesne et al.*, 2002; *Xie et al.*, 2008]. Airborne radio occultation (ARO) makes it possible to target regions of interest providing an increased number of observations within a time frame relevant for synoptic scale storm development, as opposed to spaceborne RO where the sampling is constrained by the orbits of the available LEO satellites and therefore is relatively sparse. ARO complements dropsondes and other airborne remote sensing techniques in that the limb-soundings sample the larger scale environment to the sides of the flight path and can be made at a safe distance from dangerous deep convection within storm systems.

We developed the GNSS Instrument System for Multi-static and Occultation Sensing (GISMOS) for ARO measurements as well as reflection measurements for ocean surface roughness, wind speed, salinity and surface soil moisture [*Garrison et al.*, 2007; *Voo et al.*, 2009]. The GISMOS system was tested in 2008 using the National Science

Foundation (NSF) Gulfstream V (GV) research aircraft at flight altitudes of approximately 14 km over the southeastern United States [*Lulich et al.*, 2010; *Muradyan*, 2009; *Muradyan*, 2012]. The proof-of-concept was demonstrated [*Haase et al.*, 2014] in a preliminary analysis of the data from the 2010 PRE-Depression Investigation of Cloud systems in the Tropics (PREDICT) field campaign to study developing tropical storms [*Montgomery et al.*, 2012]. The focus of this paper is an extension of the work of Haase et al [2014] to a statistical analysis of the ARO results from the complete conventional geodetic GPS receiver dataset during PREDICT, and a preliminary assessment of the utility of the measurements for studying the tropical storm environment. It includes extensive comparisons with dropsonde and radiosonde data as well as NWP model analyses. Previous studies have demonstrated the ability of spaceborne GPS RO to measure the global characteristics of mature tropical cyclone temperature structure, and to provide novel approaches for determining tropical cyclone cloud top heights and their empirical relation to storm intensity [*Biondi et al.*, 2013; *Biondi et al.*, 2011; *Vergados et al.*, 2014; *Vergados et al.*, 2013]. The motivation for this work is to provide additional data for assimilation into numerical models to improve forecasts [*Haase et al.*, 2012]. Previous case studies have indicated that the assimilation of COSMIC spaceborne RO is beneficial to numerical forecasts of tropical cyclones [*Chen et al.*, 2009; *Huang et al.*, 2010; *Liu et al.*, 2012]. However, these studies included only a limited number of profiles within 1200 km of the cyclone center. This work leads the way for future studies of the open loop analysis of the GISMOS 10 MHz data where the ARO technique will be able to provide 10 - 14 profiles near the cyclone center per day.

Section 2.2 reviews the motivation and background for the PREDICT campaign, and provides a description of the GISMOS system and its use during the campaign. We implemented a geometric ray optics retrieval method for the analysis of the data from the conventional geodetic receivers for the upper part of the troposphere, which we describe in section 2.3. Section 2.4 presents an assessment of the accuracy of the ARO results through comparisons with dropsondes, radiosondes and numerical weather model reanalysis profiles. The consistency of the refractivity variations with environmental moisture variations in the vicinity of the developing storm Karl is also examined in section2. 4. A preliminary analysis of the GISMOS 10 MHz GNSS Recording System (GRS) data, which will allow much more comprehensive sampling of the storm regions for rising as well as setting occultations, and will sample into the mid-to-lower troposphere, is given in section 2.5.

2.2 Predict Campaign

2.2.1 Campaign Objectives

The PREDICT experiment took place from 15 August 2010 until 30 September 2010 and was based at St. Croix, US Virgin Islands. It has been postulated that the presence of a dynamically protected region of convection and vorticity co-moving with a tropical wave could lead to an area of enhanced moisture favorable for cyclogenesis [*Dunkerton et al.*, 2009]. Testing this hypothesis was addressed by the PREDICT experiment in the Caribbean and western Atlantic [*Evans et al.*, 2012; *Montgomery et al.*, 2012]. During PREDICT, airborne missions were flown to investigate the developing

tropical cyclone environment before the disturbances reached tropical storm strength. The missions were planned to provide observations within the axes of the African Easterly waves. Approximately 50% of minor Atlantic hurricanes, Saffir-Simpson category 1 and 2, and over 80% of intense Atlantic hurricanes, category 3 and above, develop from an African Easterly Wave [*Landsea*, 1993]. However, determining which waves will develop is a challenge.

The location of the closed circulation region was predicted to be near the intersection of the critical line, where the wave speed matches the mean flow, and the axis of the wave trough [*Dunkerton et al.*, 2009; *Wang et al.*, 2009b]. On a given pressure surface, the critical line was typically oriented east-west whereas the axis of the wave trough was typically oriented north-south. During PREDICT, a well-defined circulation about this point of intersection combined with enhanced total column water vapor in the forecast models motivated a mission. Dropsonde sampling of the area of circulation was used to evaluate the conditions that distinguished between developing and non-developing cases [*Davis and Ahijevych*, 2012; *Komaromi*, 2013].

The primary objective of this study is to provide a preliminary assessment of the ARO method accuracy using the rich PREDICT dropsonde dataset and to develop an ARO dataset for future assimilation with associated observation error estimates. Although dropsonde and radiosonde profiles have their own associated errors, they are currently the best independent benchmark for accuracy relative to other observation systems and are often used for validation of remote sensing systems. Radiosonde biases originate from instrumental error, manufacturer type, and radiation heating. However, these biases have been extensively studied to determine corrections and quality control

for many of these effects [*Durre et al.*, 2005; *Moradi et al.*, 2013; *Reale et al.*, 2012; *Sun et al.*, 2013]. Dropsonde instrumentation is comparable to radiosonde and we expect similar error characteristics. Wang et al. [2009a] and Wang [2005] found good agreement between radiosonde and dropsonde relative humidity and temperature measurements in the lower troposphere (surface to 5 km altitude) where the mean difference was typically less than 2% in relative humidity and ~0.4 °C in temperature, based on 71 co-located radiosonde and dropsonde data [*Wang*, 2005]. We therefore define agreement with these soundings as an assessment of ARO profile accuracy, with the caveat that the observations have fundamentally different spatial characteristics [*Kuo et al.*, 2004]. The expected theoretical error for ARO refractivity is expected to be better than 0.5% up to about 1 km below aircraft height given a velocity accuracy of the navigation system of 5 mm/s or better [*Muradyan et al.*, 2010]. However, if the line of sight for the ARO geometry crosses strong horizontal gradients of refractivity, the assumption of spherical symmetry can introduce refractivity biases up to 1% in the upper troposphere increasing to a maximum of ~4.5% below 3 km altitude [*Xie et al.*, 2008]. This has motivated development of a nonlocal observation operator to account for lateral variations when radio occultation data are assimilated [*Liu et al.*, 2008; *Ma et al.*, 2009; *Sokolovskiy et al.*, 2005a; *Sokolovskiy et al.*, 2005c].

2.2.2 Campaign Measurements

The National Science Foundation (NSF) GV research jet was deployed for twenty-six research missions studying eight storm systems during the campaign. Dropsondes were deployed on all research flights to measure atmospheric conditions in

the environment of each storm. Over five hundred dropsondes were deployed during the campaign [*Montgomery et al.*, 2012]. The GISMOS ARO system was also deployed on the GV and sampled the survey area during all missions. Twenty-one ARO refractivity profiles were retrieved from the conventional geodetic receiver system over the 26 missions for this study, of which 9 were from flights into a tropical disturbance which ultimately developed into Hurricane Karl and was studied extensively during PREDICT. Six flights were made into the pre-Karl disturbance over five days from 10 to 14 September 2010. The disturbance was investigated from early in its development through its genesis to a tropical storm, which made this an ideal system to assess the characteristics of ARO refractivity profiles in the moisture environment of a developing tropical system.

GISMOS recorded occultation data from four geodetic quality dual frequency Trimble NetRS GPS receivers as well as a 10 MHz GNSS Recording System (GRS). Two high gain antennas, with the gain patterns focused on the horizon for extra sensitivity in tracking occulting satellites, were mounted on the sides of the fuselage. Two GPS avionic antennas were also mounted on each side of the aircraft. Each of the four geodetic receivers recorded 5 Hz data from one of the side antennas. A GPS inertial navigation system provided high accuracy aircraft position and velocity using another GPS avionic antenna installed on top of the GV fuselage. The GRS recorded one channel from each of the high gain side looking antennas and one channel from the top antenna. A common timing signal for each receiver was provided by a Symmetricom ET6000 GPS timing receiver with an ovenized crystal oscillator (OCXO) with stability of 3×10^{-11} over one second. Flight level in situ measurements of temperature were made at 50 Hz

with a fast response, all weather, de-iced avionics sensor (Rosemount Model 102AL TAT) with 0.5 °C accuracy (http://www.hiaper.ucar.edu/handbook/index.html). In situ pressure was measured at flight level with 0.1 hPa accuracy. Humidity measurements were made with a vertical cavity surface emitting laser hygrometer and a Buck research model 1011c hygrometer (Project managers' data quality report at https://www.eol.ucar.edu/content/predict-aircraft-documentation-summary). However, because of the inconsistency of recording accuracy, these humidity data were not used.

The precise position and velocity of the aircraft were calculated with the Applanix Mobile Mapping Suite (MMS) post-processing software [*Mostafa et al.*, 2001] using a tightly coupled Kalman filter solution combining 10 Hz GPS observations and 200 Hz inertial measurement unit (IMU) observations. Precise final orbits and clocks were used from the International GNSS Service (IGS) [*Beutler et al.*, 2009; *Beutler et al.*, 1999]. Forward and reverse Kalman filter precise point positioning solutions were averaged to provide a combined solution including optimal error corrections to the linear acceleration and angular rates measured by the IMU. The position precision is better than 6 cm in the horizontal and 90 cm in the vertical, and velocity precision is better than 5 mm/s velocity in all components, as required for accurate airborne retrievals, contributing to less than 0.5% refractivity error [*Muradyan et al.*, 2010; *Xie et al.*, 2008].

2.3 Retreival Method and Data Analysis

2.3.1 GPS Observations of Excess Phase

The travel time of the signal observed by a GPS receiver is a function of the speed of propagation, which depends on the refractive index of the atmosphere, integrated along the path length. The deviation of the latter from a straight line also depends on the refractive index. The gradient of refractivity causes bending of the GPS signals along the propagation path. The tangent point of the refracted ray path is the point of the closest approach to the Earth's surface as shown in Figure 2.1. The observable for ARO is given in terms of the total carrier phase in meters, Φ, of the GPS signal shown in equation (2.2),

$$\Phi_R^T = D_R^T + cC^T + cC_R + I_R^T + cG + \phi_R^T + M_R^T + \varepsilon \tag{2.2}$$

where D_R^T is the vacuum straight line geometric distance in meters between the transmitting GPS satellite and the GPS receiver onboard the aircraft, c is the speed of light in meters per second, cC^T and cC_R, are the satellite and receiver clock errors respectively, I_R^T is the error due to the ionosphere, cG is the relativistic time correction to compensate for the eccentricity of GPS satellite orbits, M_R^T is the integer ambiguity of the carrier wave at the start of signal tracking, ϕ_R^T is the excess phase delay caused by refraction in the neutral atmosphere and ε is the measurement error including thermal noise, and local multipath. The superscript *T* refers to the transmitting GPS satellite and the subscript *R* refers to the receiving aircraft.

Excess phase was found by subtracting the satellite clock error (provided with the IGS orbits), the relativistic effect, the geometric distance and the ionosphere correction from the total phase observed for the satellite. The ionosphere correction was obtained from the ionosphere free total phase using the L1 and L2 GPS signals from the GISMOS dual frequency geodetic receivers [*Misra and Enge*, 2006] as shown in equation (2.3).

$$I_R^T = \frac{f_{L1}^2}{f_{L1}^2 - f_{L2}^2}\phi_{L1} - \frac{f_{L2}^2}{f_{L1}^2 - f_{L2}^2}\phi_{L2} \tag{2.3}$$

Higher order corrections for ionospheric effects are neglected. The excess Doppler, f_d, was found by taking the time derivative of the excess phase, which removes the unknown integer ambiguity.

$$f_d\left(\text{m/s}\right) = \frac{d}{dt}\left\{\phi_R^T + C_R \cdot c + \varepsilon\right\} \tag{2.4}$$

The excess Doppler was smoothed with a 2nd order Savitzky – Golay filter [*Schafer*, 2011] with a span of 5 seconds to reduce the amount of noise propagated through further analysis of the data. The window size of the filter was chosen to preserve the expected vertical resolution at the tangent point defined by the first Fresnel zone of the ray [*Xie et al.*, 2008]. In order to remove the receiver clock error, cC_R, the smoothed Doppler from a GPS satellite at a high elevation, where tropospheric effects were assumed to be negligible compared to other error sources, was subtracted from the occulting satellite Doppler, as shown in Figure 2.2.

2.3.2 Refractive Bending Angle

The impact parameter, a, of the occulting signal ray path is the product of the tangent point radius from the Earth's center and the refractive index at that point (Figure 2.1). The impact parameter is constant along the ray path when refractivity is spherically symmetric. When spherical symmetry is assumed, the bending angle of the signal ray path, α, as a function of impact parameter can be determined from the excess Doppler, given the relative positions and velocities of the satellite and aircraft [*Vorob'ev and Krasil'nikova*, 1994]. The excess Doppler shift of the GPS signal from transmitter to receiver is given by equation (2.5) [*Hajj et al.*, 2002; *Melbourne*, 2005].

$$f_d = \frac{1}{\lambda}\left[n_T \mathbf{k_T} \cdot \mathbf{v_T} - n_R \mathbf{k}_R \cdot \mathbf{v}_R - \mathbf{k} \cdot \left(\mathbf{v_T} - \mathbf{v}_R \right) \right] \tag{2.5}$$

$\mathbf{v_R}$ and $\mathbf{v_T}$ are the aircraft and satellite vector velocities, $\mathbf{k}$ is the unit vector in the straight line direction from transmitter to receiver, while $\mathbf{k_T}$ and $\mathbf{k_R}$ are the unit vectors in the directions of signal departure from the transmitter and subsequent arrival at the receiver, respectively. The refractive index of the atmosphere at the location of the aircraft and the satellite are n_R, and n_T, respectively. The dot products in equation (2.5) can be evaluated to express the excess Doppler shift in terms of the scalar velocities and angles in the plane containing the aircraft, satellite and Earth center as shown in Figure 2.3 and given in equation (2.6) [*Vorob'ev and Krasil'nikova*, 1994].

$$f_d = \frac{v_T}{\lambda}\left[\sin(\eta_T - \beta_T)\sin\gamma_T + (\cos\gamma_T - 1)\cos(\eta_T - \beta_T)\right] - v_R\left[n_R \sin(\beta_R - \eta_R)\sin\gamma_R + (n_R\cos\gamma_R - 1)\cos(\beta_R - \eta_R)\right] \quad (2.6)$$

For the airborne geometry, the satellite is at an elevation where refractivity is negligible and the transmitter index of refraction, n_T, is unity. The in situ flight level data were used to calculate the refractive index, n_R, at the aircraft using equation (2.1). Because in situ flight level water vapor measurements were not functioning reliably during PREDICT, the refractivity at the aircraft flight level was calculated with only the first pressure term using the mean value of the flight level pressure and temperature over the duration of the occultation. The contribution of the wet components to total refractivity is small relative to other error sources at the typical GV flight altitude of 14 km, ~0.05% of total refractivity, [*Muradyan*, 2009]. The bending angle, α, is the sum of the two unknown angles in equation (2.6):

$$\alpha = \gamma_R + \gamma_T \quad (2.7)$$

A second equation in these variables can be derived from Bouguer's formula [*Born and Wolf*, 1999],

$$a = r_T \sin(\gamma_T - \eta_T) = n_R r_R \sin(\gamma_R + \eta_R) = \text{constant} \quad (2.8)$$

where *r* is the radial distance from the center of curvature to a point on the ray path. Note that equations (2.6) and (2.8) differ from those described in Kursinski [1997] and the spaceborne radio occultation literature because $n_R r_R$ is explicitly included and n_R is not

assumed to be unity. Equations (2.6) and (2.8) were solved iteratively using successive substitution to find γ_R and γ_T, where γ_T is expected to be small and is initially chosen to be equal to zero. To compensate for the oblateness of the Earth, the local spherical radius and center of curvature at the tangent point were calculated and the coordinates and velocities were transformed into the reference frame with its origin at the center of curvature prior to the calculation of the bending angle [*Syndergaard*, 1998].

For the setting occultations, the GPS satellite was observed beginning above the horizon of the aircraft (positive elevation angle) and continued below the horizon (negative elevation angle) until tracking was lost, as illustrated in figure 2.1. For every ray path below the horizon of the aircraft, there is a ray path above the horizon with the same impact parameter, *a* [*Healy et al.*, 2002; *Zuffada et al.*, 1999]. The maximum impact parameter occurs at zero elevation angle relative to the local aircraft horizon. The bending angle of the ray path increases slowly as the setting satellite moves from above the aircraft horizon to zero elevation angle. The bending angle then increases much more rapidly as the satellite sets below the horizon, as seen in Figure 2.4.

2.3.3 Refractivity Retrieval

The bending angle, α, in a spherically symmetric atmosphere is an integral function of the refractive index as a function of radius, *r*, from the center of curvature [*Hajj et al.*, 2002; *Kursinski et al.*, 1997].

$$\alpha = -a\int_{r_t}^{r_R} \frac{1}{\sqrt{n^2 r^2 - a^2}} \frac{d(\ln n)}{dr} dr - a\int_{r_t}^{r_T} \frac{1}{\sqrt{n^2 r^2 - a^2}} \frac{d(\ln n)}{dr} dr \qquad (2.9)$$

The radius at the tangent point is r_t and the integration continues to r_R, (the radius at the receiver) and r_T (the GPS transmitter radius) in the left and right terms, respectively. In spaceborne RO with both the receiver and transmitter outside the atmosphere, there is no bending accumulated in the vacuum from radius of the low earth orbiting satellite receiver to the radius of the GPS satellite, so the two terms are equivalent. When the receiver is inside the atmosphere as for the airborne case, these two terms are not equivalent. However, the bending angle for a negative elevation angle ray path can be expressed as a sum of the bending angle accumulated below the radius of the aircraft and the bending accumulated from the radius of the aircraft to the radius of the GPS satellite.

$$\alpha = -2a\int_{r_t}^{r_R} \frac{1}{\sqrt{n^2r^2 - a^2}} \frac{d(\ln n)}{dr} dr - a\int_{r_R}^{r_T} \frac{1}{\sqrt{n^2r^2 - a^2}} \frac{d(\ln n)}{dr} dr \qquad (2.10)$$

The second term is equivalent to the bending accumulated for a positive elevation angle ray with equivalent impact parameter. The partial bending angle, α', is defined as the difference between the bending angles of positive and negative elevation angle rays [*Xie et al.*, 2008],

$$\alpha' = \alpha_N - \alpha_P = -2a\int_{r_t}^{r_R} \frac{1}{\sqrt{n^2r^2 - a^2}} \frac{d(\ln n)}{dr} dr \qquad (2.11)$$

and depends only on the atmospheric refractivity below the aircraft. The refractive index at a specific height in the atmosphere below the receiver is found using the Abel inverse of equation (2.11),

$$n(a) = n_R \exp\left[\frac{1}{\pi}\int_{x=a}^{x=n_R r_R} \frac{\alpha'(a)}{\sqrt{x^2 - a^2}}\, dx\right] \tag{2.12}$$

where $x = nr$. Once again, equation (2.12) differs from that describing the spaceborne case by the factor n_R. The Abel transform pair given by equations (2.11) and (2.12) can be used to either make a forward calculation of partial bending angle from a known refractivity profile or an inverse calculation of refractivity from a profile of partial bending angle.

As an example, the bending angle found from the excess Doppler measured during an occultation of satellite PRN25 (GPS satellites are identified by the Pseudo-Random Number code) during research flight 18 (RF18) on 13 September 2010 is shown in Figure 2.4. To find the partial bending angle, the point with maximum impact parameter in the ARO bending profile is found. This point is taken as zero elevation angle and the profile is split into positive and negative elevation angle sections. The positive and negative elevation bending angle sections were then each interpolated at equal impact parameter intervals of 0.01 km so that the partial bending difference could be formed. The noise in the excess Doppler profile produces noise in the bending angle profile, which is greatest at zero elevation angle. To reduce the propagation of this noise in the calculation of refractivity, the retrieval process was carried out in two steps. First, a refractivity profile was derived from the Abel inverse transform of the noisy partial bending angle profile. Then a quadratic fit was made to the log of refractivity as a function of height below the aircraft. The refractivity was extrapolated upwards to 30 km height using an exponential function with a 7 km scale height. Assuming this smooth

refractivity profile, the bending angle was simulated with a forward Abel calculation from equation (2.11). The noisy section of the bending angle profile near the maximum impact parameter and the positive elevation angle section of the bending angle profile were then replaced with the simulated bending angle profile, as shown in Figure 2.4. Because the refractivity at the aircraft height is constrained by the in situ measurement, the error made by extrapolating refractivity above the aircraft is small, and will be assumed to be insignificant compared to the bending angle noise that was eliminated. A revised partial bending angle was calculated and used in a second iteration of the inverse Abel transform to find the final estimate of the refractivity profile.

For comparison to the ARO refractivity profiles, we use equation (2.1) to calculate vertical refractivity profiles from dropsonde data as well as model reanalyses estimates of geopotential height, pressure, temperature and relative humidity. Saturation vapor pressure was calculated from temperature following the Federal Meteorological Handbook no. 3 (www.ofcm.gov/homepage/text/pubs.htm). The geopotential height values in the dropsonde and model profiles, which are referenced to the equipotential surface at sea level, were converted to geometric height [*Hofmann-Wellenhof and Moritz*, 2006]. Then the geometric height was corrected for the difference between the geoid (sea level) and the WGS84 ellipsoid that serves as reference for the GPS geometric height using the EGM2008 geoid model [*Pavlis et al.*, 2012] (www.geographiclib.sourceforge.net/cgi-bin/GeoidEval).

2.4 Results

We assessed the accuracy of ARO refractivity profiles by comparing them with dropsonde, radiosonde and model reanalysis profiles at nearby locations. The location of the ray path tangent point moves horizontally with changing tangent point altitude as the receiver-transmitter geometry changes, primarily because the GPS satellite is moving significantly faster than the aircraft. To provide a consistent reference point for comparison, the ARO refractivity profile was assigned a location at the *occultation point*, which we defined as the tangent point location at 500 hPa, the height which approximately divides the mass of the atmosphere in half, or the lowest tangent point location if the profile does not extend below 500 hPa. Typically, the horizontal movement is on the order of 150 - 400 km. However, the drift is not linear in tangent point altitude, as shown in Figure 2.5. The drift is greatest at higher altitudes. The horizontal drift of the tangent point altitudes from 14 to 10 km was approximately twice the horizontal drift in the height interval from 10 to 6 km (Figure 2.5).

For each retrieved ARO profile, we selected the closest dropsonde profile for comparison. The maximum separation was 370 km. This relatively large distance criterion was chosen to provide a reasonable number of matches, and is comparable to the criterion chosen in previous RO studies [*Sun et al.*, 2010].

Dropsonde and ARO profiles were interpolated to common levels and the difference between the ARO and the dropsonde profile was found using equation (2.13).

$$\delta_N = \frac{N_{ARO} - N_{DROP}}{N_{DROP}} \times 100\% \tag{2.13}$$

The same approach was used for the model reanalyses. Because of the horizontal drift of the tangent point and the physical drift of the dropsonde descent, some differences are expected between ARO and the nearly vertical dropsonde profiles. In addition, horizontal gradients of refractivity along the signal ray path, especially due to smaller scale moisture variations, limit the accuracy of the spherical symmetry assumptions used in the refractivity retrieval. The ARO retrieval represents a weighted average of the refractivity along the line of sight between the receiver and the satellite. The values are highly weighted towards the locations of the tangent points because that is where the density is greatest. For example, we used ray tracing to calculate in a 1D atmosphere that 70% of the bending is accumulated within $\pm$50 km of the tangent point at 10 km height and within $\pm$170 km of the tangent point at 3 km height.

2.4.1 Dropsonde and Radiosonde Comparison

We analyzed the GPS ARO data for 21 occultations recorded by the GISMOS geodetic receivers over the course of the campaign. Many more occultations were recorded by the GRS and refractivity profiles will be retrieved from these data in future work. The ARO refractivity profiles extended from the aircraft height, (typically about14 km), until tracking was lost. The deepest profile was retrieved from the occultation of PRN25 satellite from flight RF18, Figure 2.5, which extended down to a height of 4.1 km. All of the ARO refractivity profiles extend from the aircraft altitude to at least 7.7 km altitude and the average height reached for all profiles was 6.3 km. Figure 2.6b shows the refractivity profile from the RF18 PRN25 occultation, as well as the profile calculated from the dropsonde nearest to the occultation point (D20100913_132359 from RF18 on

13 September 2010) (http://data.eol.ucar.edu/master_list/?project=PREDICT) and the profile calculated from the 12:00 UT Kingston (MJKP), WMO station #78397, radiosonde. For this case, the ARO refractivity differs from the dropsonde by about 1% over the height range of the profile and both ARO and dropsonde refractivity (Figure 2.6c) are significantly higher than the environmental mean defined later in section 4.3. Both the ARO and dropsonde profiles sample air that is moister than the MKJP radiosonde profile (Figure 2.6a). The contribution of temperature versus moisture in these comparisons is discussed in detail in section 2.4.3.

Each of the ARO refractivity profiles was compared to the dropsonde deployed nearest to the occultation point, and the percent differences are shown in Figure 2.7a along with the mean of all profiles at each height. In Figure 2.7c the standard deviation is shown in green and the number of profiles at each height is indicated in red. Below 7 km the sample size was too small to make a robust estimate, but the data are shown in Figure 2.7 to illustrate the penetration depth of observations below that height by the geodetic receivers. The average spatial separation between dropsonde and ARO occultation point was 118 km and the greatest separation was 367 km. Fourteen of the twenty-one ARO profiles were within 120 km of a dropsonde location. The average temporal separation between the ARO profiles and the corresponding dropsonde release times was 1.42 hours with fourteen of the twenty-one profiles separated by less than 2 hours. No attempt was made to distinguish between profiles in different convective environments. All flights were made when deep convection was present and almost all missions were flown into storms before they reached tropical storm stage [*Montgomery et al.*, 2012].

The mean difference of ARO minus dropsonde refractivity is near zero at 12 km, increasing to 0.8% at 9.3 km and decreasing to zero at 8 km, with a positive bias (ARO higher than dropsonde refractivity). The mean difference shows a negative bias below 8 km. The standard deviation as a function of height is about 0.8% in the 12 km to 8 km height range and then increases to 1% from 8 to 7 km. A 0.8% refractivity difference corresponds to a 2 K error in temperature at 10 km height assuming temperature is about -34 °C and refractivity is 95 N units at this height.

The ARO profiles were also compared with radiosonde profiles over the entire PREDICT campaign (Figure 2.8). Due to the sparseness of radiosonde stations in the Caribbean, the comparison was limited to 16 profiles that were within 400 km and 5.5 hours spatial and temporal separation, and many of these pairs occurred on the ferry part of the flight or well away from the center of most active convection. The mean difference is near zero at 12 km, increasing to a maximum of 0.8% at 9.3 km, and decreasing back towards zero at 7 km as shown in bold in Figure 2.8. The ARO - radiosonde difference has similar height dependence as the ARO - dropsonde difference. The standard deviation over this height range increases from about 0.5% at 12 km to 2% at 7 km as shown in Figure 2.8, somewhat greater than the dropsonde because of the greater spatial and temporal separation.

Given the novelty of these results, it is useful to review similar studies with spaceborne RO. The ARO profile accuracy is comparable but a little lower than spaceborne RO profiles, as expected, by the level of noise introduced by the less stable platform. Available spaceborne RO profiles are too sparse for comparison to nearest ARO geodetic receiver profiles from PREDICT. However, we can evaluate the results

relative to previous studies comparing spaceborne RO refractivity profiles with radiosonde soundings [*Kuo et al.*, 2005; *Sun et al.*, 2010; *Wickert et al.*, 2004; *Xu et al.*, 2009]. For instance, Kuo et al. [2005] compared spaceborne RO refractivity soundings from the NASA - German co-operative CHAMP mission with data from regional groups of radiosondes released within 2 hours and 300 km of CHAMP RO soundings, comparable time and distance separation to our ARO - dropsonde comparisons. Similar to the airborne ARO - dropsonde comparison, CHAMP soundings at similar latitudes as the PREDICT campaign also showed the mean difference increasing as the height decreased. The CHAMP - radiosonde refractivity bias in the Australia region varied from near zero to 0.5% in the height range of 12 to 4 km, and then decreased to negative values below 4 km, whereas in Figure 2.7c and Figure 2.8, the ARO bias transitions to negative values below 8 km. The standard deviation of spaceborne RO also increases with decreasing height in a manner similar to the airborne case. For example, spaceborne RO gives a standard deviation of about 1% above 7 km, which increases to 4% at 4 km for 366 radiosonde comparisons from Australia in Kuo et al. [2005]. The ARO – dropsonde differences would be expected to be greater than spaceborne – radiosonde, as well as terminating at higher levels, given that they were recorded in the challenging environment of the Caribbean region, always in proximity of storm systems. Despite these differences, it is encouraging to find initial results to be of comparable magnitude to results seen in the comparison of operational spaceborne RO soundings to radiosondes.

An extensive study with globally aggregated COSMIC spaceborne RO data [*Sun et al.*, 2010] revealed a refractivity bias of radiosondes under 0.2% from 12 to 6 km, and a standard deviation that increased from 0.7% at 12 km to 1.5% at 6 km. With a larger

dataset, that study also investigated the dependence of the standard deviation on spatial and temporal separation of the soundings from the spaceborne RO profiles. For 0 - 0.25 hours separation at 7.5 km height, the standard deviation increases from 0.5% to 1.2% as the separation distance increases from 0 to 275 km. Thus, the ARO standard deviations are within the expected range given the proximity to the soundings.

2.4.2 Model Analysis Comparison

The ARO refractivity profiles were also compared to refractivity profiles calculated using the European Center for Medium-range Weather Forecasts (ECMWF) European ReAnalysis interim (ERAI) model [*Dee et al.*, 2011]. The refractivity profiles were calculated from the pressure, temperature, moisture, and geopotential height values extracted from the model at the grid points nearest to the ARO occultation point for the comparison. The model values at 37 levels were interpolated to 0.75° resolution from 1.5°, but no time interpolation in the 6 hour reanalysis was made as the ARO profiles were already well co-located in time with an average separation in time of 1.2 hrs. The temporal separation has less impact than spatial separation, as Chen et al. [2011] showed no variation in COSMIC RO agreement with model forecasts for 0 - 2.5 hours separation. The average distance between ARO occultation points and the nearest model grid point was 30.6 km. Figure 2.7b shows the difference with ERAI as a function of height for each of the 21 ARO refractivity profiles and the mean difference at each height in bold. In contrast to the dropsonde comparison, the mean difference between ARO and ERAI is negative, from about -0.5%, at 12 km to 7 km height to -1% at 7 km height. In Figure 2.7d, the number of profiles available at each height is shown in red, the mean difference

again in black, and the standard deviation in green. The standard deviation is 1.5% in the 12 km to 9 km height range, increasing to 2% by 7 km height. The agreement with the independent dropsonde observations is slightly better than the agreement with the model.

The PREDICT campaign took place at tropical latitudes of 17-19^{o}. An inter-comparison among CHAMP and SAC-C spaceborne RO data and model fields [*Kuo et al.*, 2004] illustrated the strong latitude dependence of the agreement among datasets. Moisture variability of the tropical lower troposphere causes larger standard deviations than observed at higher latitudes. The ECMWF Tropical Ocean and Global Atmosphere (TOGA) analysis at 2.5° resolution was used for that globally aggregated study. A bias of less than 0.2% was seen between spaceborne RO and ECMWF-TOGA in the 7 - 12 km height range for tropical latitudes with a standard deviation of about 0.5 - 1%. However, the standard deviation reached 3% near the surface in the tropics compared to less than 2% at latitudes greater than 30^{o}. A comparison between the GRAS spaceborne RO data and the ECMWF analysis also considered the latitude dependence [*Zus et al.*, 2011]. For tropical latitudes from -30° to 30°, the standard deviation of GRAS RO refractivity differences increased from about 0.5% at 10 km to 2% at 6 km, comparable to the ARO statistics. The GRAS profiles also showed higher biases in the tropics of -3% at 1 km, compared to -1.5% biases at high latitudes. The PREDICT ARO model comparison statistics are thus more comparable to the spaceborne RO model statistics found in the tropics. In addition, the selective sampling of the ARO profiles in the vicinity of tropical storms contributes to larger differences relative to spaceborne RO that sampled the entire tropical latitude band, with a proportionally lower sampling of this

highly variable tropical storm environment. This contributes to the larger standard deviations seen in Figure 2.7 and Figure 2.8.

2.4.3 Pre-Karl Refractivity

A subset of the ARO profiles was used to examine refractivity structure as the pre-Karl system developed. In particular, we present the profiles retrieved near the National Hurricane Center (NHC) best track locations of the investigated area during the transition from tropical disturbance to tropical storm, relative to the surrounding environment. The pre-Karl disturbance first developed from the merger of a tropical wave and a low pressure trough north of the South American coast just east of Venezuela on 1 September 2010. The disturbance moved west - northwest over the next two weeks into the Caribbean. Beginning on 10 September 2010, PREDICT flights RF14 – RF19 were flown into the pre-Karl system over a five-day period ending on the 14th (Figure 2.10). Over this period, pre-Karl development was slow and convection disorganized. Up until the 13th, the low level circulation was displaced relative to the mid-level circulation [*Davis and Ahijevych*, 2012]. After the alignment of the circulations on the 13th, the disturbance developed further, reaching tropical storm strength on 14 September (day T-0). After this Karl eventually moved west across the Yucatan peninsula south of Cancun and developed into a major hurricane in the Bay of Campeche by 17 September (A detailed report is found at www.nhc.noaa.gov/pdf/TCR-AL132010_Karl.pdf).

In general, for developing disturbances observed during PREDICT, a warm core formed within 24 hours of genesis with a temperature anomaly of up to 2 K in the upper troposphere near the storm center [*Komaromi*, 2013]. The daily mean temperature

increased near the storm by about 3 K at 9 km altitude for pre-Karl flights over 10 - 14 September [*Smith and Montgomery*, 2012]. The observed warm core is consistent with previous studies of tropical cyclones [*Biondi et al.*, 2013; *Davis et al.*, 2014; *Houze et al.*, 2009; *Kidder et al.*, 2000; *Merrill*, 1991]. The mean system relative humidity remained relatively constant below about 3 km over 10 - 14 September, while humidity generally increased in the mid-level to 10 km [*Smith and Montgomery*, 2012]. We investigate the variability in refractivity as seen in the dropsonde data over this time period and then examine the consistency of the ARO refractivity with the evolution of Karl as described in these previous studies.

The mean environmental refractivity over the four day period 10 - 13 September was calculated using data from all 105 PREDICT dropsondes deployed during RF14 through RF18 (Figure 2.9a). This mean refractivity profile, which we refer to as the pre-Karl environmental mean, provides a convenient pre-genesis reference for comparison to profiles obtained with ARO data.

Atmospheric refractivity can be considered as the sum of a dry term that depends on temperature and dry pressure alone, and a wet term that contains water vapor pressure as shown by the re-arrangement of equation (2.1) where dry pressure is equal to $P - e$.

$$N_{dry} = k_1 \frac{P - e}{T}; \quad N_{wet} = k_2 \frac{e}{T} + k_3 \frac{e}{T^2}. \tag{2.14}$$

In the upper troposphere where moisture levels are low, the dry term is dominant and most of the variations in refractivity are due to temperature variations. The wet component begins to make a greater contribution to refractivity variations below 9.4 km

where moisture levels are greater (Figure 2.9b). On average, the wet contribution to the dropsonde refractivity is about 30 - 35% of total refractivity near the surface while just 0.3% of total refractivity at 12 km for the pre-Karl environmental mean profile. However, there is a significant difference between the magnitude of variations for the two components. Figure 2.9c shows the difference between the dry component calculated from each individual dropsonde and the pre-Karl environmental mean total refractivity using equation (2.15).

$$\delta N_i^{dry} = \frac{N_i^{dry} - \overline{N^{dry}}}{\overline{N^{total}}}; \quad \delta N_i^{wet} = \frac{N_i^{wet} - \overline{N^{wet}}}{\overline{N^{total}}} \tag{2.15}$$

The dry dropsonde refractivity varies at most by 0.5% from the mean over the five flights (RF14 through RF18). The difference between the wet component of refractivity for each dropsonde and the pre-Karl environmental mean total refractivity over the same period is shown in Figure 2.9b. The variation ranges from 3 - 10% with large variations in the 4-6 km height interval. Even at 9.4 km the standard deviation of the moist dropsonde refractivity variations about the mean are more than 3 times the dry refractivity standard deviation. This illustrates that over this pre-genesis time period, the refractivity variations from the surface to as high as 9.4 km are associated primarily with moisture rather than temperature variations.

Komaromi [2013] found a warm core temperature anomaly up to 2 K in the upper troposphere of developing PREDICT tropical disturbances over the 24 hr period before genesis. This would lead to a 0.5% variation in refractivity, so any warm core signature in the ARO profiles remains small in comparison to the moisture signal. Relative to this

background, the 3-10% variation due to moisture variations dominates the refractivity profiles. We conclude that direct observations of ARO refractivity will definitely be a sensitive indicator of humidity variations in this type of environment. Of course, the signal from both the warming core and changes in humidity are contained in the refractivity measurement, and would impact both fields in a data assimilation experiment.

The pre-Karl storm track positions provided by the NHC (www.nhc.noaa.gov) and the occultation tangent point paths tracked by GISMOS geodetic receivers over the same period are shown in Figure 2.10. Nine ARO refractivity profiles were available for 10 - 13 September. No usable retrievals were available from the geodetic receiver data from RF19 on 14 September, although data are available from the GRS system (see section 4.4).

The dynamically protected region hypothesized to enable thermodynamically favorable conditions for tropical cyclone development is on the meso - α scale [*Wang*, 2012]. We used a 6° by 6° box as defined by Wang [2012] around the NHC best track storm locations to describe this region. Seven of the nine ARO refractivity profiles fall within this distance range and were used to examine the change in refractivity over the development of the system from day T-4, 10 September, until day T-1, 13 September, where T is the day of genesis of the tropical storm (boxes in Figure 2.10). ARO occultations PRN25 and PRN30 from RF14 (10 September, T-4), PRN24 from RF15 (T-4), PRN24 from RF16 (T-3), PRN22 from RF17 (T-2), and PRN25 and PRN30 from RF18 (T-1), fall within this spatial scale. These profiles are compared to the pre-Karl environmental mean refractivity in Figure 2.11, where the profile differences are labeled by time before genesis. The seven ARO profiles were sampled between 8 A.M. to 4 P.M.

local time. The largest change from one day to the next is 4% and we can conclude, based on the small temperature variation shown in Figure 2.9c, that the refractivity variation is primarily due to moisture. The two RF14 occultations from day T-4 have the lowest refractivity while the refractivity of the RF15 (T-4), RF16 (T-3) and RF18 (T-1) profiles are greater, consistent with moistening within the mesoscale area containing the storm center as pre-Karl disturbance approaches genesis. This preliminary result is based on only a limited number of profiles, but is consistent with the increase in moisture observed at mid to upper levels in the interior of the tropical wave for the pre-Karl case [*Davis and Ahijevych*, 2012; *Smith and Montgomery*, 2012].

2.5 Discussion

As noted above, the ARO refractivity agrees best with dropsondes and the ERAI reanalysis in the range from 7 to 12 km, however there are profiles that deviate greatly below 7 km as moisture levels increase in the lower troposphere [*Sokolovskiy*, 2001]. Sharp gradients in moisture can create atmospheric multipath, where the measured Doppler shifts will not represent unique signal paths but composites of more than one signal arriving at the receiver simultaneously [*Melbourne*, 2005]. The increased error in cases extending below 7 km near the end of tracking is likely due to atmospheric multipath [*Ao et al.*, 2003; *Sokolovskiy*, 2001]. Additionally, the greater variability of moisture discussed in section 2.4.3 (Figure 2.9b) and resulting variability in refractivity can exacerbate differences resulting from spatiotemporal mismatches. Closer agreement was achieved as expected at higher altitudes, where refractivity is dominated by temperature and refractivity is less variable horizontally.

The geodetic GPS receivers were included in the GISMOS design in order to provide straightforward verification of system operation without complex signal analysis. The majority of refractivity profiles retrieved from the geodetic GPS receivers do not extend below 6 - 7 km height, and only a few of the many possible occultations were successfully recorded by these receivers. Even in this limited height range, however, it is possible to see significant variations in moisture. The dropsonde data in Figure 2.9 illustrate that the variability at this height is still dominated by moisture rather than temperature variations over the 4-day genesis period for Karl. In studies of other storms during PREDICT, moisture variability in the upper tropospheric levels was associated with dry air intrusion from large-scale subsidence or advection that can suppress deep convection and tropical cyclone formation [*Fritz and Wang*, 2013; *Wang*, 2012]; therefore, it is useful to have these observations above 6 km. However, further science benefit will result from the data analysis from the GRS instrumentation that samples the raw RF signal and penetrates deeper into the low to middle tropospheric region that is important to deep convection.

An example of the total number of possible setting and rising occultations is shown in Figure 2.12 for research flight RF18. The 14 possible ARO profiles that can be retrieved with open loop tracking is a significant increase over the one available COSMIC spaceborne profile during the time period of RF18 and the 3 ARO profiles retrieved by the GISMOS geodetic receivers (Figure 2.12). The geodetic GPS receivers recorded only a small subset of occultations because the conventional phase-lock loop (PLL) tracking relies on feedback from the incoming signal to maintain a zero phase error between the incoming signal and replica. They typically lose lock on the signal if there

are rapid phase changes or large fluctuations in signal amplitude, as can be produced by sharp gradients in refractivity. These types of signal variations are expected to occur in the mid to lower troposphere where moisture is increasing with decreasing altitude and has higher variability. This has been extensively observed in GPS/MET and CHAMP [*Ao et al.*, 2003; *Rocken et al.*, 1997]. The early termination of tracking at low altitudes was expected and influenced the design of the earliest spaceborne occultation receivers [*Melbourne*, 2005], as well as the design of GISMOS [*Garrison et al.*, 2007]. GISMOS was designed with the GRS to sample the raw GPS signals at 10 MHz for later post-processing with a software receiver. An open loop tracking algorithm uses an a priori geometric model of the Doppler shift that does not rely on signal feedback for tracking Doppler in the post-processing. This method avoids the problems introduced by rapidly changing phase, allows recovery of the data deeper into the moist lower troposphere, and makes analysis of rising occultations possible [*Lulich et al.*, 2010; *Sokolovskiy*, 2001], (K.-N. Wang et al, Open-loop tracking of rising and setting GPS radio-occultation signals from an airborne platform: signal model and error analysis, submitted to *Transactions on Geoscience and Remote Sensing*, 2014). Data from a test case were analyzed with the open loop method for occulting PRN25 during RF18 and the resulting refractivity profile was compared to the result from the Trimble NetRS conventional geodetic receiver (Figure 2.13a,b) [*Haase et al.*, 2014]. The open loop result extends about 2 km lower than the profile from the geodetic receiver. The small differences between the two profiles are much smaller than the differences found in the dropsonde comparisons.

Rising occultations can be analyzed using the open loop approach as well, since it operates on the pre-recorded intermediate-frequency (IF) GPS data, so signal acquisition

and initiation of tracking can occur after the satellite reaches a high elevation. In a second test case of open loop tracking, the RF18 prn20 rising occultation was retrieved beginning near 4 km altitude (Figure 2.13c). The use of open loop tracking has demonstrated superior results in previous GISMOS validation campaigns and produced one to two rising or setting occultations per hour of flight [*Muradyan*, 2012]. A preliminary analysis of the recovered carrier phase signals from PREDICT indicates that 10 to 15 ARO profiles will be available for each mission, comparable to the number of dropsondes released. The open loop tracking dataset will contribute a significantly increased number of profiles so that the statistics can be evaluated at lower altitudes, and with respect to temporal and spatial separation as has been carried out for spaceborne RO (i.e. Chen et al. [2011]). The analysis of the open loop tracking data is ongoing and will be the subject of future work.

While the geometric optics retrieval technique was adequate above 6-7 km, it is possible that the refractivity errors below that height are increased due to atmospheric multipath just prior to loss of signal tracking. The small number of profiles that extend below 6 km is insufficient to provide a statistically robust conclusion. However, the availability of the open loop data will make it worthwhile to implement the Full Spectrum Inversion method [*Jensen et al.*, 2006; *Jensen et al.*, 2003], for example, to extend the profiles further into the lower troposphere in the presence of atmospheric multipath.

The extensive GPS ARO dataset was collected with the ultimate goal of providing additional data for assimilation into numerical models to improve tropical cyclone forecasts. Given that previous case studies that assimilated sparsely sampled COSMIC spaceborne RO data indicate an improvement to numerical forecasts of hurricane

development [*Huang et al.*, 2010; *Liu et al.*, 2012], assimilation of the denser observations possible with ARO [*Lesne et al.*, 2002], particularly in the near-storm environment (Figure 2.12), could potentially show significant further impact on hurricane forecasts. The nonlocal refractivity assimilation operator for the Weather and Research Forecasting Data Assimilation (WRFDA) system has been developed for airborne observations based on Zou et al [1999]. It includes the modifications for the asymmetric recording geometry below flight level and assimilation of observations at each height at the actual horizontal location of the tangent point to account for the larger tangent point drift of airborne observations, thus mitigating the impact of the spherical symmetry assumption [*Haase et al.*, 2012]. The future results from the complete ARO open loop tracking analysis will be useful for this assimilation study.

The assimilation of dropsonde and airborne radio occultation observations into NWP models are complementary, since dropsondes measure the local properties at specific points, and the ARO observations measure the properties of the larger scale environment. Dropsondes measure temperature and moisture directly and additionally provide wind observations. However, dropsondes have a high cost per observation (~$700), require special modifications to the aircraft, permission from air traffic control for release, and have significant safety restrictions that limit deployments over land. The ARO technique, on the other hand, has the potential to be adapted to a wider range of aircraft for continuous observations at low additional cost.

2.6 Conclusions

The GISMOS airborne radio occultation (ARO) system was deployed during the PRE-Depression Investigation of Cloud systems in the Tropics (PREDICT) field experiment and operated continuously throughout the 45 day campaign. The system includes a conventional geodetic GPS receiver component for straightforward validation of the analysis method in the mid-to-upper troposphere, and a high sample rate (10 MHz) GPS recorder for post processing of complex signals that probe the lower troposphere. This is the first study to assess the quality of ARO data, and to demonstrate the potential of this new technique as well as provide a first look at the usefulness of the technique for observing moisture variability above 6 km with the complete geodetic GPS receiver dataset.

A dataset of 21 ARO refractivity profiles were retrieved that sampled the atmosphere in the environment of 6 tropical disturbances, several of which developed into tropical storms. The ARO profiles were compared with refractivity profiles calculated from the PREDICT dropsonde data, and to refractivity profiles derived from the ECMWF interim reanalysis within about 30 km of the occultation point. Overall, the ARO refractivity compared favorably with PREDICT dropsonde refractivity and ERA-Interim refractivity, even in this rapidly changing heterogeneous environment. The standard deviation of the difference of the ARO refractivity from dropsondes did not exceed 1.5% and the bias was less than 0.5% from 7 to 12 km altitude. The standard deviation of the difference of the airborne refractivity from ERA-Interim was less than 2% and the bias was also less than 0.5% over the 7 - 12 km height range. These values are

comparable to results found at similar tropical latitudes for spaceborne radio occultation profiles, even though the ARO sampling was primarily in challenging near-storm environments with highly variable moisture fields.

Refractivity profiles were shown for 7 occultations in the environment of the pre-Karl tropical disturbance over the pre-genesis period 10 -13 September 2010. Dropsondes over this period show that in the tropical environment, the refractivity variations are primarily indicative of moisture variations rather than temperature. With this limited preliminary dataset available from the conventional geodetic GPS receivers, we found that the change in the measured refractivity of the ARO profiles relative to the pre-Karl environmental mean refractivity was consistent with moistening in the vicinity of the pre-Karl storm center [*Davis and Ahijevych*, 2012; *Smith and Montgomery*, 2012]. One day prior to genesis, the ARO profile nearest the NHC best track location had systematically higher refractivity relative to the pre-Karl environmental mean over the 7 - 10 km height interval. In contrast, four days prior to genesis, the profile nearest the center had refractivity consistent with the background environmental mean over that height range. This example illustrates that the ARO technique is capable of making reliable measurements in the near storm region.

The conventional GPS geodetic receivers performed surprisingly well in this moist tropical environment using standard GPS avionics antennas for setting occultations above 7 km. The relatively small number of occultations available was due to the limitations of phase locked loop tracking, so the profiles were not tracked consistently below 6 -7 km height and no rising occultations were observed. GISMOS was designed with the additional 10 MHz GNSS recording system (GRS) to handle this well known

difficulty. With the data recorded during PREDICT from this instrument, it will be possible to retrieve many more profiles from the recorded occultation data (on the order of 10 - 15 per flight). In a test case, the occultation of PRN25 during RF18 was measured using open loop tracking. The refractivity profile retrieved from the open loop technique extends about 2 km below the lower limit of the profile obtained using data from the conventional receiver. In addition to tracking GPS signals lower in the troposphere, rising occultations can be reliably measured by using the open loop tracking, which was not possible with the geodetic GPS receivers. The combination of the additional rising occultations with an increase in the measured setting occultations will result in a valuable dataset for testing the impact of assimilating ARO data on improving tropical storm genesis, intensity, and track during the PREDICT campaign, as well as characterizing the near storm environment for each case.

2.7 Acknowledgements

The analyzed refractivity profiles are available at the webpage, http://www.igpppublic.ucsd.edu/~jhaase/airborne_ro. This work was funded by contributions from the following grants: HIAPER UCAR Subcontract S05-39696, NSF grant SGER-0802887, NSF grant AGS 1015904, NSF grant AGS 1301835, NASA grant NNX12AK30G. Partial support for BM was provided by the Ross Fellowship. PM was supported by the Schlumberger Faculty for the Future Fellowship. We would also like to thank the following: Ulvi Acikoz, Tyler Lulich, and Brian Ventre who contributed to software development for our use in the open loop analysis; Alexandria Johnson who assisted with the GISMOS data collection and preliminary analysis during the PREDICT

campaign; J. Jensen, J. Meitin, A. Cooper, A. Schanot, R. Sherman, and the NCAR-EOL and NCAR-RAF staff for their logistical support during the PREDICT campaign; PREDICT PI's M. Montgomery and C. Davis; M. Bell, D. Raymond, and C. Lopez who assisted with GISMOS operation; and J. Dunion, J. Cordeira, K. Griffin and the PREDICT/NASA/NOAA forecast teams. ERAI reanalyses were provided by the European Center for Medium Range Forecasts (ECMWF), http://apps.ecmwf.int/datasets/, and PREDICT dropsonde data were provided by NCAR-EOL sponsored by the NSF, http://data.eol.ucar.edu/master_list/?project=PREDICT. Radiosonde data were provided through the University of Wyoming, Dept. of Atmospheric Science website, http://weather.uwyo.edu/upperair/sounding.html. We thank UNAVCO for technical support with testing and operation of the commercial GPS receivers. We thank Chris Davis for an early review of this paper, and the editor and four anonymous reviewers for their helpful comments.

2.8 Figures

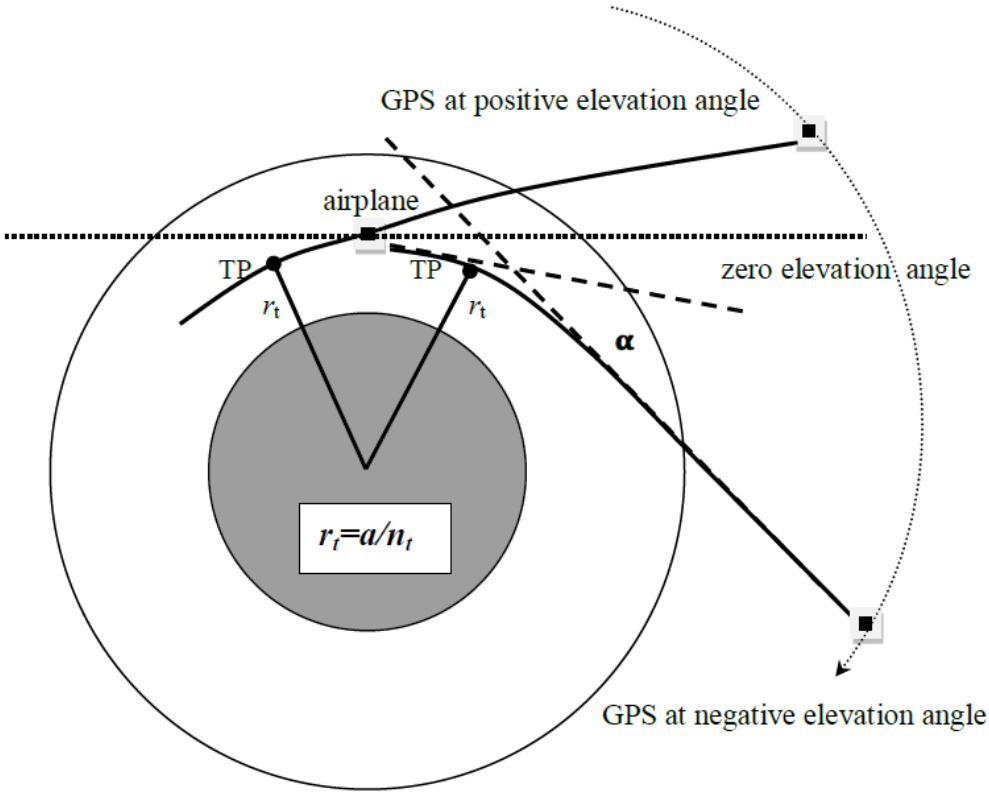

Figure 2.1: An occulting GPS satellite shown at positive and negative elevation angle relative to the local horizon of the aircraft. The radius vector to the tangent point, r_t, is the point of closest approach of the ray path to the surface of the Earth, and α is the bending angle due to refraction. The index of refraction at the tangent point is n_t and the impact parameter is $a_t = n_t r_t$.

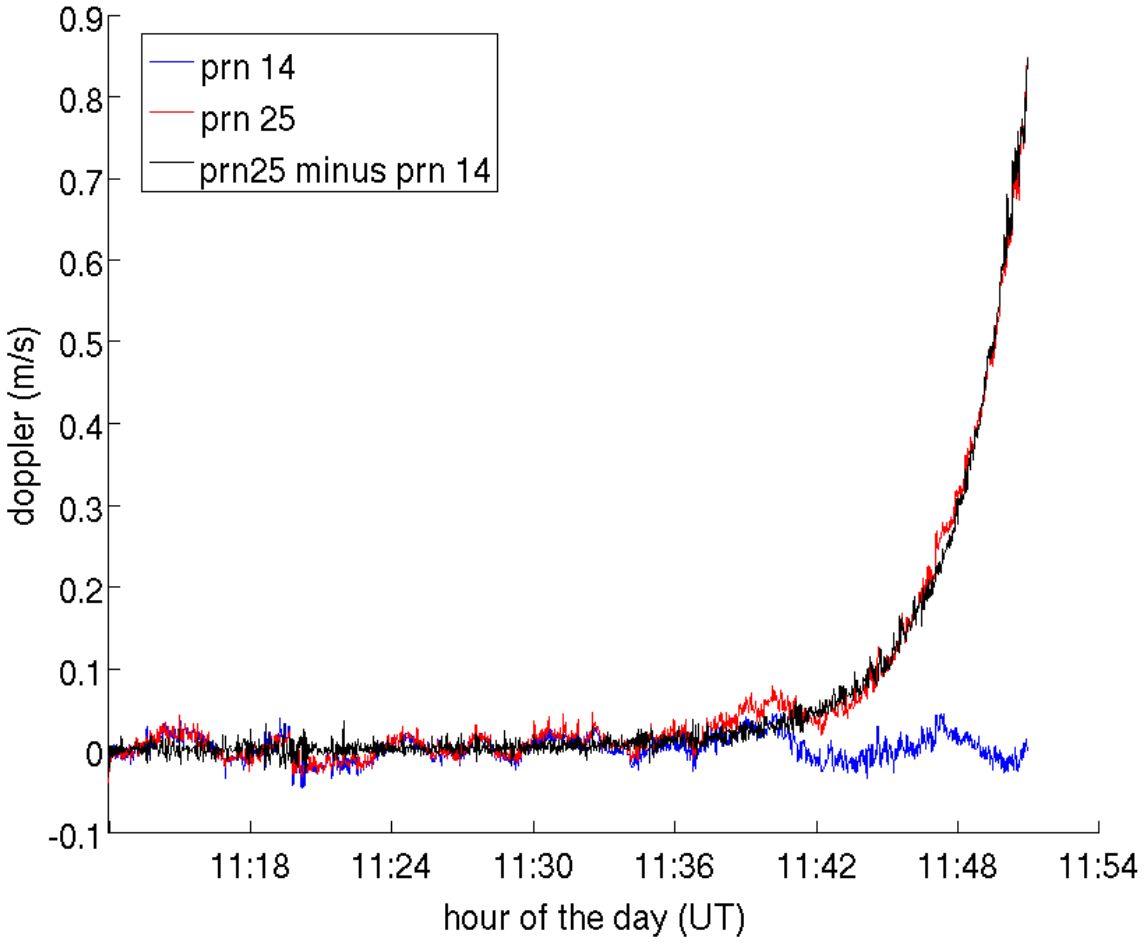

Figure 2.2: The excess Doppler shift (observed minus straight line vacuum path) is shown for the occulting satellite PRN25 (red) during RF18 and high elevation satellite PRN14 (blue) for the same flight. The difference, PRN25 minus PRN14 (black), is taken to remove the variation due to the receiver clock error. At later times, the ray path samples deeper in the atmosphere producing a greater Doppler shift. (From Haase et al. 2014).

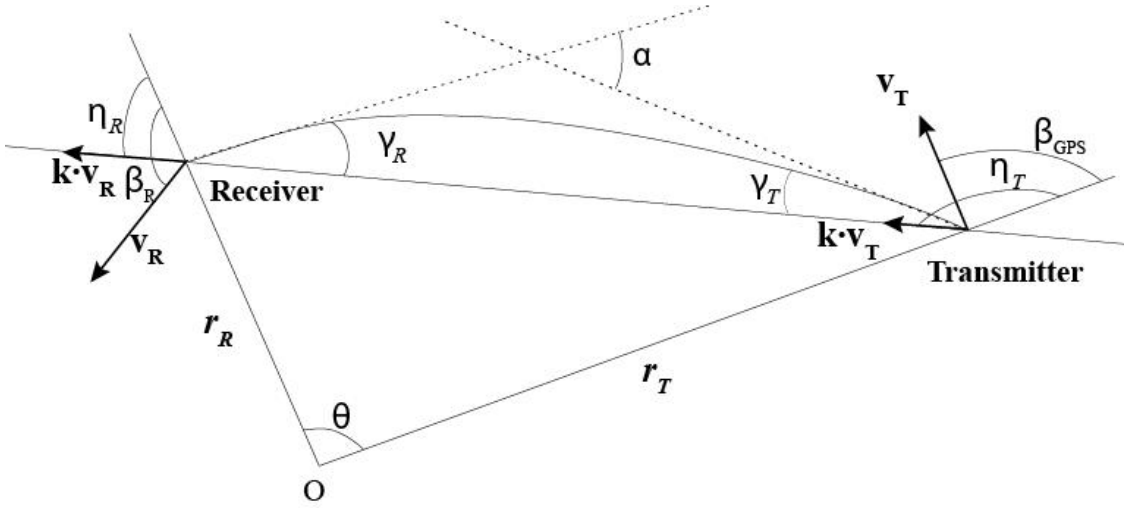

Figure 2.3: The geometry of the airborne receiver and GPS satellite in the occultation plane containing the center of Earth curvature, the aircraft, and satellite. The tangents to the signal ray path at the source and receiver define the total bending angle, α, which provides information on the refractivity of the atmosphere. Subscript T refers to the GPS satellite transmitter and subscript R refers to the aircraft GPS receiver. The satellite and airplane velocities are labeled by $\mathbf{v_T}$ and $\mathbf{v_R}$ respectively. This illustration defines the angles used in equation (2.6).

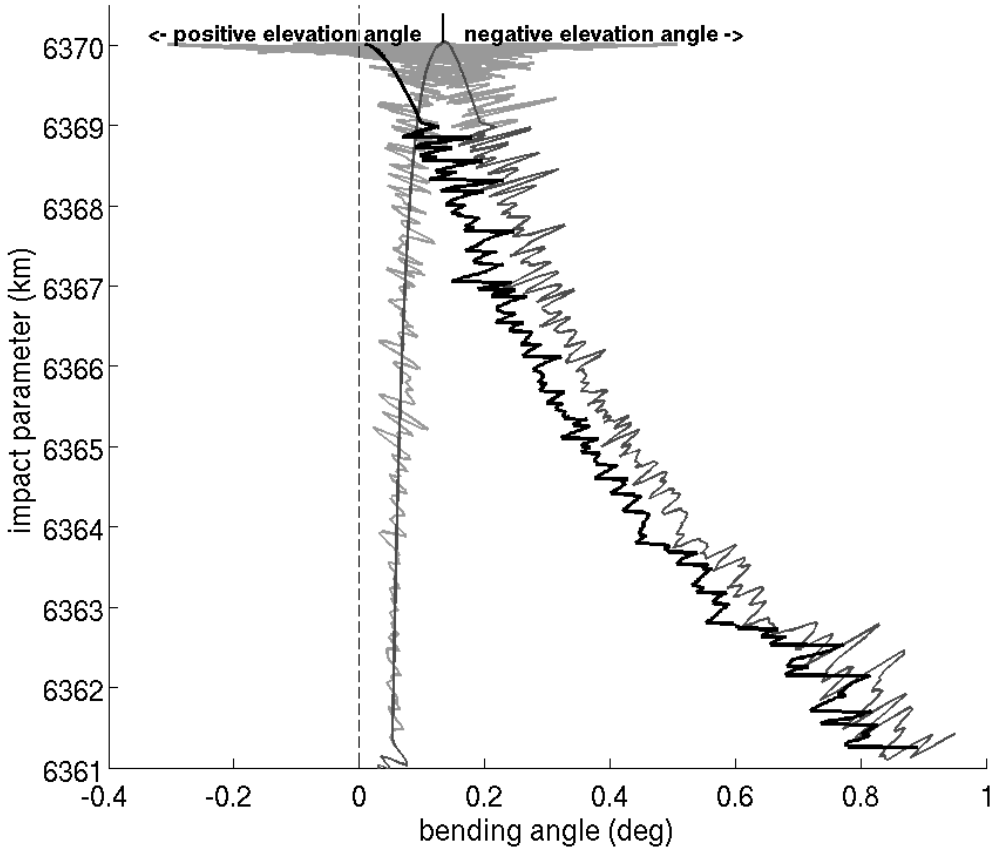

Figure 2.4: The bending angle from the occultation of satellite PRN25 during RF18 on 13 September 2010 (gray). Superimposed is the bending angle profile with the noisy section near zero elevation angle and the positive elevation angles replaced with simulated values from an initial estimate of the refractivity profile (darker gray). The partial bending angle is shown in black.

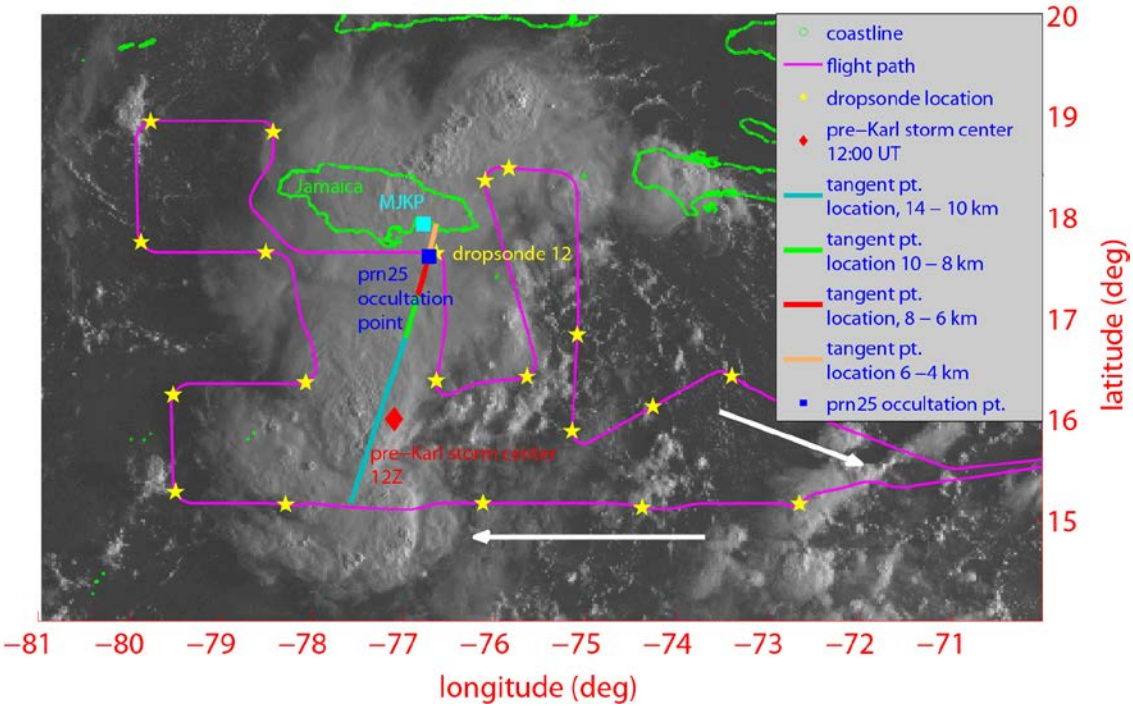

Figure 2.5: The RF18 flight path on 13 September 2010 (magenta) south of Jamaica superimposed on GOES-13 11:45 UT visible imagery. The yellow stars mark the deployed dropsondes. The tangent point drift for the occultation of GPS PRN25 is shown in cyan to orange. The horizontal tangent point drift rate becomes progressively smaller at lower heights. The pre-Karl storm center (red diamond) is shown south of Jamaica approximately 24 hours before developing into a tropical depression and then tropical storm over the northwest Caribbean Sea on 14 September 2010.

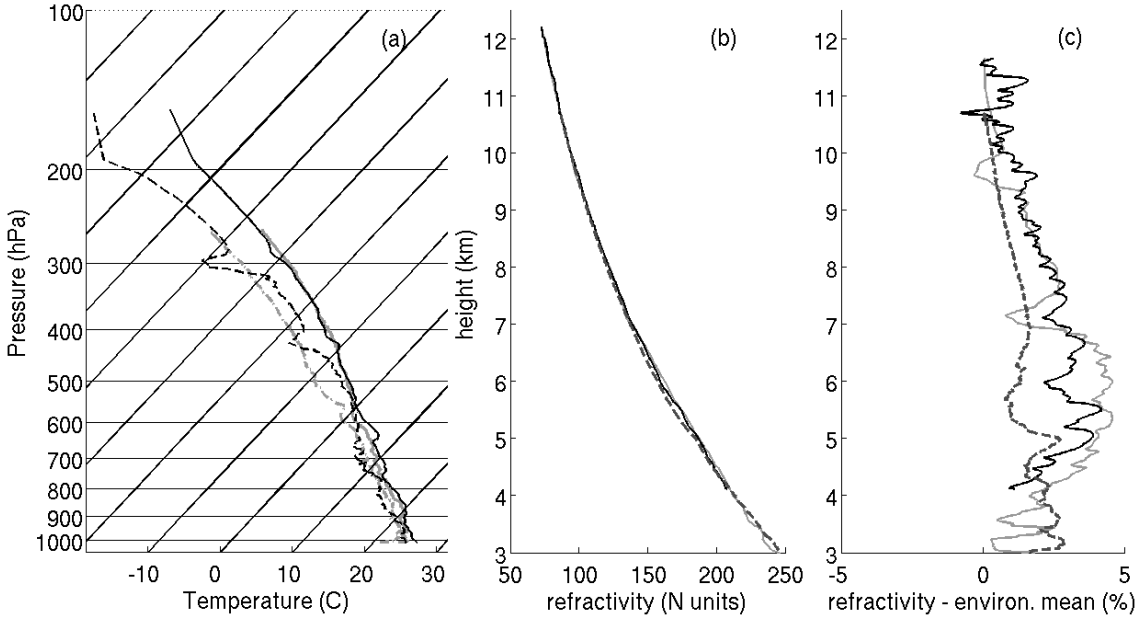

Figure 2.6: (a) The dewpoint (dashed) and temperature (solid) profiles measured by the nearby dropsonde (black) and radiosonde 12:00 UT MKJP (gray) on 13 September 2010. (b) Refractivity profiles derived using the PRN25 occultation data from RF18 (black), radiosonde MKJP (dashed), and dropsonde (gray). (c) The difference relative to the environmental mean of the ARO (black), radiosonde (dashed) and dropsonde (gray) refractivity. ARO differs by about 1% from the dropsonde over the height of the profile. ARO agrees well with the dropsonde and both indicate high moisture relative to the environmental mean.

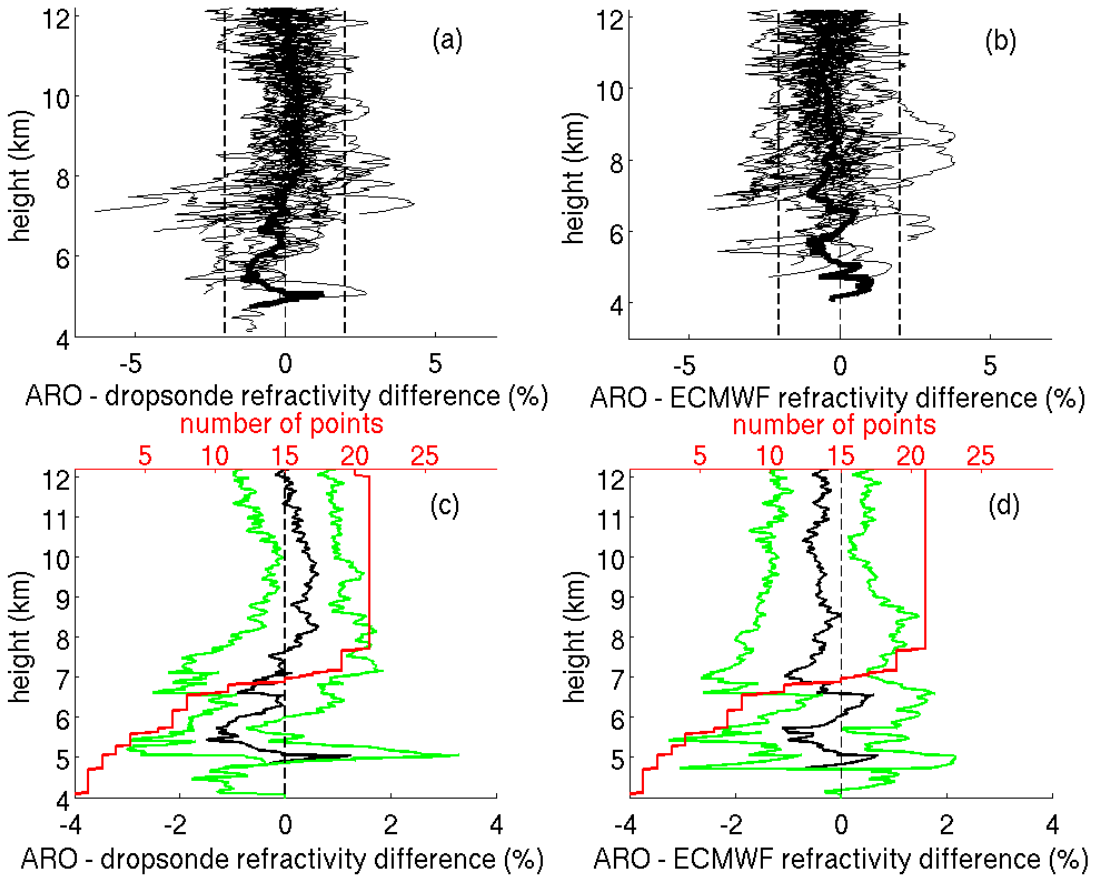

Figure 2.7: (a) Percent difference of RO refractivity profiles from dropsonde refractivity profiles (see equation 13). In all panels, the mean is shown in bold black. The mean difference between RO and dropsondes is less than 1% for heights where the number of observations (red) is greater than 15. (b) Percent difference of RO refractivity profiles from the refractivity profile at the nearest ECMWF Interim reanalysis grid point. (c) The mean (black) and standard deviation (green) of RO–dropsonde refractivity and the number of observations (red) are shown at each height. (d) The mean (black) and standard deviation (green) of RO minus ERAI refractivity and the number of observations at each height (red). The standard deviation is less than 2% for all heights where the number of observations is greater than 15, roughly above 7 km.

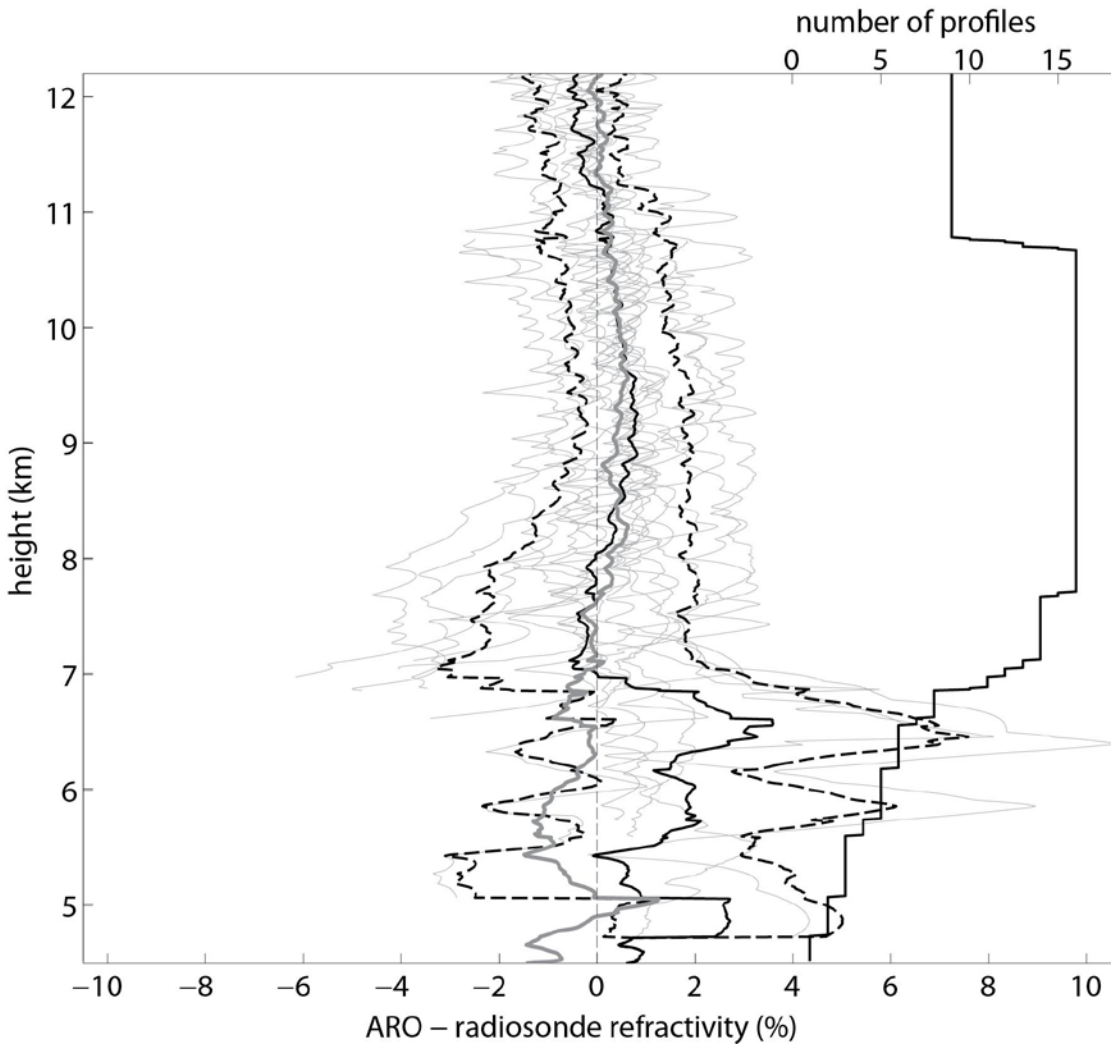

Figure 2.8: Refractivity difference between ARO and radiosonde profiles for all flights (gray). The mean difference (black) is less than 1% above 7 km where there are more than 10 profiles. The mean follows closely the mean difference from the ARO and dropsonde comparison, which is also shown (bold gray). The standard deviation (dashed black) increases from 1% at 12 km to 2% at 7 km. The number of profiles used in the mean for each height is shown on the right (black).

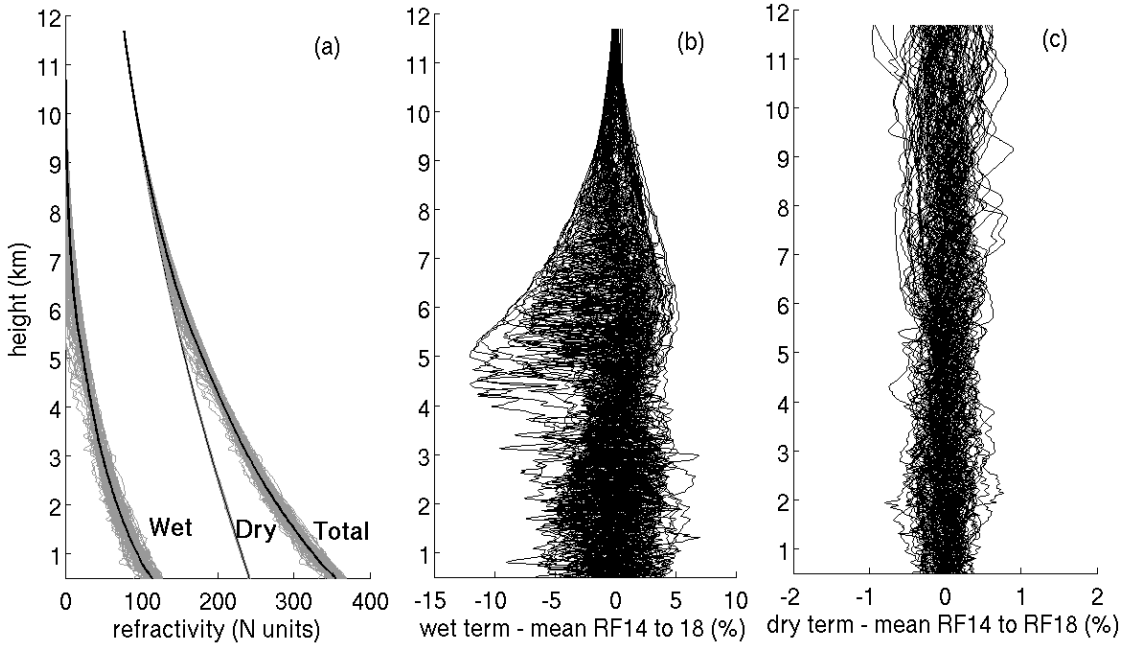

Figure 2.9: (a) The dropsonde pre-Karl environmental mean dry refractivity, total refractivity and wet refractivity were calculated using all 105 PREDICT dropsondes from Karl flights RF14 - RF18 over 10 - 13 September 2010. The pre-Karl environmental mean profile (black) is superimposed on all 105 profiles. (b) Variation of dropsonde wet refractivity relative to total refractivity (see equation 15). (c) Variation of dropsonde dry refractivity relative to total refractivity. Even at 9.4 km, wet refractivity variations (sd 0.9%) measured by dropsondes are more than three times the dry variations (sd 0.3%).

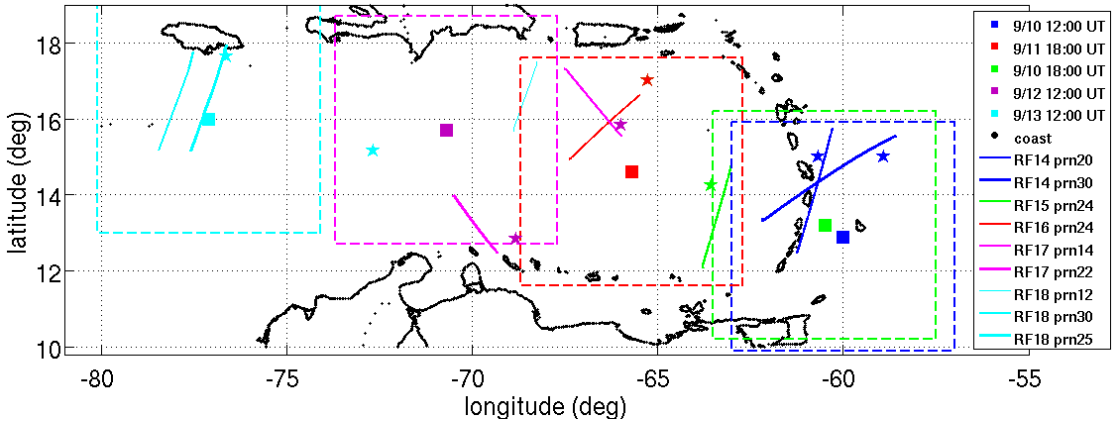

Figure 2.10: The mesoscale-α (Wang 2012) storm region is defined for each day with a 6° by 6° box around the National Hurricane Center best track Pre-Karl storm positions (squares) for the period 10-13 September 2010. Tangent point paths (thin lines) are shown for the occultations tracked by GISMOS geodetic receivers during missions RF14 thru RF18. The pre-Karl disturbance developed into a tropical depression and then tropical storm on 14 September, one day after RF18 (cyan).

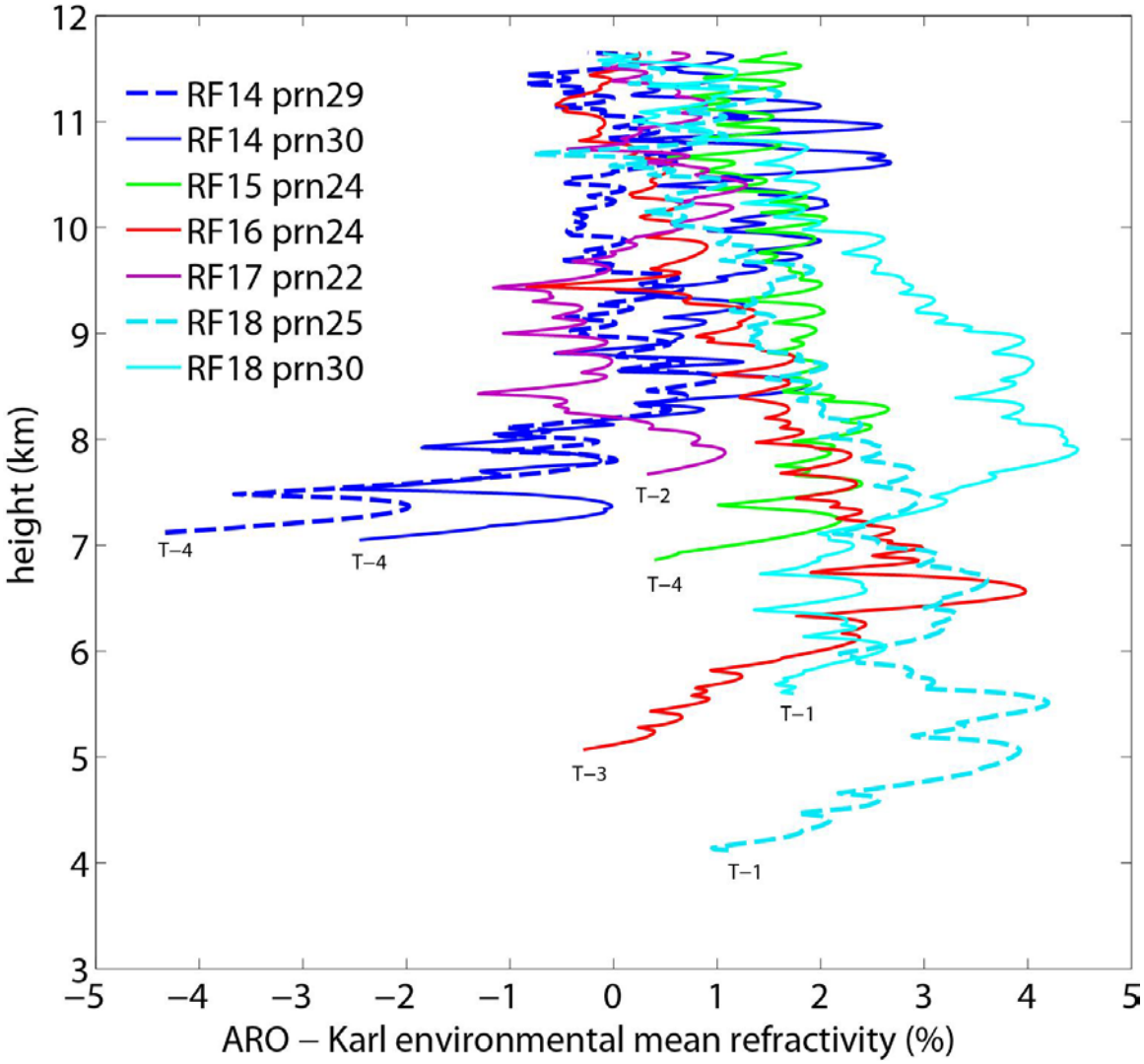

Figure 2.11: The refractivity difference as a function of time relative to the pre-Karl environmental mean indicates greater moisture at mid-levels as the storm system evolves. For example, refractivity on 10 September (dark blue) four days prior to genesis (T-4) is relatively low above 7 km, likely indicating dry air, and refractivity is high on 13 September (pink) at T-1. Genesis of pre-Karl to tropical storm strength occurred on 14 September 2010 (T – 0).

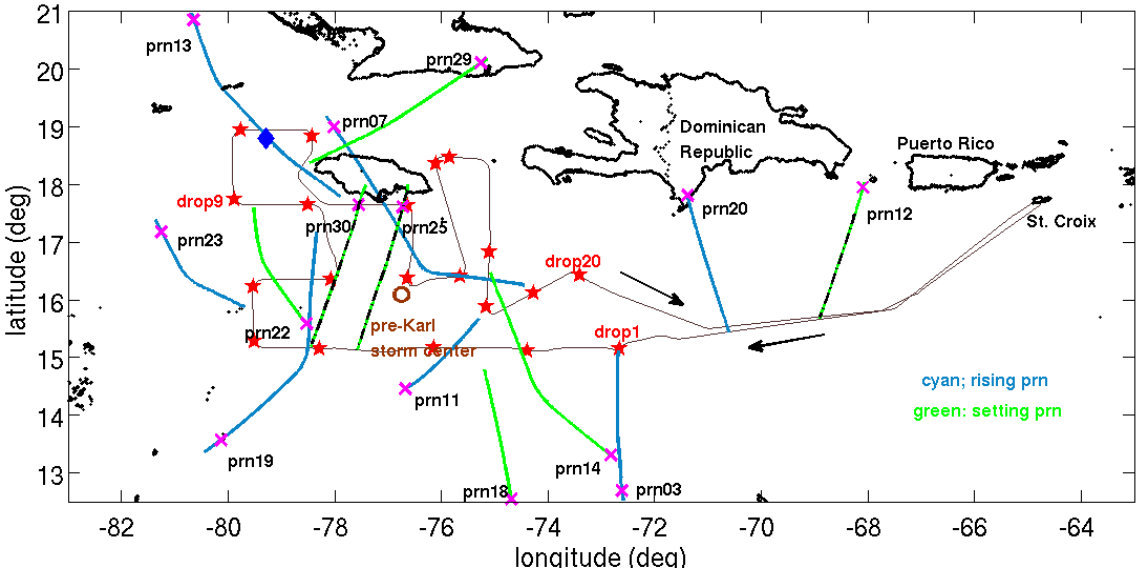

Figure 2.12: Flight path of RF18 on 13 September 2010, 10:00 – 16:00 UT. Tangent point paths of rising and setting occultations are shown in cyan and green respectively. Setting occultations (prn12, 25 and 30) are overlaid with a black dashed line. Dropsonde locations are marked by red stars and ARO occultation points are marked with magenta crosses. The occultation point of the single COSMIC retrieval (13:00 UT) available during RF18 is marked by the blue diamond.

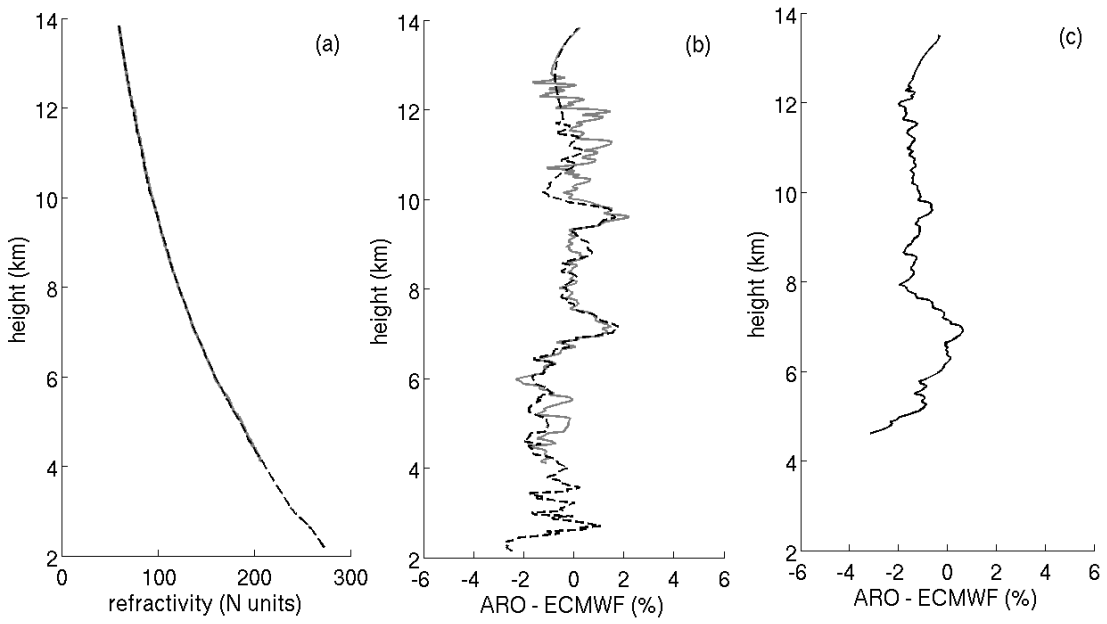

Figure 2.13: (a) Comparison of the open loop refractivity retrieval (dashed line) with the conventional geodetic receiver refractivity retrieval (gray) for the RF18 PRN25 occultation. The open loop method tracked ~2 km lower than the geodetic receiver. (b) Percent refractivity difference relative to the ECMWF interim reanalysis profile for the open loop retrieval (dashed line) and conventional geodetic receiver retrieval (gray). (c) Percent refractivity difference relative to the ECMWF interim reanalysis profile for rising RF18 PRN20 occultation.

CHAPTER 3. OPEN LOOP TRACKING AND RADIO HOLOGRAPHIC TECHNIQUES FOR AIRBORNE RADIO OCCULTATION RETRIEVALS

3.1 Introduction

GISMOS was designed with a high speed 10 MHz GNSS recording system (GRS) to record the signals of both rising and setting occulting GPS satellites with sufficient resolution to make reliable measurements in the lower troposphere. Sharp gradients in atmospheric refractivity due to high moisture in the lower troposphere are known to cause rapid fluctuations in signal phase and amplitude that limit the use of conventional receivers. The GISMOS geodetic receivers, which use conventional phase lock loop (PLL) tracking to maintain lock on the received GPS signal as described in chapter 2, served to demonstrate the proof of concept for the upper troposphere where these effects are less severe. During tracking of GPS occultations by these receivers, signal lock is acquired through correlation of the received signal with a local replica signal generated by the receiver using estimates of the expected signal delay and Doppler frequency. In PLL tracking, estimates of the delay are made with assistance of feedback from the received signal phase; therefore maintaining lock relies on phase changing smoothly. During PREDICT, the geodetic receiver tracking terminated in the lower troposphere when the PLL could no longer track rapid fluctuations in signal phase caused by moisture gradients. The geodetic receivers also did not track any rising occultations because of the

difficulty in acquiring lock on the signal when the initial Doppler had large fluctuations for satellites appearing low on the aircraft horizon.

The recorded signals from the GRS, however, can be used to track occulting satellites in post processing using a software receiver with a more robust open loop technique, which does not require feedback to maintain signal lock [*Lulich*, 2010; *Sokolovskiy*, 2001; *Ventre*, 2006]. The signals were recorded for post processing in order to allow the greatest flexibility in developing and testing new analysis techniques, because the open loop method requires the raw sampled RF signal prior to cross-correlation with the replica signals, in contrast to the conventional receivers. Post-processing also allows increased precision in the trajectory of the aircraft and satellite orbit over the duration of the occultation, which is needed for estimating signal delay and model Doppler during tracking.

Because the open loop technique does not rely on signal feedback, retrieval of the Doppler and phase measurements will not be disrupted in the lower troposphere and rising occultations can be retrieved as well as setting. For PREDICT GRS data, open loop tracking was implemented using a modified version of the Purdue Software Receiver (PSR) [*Heckler and Garrison*, 2004; *Wang et al.*, 2015a].

While open loop tracking allows occultation excess phase to be obtained down to near the Earth's surface, the accuracy of the bending angle derived from the geometric optics calculation is greatly degraded by multipath reception which commonly occurs in the lower troposphere at tropical latitudes. Because of this problem, Full Spectrum Inversion (FSI) and Phase Matching (PM) methods [*Jensen et al.*, 2003; *Jensen et al.*,

2004] that can distinguish multiple superposed signals are being developed to accurately compute ARO bending angle profiles in multipath environments [*Wang et al.*, 2015b].

Section 3.2 describes the open loop method for obtaining excess phase. Section 3.3 describes the implementation of the open loop method for rising occultations. Section 3.4 develops signal to noise thresholds for evaluating the quality of the retrieved excess phase. Section 3.5 describes the processing method developed for the geometric optics refractivity retrieval from the open loop data and section 3.6 compares NetRS geodetic receiver results with open loop. Section 3.7 examines factors which affect the ARO signal strength and section 3.8 provides a preview of the potential improvements that will be achievable in the future using the radio holographic inversion techniques. Finally, section 3.9 investigates the biases discovered in the retrievals and section 3.10 summarizes conclusions.

3.2 Open Loop Residual Phase

The transmitted GPS signal can be written as,

$$u(t) = A_T(t)\,D(t)\,p(t)\exp\left(i\left(2\pi f_c t + \Phi_0\right)\right) \tag{3.1}$$

where $A_T(t)$ is the signal amplitude at transmission, $p(t)$ is the PRN (Pseudo-Random Noise) code and $D(t)$ is the navigation data message (databits) modulated onto the signal, f_c is the signal carrier frequency, and Φ_0 is an initial phase offset. The PRN code is a unique repeating one millisecond Gold code [*Gold*, 1967] assigned to each GPS satellite. Each Gold code is orthogonal to the others and can be identified though

correlation with a replica code, allowing individual satellite broadcasts to be distinguished while all broadcasting on the same frequency. The navigation message is a 50 Hz signal which encodes orbit and clock parameters and satellite clock corrections to aid in receiver positioning. The navigation message is 12.5 minutes long and repeating. About every 2 hours the navigation message is updated by ground control.

The GRS recorded GPS L1 (1575.42 MHz) and L2 (1227.60 MHz) signals during PREDICT research flights. The GPS L1 signal was used for open loop tracking of the occultations. The received signal is down-converted to an intermediate frequency of 420 kHz and is written as

$$u_{IF}(t) = A(t)\,p(t-\tau)\,D(t-\tau)\exp\left(i\left(2\pi f_{IF} + \Phi(t) + \Phi_0\right)\right) + n(t) \qquad (3.2)$$

where $A(t)$ is the received amplitude which is much reduced from the transmitted amplitude, $p(t-\tau)$ and $D(t-\tau)$ are the prn code and navigation message respectively delayed by propagation time , τ , $\Phi(t)$ is the time varying total phase whose derivative is equal to the Doppler shift of the frequency and $n(t)$ represents the received signal noise. We assume that the random noise properties of the noise processes are preserved throughout the following operations and therefore will continue to represent the noise with the same notation $n(t)$. The intermediate frequency signal is sampled and recorded by the GRS at 10 Mhz.

The open loop tracking technique implemented in the PSR is modeled after Beyerle et al. [2006]. The practical implementation of open loop tracking for operational use in the PSR is described by [*Acikoz*, 2011; *Lulich*, 2010; *Ventre*, 2006]. The goal of

the open loop tracking is to determine the total phase accumulated during transmission through the atmosphere from complex correlation between the received signal and the local replica signal. In order to do this without relying on a feedback control algorithm, an initial estimate of the local replica signal Doppler shift due to propagation must be estimated that is close enough to the observed Doppler that the signal correlation is high. The total phase, Φ_T, accumulated in the received signal is the sum of the excess phase due to the atmosphere, Φ_E, and the geometric phase, Φ_G, due to the path length.

$$\Phi_T = \Phi_E + \Phi_G \tag{3.3}$$

The residual phase, Φ_R, is defined as the difference between the total phase and the phase of local signal computed from the Doppler model used in open loop tracking.

$$\Phi_R = \Phi_T - \Phi^{\text{model}} \tag{3.4}$$

In open loop tracking, the residual phase is determined from complex correlation between the received signal and the local replica signal. The residual phase can be expressed in terms of the excess phase, geometric phase and model phase using equations 3.3 and 3.4.

$$\Phi_R = \Phi_E + \left(\Phi_G - \Phi^{\text{model}}\right) \tag{3.5}$$

If the model Doppler is constructed only using geometric phase, $\Phi_G = \Phi^{\text{model}}$, the residual phase is considered the estimate of the excess phase.

$$\Phi_R = \Phi_E \tag{3.6}$$

Otherwise, for example if the model phase includes an initial estimate of the phase delay due to a climatological refractivity profile, then the excess phase is equated with the residual plus model phase minus the geometric phase.

$$\left(\Phi_R + \Phi^{\text{model}}\right) - \Phi_G = \Phi_E \tag{3.7}$$

The first step, code wipeoff, removes the prn code from the down converted received signal by multiplying with a replica code having a delay computed from the Doppler model.

$$u_s(t) = u_{IF} \cdot p\left(t - \hat{\tau}\right) \tag{3.8}$$

The estimated delay, $\hat{\tau}$, is assumed accurate enough that the product of the locally generated prn Gold code and received code is approximately an identity.

$$p(t-\tau)\, p\left(t - \hat{\tau}\right) \approx 1 \tag{3.9}$$

After the code wipeoff, the received signal is given by equation 3.10.

$$u_s(t) = A(t) D(t-\tau) \exp\left(i\left(2\pi f_{IF} + \Phi_T(t) + \Phi_0\right)\right) + n(t) \tag{3.10}$$

A complex conjugate signal, $v(t)$, is generated locally from the predicted Doppler model.

$$v(t) = \exp(-i(2\pi f_{IF} t + \Phi^{\text{model}}(t))) \tag{3.11}$$

The received, $u_s(t)$, and replica complex conjugate, $v(t)$, signals will be correlated to determine the remaining residual phase shift between the model estimate and the total phase.

The predicted model phase for the replica signal is found from the model Doppler frequency which is the time derivative of the phase.

$$f_D^{\text{model}}(t) = \frac{1}{2\pi}\frac{d\Phi^{\text{model}}(t)}{dt} \tag{3.12}$$

For the digitized signal, the model phase at time, t_n, is given by the accumulated Doppler over the preceding $n-1$ integration times,

$$\Phi_n^{\text{model}} = 2\pi T_I \sum_{j=1}^{n-1} f_{D\,j}^{\text{model}} \tag{3.13}$$

where $\Phi_n^{\text{model}} \equiv \Phi^{\text{model}}(t_n)$ and $f_{D,j}^{\text{model}} \equiv f_D^{\text{mod}\,el}(t_j)$. The product $u_s(t)v(t)$ is integrated to produce a complex correlator sum, Ψ_n, over time T_I, which is chosen to be one code period,

$$\Psi_n = \frac{1}{T_I}\int_{t_n}^{t_n+T_I} u_s(t)v(t)\,dt + n(t) \tag{3.14}$$

For the digitized signal in discrete time, equation 3.14 is the complex sum of the received and local replica signal over one code period, which may vary in number of samples

depending on the Doppler Effect. After substituting in equation 3.10 and 3.11, equation 3.14 is written as

$$\Psi_n = \frac{A_n D_n}{T_I} \int_{t_n}^{t_n+T_I} \exp(i(\Phi(t) - \Phi^{\text{model}}(t)))dt + n(t) \tag{3.15}$$

where it is assumed that the amplitude and frequency can approximated as piecewise constant and that the data bit is constant over the period of integration. The complex correlator sum can be expressed as a sinc function, $\text{sinc(x)} = (\sin x)/x$, after integration.

$$\Psi_n = A_n D_n \,\text{sinc}(\pi \delta f_{D,n} T_I) \exp(i\left(\frac{\delta\Phi_n + \delta\Phi_{n+1}}{2}\right) + n(t) \tag{3.16}$$

where $\delta f_{D,n} = f_{D,n} - f_{D,n}^{\text{model}}$ and $\delta\Phi_n = \Phi_n - \Phi_n^{\text{model}}$ represent the error between the true and model Doppler and phase. The complex correlator, Ψ_n, consists of an imaginary part, called the quadrature, q_n, and real, called inphase, i_n, components. When the data bit, D_n, is divided out of the complex correlator sum, the angle of the resulting complex number is the difference between the true and model phase. The data bits were acquired from the COSMIC data bit archive available through the COSMIC Data Analysis and Archive Center (http://cdaac-www.cosmic.ucar.edu/cdaac). If data bits were missing from the archive or corrupted, gaps were filled by generating data bits based on knowledge of previous data bits expected to reoccur in the repeating navigation message.

After the databits, D_n, have been divided out, the inphase, i_n / D_n, and quadrature, q_n / D_n, components of the complex correlation sum, are coherently integrated over the length of one navigation message data bit which is 20 ms.

$$I_k = \sum_{n=20(k-1)+1}^{20k} i_n / D_n \tag{3.17}$$

$$Q_k = \sum_{n=20(k-1)+1}^{20k} q_n / D_n \tag{3.18}$$

The coherent integration raises the SNR and reduces the data from 1000 Hz to 50 Hz. The residual phase is found from the angle between the coherently summed inphase and quadrature components using the four-quadrant arctangent function.

$$\Phi_{k+1}^R = \text{atan2}\left(Q_k, I_k\right) + C_k \tag{3.19}$$

When the phase exceeds the $[-\pi, \pi]$ output range of the four-quadrant arctangent function, the angle is wrapped within the $[-\pi, \pi]$ range, causing discontinuities of 2π in the residual phase. The constant, C_k, is added to correct the shifts in the wrapped angles using the rubric,

$$C_k = \begin{cases} C_{k-1} + 2\pi & \text{if } \Phi_k^R - \Phi_{k-1}^R < -\pi \\ C_{k-1} - 2\pi & \text{if } \Phi_k^R - \Phi_{k-1}^R > +\pi \\ C_{k-1} & \text{otherwise} \end{cases} \tag{3.20}$$

and $C_1 = 0$.

3.3 Implementation of Open Loop Tracking and Backward Tracking for Rising Occultations

Before open loop tracking is initiated, the PSR uses conventional tracking with feedback loops, or 'closed loop' tracking, to acquire the GPS satellite signal and make initial estimates of Doppler frequency and code delay. During the acquisition process a signal replica with a specific PRN code sweeps through a range of model Doppler frequency and code delay as the replica is correlated against the received signal. The maximum cross-correlation determines the initial estimate of the Doppler and code delay. The signal is squared to make the process insensitive to the data bit message. Once acquisition is complete, closed loop tracking is run to determine the code frame edge. To achieve this, the PSR also must obtain a frame lock on the 50 Hz navigation message which is modulated onto the GPS carrier frequency. The navigation message repeats every 750 s and is divided into 125, six second, sub-frames. Frame lock is necessary to locate the beginning of a prn code cycle, which facilitates the accurate removal of the navigation message data bits, and the coherent integration of complex correlator sums over just one data bit [*Ventre*, 2006].

Because closed loop tracking must always run first in the PSR before handover to open loop, tracking should begin when the satellite is at a high elevation and the received signal strength is greatest. This is the case for a setting occultation as shown in Figure 3.1 on the right. For a rising occultation, however, the satellite will begin at a low elevation, as shown on the left in Figure 3.1, and it is hard to acquire with this low SNR. A 'backward tracking' option was implemented in the PSR in order to allow acquisition of rising satellites when they are at high elevation [*Acikoz*, 2011]. This approach takes

advantage of the fact that the open loop tracking for ARO is done in post processing with the recorded GRS data. The tracking is initiated at a time when satellite has reached a high elevation relative to the aircraft horizon. The open loop tracking algorithm is then run backward in time through the recorded data to obtain the residual phase. The backward tracking uses the same algorithms as forward tracking except the GRS files are read in reverse. The two main differences in backward tracking are the updating of the code delay, which must integrate the opposite change in model Doppler frequency as tracking proceeds, and the data bit frame location for the handover from closed loop tracking to open loop [*Acikoz*, 2011]. In forward tracking the hand off occurs on the first sample of the next sub-frame after frame lock while in backward tracking it occurs at the last sample of the current sub-frame.

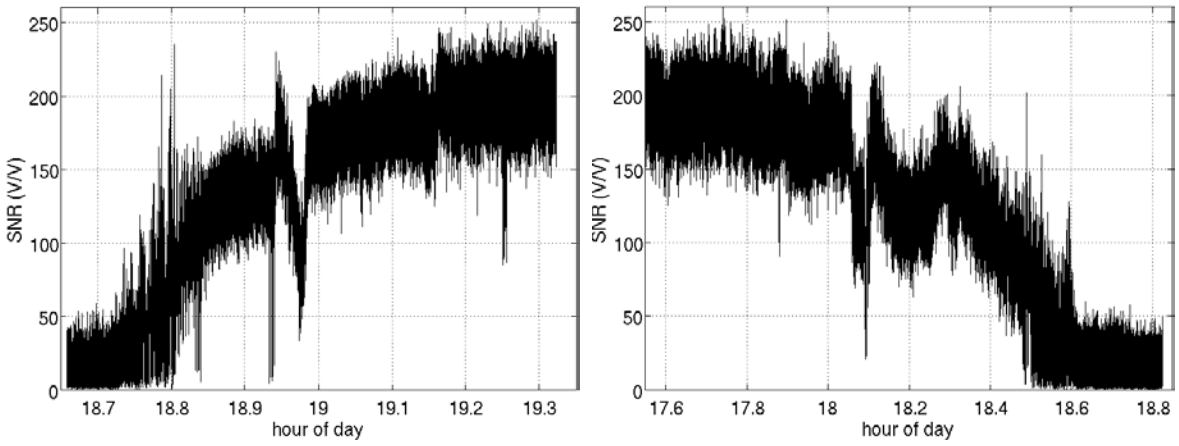

Figure 3.1 LEFT: Signal-to-noise ratio for RF16 prn04 rising occultation. RIGHT: Signal-to-noise ratio for RF16 prn06 setting occultation.

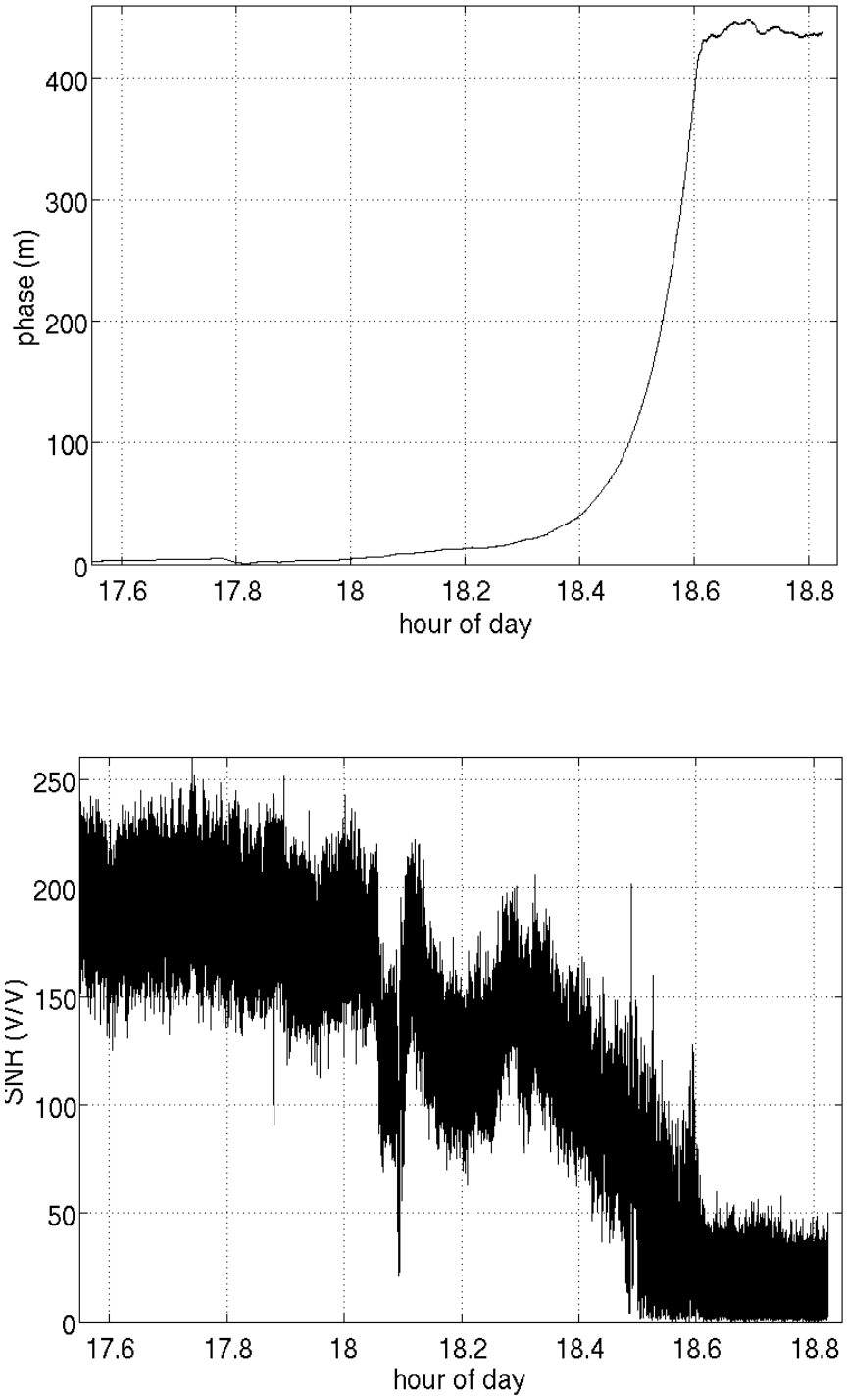

Figure 3.2 UPPER: RF16 prn06 setting occultation excess phase. After 18.6 UT, the PSR continues to produce residual phase estimates after the signal has disappeared and the excess phase follows a random walk. BOTTOM: RF16 prn06 SNR reaches the noise floor after 18.6 UT.

3.4 Signal-to-Noise Threshhold of ARO Retrievals

As an occulting satellite descends to lower elevation angle and the ray path passes through a greater amount of the atmosphere, the SNR diminishes. The signal falls to zero at the end of setting occultations and increases from zero for rising occultations (figure 3.1). The PSR will continue the open loop cross-correlation procedure and calculation of residual phase even if there is no signal in the recorded data, since it requires no signal feedback. After the transmitted signal has disappeared, the residual phase will continue to vary as a random walk processs (figure 3.2).

While there is a theoretical description of the random phase variation when there is no longer a usable signal relative to the noise [*Wang et al.*, 2015a], in practice there is no simple implementation that is appropriate for every occultation case. For this work, the cut-off time for setting occultations and start time for rising occultations was determined on a case by case basis. First, the mean of the noise floor was calculated from the SNR data after the lower limit of the noisy SNR is ~ 0 V/V as is seen in the lower panel of figure 3.2 after 18.6 UT for the case of setting RF16 prn06 occultation. As a general practice, a setting excess phase retrieval was ended when the 5 s moving average of the SNR fell below one standard deviation above the mean noise floor (figure 3.3). Similarly for a rising occultation, the excess phase retrieval was started after the 5 s moving average reached one standard deviation above the mean noise floor.

As an additional criterion, the excess phase was visually examined before applying the SNR threshold. When the elevation of the satellite is lower, the ray paths are also lower in the troposphere where moisture levels are high and larger gradients of

refractivity result in greater multipath reception at the receiver. The multipath causes sharp changes in the excess phase and if the fluctuations increase rapidly, the retrieval is terminated at that time even if the SNR is still above the one sigma level. In order to more clearly display the fluctuations in the phase, a rising or falling trend is subtracted from the excess phase (figure 3.4).

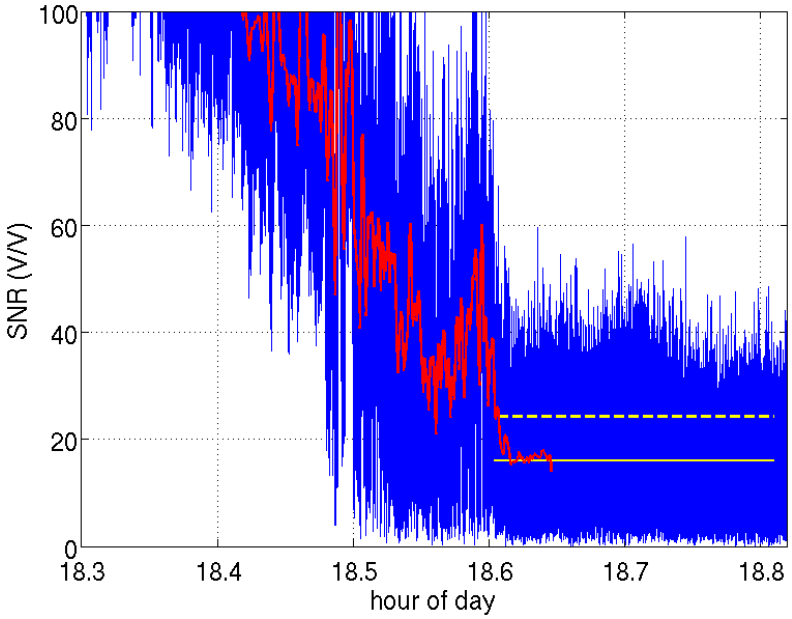

Figure 3.3 RF16 prn06 setting occultation SNR is shown in blue with the five second moving average in red. The mean noise floor is shown by the solid yellow line while one standard deviation above is marked by the dashed yellow line. The retrieval was terminated at 18.59 UT, before the moving average fell noticeably below the one sigma level.

3.5 Open Loop Refractivity retrieval

The linux- based PSR is a software suite which integrates C++ and Matlab programs. Before processing with PSR, the raw signals recorded by the GRS are read off the SCSI disks and written to binary GRS files containing 10 minutes of data. Typically

each flight will have 35 – 40 GRS files of recorded data (about 6 – 7 hours of recording time). The PSR will read in the data from these files and then PSR processing entails four stages:

1) Prep.
2) Doppler prediction.
3) Open loop tracking.
4) Calculation of phase from complex correlator components (i_n and q_n).

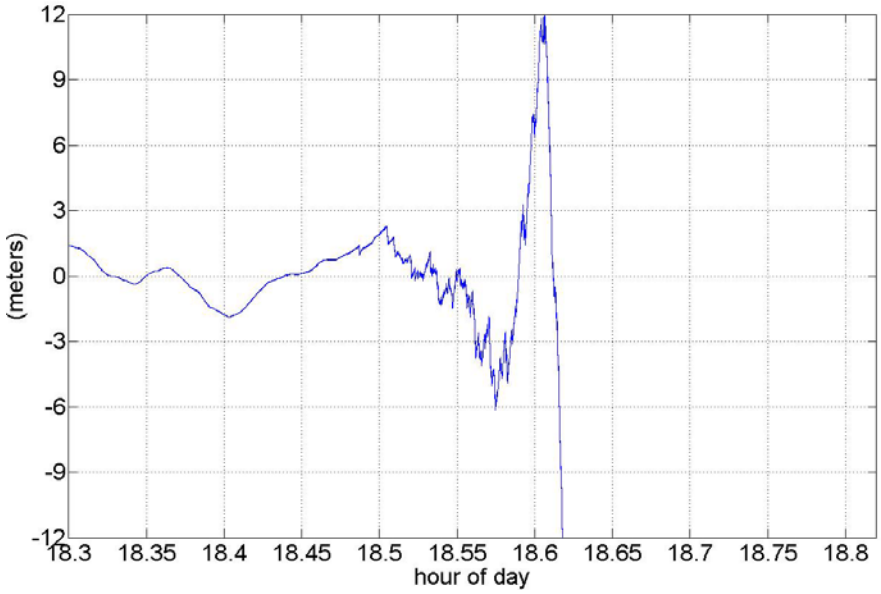

Figure 3.4 Excess phase for RF16 prn06 setting occultation. The rising trend has been subtracted to help display the sharp fluctuations which begin at ~ 18.5 UT, about 4.5 km altitude. The retrieval was cut-off at 18.59 UT, while the SNR was still above the one sigma level but before the large spike which occurred about 18.60 UT.

3.5.1 PSR Processing Prep

There are two steps carried out in the Prep stage. First, the acquisition routines from the PSR are run for selected GRS files. The top avionics antenna input was recorded

through the GRS channel 1. The port and starboard high gain antenna input was recorded through GRS channels 2 and 3 respectively. The data used for this work came from the top antenna (CH1) only as the side antennas were susceptible to losing sight of a satellite if the plane turned, cutting off a potential occultation. The PSR is run from the command line of the linux operating system. The prep stage acquisition is run by a program *psr_prep.csh*. The user selects the GRS channel and number of GRS files to be processed. Only acquisition is run on the data in the GRS files, and each prn acquired from data in a GRS file is written to a text file called sv_chans.dat. The acquisition is also run in reverse order in the files for backward tracking and the results written to a text file called sv_chans_b.dat.

The second step in the prep stage is to sort the prns acquired and predict the times for occultations. The program *olpredict_prep.csh* is used. The user inputs the elevation ranges in which rising and setting prns are to be identified. For this research the same settings were always used:

Rising prn: -3 to 10 degrees relative to local horizon.

Setting prn: -5 to 10 degrees relative to local horizon.

A time interval is also input to define the start of a rising occultation or end of setting occultation. An interval of 600 seconds was always used for this work. Therefore, a rising occultation would be considered to start 10 minutes before it reached -3 degrees and would be ended at 10 degrees. A setting occultation would begin at 10 degrees and end 10 minutes after reaching -5 degrees. These choices were made based on previous processing experience. The path to the navigation file from the Applanix system, containing the position and velocity data for the flight, was also input.

Additionally, an orbital file with precise satellite positions is needed. This data is obtained online from the Center for Orbit Determination in Europe (CODE) or the International GPS Service (IGS). Precise orbit files from CODE were used for this work. The standard precise orbit file is given in 15 minute intervals and the PSR must interpolate this data ultimately to 1000 Hz for Doppler prediction in stage 2. While GPS satellites carry precise atomic clocks, 60% have exceeded their design life [*Huang et al.*, 2013] and could be experiencing some frequency instability. GPS clock data files are available from CODE at 5 second intervals and were used increase the accuracy of interpolation, further mitigating effects of clock instabilities. CODE precise orbit files were chosen for consistency when using CODE clock files. The navigation file and orbit files are used by the PSR to predict the times of occultations. A summary text file, occtab.out, is written with the predicted times and the corresponding GRS file numbers for each occultation. A second text file, hielev.out, is written that lists the time intervals and GRS file numbers for prns when they are above 10 degrees elevation. With this output, a list can be made of all occultations to be processed and the corresponding high elevation prns that are available. A high elevation prn is needed to subtract its excess Doppler from the occulting prn to correct for receiver clock error.

3.5.2 Doppler Model Prediction

In this stage, the PSR will construct the predicted Doppler frequency model to be used in the replica signal for OL tracking. The predicted model may only include the geometric phase, or the geometric phase plus excess phase accumulated due to refraction in the neutral atmosphere estimated from climatology. For the results presented in this

work, the option was always used to include the climatological model estimate of excess phase for occulting prns. The climatology option was not used for high elevation prns as it is expected the atmospheric phase in these cases will be negligible. The estimate of the excess phase was obtained from a 1-D ray tracing program, the Radio Occultation Simulator for Atmospheric Profiling (ROSAP) [*Hoeg et al.*, 1996; *Syndergaard*, 1999]. The ROSAP program uses navigation data of the receiver and transmitter along with a vertical refractivity profile of the atmosphere to simulate the signal ray paths over the occultation and calculate a bending angle and excess phase. A climatological refractivity profile from the Committee On Space Research (COSPAR) International Reference Atmosphere with humidity (CIRAQ) [*Kirchengast et al.*, 1999] was used with ROSAP to predict the excess phase. A CIRAQ provides a profile available by latitude for each month.

In this stage of the processing, the program, *olpredict_dopp.csh* is used. This program will run the Doppler prediction code at higher sample rate. It will need the paths to the Applanix navigation file for the receiver and the precise orbit positions as input. The user selects the prns for Doppler prediction and the GRS file interval which covers the period of interest as determined from occtab.out. The latitude chosen for the CIRAQ climatology profile was that of the occultation point, which is estimated in a separate ROSAP simulation. The Doppler prediction output is written to files to be used in the next stage when OL tracking is run.

3.5.3 Open Loop Tracking

The OL tracking is performed using the program *psr_ol.csh* in this stage. The program input first requires the prn and the GRS files over which it is to be tracked. The user would already have determined this information to run the Doppler prediction in the previous stage. A flag is also chosen in the input to indicate whether the Doppler climatology prediction is included so that the program looks for an extra file with this information. The path to the GRS files needs to be specified as well as a path to the archived navigation data bits. The data bits were downloaded from the COSMIC Data Analysis and Archive Center (CDAAC). Input to *psr_ol.csh*, also specifies if the tracking should be forward for setting and high elevation prns, or backward for rising prns. In this stage, the GRS files will be read and the prn will be acquired. Then, closed loop tracking will be run to obtain frame lock on the navigation message and determine the code edge frame. After the code edge is determined, open loop tracking will compute the complex correlation sums and record the inphase $\left(i_n\right)$ and quadrature $\left(q_n\right)$ components.

3.5.4 Calculation of Phase from Complex Correlator Components (i_n and q_n)

The final stage of processing is run entirely in the Matlab environment using the program *OLchanlook.m*. For this program, the prn is input so that it can identify the required OL tracking output files and a flag indicating whether or not climatology was used in the Doppler prediction. The complex correlator sum components are first summed to form a complex number $\left(i_n + j * q_n\right)$. The program will then remove the databits from the complex correlator sums by division. If climatological Doppler

prediction was chosen, the estimated excess Doppler will be added back to the complex correlator sums. Then, the complex correlators are coherently integrated over 20ms (equation 3.17-18). Tests have been made to determine if an increase in coherent integration would improve SNR, but results were inconclusive so an integration time of 20 ms was used for all processing for this thesis. The phase angles (equation 3.19) and amplitudes of the coherently integrated correlators are calculated. Finally the angles are unwrapped (equation 3.20) to give the excess phase.

3.5.5 Retrieval of Refractivity from Excess Phase

The excess phase of an occultation is obtained from the PSR at 50 Hz measured in GPS seconds of the week and generally the signal contains significant noise (figures 3.5 and 3.11). Several noise reduction steps are taken during the ARO retrieval analysis (table 3.1). The excess Doppler is found by numerically differentiating the 50 Hz excess phase (figure 3.5). A five point central difference numerical differentiation is used. A noise robust algorithm was also tested (http://www.holoborodko.com/pavel/numerical-methods/numerical-derivative/smooth-low-noise-differentiators), but it was determined that using a standalone smoothing filter with standard numerical differentiation was more robust. The excess Doppler is noisy and is smoothed with a LOcally Weighted Scatterplot Smoothing (Lowess) filter (LF) [*Cleveland*, 1979] with a span of 10 s. This filter was selected over Savitzky-Golay (SG) [*Schafer*, 2011] or a simple low pass filter because it is robust in removing outliers in a non-zero mean time series. This time span corresponds to a vertical interval on the order of 200-250m at about 10 km altitude, which is comparable to the first Fresnel zone which constrains the vertical resolution of a

geometric optics retrieval [*Xie et al.*, 2008]. It was also found that implementing smoothing after differentiation produced no worse results than smoothing the excess phase before differentiation.

Table 3-1 ARO analysis options. Options used for this work are shown in red.

Processing stage	Selections
PSR: precise orbit files	1. CODE 2. IGS
PSR: coherent integration	1. 20 ms 2. 40 ms 3. 60 ms etc,
Numerical differentiation of excess phase	1. Holoborodko noise robust 2. Simple difference 3. Central Limit (5 pt.)
Implementation of smoothing	1. Smooth excess phase 2. Smooth excess Doppler 3. Smooth Is and Qs
Smoothing filter for occulting excess Doppler and high elevation excess Doppler	1. Savitzky-Golay 2. Low pass FIR 3. Lowess
Remove outliers: occulting Doppler	Yes, replace with successive average
Remove outliers: high elevation Doppler	No
Refractivity at receiver	Average over duration of occultation Calculated from GV in situ data
Receiver height	Average over duration of occultation Calculated from Applanix nav. data
Doppler to bending angle: smooth receiver velocity components.	1. Savitzky-Golay 2. Low pass FIR 3. Lowess
Doppler to bending angle: solve equations 2.6 and 2.8	1. Successive substitution 2. Matlab: *fsolve*
Doppler to bending angle: 'fixtop'	Yes, positive +1.1 km negative bending

After smoothing, the excess Doppler of a high elevation satellite is subtracted from the occulting satellite Doppler to remove receiver clock errors (figure 3.6 - 7). Before finding the bending angle profile, the 50 Hz Doppler is decimated to 1 Hz using

successive averages of 50 samples assigned to each integer second of the week. Finally, outlier points with magnitude 0.01 m/s over the running average of the de-trended excess Doppler are removed and replaced with a successive average (figure 3.8). It was not necessary to remove outliers from the high elevation Doppler.

The atmospheric refractivity at the receiver altitude is needed for both calculating the bending angle from excess Doppler and to find refractivity using the inverse Abel transform. The receiver altitude is also needed for the inverse Abel calculation. The refractivity at receiver height is calculated from in situ data recorded by avionics on the GV as described in section 2.3.2. The receiver height is determined from the navigation data provided by the Applanix system. Both are taken as an average over the duration of the occultation. For the purpose of calculating these means, the start of a setting occultation is defined as when the excess Doppler reaches 0.013 m/s and ends when the signal is lost. A rising occultation begins when the signal is acquired and the end is defined when the Doppler reaches 0.013 m/s.

After the smoothed excess Doppler has been reduced to 1Hz, the bending angle is calculated using the excess Doppler along with the position and velocity data of the transmitter and receiver [*Hajj et al.*, 2002; *Vorob'ev and Krasil'nikova*, 1994] by solving equations 2.6 and 2.8 by successive substitution. The successive substitution result was compared to results from the Matlab function ,*fsolve*, for solution of non-linear equations with optimization options, (http://www.mathworks.com/help/optim/ug/fsolve.html). But, no significant difference was found between the two approaches. Before this calculation, the x, y and z Earth-centered-Earth-fixed (ECEF) receiver velocity components are smoothed with a

Savitzky-Golay filter with a five second span to reduce noise in the calculated bending angle profile. The noisy section of the bending angle near zero elevation and the noisy positive elevation section are replaced with a smooth simulation as described in section 2.3.3. The complete positive bending angle section is replaced while the negative bending is replaced to 1.1 km below zero elevation. This process is referred to as 'fixtop'. The choice of 1.1 km was made to reduce to minimize the amount of negative bending angle replaced while removing the majority of noise near the zero elevation point at the top of the profile (figure 2.4). The partial bending angle (section 2.3.3) is computed and refractivity is retrieved using the inverse Abel transform with the same procedures described for the geodetic receiver data. The bending angle and refractivity results for the RF16 prn06 setting case are shown in Figures 3.9 and 3.10.

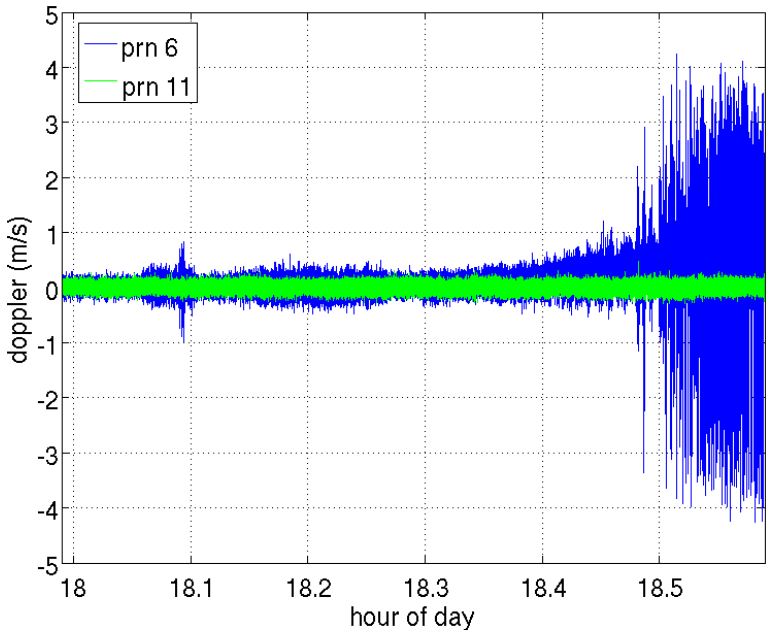

Figure 3.5 RF16 setting prn06 50 Hz excess Doppler (blue) and high elevation prn11 excess 50 Hz Doppler (green). After smoothing, the high elevation Doppler will be subtracted from the setting Doppler to remove receiver clock error.

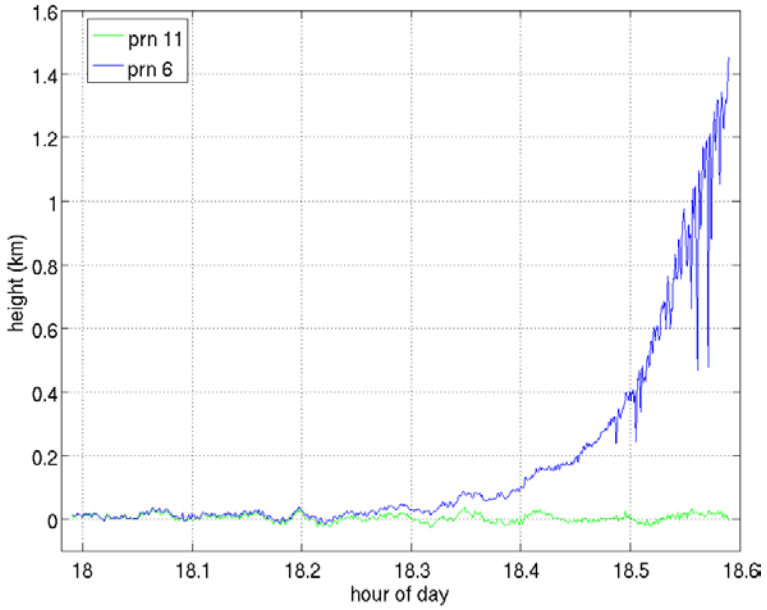

Figure 3.6 RF16 1 Hz prn06 setting Doppler (blue) and high elevation prn11 Doppler (green) after smoothing and decimation to 1 Hz.

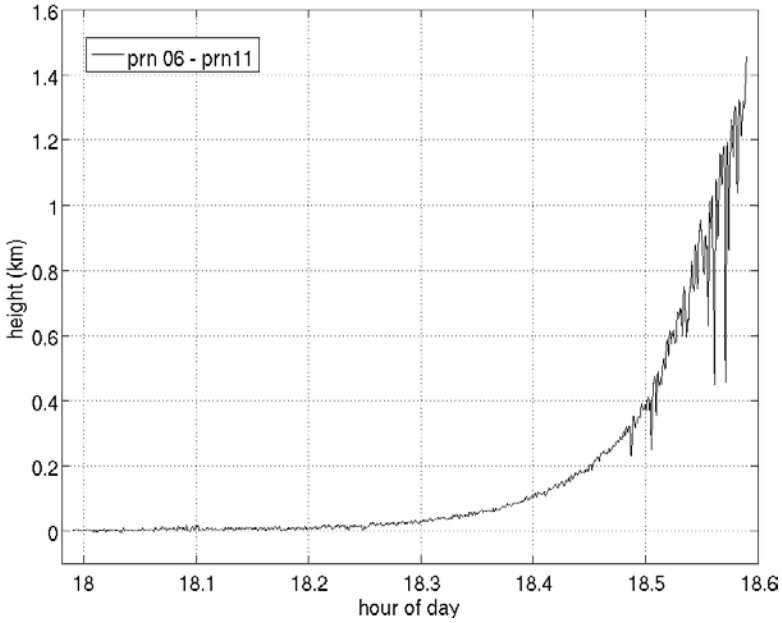

Figure 3.7 The 1 Hz prn06 excess Doppler after the high elevation prn 11 Doppler has been subtracted.

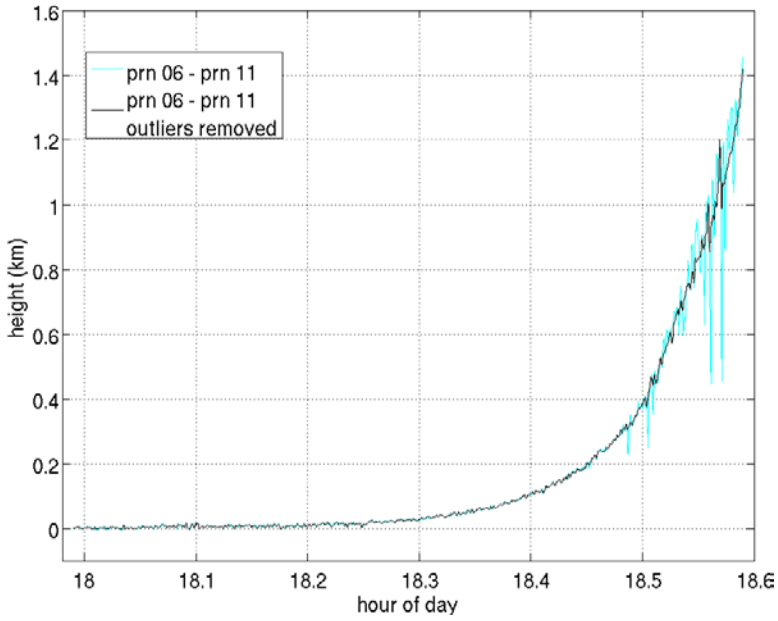

Figure 3.8 The 1 Hz prn06 - 11 excess Doppler is shown in cyan. The same Doppler with outliers removed is shown in black.

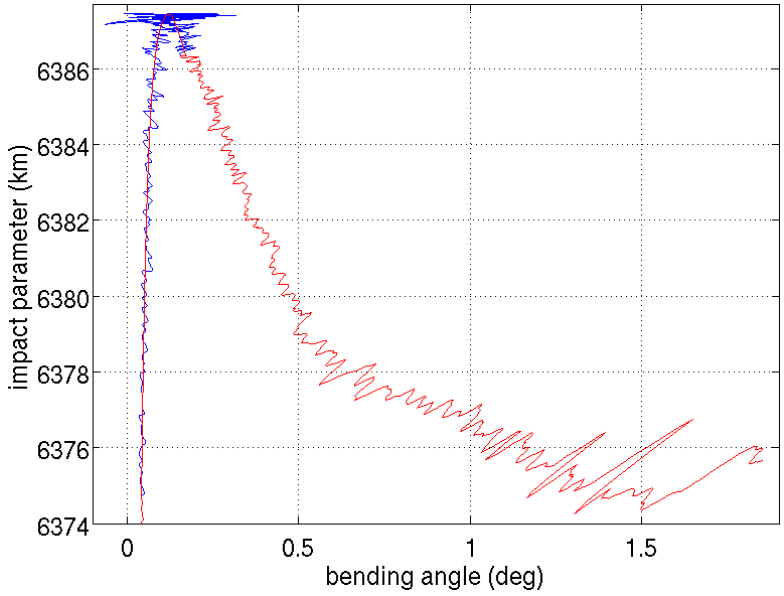

Figure 3.9 Bending angle profile of RF16 prn06 setting occultation in blue. The profile with zero and positive elevation sections replaced is overlaid in red.

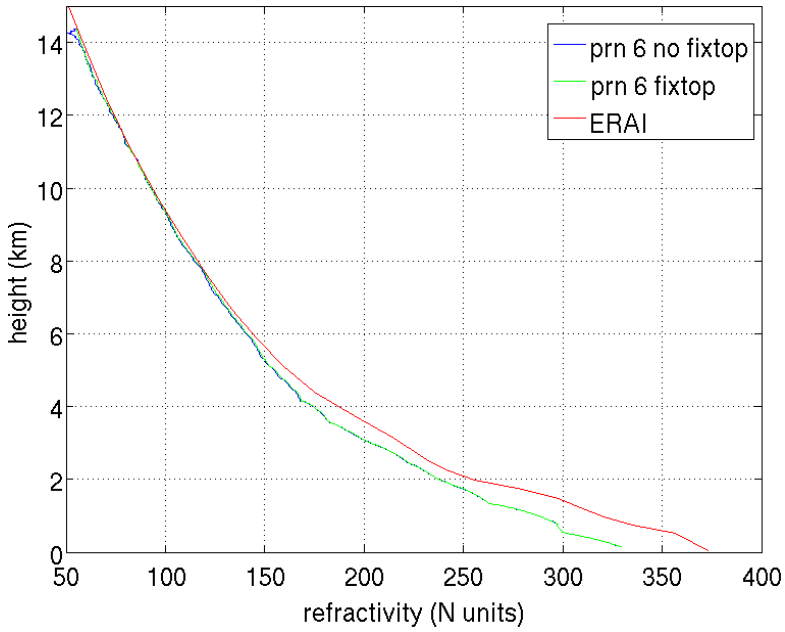

Figure 3.10 Retrieved refractivity of RF16 prn06 setting occultation is given in blue (no fixtop). The retrieval after replacement of noisy zero and positive elevation sections is shown in green and is labeled as fixtop in the legend. The refractivity based on ERAI grid point nearest the occultation point is shown in red.

The refractivity retrieval extends well into the lower troposphere nearly to the surface. The SNR of the excess phase was maximized by using the climatology option when running the PSR where the model phase for OL tracking included the geometric phase and an estimate of the phase accumulated due to the neutral atmosphere. The more accurate Doppler in the local replica signal was obtained from differentiation of the model phase from the atmospheric climatology. The improved Doppler model allows better estimates of the code delay, which gives a better alignment of replica and received signal during correlation, increasing SNR.

The ARO result is compared to a profile calculated with ERAI reanalysis in figure 3.10. The ERAI profile was calculated at each ARO tangent point height and location obtained from the ROSAP simulation used in the PSR processing to estimate atmospheric

phase for the climatology option (section 3.5.2). The retrieved ARO refractivity has a large negative bias below 6 km, which is most likely due to the effects of multipath reception in the bending angle from signals traveling through the moist lower troposphere. Radio holographic methods use spectral methods to retrieve bending angle in the presence of multipath and should produce much improved results compared to geometric optics retrievals, and are discussed in section 3.8.

An additional retrieval example from RF18, prn20 minus prn14, is shown in figures 3.11 – 16. This case is a rising occultation. The retrieved refractivity shows a smaller difference the ERAI profile than the prn06 example.

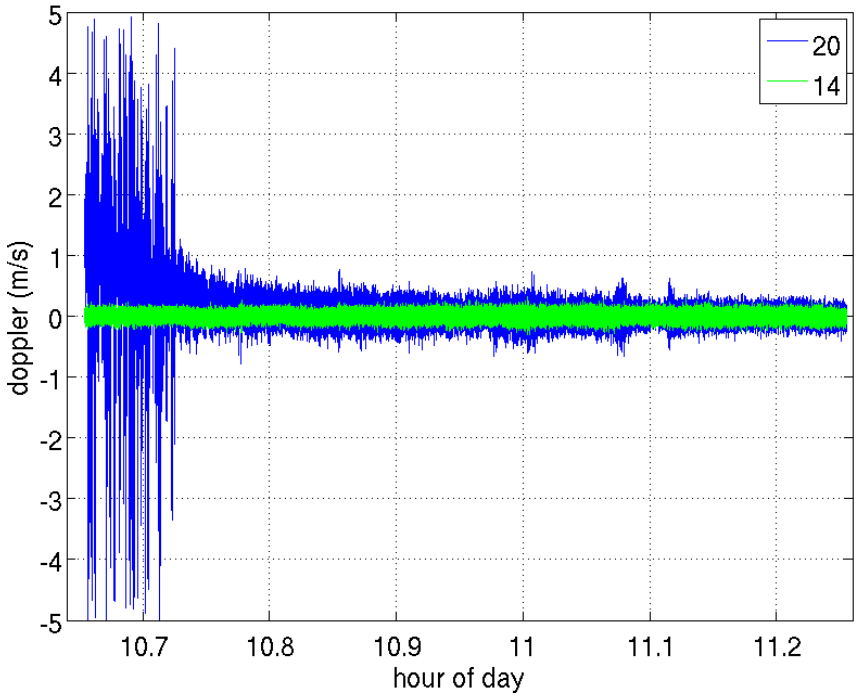

Figure 3.11 RF18 rising prn20 50 Hz excess Doppler (blue) and high elevation prn14 excess 50 Hz Doppler (green). After smoothing, the high elevation Doppler will be subtracted from the setting Doppler to remove receiver clock error.

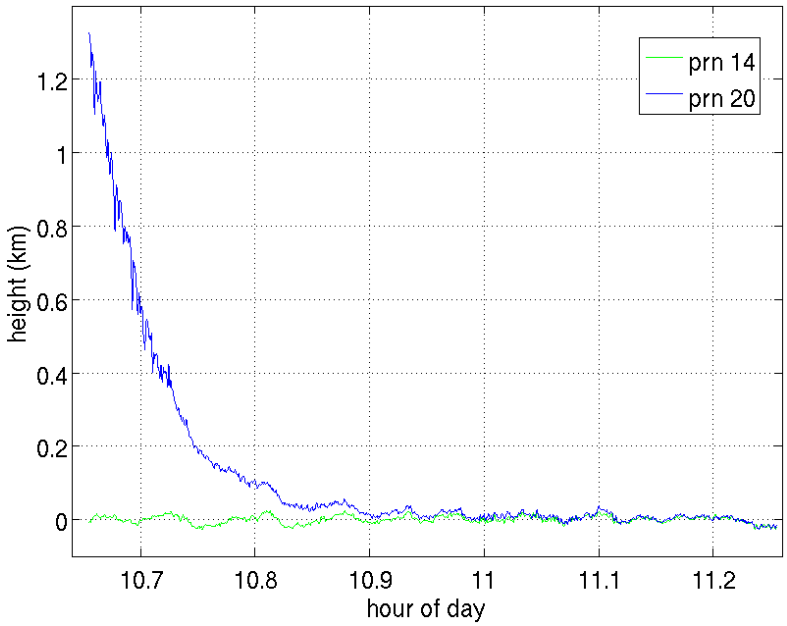

Figure 3.12 RF18 1 Hz prn20 setting Doppler (blue) and high elevation prn14 Doppler (green) after smoothing and decimation to 1 Hz.

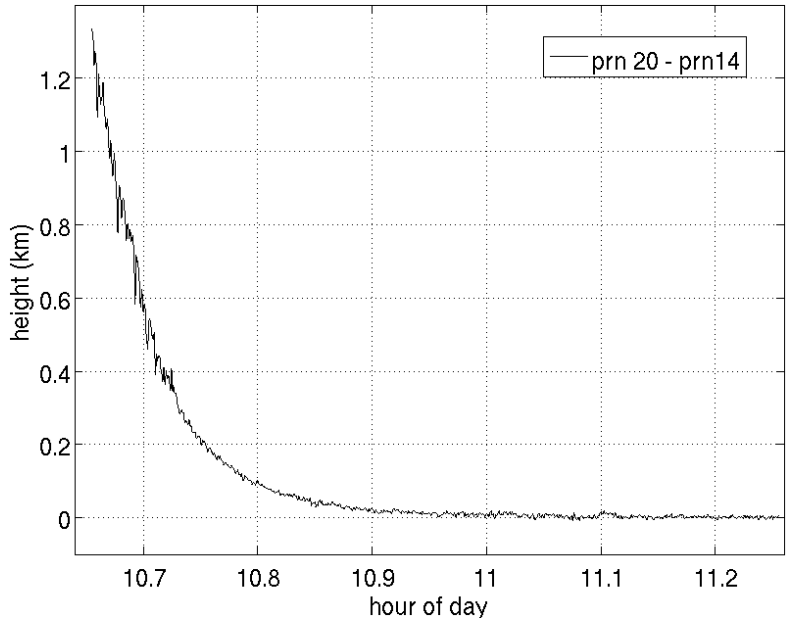

Figure 3.13 The 1 Hz prn20 excess Doppler after the high elevation prn 14 Doppler has been subtracted.

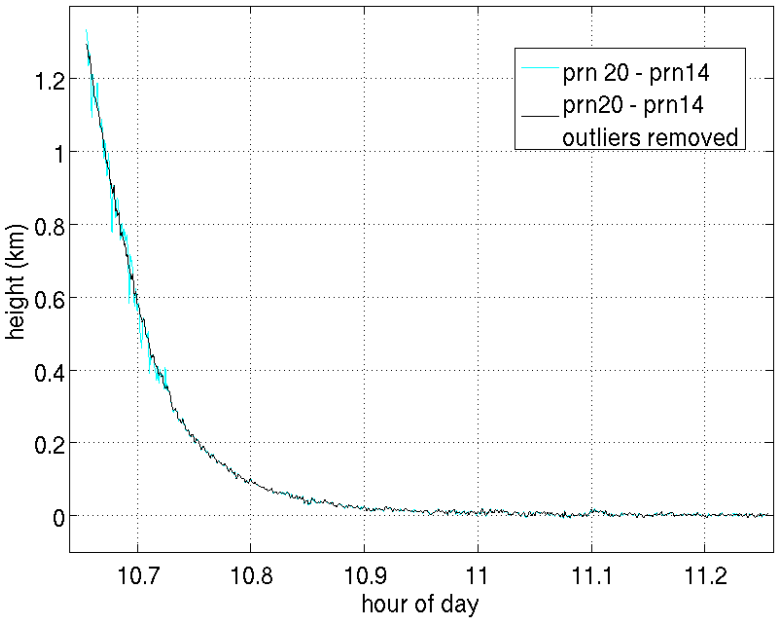

Figure 3.14 The 1 Hz prn20 - 14 excess Doppler is shown in cyan. The same Doppler with outliers removed is shown in black.

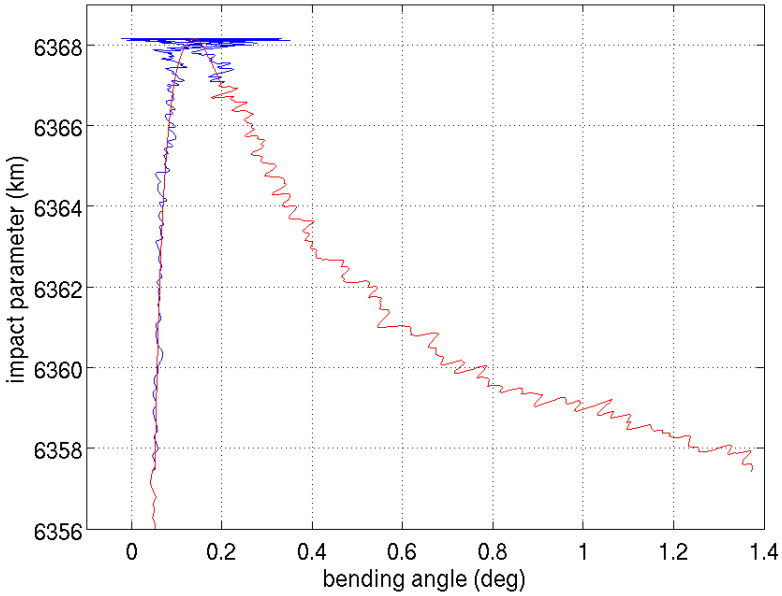

Figure 3.15 Bending angle profile of RF18 prn20 setting occultation in blue. The profile with zero and positive elevation sections replaced is overlaid in red.

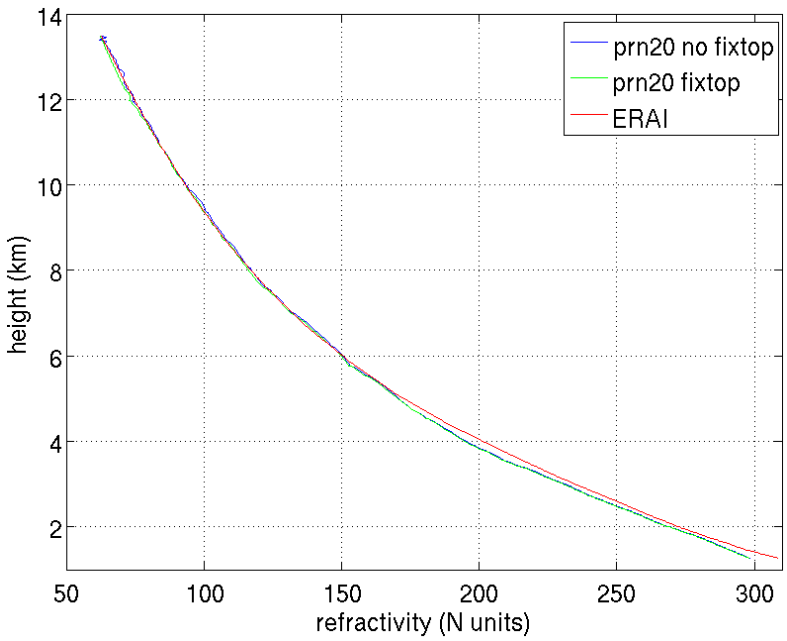

Figure 3.16 Retrieved refractivity of RF16 prn06 setting occultation is given in blue (no fixtop). The retrieval after replacement of noisy zero and positive elevation sections is shown in green and is labeled as fixtop in the legend. The refractivity based on ERAI is shown in red.

3.6 Comparison of Geodetic NetRS Receivers with Open Loop

The conventional PLL tracking used by the commercial NetRS geodetic receivers used by GISMOS is not optimal in the lower troposphere because of the use of signal feedback in a tropical environment where moisture can result in sharp gradients of atmospheric refractivity (section 3.1). OL tracking was implemented to improve tracking in the lower troposphere where a pre-computed Doppler model is used in place of signal feedback. Because of the difficulty encountered by PLL tracking during PREDICT, only one or two ARO profiles were retrieved per flight (chapter 2). The geodetic receivers also tended to lose lock on the signal at tangent point heights below 6 km on average and did not track as long as open loop retrievals (figure 3.17).

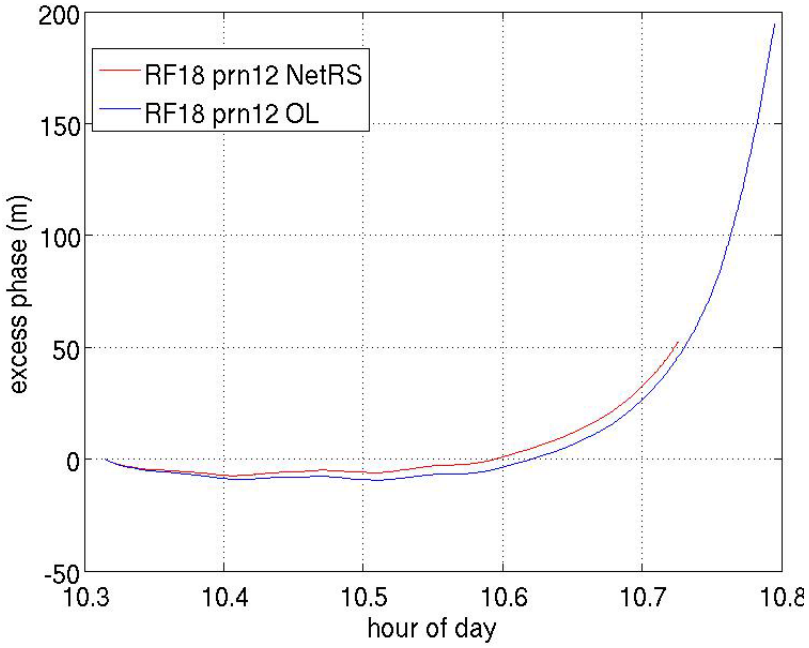

Figure 3.17 Comparison of excess phase measured by NetRS geodetic receiver (red) and open loop (blue) during RF18 prn12 setting occultation. Open loop tracked excess phase longer than NetRS receiver.

A difference is also seen in the magnitude of the NetRS excess phase compared to the open loop excess phase in two cases from RF18, prn12 and prn25 (figure 3.18 - 19). The slopes of the approximately linear differences in phase represent constant Doppler differences of about 0.004 m/s. This magnitude of Doppler difference could lead to about 1-2 % difference in the retrieved refractivity (see section 3.9 for sensitivity test results). Further investigation will be needed to determine the cause of the difference seen in excess phase. All inputs for both the geodetic receivers and open loop tracking will need to be checked. Some inputs to look at are that the NetRS measurement was obtained using IGS clock and orbit products while CODE products were used with open loop and the time tagging for open loop that was recently updated.

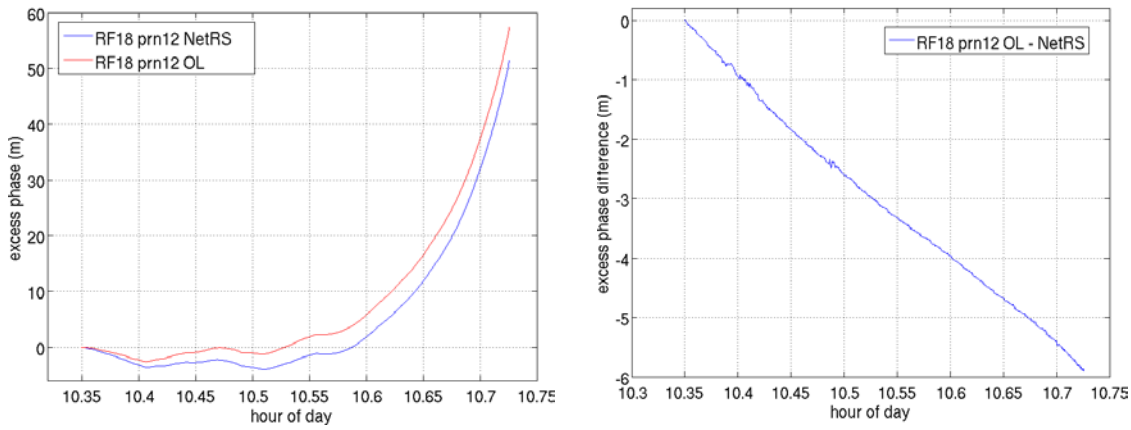

Figure 3.18 LEFT: RF18 prn12 excess phase measured buy NetRS and open loop over 10.35 to 10.72 UT. RIGHT: Difference of RF18 prn12 OL and NetRS excess phase over this interval.

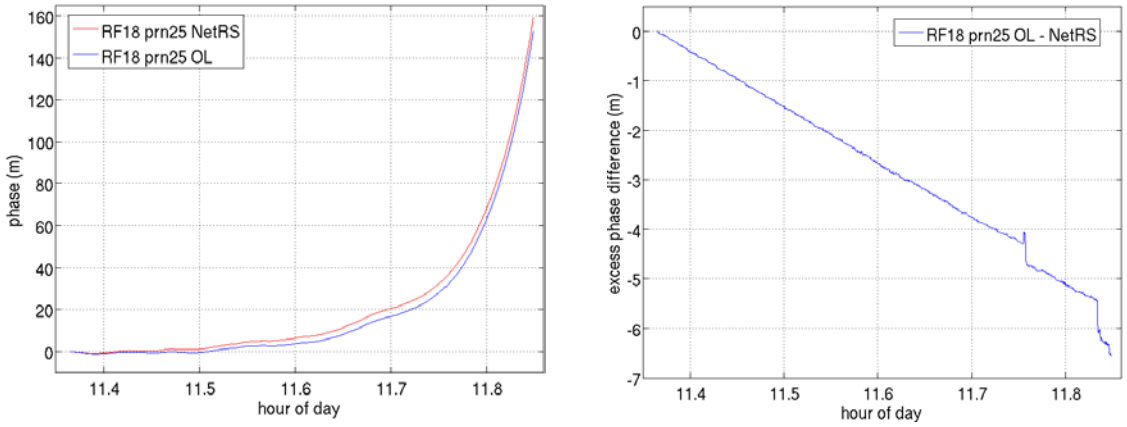

Figure 3.19 LEFT: RF18 prn25 excess phase measured by NetRS and open loop over 11.35 to 11.84 UT. RIGHT: Difference of RF18 prn25 OL and NetRS excess phase over this interval.

3.7 Factors Impacting ARO Signal-to-Noise

The quality of many of the ARO profiles is significantly lower than theoretically expected, based on the controlling error source of velocity error in the Doppler observations [Xie et al., 2008]. Although many of the retrieved profiles indicate

sensitivity to vertical structure that is consistent with the variations seen in dropsondes, there is sometimes present a refractivity bias in the upper levels, and often a refractivity error that trends negative with lower altitude. This is a surprising result, and therefore we investigate possible sources for these errors.

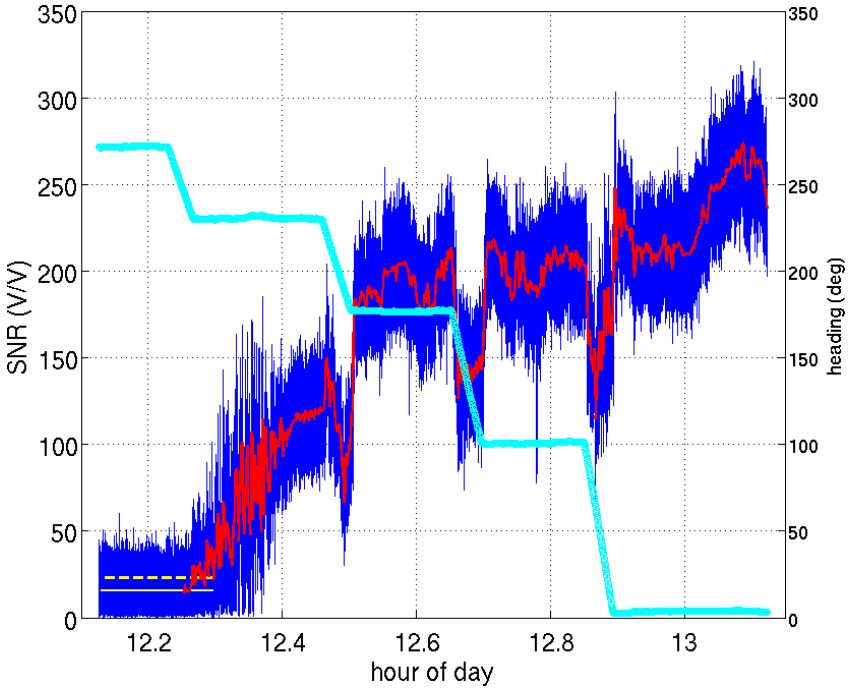

Figure 3.20 SNR measured during RF17 prn19 rising occultation recorded through the top antenna (CH1) with a ten second moving average shown in red. The heading of the aircraft is given by the cyan line in degrees. The mean noise floor is shown by the solid yellow line and the dashed yellow line denotes one standard deviation above the mean noise floor. The SNR drops when the plane makes a turn.

The accuracy of the ARO excess phase obtained from OL tracking, and hence the ARO retrievals, was degraded by low signal to noise ratio (SNR). SNR decreases as elevation angle decreases because of attenuation of the signal through a thicker atmosphere. Aircraft turns also caused drops in SNR as the antenna gain pattern is rotated relative to the occulting satellite. Figure 3.20 shows sharp drops in SNR occurring at the

times of aircraft turns. These drops in SNR were superimposed on the overall decrease in SNR as the occulting prn descended below the aircraft horizon and gain pattern of the receiving antenna. The SNR of the high gain side mounted antennas will be greater than that obtained from the top antenna (figure 3.21) although SNR of the side antennas also falls during a turn. Additionally, the aircraft could turn such that the view of the occultation is lost by the side antenna. (figure 3. 22). The top antenna was able to track an occultation through all turns because of its isotropic gain pattern, although SNR would generally fall after a turn.

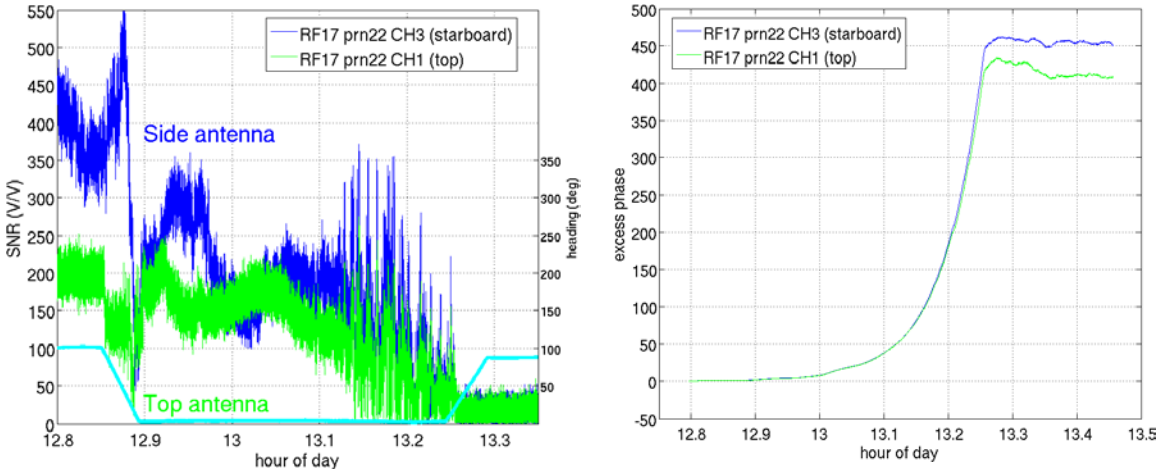

Figure 3.21 LEFT: SNR of RF17 prn22 setting signal received through the high gain side antenna (blue) and lower gain top antenna (green). The high gain antenna obtains greater SNR, though SNR of both top and side antenna are affected by turns RIGHT: The RF17 prn22 open loop excess phase obtained from the side and top antenna signals.

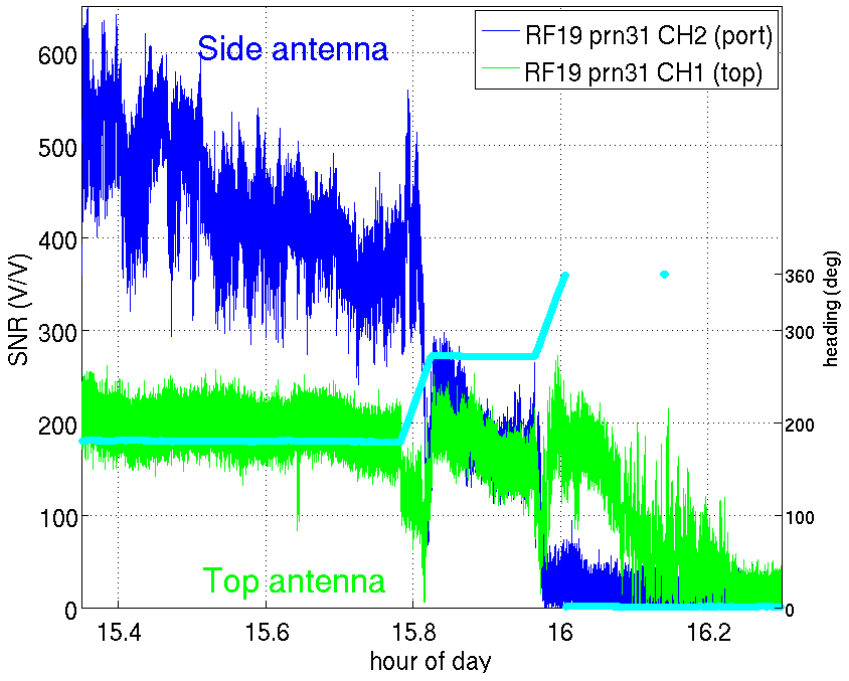

Figure 3.22 SNR of RF19 prn31 setting signal received through the high gain side antenna (blue) and lower gain top antenna (green). By 16 UT, the side antenna lost view of occultation due to turns, but top antenna continued to see the signal.

However, by far the most challenging effect is the signal fading and variations in SNR due to atmospheric multipath. Multipath occurs when more than one GPS signal arrives simultaneously at the receiver along different ray paths with different tangent point heights. In this case, the bending angle retrieved from the measured excess Doppler will not represent a unique ray path. Multipath is likely in the lower troposphere where strong gradients of moisture exist in the refractivity field. Atmospheric multipath also contributes to the errors in the geometric optics retrievals [*Kursinski et al.*, 1997]. A negative bias of refractivity has been observed in geometric optics retrievals of spaceborne RO in the lower troposphere which was probably due in part to the effects of multipath [*Ao et al.*, 2003; *Rocken et al.*, 1997].

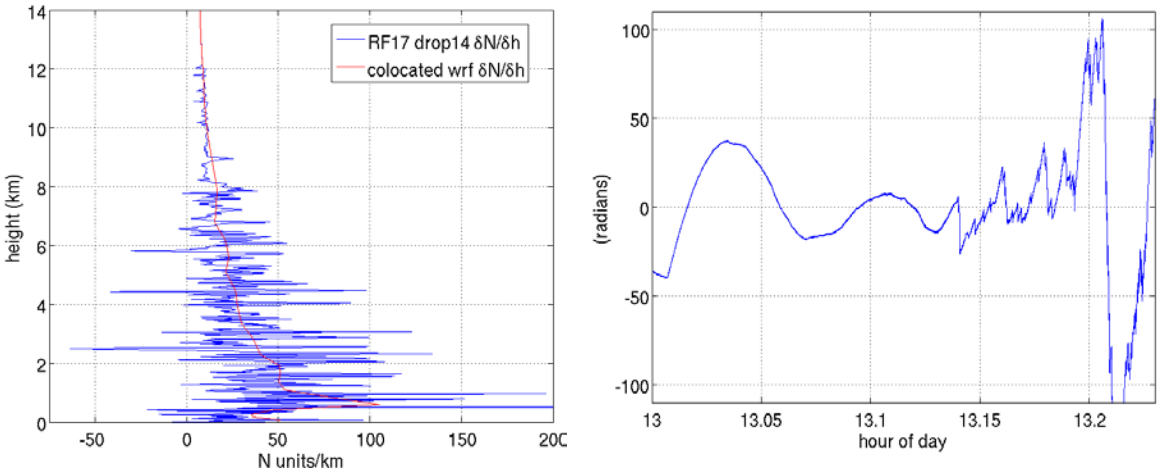

Figure 3.23 The vertical gradient in refractivity calculated from RF17 dropsonde 14 (nearest to prn22 setting occultation) begins to fluctuate rapidly below 8 km indicating the possibility of multipath reception of GPS signals passing through these levels. RIGHT: The prn22 excess phase with increasing trend removed. Noise in the prn22 excess phase worsens noticeably after 13.14 UT, the time at which the ARO tangent point height passes through 7.3 km altitude. The excess phase noise introduces error into the geometric optics retrieval.

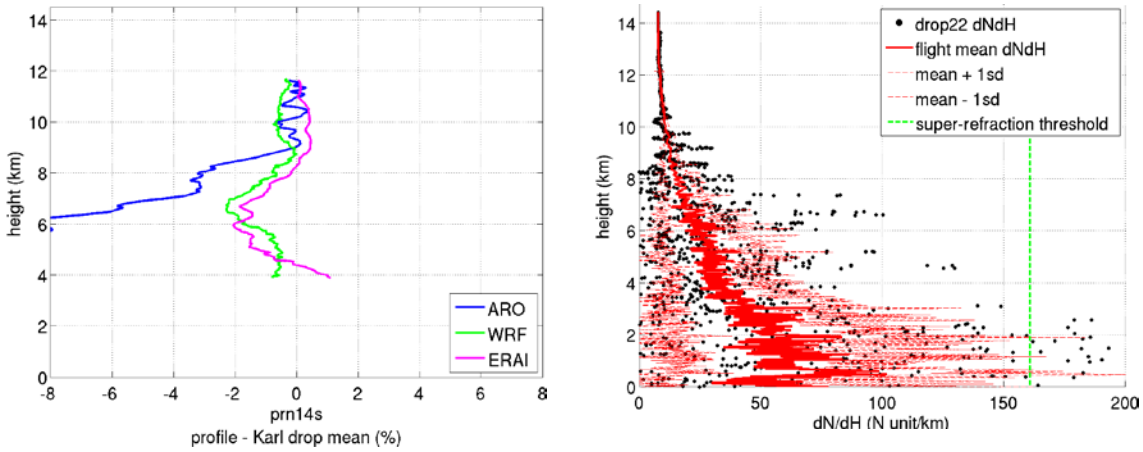

Figure 3.24 LEFT: The RF17 prn14 setting occultation refractivity profile relative to the pre-Karl mean background and compared to profiles along the tangent point path derived from ERAI and WRF model output. There is a noticeable negative bias in the ARO profile beginning at 9 km, likely related to multipath. RIGHT: The increasing fluctuations in vertical gradient of refractivity calculated from data recorded by a dropsonde near the prn14 occultation shown by the black scatterplot contrasted with the mean gradient of all dropsondes from RF17 plotted in red. Noticeable large gradients begin at 9 km height coincident with the onset of negative bias in the ARO profile.

All airborne occultations observed during PREDICT were observed in the environmental conditions of a developing tropical storm where atmospheric moisture increases significantly below 9 km height as indicated by the strong vertical gradient of refractivity shown by the left panel of figure 3.23. Multipath is most likely significant where vertical refractivity gradients are high below 8 km height (figure 3.24) and a negative bias in a geometric optics retrieval is seen in this environment (left panel of figure 3.24). Because the geometric optics retrieval is not optimal in a multipath environment, research is currently being carried out by project collaborators to implement radio holographic retrieval techniques in order to improve retrievals below this altitude (section 3.8).

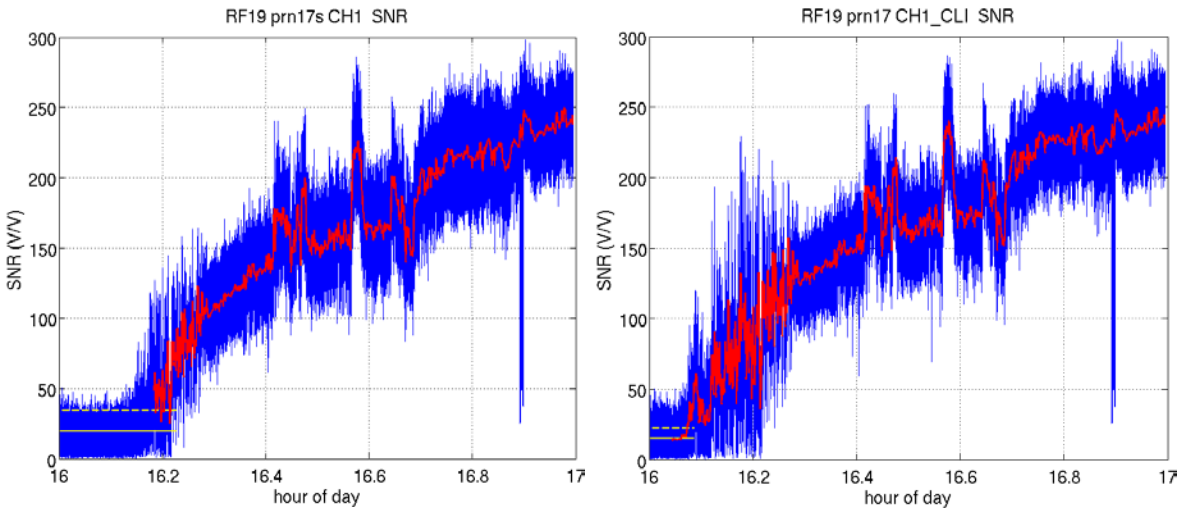

Figure 3.25 LEFT: SNR from RF19 prn17 setting occultation when only using geometric phase in the Doppler prediction model for open loop. RIGHT: The SNR from RF19 prn17 when the Doppler prediction model includes an estimate of excess phase from climatology with geometric phase. SNR has been increased from 16.1 to 16.4 UT compared to the case not using climatology.

In open loop tracking, a more accurate Doppler model results in higher SNR as the code edge can be located more accurately and there is an increased complex

correlation sum over each code interval. While open loop tracking is possible using a Doppler model based only on the geometric phase, an estimate of the expected excess phase from the atmosphere can be included in the predicted Doppler model (section 3.5.2). The use of climatology for open loop soundings retrieved in this work increased the signal SNR obtained from the PSR and resulted in the refractivity profiles reaching closer to the surface (figure 3.25 – 3.26).

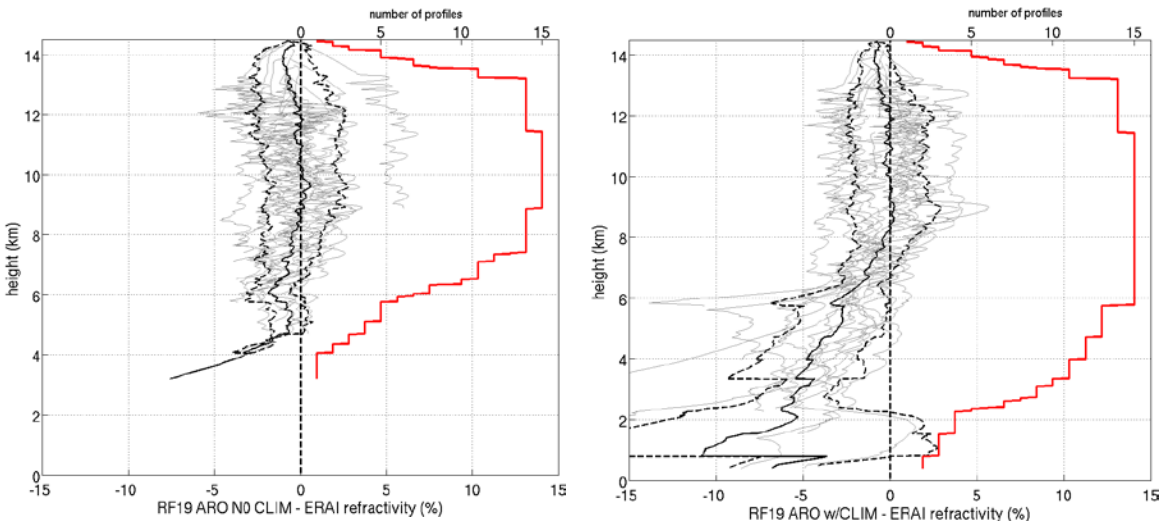

Figure 3.26 LEFT: The RF19 ARO profiles (gray) retrieved from open loop when climatology was not used in Doppler model. RIGHT: The same retrievals when climatology is used. The increase in SNR allows tracking to closer to the Earth's surface.

3.8 Radio Holographic Inversion of Open Loop Data

Radio Holographic methods have been developed to correctly derive spaceborne radio occultation bending angles in regions of high multipath. Two of these methods are being adopted for ARO. A Full Spectrum Inversion (FSI) [*Jensen et al.*, 2003] retrieval method for ARO bending angle from open loop excess phase is being developed by our collaborators, Feiqin Xie and Loknath Adikari at Texas A&M University, Corpus Christi.

Another radio holographic approach, Phase Matching (PM) [*Jensen et al.*, 2004], is being adopted for ARO by collaborators James Garrison and his student Kuo-Nung Wang at Purdue University, West Lafayette, [*Wang et al.*, 2015b]. The purpose of the FSI and PM techniques is to disentangle instantaneous frequency components which are combined in the RO signal due to multipath interference. Geometric optics would return a bending angle value at the arrival time corresponding to a single tangent point impact parameter, whereas the FSI and PM would return multiple values of bending for multiple impact parameters for different rays arriving at the receiver at the same time.

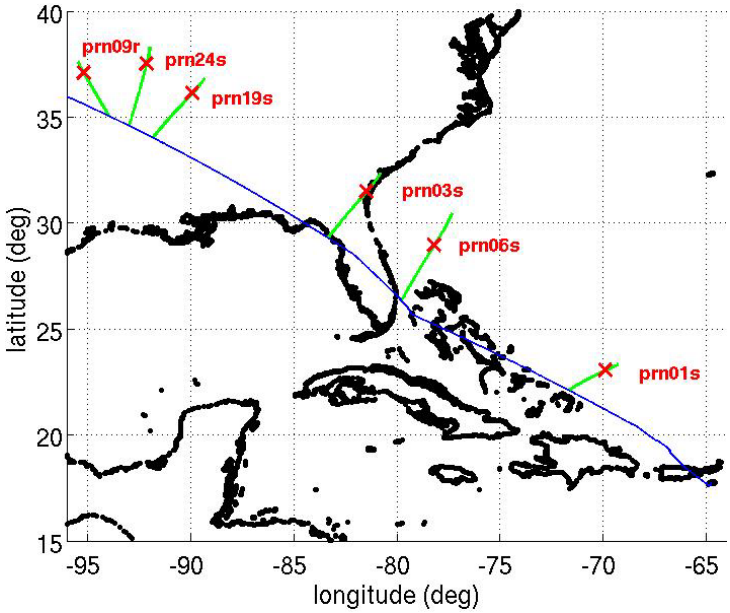

Figure 3.27 FF04 flight path (heading northwest) on 02 October 2010 is shown in blue with ARO occultation tangent point paths shown in green for occultations recorded on the starboard antenna. Occultation points are marked by red crosses.

Based on their preliminary results, we present a test case comparison with the geometrics optics retrievals, to illustrate the potential improvement in the refractivity

retrieval. Because the methods are new and have not been tested extensively, we rely on our geometric optics retrievals for the further chapters presented in this thesis.

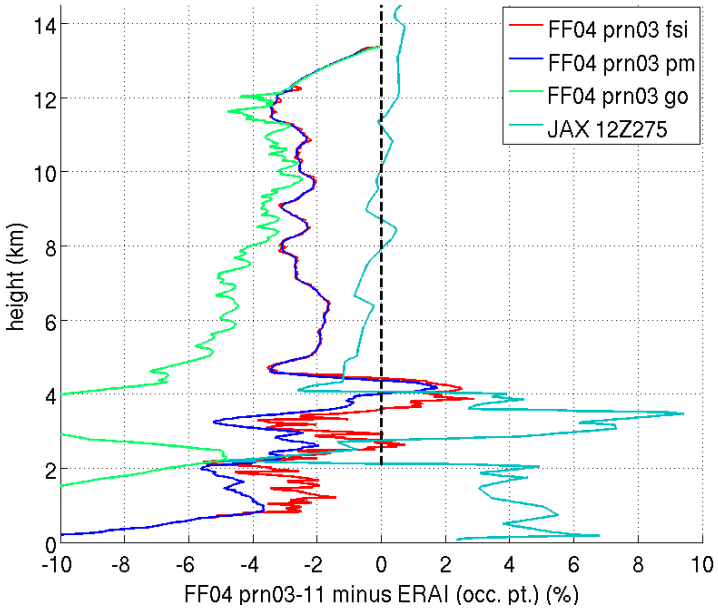

Figure 3.28: Differences of ARO FF04 CH3 (starboard antenna) prn03 refractivity with ERAI as calculated with Full Spectrum Inversion (FSI), Phase Matching (PM) and Geometric optics (GO). The difference of the nearby 02 October 2010 Jacksonville 12:00 UT radiosonde launch with ERAI is also shown.

The test case is from the GV ferry flight (FF04) from St Croix, US Virgin Islands to Jefferson County Airport in Broomfield, CO on 02 October 2010. This flight was chosen because of the straight and level flight path where occultations measured by the side antennas would not be terminated by aircraft turns. The prn03 setting occultation was chosen as the test case (figure 3.27). Refractivity retrievals for this occultation were retrieved using geometric optics, FSI and PM. The results are shown in figure 3.28 compared to the refractivity calculated from ERAI co-located with the occultation point.

The refractivity profile calculated from the nearby 12:00 UT Jacksonville radiosonde sounding is also shown.

Overall the results of this initial implementation of FSI are promising and indicate the possibility that the technique may significantly reduce most of the negative bias seen in GO retrievals. It is also encouraging that there is close agreement between FSI and PM, which were developed independently.

3.9 Open Loop Rising and Setting Occultation Bias

When a comparison was made between the rising and setting occultations over RF16 – RF19, an unexpected bias was found between rising and setting occultations (Figure 3.29). The setting ARO cases had a negative mean difference with ERAI while the rising cases had a positive mean difference with ERAI. The dropsondes from RF16 - 19 show a negative mean difference with ERAI between 5 – 14 km altitude similar to ARO setting cases (Figure 3.30), though not as pronounced. Because the dropsonde bias to ERAI was similar to the ARO setting bias to ERAI, it was suspected a positive bias might be introduced during backward tracking which would be greater than any negative bias that might be introduced by forward tracking. However, because backward tracking uses the same algorithms there is not an obvious reason why there would be a bias in the backward tracking relative to forward.

It is not easy to conduct tests with the PSR comparing forward and backward tracking since forward tracking is not designed to run with a rising satellite or vice versa. It is possible to run forward and backward tracking on a high elevation satellite in some cases. A very small bias in backward tracking excess Doppler relative to forward was

found from these tests (figure 3.31). For the RF18, a bias was found between rising and setting excess Doppler on the order of 0.001 – 0.005 m/s (Figure 3.32).

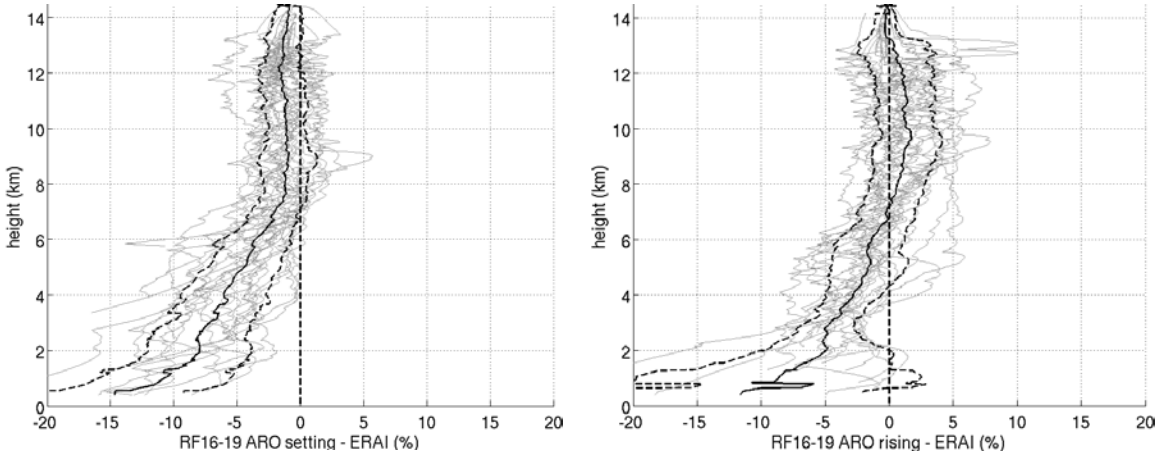

Figure 3.29 LEFT: Difference of RF16 – 19 setting occultations with ERAI. The setting cases show a consistent negative bias from 6 – 14 km. RIGHT: Difference of RF16 -18 rising occultations with ERAI. The rising cases show a positive bias relative to ERAI over the height range from 6 to 14 km. The dropsondes from RF16 -19 show a negative bias relative to ERAI between 6 – 14 km altitude, similar to ARO setting cases (Figure 3.20), though not as pronounced.

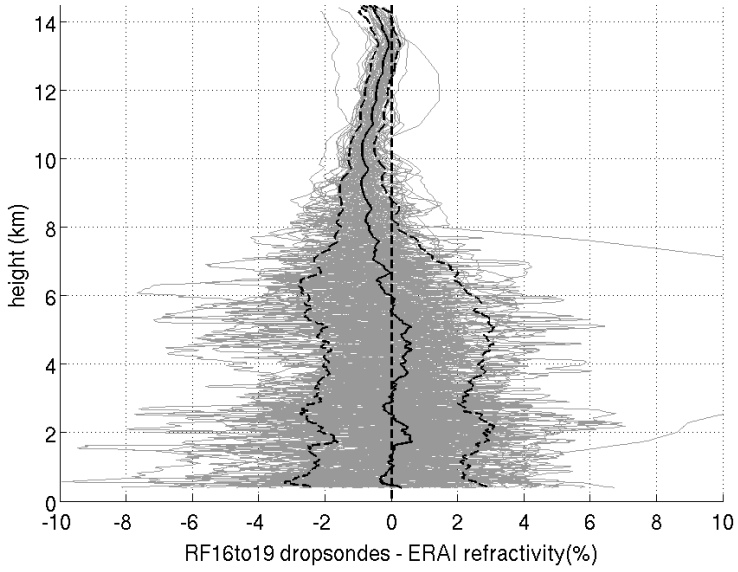

Figure 3.30 Difference of RF16-19 dropsonde refractivity with ERAI.

The bias between the setting and rising is small, but sensitivity tests do show small differences in excess Doppler can result in a significant change in the retrieved refractivity (figure 3.33). More testing will need to be done with the PSR to determine if some aspect of the backward tracking is responsible for the observed bias. Additionally, more flights will need to be processed to confirm if the bias seen in the Karl retrievals extend to other research missions flown during PREDICT.

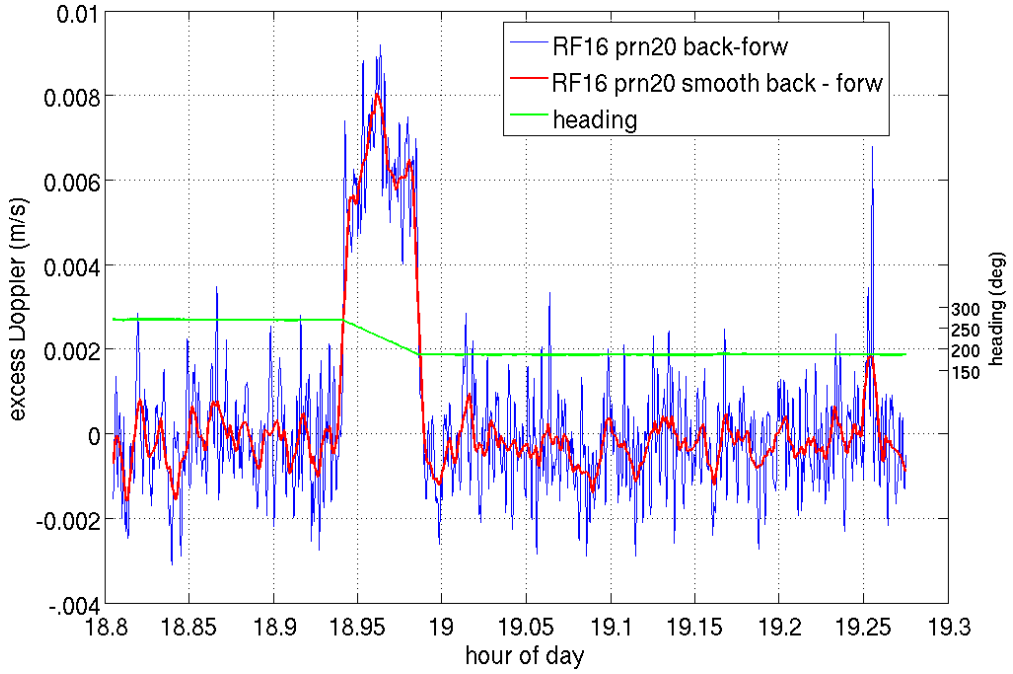

Figure 3.31 Difference of high elevation RF16 prn20 backward tracked excess Doppler (m/s) minus forward tracked (blue) as a function of the hour of day. The smoothed Doppler difference is given in red. The difference becomes worse during a turn at 18.95 UT. The aircraft heading is shown in green.

Another possibility for the bias of rising versus setting occultations is a possible mis-modeling of the Doppler velocity with time, because it would produce opposite effects in the retrievals. Further support for this type of bias is the strong effect that a change in orientation of the flight path has on the excess Doppler when the geometric

Doppler should have removed any such effect. While we do not have a hypothesis for the cause of the Doppler mis-modeling, we have carried out two sensitivity tests to determine their effects on the retrievals.

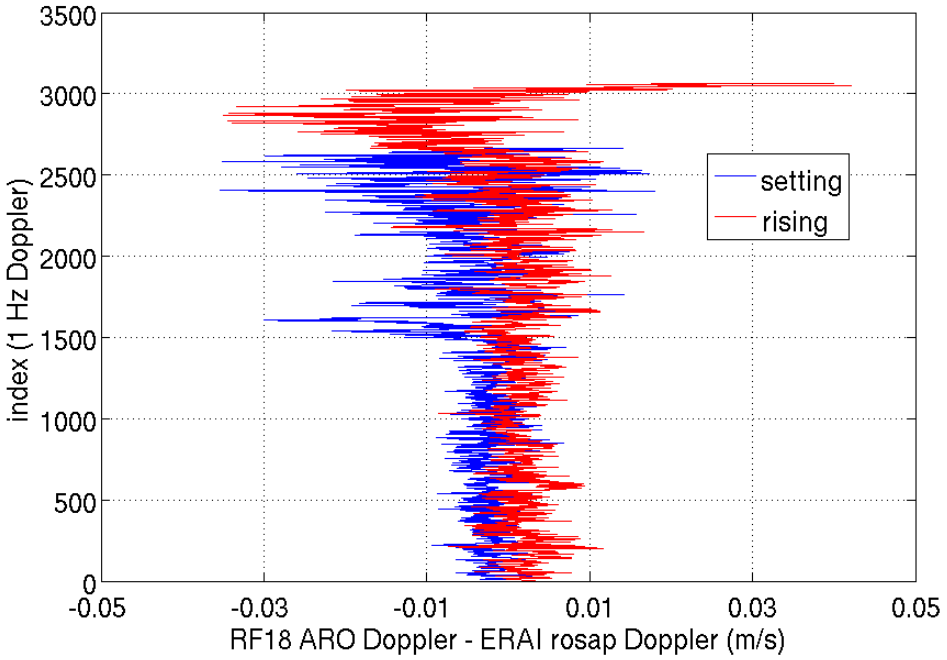

Figure 3.32 Mean of RF18 OL CH1 [setting (blue) and rising (red) smoothed, differenced Doppler] minus [Doppler simulated with ROSAP using co-located ERAI]. The means were found by shifting all the ARO-ERAI Doppler profiles to start at the same time (index = 1). After index 1600 (~25 min) there were only 1 - 2 profiles contributing to the mean, so the variance increases.

The first test examines a simple time offset in the observed phase. The ROSAP ray tracing program (section 3.5.2) is used to simulate excess phase. RF18 prn25 receiver and satellite position and velocity data are used with a refractivity profile from CIRAQ climatology (section 3.5.2) as input for ROSAP. The process is:

1) RF18 prn25 navigation data + CIRAQ (lat=15°, Sept) → ROSAP
   → Excess phase
2) Differentiate excess phase to get excess Doppler and smooth, then:
   → Shift in time relative to navigation data

3) Use shifted Doppler and navigation data in Doppler to bending angle program:
   ➔ Bending angle based on time offset excess Doppler
4) 'fixtop' (section 3.5.5) bending angle profile → partial bending angle
   ➔ Refractivity from inverse Abel transform

The bending angle sensitivity to the time shifts is shown in figure 3.34 and the refractivity sensitivity is shown in figure 3.35.

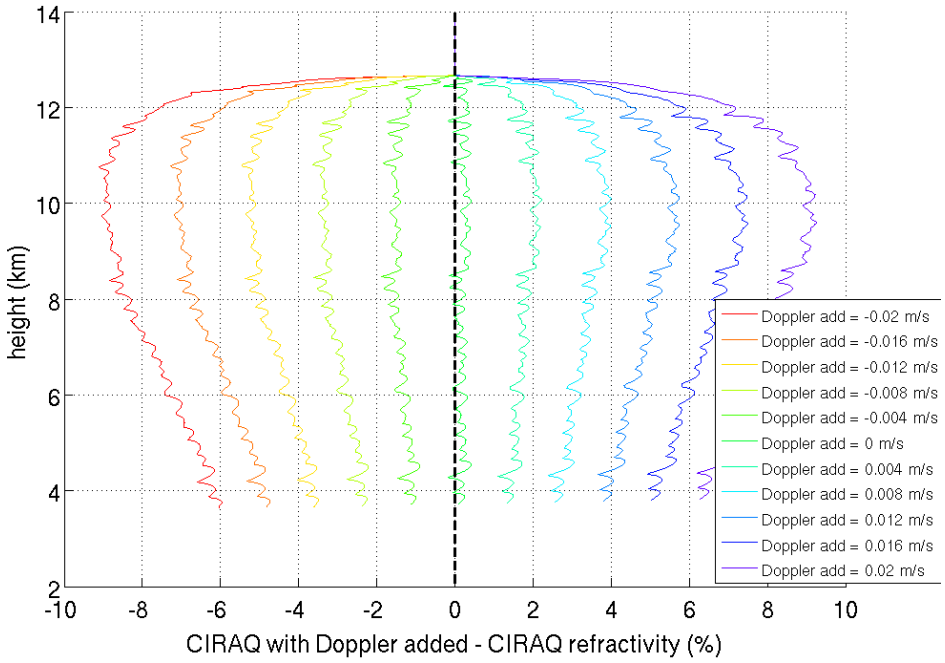

Figure 3.33 RF18 prn25 setting refractivity sensitivity to constant Doppler bias resulting from linear phase addition to excess phase.

The second sensitivity test examines a bias in the Doppler due to the addition of a linearly changing phase. Again, the ROSAP ray tracing program (section 3.5.2) is used to simulate excess phase. Similar to previous test, RF18 prn25 receiver and satellite position and velocity data is used with a refractivity profile from CIRAQ climatology (section 3.5.2) as input for ROSAP.

The process is:

1) RF18 prn25 oblate corrected geometry + ciraq → ROSAP
   → Excess phase
2) Differentiate phase to get Doppler and smooth, then
   → add a constant Doppler equivalent to a linearly changing phase
3) Doppler w/shift + RF18 prn25 navigation data → Doppler to bending program
   → bending angle profile
4) 'fixtop' (section 3.5.5) bending angle profile → partial bending angle
   → refractivity from inverse Abel transform

The bending angle sensitivity to the time shifts is shown in figure 3.36 and the refractivity sensitivity is shown in figure 3.33.

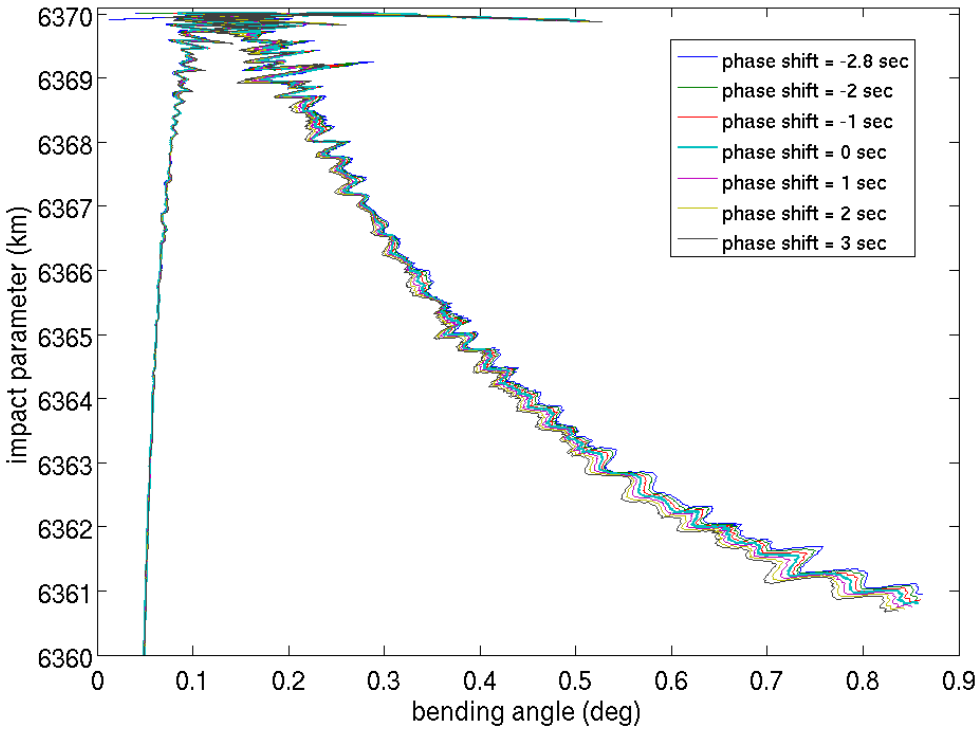

Figure 3.34: ARO bending angle sensitivity to time shifts of excess phase relative to the receiver-prn geometry. Bending was derived using RF18 prn25 navigation data and CIRAQ refractivity.

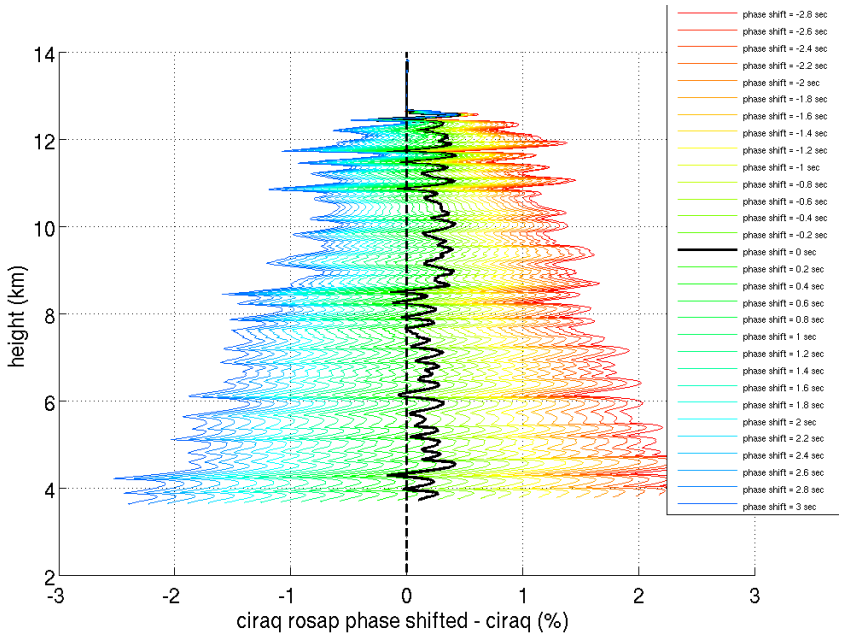

Figure 3.35: Difference of refractivity obtained from time shifted excess Doppler with original refractivity corresponding to non-time shifted Doppler. Derived using RF18 prn25 navigation data and CIRAQ refractiity. The time shift profiles, including the zero time shift, show a positive bias to zero mean which will require further investigation.

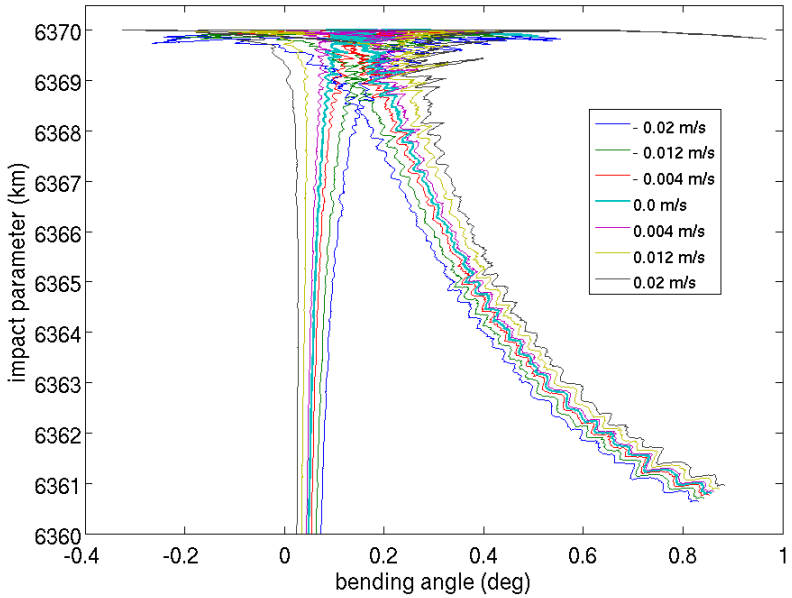

Figure 3.36: ARO bending angle sensitivity to excess phase error due to constant Doppler shift. Bending was derived using RF18 prn25 navigation data and CIRAQ refractivity.

3.10 Conclusions

Open loop tracking is not susceptible to loss of signal lock in the moist tropical environment that is seen in the conventional geodetic receivers. Therefore it is possible to track and obtain excess phase for nearly all visible rising and setting occultations within view of the aircraft antennas during a research flight and below 6 km altitude where the geodetic receivers usually lost track. The PSR has an improved Doppler frequency model that includes the estimated delay due to the neutral atmosphere based on CIRAQ climatology. Using a Doppler model that includes climatology increases the SNR of the excess phase, allowing occultations to be tracked to altitudes below 1 km. Geometric optics analysis is used to obtain bending angle from the excess Doppler. In a moist tropical environment, atmospheric multipath is likely and the geometric optics technique will not give a correct bending angle in the presence of multipath. Radio holographic techniques which correctly calculate bending angle in a multipath environment have been developed for ARO (Eric Wang personal communication; Loknath Adhikari personal communication). In a test case comparing results from the setting prn03 occultation during FF04, radio holographic retrievals of refractivity showed a significant improvement over the geometric optics retrieval below 8 km altitude.

Because the flight tracks, typically a variant of a lawnmower or square spiral pattern, used to investigate storm systems during PREDICT were not optimal for observation of an occultation using a side mounted antenna due to turns, not all occultations could be measured with the side looking high gain antennas. However, despite having lower gain, the top antenna with an isotropic gain pattern and was able to

measure most occultations. During turns, SNR fell for both side and top antennas as the gain pattern rotated.

A bias between rising and setting OL ARO occultations has been found when compared to ERAI. It is possible the bias originates from an error in the OL tracking, but tests have been inconclusive. Another possibility is the error arises from a mis-modeling of the Doppler frequency model. This type of error cannot be excluded at this point. Note that these errors, would also affect the quality and SNR of the open loop tracking results. Future work will need to address these potential causes of these biases. For the present, we continue the analysis of the refractivity profiles in the next chapter, keeping in mind 1) that we should be cautious in our interpretation of refractivity unless the variations seen are larger than these types of biases, and 2) the analysis results presented are of significant value in anticipating the utility of the data and developing techniques for analyzing the horizontal variability, that will be especially useful when considering future potentially improved datasets that exploit FSI or other radio holographic inversion methods

CHAPTER 4. AIRBORNE RADIO OCCULTATION REPRESENTATION OF MOISTURE VARIABILITY NEAR A DEVELOPING TROPICAL STORM

4.1 Introduction

Currently, much effort is being made in the scientific community to better understand tropical cyclogenesis and improve forecasts of the intensity and storm track of newly formed hurricanes. Moisture is one of the most critical observations, along with temperature and winds, needed for numerical weather prediction (NWP) hurricane forecasting [*Zheng et al., 2015*]. Deep moisture is a critical factor in tropical cyclogenesis [*Sippel and Zhang 2008, 2010*] as the latent heat from condensation of water vapor in the humid tropical air is the primary energy source for a developing hurricane. Atmospheric refractivity measured by ARO is directly related to temperature and moisture, and a recent study has shown that a multi-event composite of the moist thermodynamic structure of tropical cyclones can be mapped using spaceborne RO data [*Vergados et al.*, 2013]. Vergados et al. [2013] used GPS RO vertical profiles found in the vicinity of 42 tropical cyclones (TC) from 2002 to 2010. The profiles were viewed as a function of distance from the TC centers in order to analyze the surrounding environment. The averaged RO data revealed interesting features such as a low level injection of water vapor in the mid to lower troposphere about 50 km from the TC center corresponding to the typical location of the eyewall. Sections of the radial profile at regular distance

intervals from the storms' centers were found to have increased relative humidity in the 3 to 8 km height range, indicative of rain bands. These features were also seen in ECMWF ERA interim re-analysis humidity, confirming the efficacy of the RO profiles to resolve these features.

Because radio occultation observations integrate the refractivity information over a large horizontal extent, the technique is usually not considered optimal for sampling and resolving mesoscale structure in the atmosphere [*Anthes*, 2011b]. However, studies have found assimilation of serendipitously located spaceborne RO data to have generally favorable impacts on NWP hurricane and typhoon forecasts [*Huang et al., 2008;Kunii et al., 2012;Kuo et al.,2008;Liu et al. 2012*]. Above the planetary boundary layer, the majority of the bending due to atmospheric refractivity occurs within ± 50 to 170 km of the tangent point, theoretically allowing resolution of horizontal variations of this scale in the area sampled by the tangent point path. Historically, since spaceborne RO has such sparse coverage in the vicinity of a particular storm track, it has been difficult to show that this is the case. For example, during the day prior to development of Karl in 2010, only one spaceborne occultation was available from the COSMIC RO mission within 400 km of the storm center. An airborne RO system, on the other hand, provides multiple occultation profiles sampling a targeted mesoscale region around the developing tropical cyclone. Therefore airborne observations provide a promising means to investigate what scale of moisture variations are best resolved by the occultation technique, and help define the potential impact this type of data would have in NWP models.

This thesis lays the groundwork to carry out assimilation tests for forecasting tropical storms by providing a first look at horizontal and temporal variations in

atmospheric properties over the early stages of tropical cyclone development as determined by these observations. Comparison of the observed refractivity profiles with those calculated from model fields and dropsonde data provides a basis for the observation errors required for NWP model assimilation. Using observations of the system that would eventually become hurricane Karl, it describes the expected and observed scales of temporal and spatial moisture variability evident directly in the refractivity profiles and how it compares with moisture variations in high- and low-resolution model fields over the course of tropical storm development. It investigates the observed contrast in refractivity in the larger scale environment compared with that near the storm center at different stages of development.

The synoptic evolution of the pre-Karl hurricane system is described in section 4.2, the representation of pre-Karl moisture by ARO refractivity is described in section 4.3, the high resolution mesoscale modeling of the event is described in section 4.4, the high resolution model and reanalysis intercomparisons with ARO data are described in section 4.5, with model validation statistics provided in section 4.6. Spatial refractivity variability along the tangent point path is discussed in section 4.7. Temporal variability over RF16 to 19 is shown in section 4.8 and spatial variability at the occultation points is shown in section 4.9. The radial structure of the tropical storm environment is discussed in section 4.10. Conclusions are summarized in section 4.11.

4.2 Development of the Pre-Karl System

The system which developed into hurricane Karl in September of 2010 initially formed from the merger of a tropical wave moving westward from Africa with a low

pressure trough situated over the Atlantic northeast of the Venezuelan coast about 8 September 2010 (figure 4.1). After the merger of the wave and trough, the system moved eastward into the Caribbean Sea over the next two days, producing intermittent convection. As the system moved across the Caribbean over 10 – 13 September, convection increased, eventually resulting in a large band of deep convection aligned along a southwest – northeast tilted axis near the circulation center [*Davis and Ahijevych*, 2012]. The mid and lower level circulation centers of the system were found to be misaligned when the system entered the Caribbean, which may have delayed storm development [*Davis and Ahijevych*, 2012]. The misalignment reduced over time until the mid-level center was slightly southeast of the lower level circulation on the 13th. Shortly thereafter, on 14 September, the system attained tropical depression strength. Karl continued to develop, reaching tropical storm strength six hours later. Karl further strengthened as it approached the Yucatan peninsula, which it crossed at midday on 15 September. After moving into the Bay of Campeche, Karl rapidly developed into a major hurricane. Karl reached peak intensity of 127 miles per hour wind speed at 12 UT 17 September, making landfall later that day northeast of Veracruz, Mexico.

Increased moisture levels are expected within an area of closed circulation co-moving with a tropical wave compared to the outside environment, as the region is protected from dry air intrusion and wind shear [*Dunkerton et al.*, 2009]. Studies of dropsonde and satellite data from PREDICT have confirmed the higher moisture near the circulation center, especially within 200 km of the circulation center for developing storms and with increasing moisture in this region as genesis approaches [*Davis et al.*,

2014; *Komaromi*, 2013]. We extend this investigation to include ARO data by quantifying larger scale variations of moisture represented by refractivity.

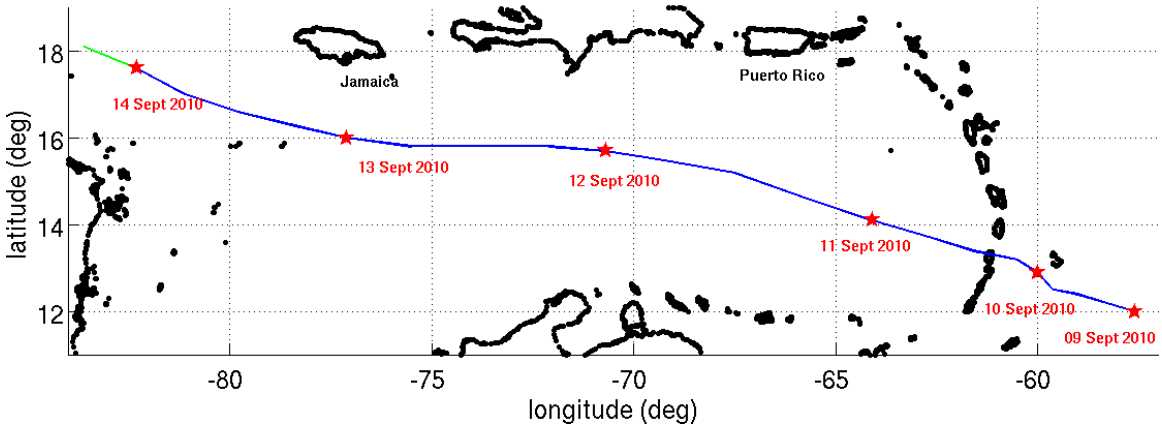

Figure 4.1 Track of developing pre-Karl system over 9 – 14 September 2010. The 12 UT storm locations for each day are marked by red stars. The green section of the storm track indicates tropical depression strength.

The pre-Karl system was sampled extensively by six PREDICT research flights between 10 September to 14 September before it strengthened into a tropical storm. ARO data were recorded on all research missions flown during the PREDICT campaign. The National Science Foundation (NSF) PREDICT campaign was coordinated with other field campaigns studying Atlantic hurricanes in 2010. The National Aeronautics and Space Administration (NASA) sponsored the Genesis and Rapid Intensification Processes experiment (GRIP) to investigate the formation of major hurricanes and the occurrence of rapid intensification [*Braun et al.*, 2013]. The NASA DC-8 research aircraft was the primary platform used in GRIP, carrying a payload of advanced remote sensing technologies as well as dropsondes. It also flew three research missions investigating the pre-Karl system from 12 - 14 September 2010.

Ten to fifteen ARO soundings were derived from data recorded by the GISMOS GRS for each Karl flight after open loop processing. The pre-Karl system represented an interesting case that sampled a pre-depression storm, which developed to hurricane strength. It was chosen as a case study in chapter 2 to assess the upper level moisture representation by ARO profiles derived from GISMOS geodetic receiver data. Given the sizeable number of ARO profiles retrieved from the open loop analysis of the GRS data over the development of the pre-Karl system along with the extensive set of dropsonde data from PREDICT and GRIP flights, it is again chosen as a case study to evaluate the description of the moisture field of a developing tropical storm, this time using open loop data which extends as low as 1 km of the surface.

4.3 Representation of Pre-Karl Moisture by ARO Refractivity

The refractivity retrieved from an ARO sounding is related to pressure, temperature and moisture as given in the refractivity equation,

$$N = k_1 \frac{P}{T} + \frac{(k_2 - k_1)e}{T} + k_3 \frac{e}{T^2} \tag{4.1}$$

where N is refractivity in N-units, P is total atmospheric pressure in hPa, e is water vapor pressure in hPa, T is temperature in Kelvin [*Healy*, 2011; *Smith and Weintraub*, 1953] and the constants $k_1 = 77.6$ hPa^{-1}; $k_2 = 70.4$ K hPa^{-1}; $k_3 = 3.739 \times 10^5$ K^2 hPa^{-1}, are determined empirically [*Bevis et al.*, 1994].

In order to solve for e using a retrieved ARO refractivity profile, a known temperature profile is assumed a priori, either from numerical weather model output or in

situ measurements. Then, using the assumption of hydrostatic equilibrium and the ideal gas law, a second equation in e is formed to be solved iteratively with equation 4.1 [*Hajj et al.*, 2002]. Alternatively, a variational approach to find e can be used which accounts for error in the a priori information as well as measurement error by combining them in a statistically optimal way [*Healy and Eyre*, 2000; *Rodgers*, 1976]. In this approach, the assumed temperature and pressure are adjusted within their expected error to best fit within the expected error of the measured refractivity. However, the retrieved ARO refractivity itself can serve as a direct indication of the moisture variations.

Atmospheric refractivity can be separated into a wet and dry component, as described in section 3.4.3, where the dry and wet components are given by equation 4.2,

$$N_{dry} = k_1 \frac{P-e}{T};\ N_{wet} = k_2 \frac{e}{T} + k_3 \frac{e}{T^2} \tag{4.2}$$

Because of the relatively homogenous temperature field of the tropical atmosphere, the variation of the dry component is found from the dropsonde profiles to be less than 0.5% over the entire height range (figure 2.9) and 4 day time period. The variation in atmospheric refractivity in this environment is mostly due to variations in the wet component, which are three times that of the dry component even at 9 km altitude. Below 9 km altitude, the variations in atmospheric refractivity can be almost entirely attributed to variations in moisture. Therefore, the ARO refractivity sounding can be used as a proxy for vertical moisture profiles in the vicinity of developing tropical storms. Research flights 16 (RF16), 17 (RF17), 18 (RF18) and 19 (RF19) were the third, fourth, fifth and sixth PREDICT missions investigating the pre-Karl storm system. The first

three of these flights occurred over the three days preceding genesis of the pre-Karl system into a tropical depression with RF19 occurring on the day of genesis. The RF16 mission flew on 12 September 2010 from 15:23 to 20:40 UT and RF17 followed on 12 September from 11 to 15.84 UT. The storm center moved from the western Caribbean to south of the Dominican Republic at approximately, 70W, 16N by the take-off time of RF17. RF18 took off at 10:00 UT on the 13th, by which time the disturbance had reached south of Jamaica. A lawnmower pattern was flown for these missions, modified during the flight to avoid areas of intense convective activity and stay within approved airspace (figure 4.2 - 4.5).

About twenty dropsondes were deployed during each flight to sample the developing storm. Eight ARO refractivity profiles were retrieved from RF16 using open loop tracking of GRS data, ten profiles were obtained from RF17 data and thirteen more from RF18. Finally, fifteen ARO soundings were retrieved from RF19 data. Soundings from RF16 dropsondes were generally moist, especially in the region of convective activity on the north side of the system. During RF17, the main arc of clouds and convection was developing to the north and northwest of the system center. The convective activity was strong after the take-off of RF18 and the main area of clouds and convection had become tilted along a north-south axis near the storm center where dropsondes were generally moist.
(http://catalog.eol.ucar.edu/predict/missions/missions.html). On 14 September, the storm was declared a tropical depression and within 6 hours pressures and winds indicated genesis of tropical storm Karl. RF19 was flown on this day with a later take off time of 13:00 UT, just after Karl reached tropical depression strength, and the flight returned at

21:30 UT. The cloud system and convection had increased in extent at this time, reaching north and west of Honduras to past Jamaica. For all four missions, the ARO profiles were well distributed spatially around the storm center and can be used to identify the variation of moisture across the extent of the system below 10 km. Information from dropsondes can be compared to ARO either directly using refractivities calculated from the dropsonde pressure, temperature, and relative humidity, or indirectly by use of numerical weather model output after assimilation of dropsonde measurements.

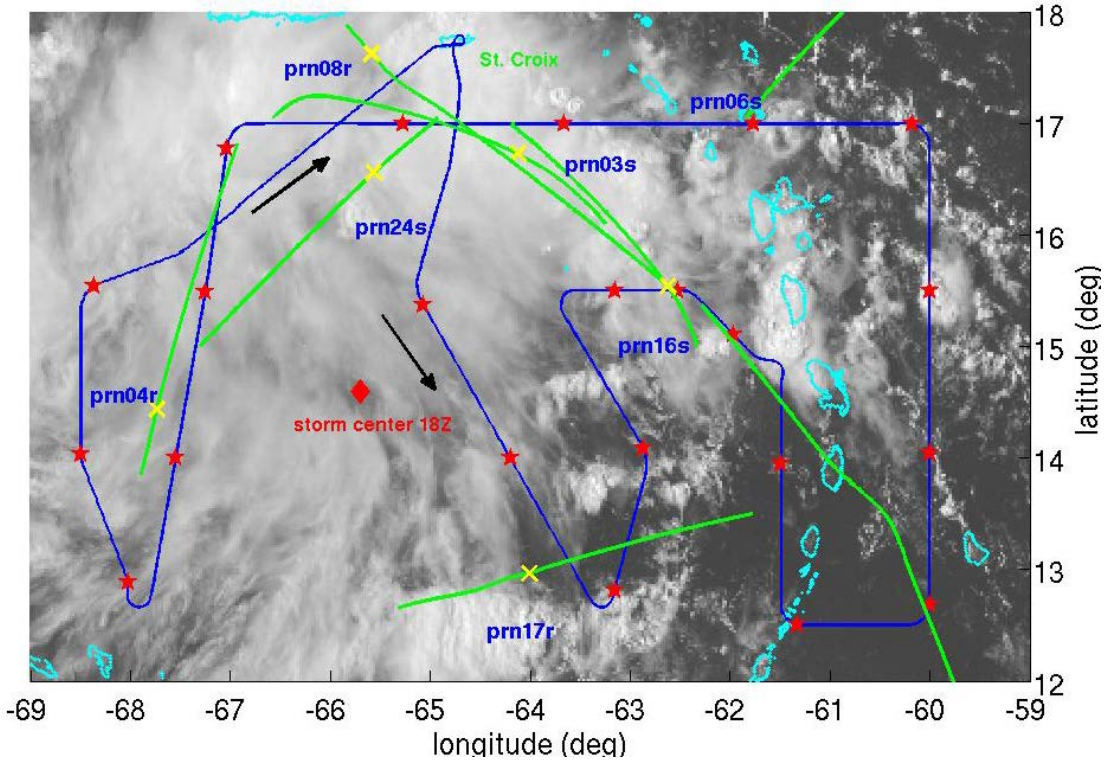

Figure 4.2 Karl RF16 flight track (blue) with dropsondes marked by red stars overlaid on GOES 13 visible imagery 19.25Z. ARO tangent point drifts are shown in green with occultation points marked by yellow x's.

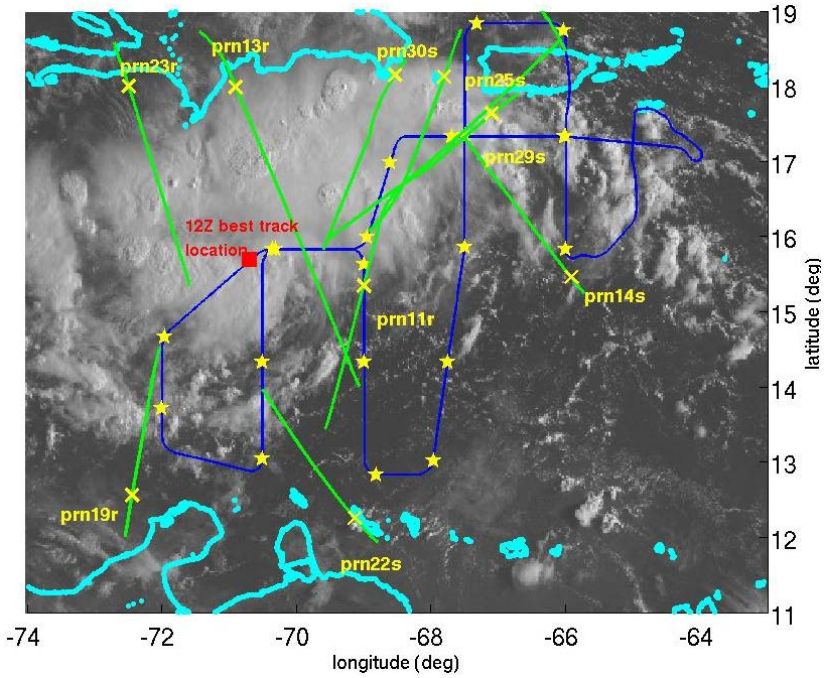

Figure 4.3 RF17 flight path (blue) with dropsonde deployments marked by yellow overlaid on 12 September 2010 12:15 UT visible imagery. ARO tangent point drifts are shown in green with occultation points marked by yellow x's.

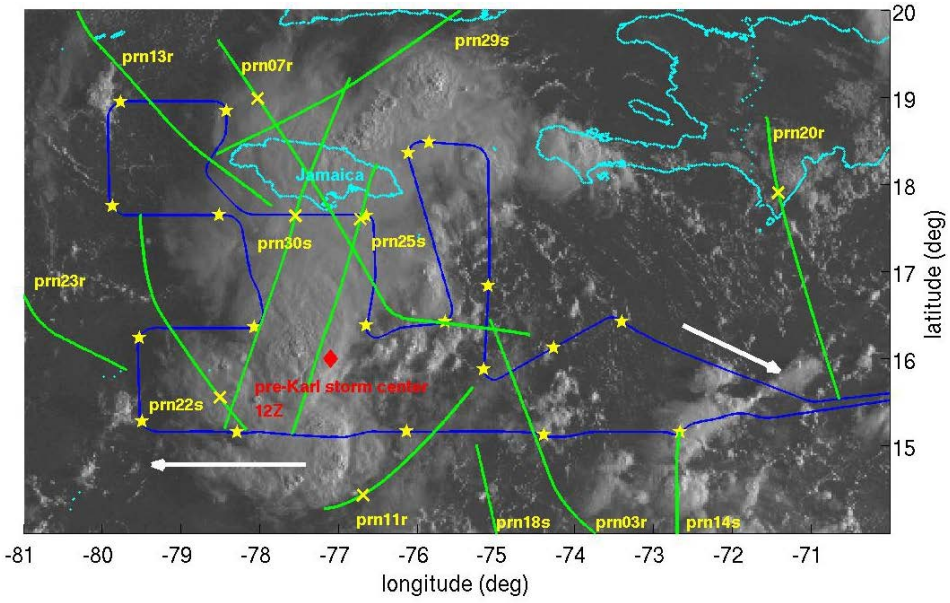

Figure 4.4 RF18 flight path (blue) with dropsonde deployments marked by yellow stars overlaid on 13 September 2010 12:45 UT visible imagery. ARO tangent point drifts are shown in green with occultation points marked by yellow x's.

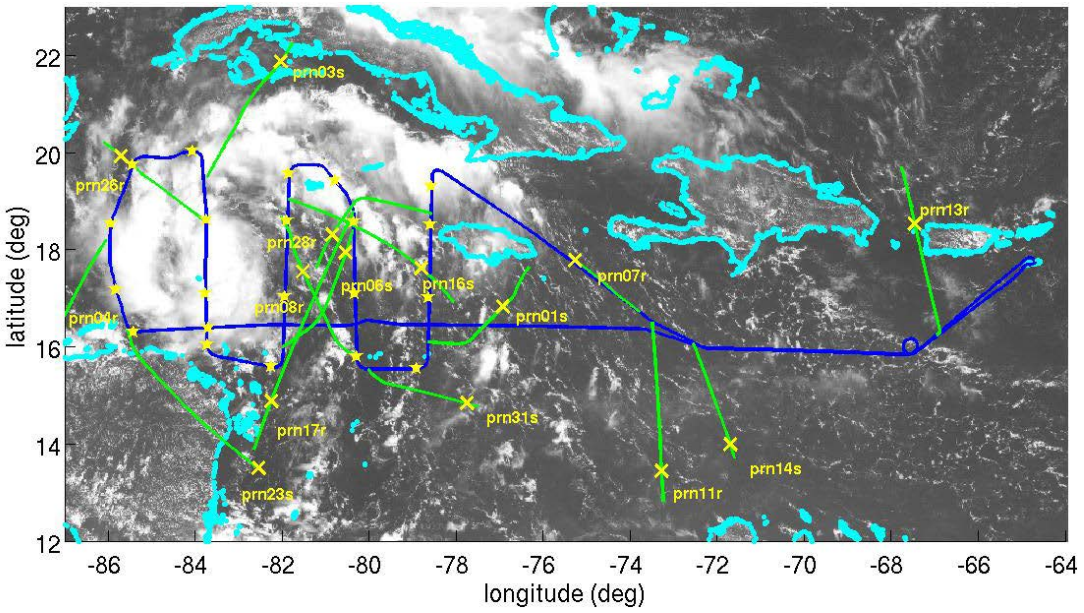

Figure 4.5 RF19 flight path (blue) with dropsonde deployments marked by yellow stars overlaid on 14 September 2010 16:25 UT visible imagery. ARO tangent point drifts are shown in green with occultation points marked by yellow x's.

4.4 High Resolution WRF Model Simulation

For this study, dropsondes were assimilated into a high-resolution Weather and Research Forecast (WRF) model simulation [*Haase et al.*, 2012; *Skamarock et al.*, 2008]. The model output was used for an intercomparison with the European Center for Medium-range Weather Forecasting (ECMWF) Interim Re-Analysis (ERA-Interim or ERAI) fields [*Dee et al.*, 2011], ARO data and dropsondes. The WRF model has 44 vertical levels between the surface and about 20 km height and uses three nested grids. The inner domain, which extends over the area including the flight paths of the six PREDICT flights, has a horizontal resolution of 3 km and did not move with the location of the tropical storm center. The parameterizations for the simulation are given in Table 4.1.

Table 4-1 WRF model physics

Parameter	Domain 1/2/3	
Resolution	27 km/9km/3km	
Microphysics	Morrison	[*Morrison et al.*, 2009]
Longwave radiation	Goddard new LW	[*Chou and Suarez*, 1999]
Shortwave radiation	Goddard new SW	[*Chou and Suarez*, 1999]
Radt: min between radiation calls	30	
Surface layer physics	Monin-Obukhov	[*Jiménez et al.*, 2011]
Land surface physics	Noah	[*Niu et al.*, 2011]
Planetary Bound. layer	Yonsei Univ. scheme	[*Hong et al.*, 2006]
Bldt: min between BL calls	0: every time step	
Cumulus Parameterization	Kain-Fritsch (none for domain 3)	[*Kain*, 2004]
Cudt: time in min between cumulus call	5	
Surface urban physics	Noah	
Surface_input_source	1(WPS/geogrid)	
Num_soil_layers	4	
Initial/boundary conditions	ECMWF ERA Interim	[*Dee et al.*, 2011]

For the WRF analysis, all dropsonde data from PREDICT and GRIP flights over 10 – 14 September were assimilated using 3DVAR [*Barker et al.*, 2004]. The dropsondes, as well as surface and radiosonde observations collected through the Global Telecommunications System (GTS) were assimilated at the initial start time and every three hours in model time thereafter. After each assimilation time, the model ran for a 3 hour forecast period. At the end of the forecast period, the WRF output initialized the next model analysis and provided new domain one boundary conditions for the next

assimilation time to conform with possible observation points assimilated near the domain boundary. The ERAI reanalysis was used for the initial and boundary conditions. In addition to the 3DVAR assimilation of dropsonde data and GTS observations, four-dimensional data assimilation (FDDA) [*Stauffer and Seaman*, 1990] of ECMWF reanalysis was made every 6 hours to help constrain the large scale model evolution over the relatively long five day simulation. Examples of high resolution precipitable water fields from the WRF model are shown in figures 4-6 to 4.9.

For comparison to the high resolution run, the ERA-Interim reanalysis (ERAI) was available at 37 pressure levels and was interpolated to 0.125° spacing from ~ 0.75° model resolution. The atmospheric parameters were then obtained and refractivity calculated at each grid point of the ERAI reanalysis and the innermost 3 km resolution WRF domain.

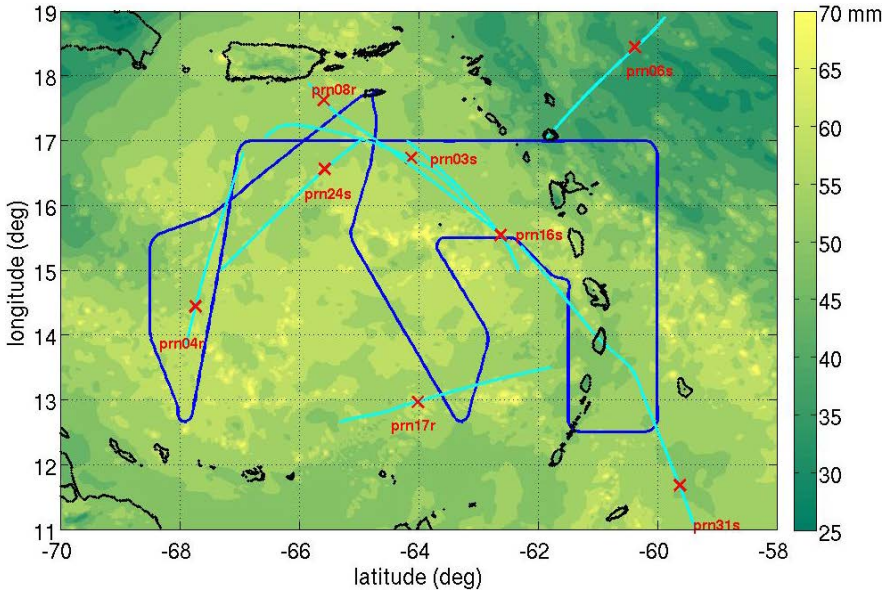

Figure 4.6 RF16 OL CH1_cli ARO occultation tangent point paths shown in cyan with occultation points (tangent point at 500 hPa) marked by red x's and overlaid on the total column precipitable water output from a high resolution WRF simulation. The flight track is shown in blue.

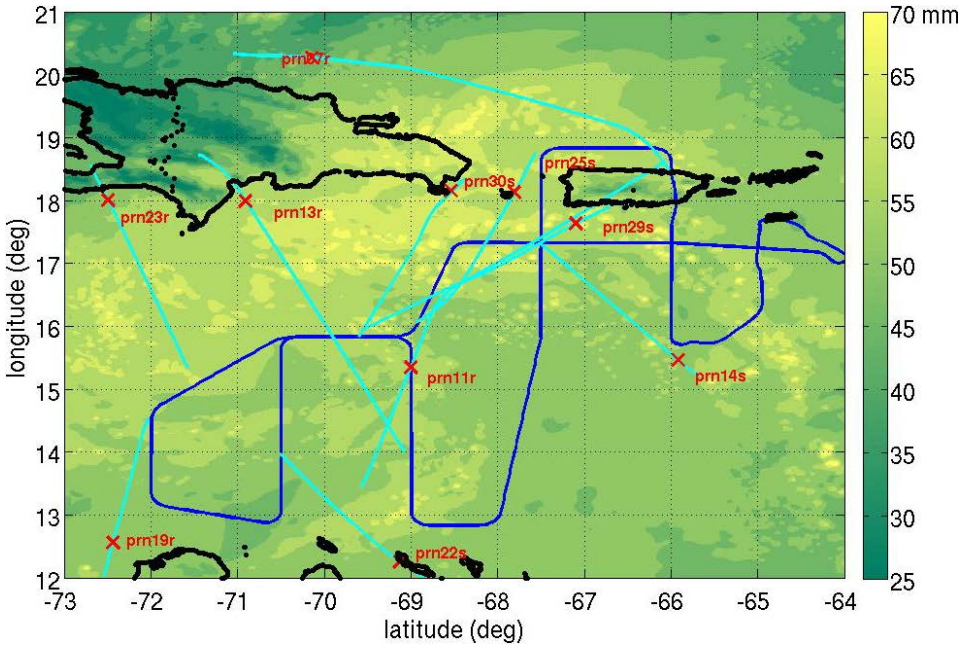

Figure 4.7 RF17 OL CH1_cli ARO occultation tangent point paths shown in cyan with occultation points marked by red x's and overlaid on the total column precipitable water output from a high resolution WRF simulation. The flight track is shown in blue.

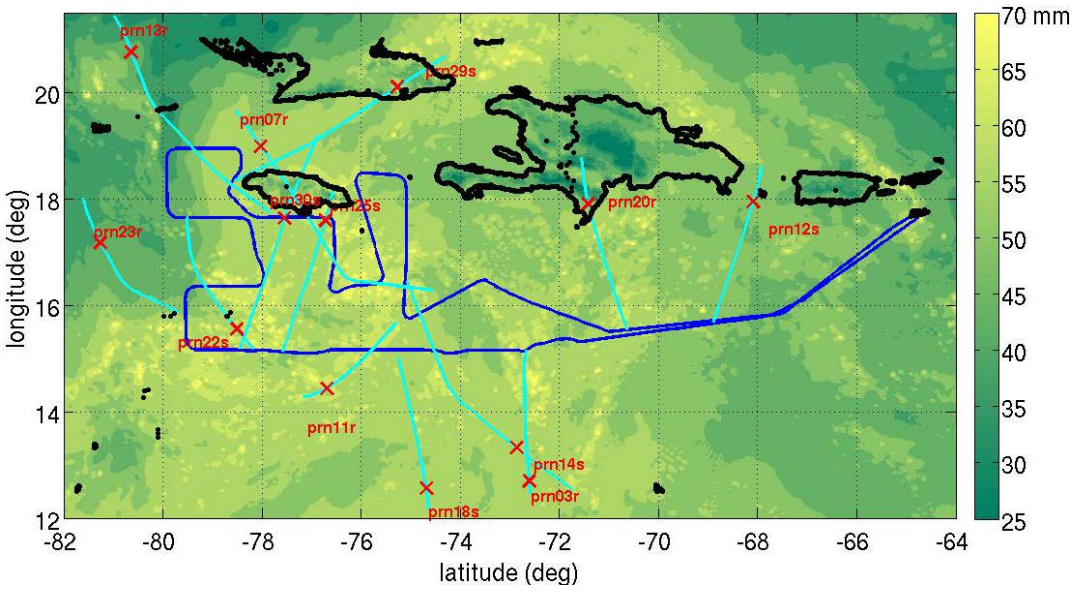

Figure 4.8 RF18 OL CH1_cli ARO occultation tangent point paths shown in cyan with occultation points marked by red x's and overlaid on the total column precipitable water output from a high resolution WRF simulation. The flight track is shown in blue.

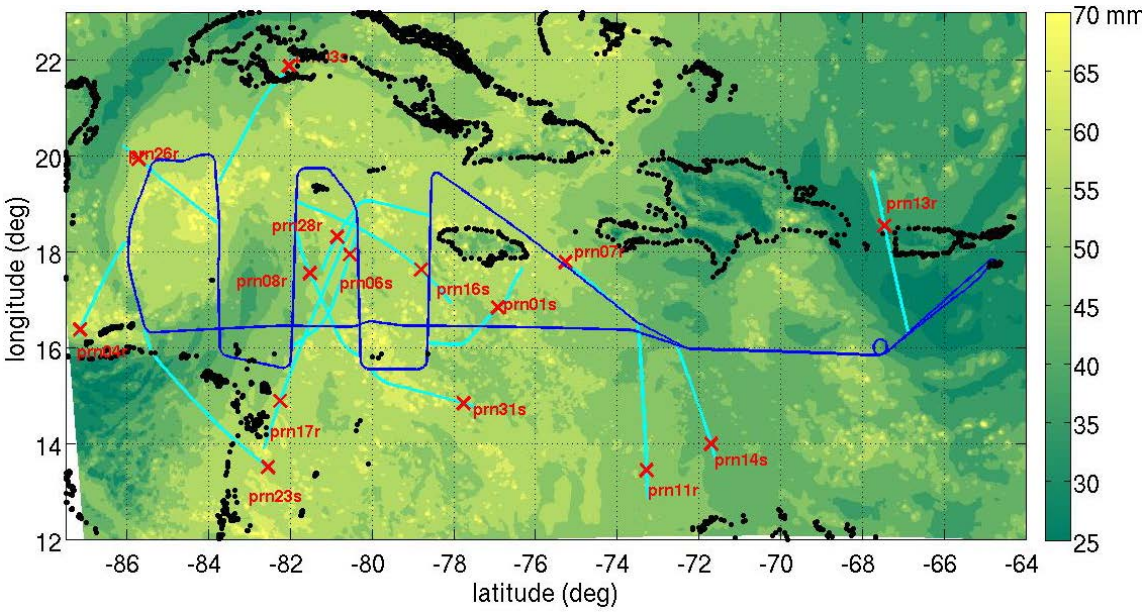

Figure 4.9 RF19 OL CH1_cli ARO occultation tangent point paths shown in cyan with occultation points marked by red x's and overlaid on the total column precipitable water output from a high resolution WRF simulation. The flight track is shown in blue.

4.5 Consideration of ARO Tangent Point Drift in Model Comparisons

Because the aircraft moves slowly relative to the transmitting satellite, the point of closest approach to the Earth, the tangent point, moves systematically further away from the aircraft location as the satellite sets. ARO observations, compared to spaceborne RO, have a larger tangent point drift, on the order of 400-600 km. We propose that the best way to treat the profile data in a mesoscale system is as individual samples of refractivity with distinct horizontal location and height at the tangent point. To demonstrate this we compare ARO with the NWP model values at the exact tangent point location and also with the NWP values at the representative vertical profile at the "occultation point" defined as the 500 hPa tangent point location. We carry out this comparison with respect to a reference mean environmental profile.

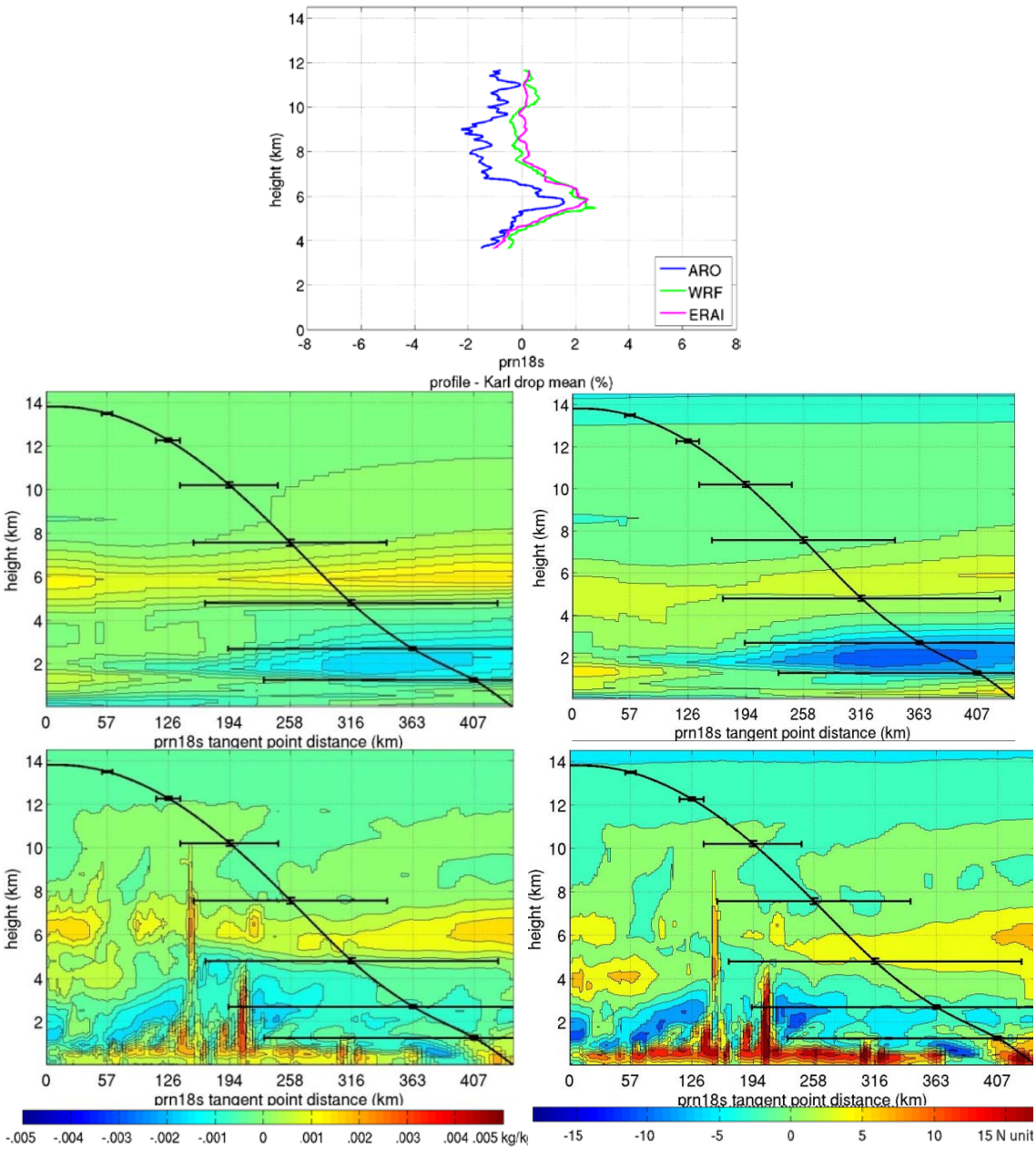

Figure 4.10 TOP: ARO, WRF and ERAI refractivity profiles from prn18 setting occultation during RF18 relative to the mean Karl background. While the ARO profile has a bias relative to the model profiles, all three represent the increase in moisture from 11 to 5 km height followed by a decrease. MIDDLE LEFT: ERAI cross section of specific humidity relative to background along the ARO tangent point path illustrating the analogous moisture variations to the refractivity variations seen in the ARO and model profiles. MDDLE RIGHT: ERAI cross section of refractivity relative to the background. BOTTOM: Same as middle but for WRF. The error bars represent estimated vertical and horizontal resolution.

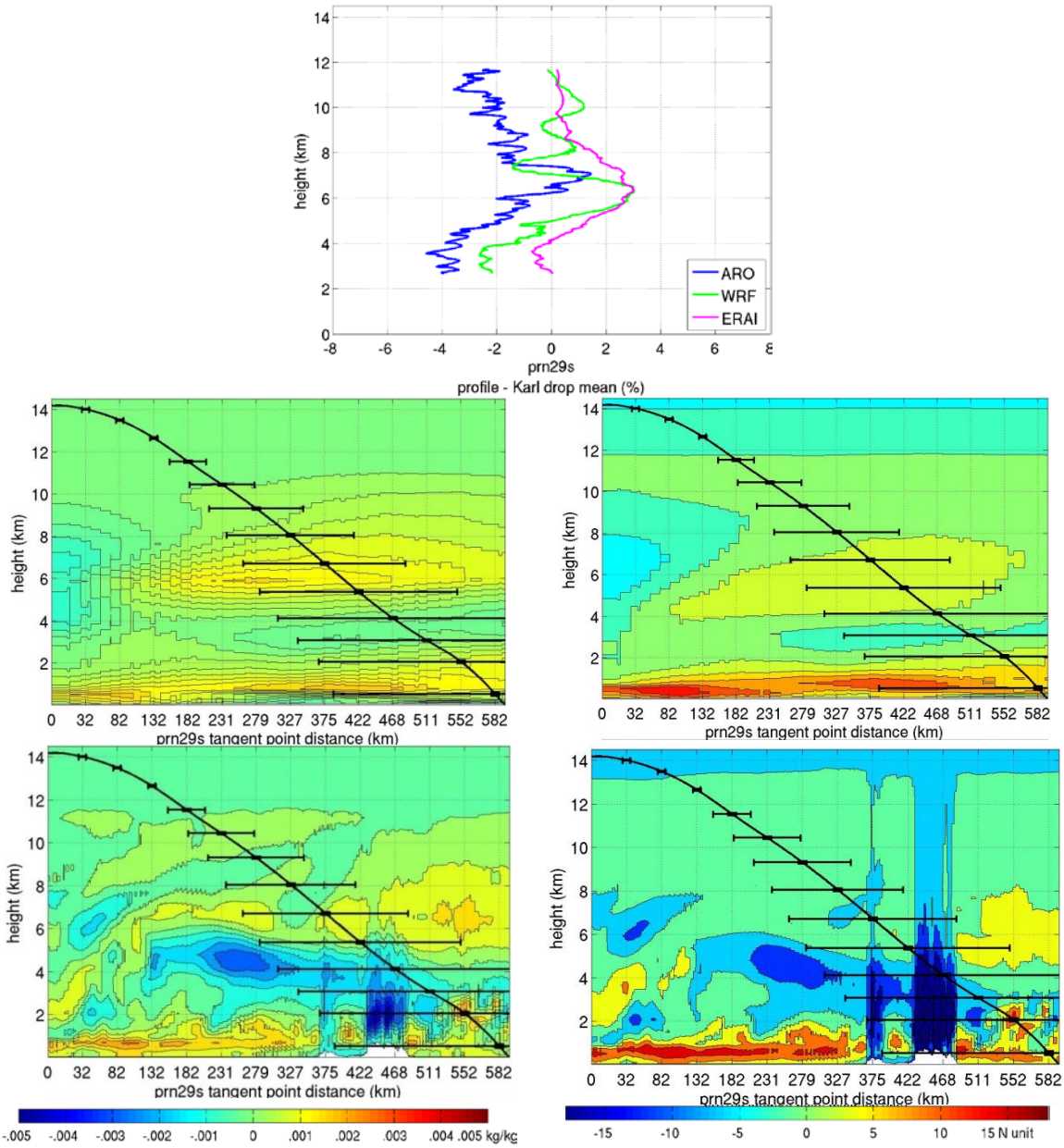

Figure 4.11 TOP: ARO, WRF and ERAI refractivity profiles from prn23 rising occultation during RF18 relative to the mean Karl background. While the ARO profile has a bias relative to the model profiles, all three represent the increase in moisture from 11 to about 6 km height followed by a decrease to 2 km after which moisture increases again. MIDDLE LEFT: ERAI cross section of specific humidity relative to background along the ARO tangent point path illustrating the analogous moisture variations to the refractivity variations seen in the ARO and model profiles. MIDDLE RIGHT: ERAI cross section of refractivity relative to background. BOTTOM: same as middle but for WRF. The errors bars represent estimated vertical and horizontal resolution.

The background reference mean refractivity and specific humidity was computed using data from all 105 PREDICT dropsondes deployed from RF14 on 10 September through RF18 on 13 September. It is the same pre-Karl environmental mean profile used as a reference for the analysis of geodetic receiver ARO profiles described in section 2.4.3. For a given airborne occultation, a vertical cross-section of the WRF and ERAI output minus the pre-Karl environmental mean profile was plotted following the ARO tangent point locations to highlight the relative variation in refractivity (right) and moisture (left) along the profile (figure 4.10-11). The relative increase or decrease in refractivity relative to the mean seen in the cross-section is indicative of a similar variation in moisture. The individual ARO, WRF and ERAI refractivity profiles relative to the background mean are also plotted for comparison to refractivity (figure 4.10-11 top). The full dataset can be viewed in the Appendix.

All ARO retrievals are made using the geometric optics technique described in chapter 2. Excess Doppler was obtained from OL tracking, described in chapter 3, of signals recorded from the top mounted antenna on the GV aircraft. The variation in Doppler was predicted from the variation in geometric phase due to the relative satellite-receiver motion as well as the variation based on a climatological refractivity profile that depends on month and latitude (CIRA-Q) [*Kirchengast et al.*, 1999]. The excess Doppler time series was smoothed over a 10 second span. The vertical resolution of the ARO profile was estimated as the vertical descent of the tangent point over the 10 s smoothing span, which is approximately 250 – 300 m. To illustrate graphically the horizontal resolution of the retrieved ARO refractivity at the tangent point height, we estimated the horizontal extent over which 70% of the bending occurs along the ray path: within ±50

km of the tangent point path at 10 km, and within ±170 km at 3 km. We illustrate this extent as the width of the horizontal error bar in figure 4.10 - 11, linearly increasing from ±50 km at 10 km altitude to ± 170 km at 3 km.

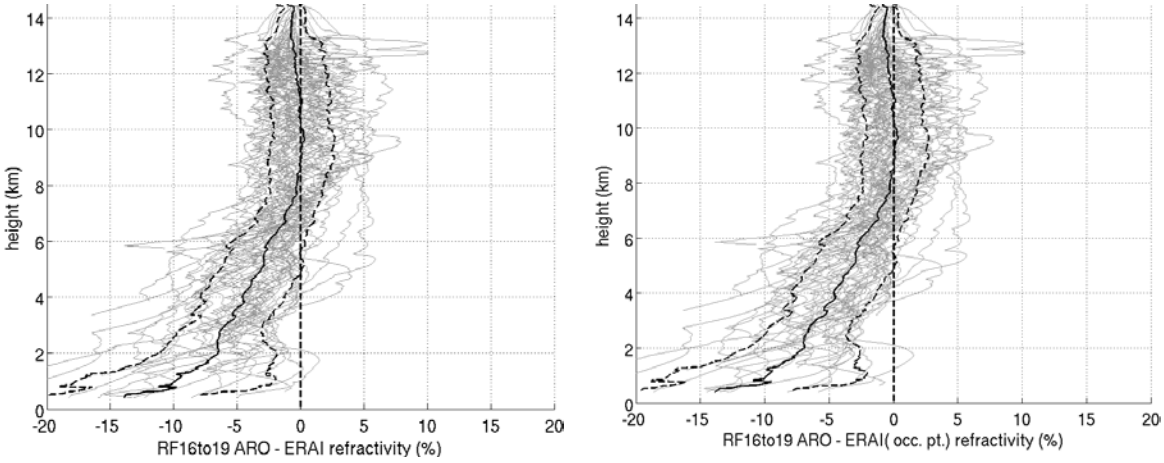

Figure 4.12 Difference of ARO with ERAI refractivity calculated along the ARO tangent point path is shown for each profile (gray lines). The mean difference is given by the black line and standard deviation is shown by the black dashed lines. RIGHT: Same as on left but showing difference of ARO with ERAI refractivity calculated at the occultation point (gray lines).

Table 4-2 LEFT: Mean difference and standard deviation of ARO and ERAI following tangent point path as a function of height. RIGHT: Mean difference and standard deviation of ARO and ERAI at the occultation point.

Height (km)	Mean (%)	Std (%)	Height (km)	Mean (%)	Std (%)
1	- 9.9	7.8	1	-9.8	7.6
2	- 6.5	4.6	2	-6.9	4.4
3	-6.0	2.9	3	-6.0	2.8
4	-4.6	3.3	4	-4.7	3.3
5	-3.1	3.2	5	-3.1	3.2
6	-2.5	2.8	6	-2.5	2.9
7	-1.2	2.2	7	-1.1	2.3
8	-0.31	2.1	8	-0.26	2.2
9	-0.08	2.6	9	0.13	2.6
10	0.15	2.3	10	0.19	2.3
11	0.17	2.3	11	0.18	2.3
12	-0.32	2.4	12	-0.31	2.4
13	-0.51	2.2	13	-0.52	2.3
14	-0.64	1.0	14	-0.63	1.0

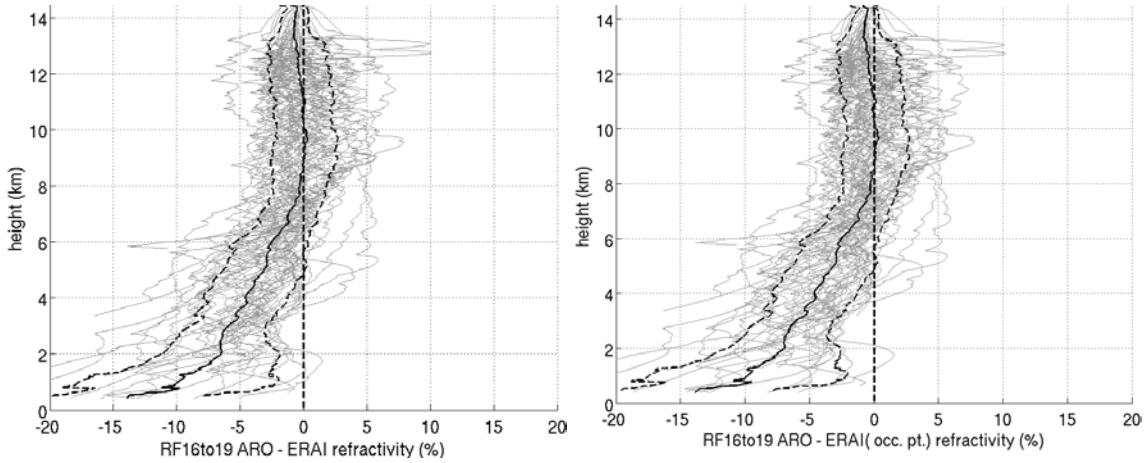

Figure 4.13 LEFT: Difference of ARO with WRF refractivity calculated along the ARO tangent point path is shown for each profile(gray lines). The mean difference is given by the black line and standard deviation is shown by the black dashed lines. RIGHT: Same as on left but showing difference of ARO with WRF refractivity calculated at the occultation point (gray lines).

Table 4-3 LEFT: Mean difference and standard deviation of ARO and WRF following tangent point path as a function of height. RIGHT: Mean difference and standard deviation of ARO and WRF at the occultation point.

Height (km)	Mean (%)	Std (%)	Height (km)	Mean (%)	Std (%)
1	- 9.67	7.8	1	-8.5	6.6
2	- 5.7	6.0	2	-5.4	4.9
3	-4.8	3.7	3	-5.2	3.4
4	-4.5	3.4	4	-4.4	3.4
5	-3.3	3.4	5	-3.4	3.8
6	-2.9	3.8	6	-2.9	3.8
7	-1.5	2.7	7	-1.3	2.6
8	-0.49	2.3	8	-0.47	2.3
9	-0.16	2.4	9	0.04	2.4
10	0.13	2.2	10	0.13	2.3
11	0.3	2.3	11	0.16	2.4
12	-0.06	2.4	12	-0.02	2.4
13	-0.19	2.2	13	-0.18	2.2
14	-0.65	1.1	14	-0.60	1.0

Complete results of the RF16-19 ARO retrievals are shown in the Appendix. In the original analysis of ARO data from closed loop geodetic receivers, Murphy et al. [2015], for comparison with NWP models, the vertical model profile was selected at the location of the "occultation point" which was defined as the location of the tangent point where half the mass of the atmosphere was located below, consistent with the spaceborne RO conventions. In figure 4.12, the comparison with ERAI refractivity calculated at the tangent point is shown for all of the open loop profiles and a similar comparison with WRF model output is shown in figure 4.13. The mean difference as a function of height is shown by the solid black line. The locations of the individual tangent points were estimated using ROSAP to ray-trace through the environmental mean atmosphere for each occultation. The ERAI and WRF model values were interpolated to the tangent point height at the grid point nearest the location of the tangent point. The model values at the occultation point were also compared with each ARO profile. The error statistics compiled in tables 4.2 and 4.3 will provide the basis of the required observation errors needed for an assimilation of ARO into a NWP model.

The results in table 4.2 show that the agreement at the tangent point location is comparable to the comparison made to the vertical profile at the representative occultation point. These results show the impact of the additional tangent point drift of ARO is small as most of the drift occurs in the upper troposphere where the contribution to ray path bending angle is small (see figure 2.5). Using the tangent point locations for the comparisons as well as in the data assimilation [*Chen et al.*, 2014b] removes the relatively small effect of the tangent point drift. It is worth noting here that because the dropsondes sample the atmosphere directly beneath the flight path (or nearby, given

potentially strong winds) and the ARO observations sample the atmosphere farther from the flight path, the two observing systems when used in tandem are highly complementary.

4.6 Potential Use of ARO for Numerical Model Validation

The ARO technique provides a dataset with both high vertical resolutions and extensive horizontal coverage. A mesoscale dataset with dense spatial and temporal observations with high vertical resolution is appealing for both assimilation into a regional NWP model but also for validating model forecasts [*Salonen et al., 2008*]. ARO has the potential to produce a dense dataset of observations in a targeted area with just a few flights of a research aircraft. In the future, the development of a compact ARO receiver for installation on commercial aircraft could lead to the production of a dataset [*Lesne et al.*, 2002] which could be used for operational assimilation and forecasting as well as for validation of model output.

PREDICT is a unique example where high density aircraft observations are available to improve and assess high resolution models of hurricane development. In a long simulation such as the WRF study of the developing pre-Karl system, error in the intensity and track of the system is expected to increase somewhat with time even with the regular cycling of assimilated dropsondes. It is important to have independent datasets available to assess the quality of the high resolution modeling. In this section we give an example of how ARO observations could potentially be used to provide additional data for quantitative assessment the ability of two competing models to represent the atmospheric state. We carry out this comparison with the caveat that there

are known biases in the lower part of the retrieved profiles, and that it will be worthwhile to re-evaluate when radio holographic retrievals are available.

For RF16-19, we first compare the two models with dropsonde data (Fig 4.14) selecting the model values at the closest grid point for WRF and ERAI. The drift of the dropsonde was not considered and a vertical profile was extracted. We then compare the two models using ARO data (Fig 4.16). , Model refractivity was calculated at the closest grid point to the tangent points of each ARO occultation for the model-ARO refractivity differences. Both model and observations were interpolated to common heights for comparison. In the second case, figure 4.15, the high vertical resolution dropsonde observations were smoothed by curve fitting to reduce the fluctuations due to in-situ observation errors at consecutive model levels that are considered random and insignificant.

Dropsonde refractivity compared more favorably with ERAI output than with the WRF output. It cannot be assumed that the refractivity differences between WRF and dropsondes will be small even though the dropsonde data were assimilated into WRF, because refractivity has more sensitivity to moisture than temperature below 8 km. Much larger magnitude moisture variations can develop in the high resolution WRF model, so if their location is not exact, large differences can be found. On the other hand, because of the large scale of ERAI, extreme moisture variations cannot develop and the model values are unlikely to be extremely different from the observed values. One may interpret that while this WRF model output has resolution sufficient to capture mesoscale dynamics, it may not have the overall average environment exactly correct. Additionally, the ERAI reanalysis has a continuous assimilation of a larger data set of observations,

including more satellite. So, the WRF model error might still become larger than the reanalysis error with time.

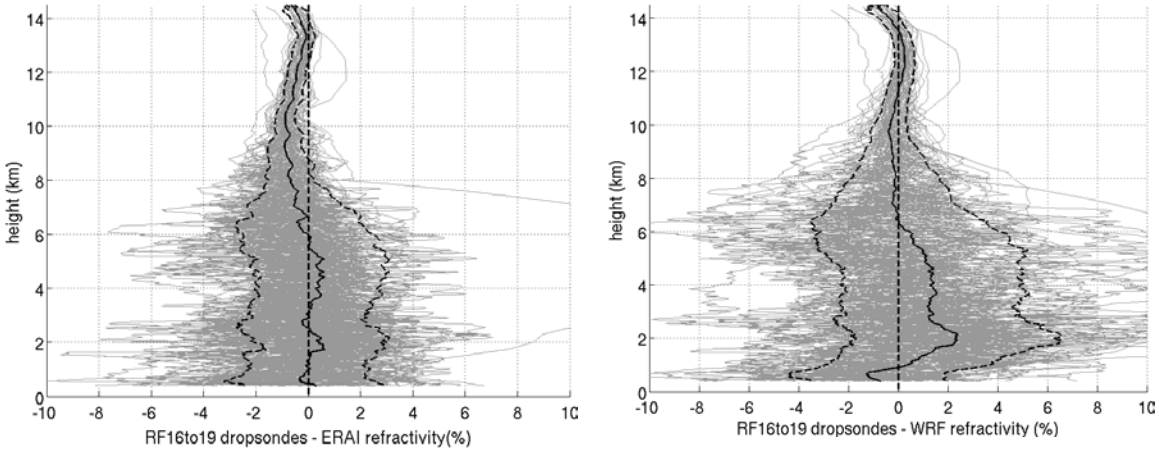

Figure 4.14 LEFT: Refractivity difference of RF16-19 dropsondes with profiles calculated from ERAI output at the nearest co-located gridpoints. RIGHT: Refractivity difference of RF16-19 dropsondes with profiles calculated from WRF output at the nearest co-located gridpoints.

Table 4-4 LEFT: Mean difference and standard deviation of RF16 to 19 dropsondes with ERAI. RIGHT: Mean difference and standard deviation of RF16 to 19 dropsondes with WRF.

Height (km)	Mean (%)	Std (%)_	Height (km)	Mean (%)	Std (%)
1	0.04	2,3	1	0.37	3.3
2	0.44	2.5	2	2.3	4.0
3	0.04	2.2	3	1.4	3.5
4	0.28	2.3	4	1.3	3.6
5	0.47	2.6	5	1.1	3.9
6	0.00	2.5	6	0.47	3.6
7	-0.45	1.9	7	-0.18	2.5
8	-0.66	0.86	8	-0.09	1.8
9	-0.84	0.71	9	-0.24	1.1
10	0.84	0.43	10	-0.30	0.67
11	-0.55	0.35	11	-0.05	0.48
12	-0.44	0.34	12	0.21	0.43
13	-0.19	0.35	13	0.21	0.39
14	-0.31	0.35	14	-0.34	0.43

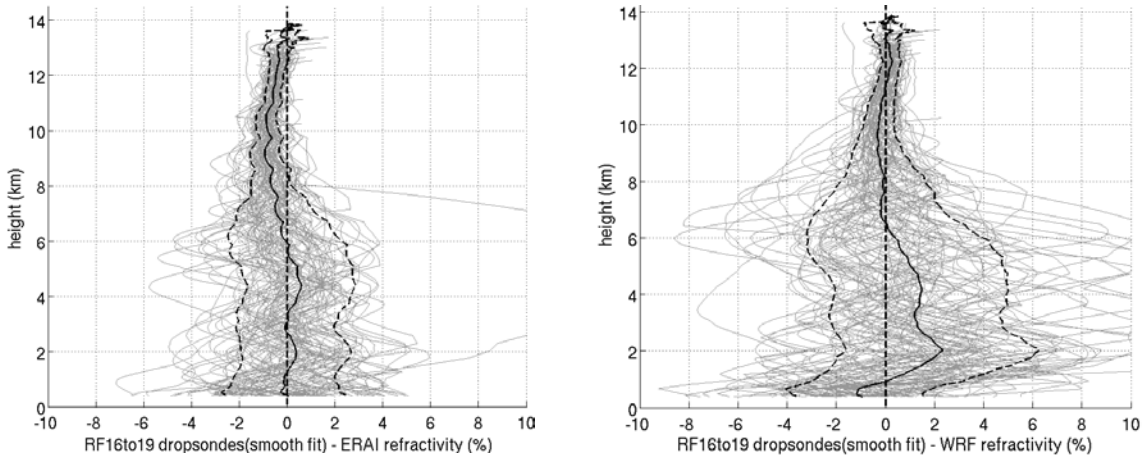

Figure 4.15 LEFT: Refractivity difference of RF16-19 dropsondes after being fit to smooth curves with profiles calculated from ERAI output at the nearest co-located gridpoints. RIGHT: Refractivity difference of RF16-19 dropsondes after being fit to smooth curves with profiles calculated from WRF output at the nearest co-located gridpoints.

Table 4-5 LEFT: Mean difference and standard deviation of RF16 to 19 smooth dropsonde profiles with ERAI. RIGHT: Mean difference and standard deviation of RF16 to 19 smooth dropsonde profiles with WRF

Height (km)	Mean (%)	Std (%)_	Height (km)	Mean (%)	Std (%)
1	-0.12	2.1	1	0.21	3.1
2	0.39	2.3	2	2.3	3.9
3	-0.04	2.1	3	1.3	3.5
4	0.43	2.2	4	1.4	3.5
5	0.42	2.3	5	1.1	3.9
6	-0.05	2.4	6	0.42	3.6
7	-0.44	1.7	7	-0.18	2.5
8	-0.66	0.85	8	-0.09	1.7
9	-0.90	0.65	9	-0.30	1.1
10	0.80	0.47	10	-0.26	0.62
11	-0.57	0.36	11	-0.08	0.48
12	-0.47	0.31	12	0.18	0.38
13	-0.32	0.61	13	0.06	0.55

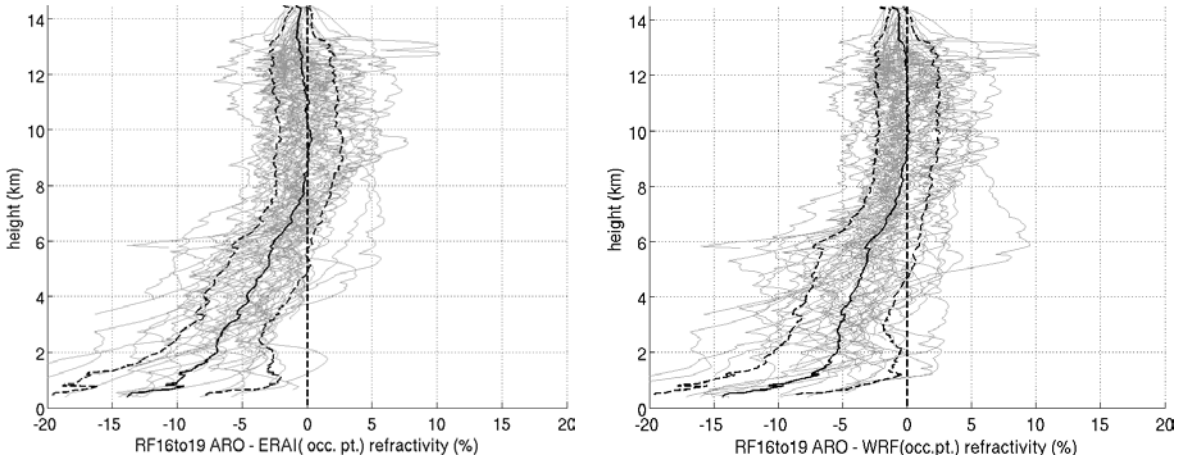

Figure 4.16 LEFT: Refractivity difference of RF16-19 ARO with profiles calculated from ERAI output at the nearest co-located gridpoints to the occ. pt.. RIGHT: Refractivity difference of RF16-19 ARO with profiles calculated from WRF output at the nearest co-located gridpoints to the occultation. point.

Table 4-6 LEFT: Mean difference and standard deviation of RF16 to 19 ARO profiles with ERAI (occ. pt.). RIGHT: Mean difference and standard deviation of RF16 to 19 smooth ARO with WRF(occ. pt.).

Height (km)	Mean (%)	Std (%)_	Height (km)	Mean (%)	Std (%)
1	-9.8	7.6	1	-8.5	6.6
2	-6.9	4.4	2	-5.4	4.9
3	-6.0	2.8	3	-5.2	3.4
4	-4.7	3.3	4	-4.4	3.6
5	-3.1	3.2	5	-3.4	3.8
6	-2.5	2.9	6	-2.9	3.8
7	-1.1	2.3	7	-1.3	2.6
8	-0.26	2.2	8	-0.47	2.3
9	0.13	2.6	9	-0.04	2.4
10	0.19	2.3	10	0.13	2.3
11	0.18	2.3	11	0.16	2.4
12	-0.31	2.4	12	0.02	2.4
13	-0.52	2.3	13	-0.18	2.2
14	-0.63	1.0	14	-0.60	0.97

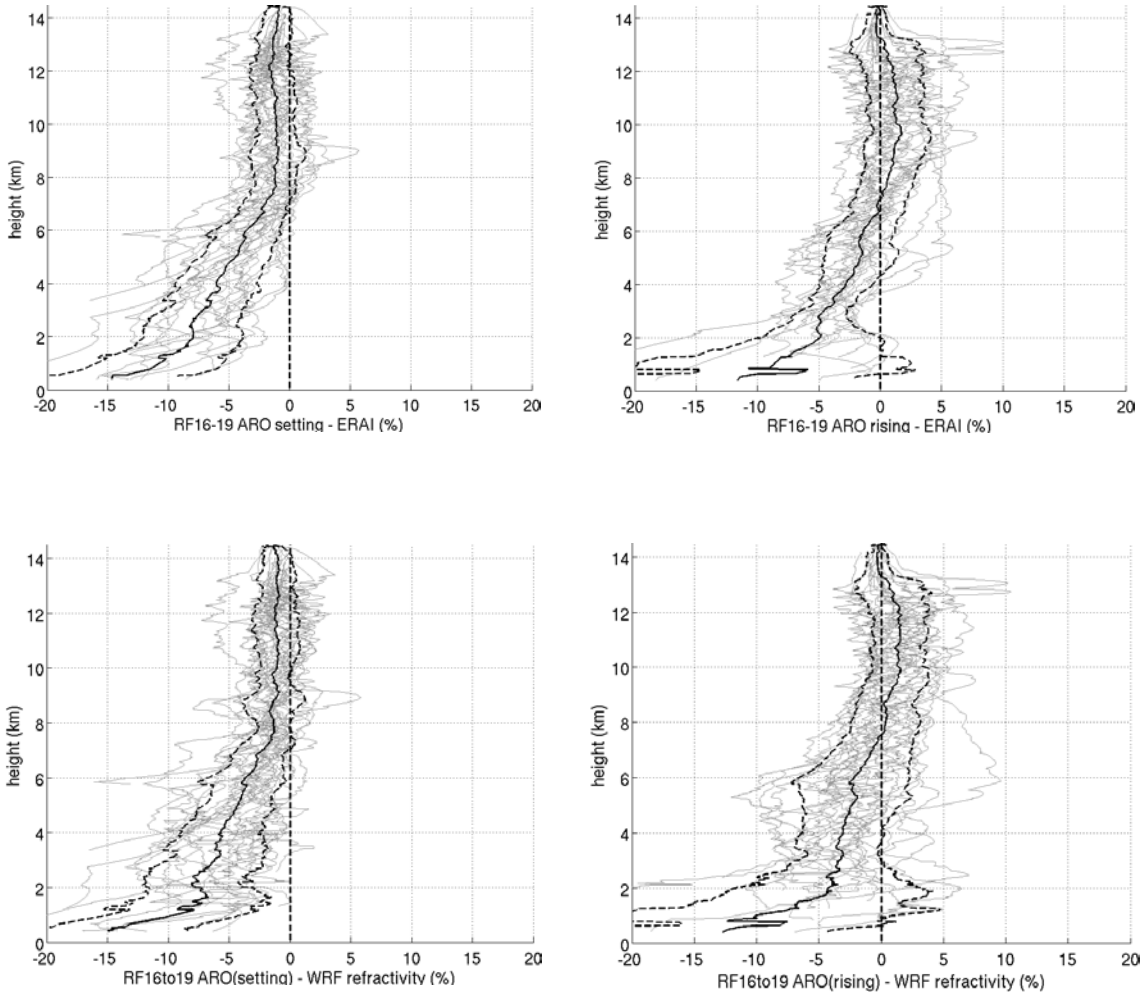

Figure 4.17 RF16-19 refractivity differences of ARO setting (top left) and rising (top right) occultations with ERAI and setting (bottom left) and rising (bottom right) WRF.

Table 4-7 RF16-19 ARO mean difference and standard deviation from ERAI and WRF as a function of height for rising and setting occultations.

Height (km)	Setting erai mean	Seting erai Std. dev.	Rising erai mean	Rising erai Std. dev.	Setting wrf mean	Setting wrf Std. dev.	Rising wrf mean	Rising wrf Std. dev.
1	-10.7	5.2	-8.6	11.1	-9.4	5.5	-10.0	11.1
2	-7.9	4.1	-4.9	4.8	-7.3	4.3	-4.2	7.4
3	-7.2	3.2	-4.6	1.9	-6.2	3.8	-3.3	3.3
4	-6.1	3.4	-2.8	2.2	-5.7	3.2	-3.0	3.3
5	-4.4	2.9	-1.6	2.9	-4.3	2.7	-2.3	4.0
6	-3.6	2.7	-1.4	2.6	-3.6	3.1	-2.2	4.4
7	-2.0	1.9	0.20	2.3	-2.3	2.1	-0.66	3.1
8	-1.2	1.8	0.64	2.1	-1.3	1.3	0.35	2.8
9	-0.93	2.3	1.1	2.6	-0.97	2.1	0.68	2.4
10	-1.1	1.4	1.5	2.2	-1.1	1.3	1.5	2.1
11	-1.0	1.6	1.4	2.3	-0.90	1.7	1.5	2.1
12	-1.5	1.7	1.0	2.4	-1.1	1.8	1.4	2.3
13	-1.3	1.2	0.42	2.8	-1.0	1.3	0.71	2.8
14	-0.97	1.2	-0.28	0.79	-0.96	1.2	-0.33	0.83

In contrast, the scale of ARO observations is more consistent with the scale of variations allowed by the ERAI grid. ARO did not definitively distinguish between ERAI and WRF output, however standard deviations are consistently larger for WRF than ERAI in the 2 – 8 km height range. It is important to investigate whether the better performance of ERAI will hold up after improvement of the model profiles with the implementation of the radio holographic retrieval, after which a much more rigorous assessment can be made.

Given the biases discovered and described in Chapter 3, the comparison is broken down further by separating rising from setting occultations (figure 4.17). Despite these biases, the relationship holds true that the standard deviation is smaller, with ARO closer to ERAI than to WRF in the range from 2-8 km.

4.7 Investigating Spatial Variability Using Bias Adjusted Profiles

Given the surprisingly high correlation of height dependent refractivity variations with model refractivity variations in some profiles despite the relatively large bias, it is of interest to investigate on a profile-by-profile basis if the ARO profiles are capturing similar spatial features of the moisture variability. This is investigated below with an ad hoc bias correction. The objective is to examine with what confidence, a statement such as the following can be made: "in this location both ERAI and ARO show consistently [higher or lower] than average moisture in the height range 8-12 km and consistently [higher or lower] than average moisture in the height range 6-8 km.

In general, the geometric optics ARO retrievals are most reliable between 6 – 12 km altitude, as described in our earlier discussion of errors related to low SNR, especially in the presence of atmospheric multipath. Of course it is not expected to have ARO entirely correlated to ERAI re-analyses given the observation errors associated with ARO profiles and the differing representativeness errors [*Kuo et al.*, 2004]. However, it is expected the ARO profiles will generally have higher moisture where the ERAI moisture is higher, using as a reference the pre-Karl background mean (section 3.4.3). The log of the ARO and ERAI refractivity profiles were linearly interpolated to common heights and the pre-Karl environmental mean was then subtracted from each profile to compare the profiles relative to a common background.

The ad hoc bias correction was motivated by the fact that ARO retrievals have shown consistent biases with profiles derived from model output and dropsonde data (section 3.9), especially with respect to whether the profiles were rising or setting. The

mean bias of ARO relative to dropsondes is similar to that seen with models (figure 4.18). Below 6 km there is a trend in the ARO retrievals towards low refractivity that likely results from the limitations of geometric optics retrievals in a very moist tropical environment. However in some cases, in particular prn23 occultation for RF18 (Figure 4.19), the similarity of the model profiles below 6 km is clear despite the negative bias.

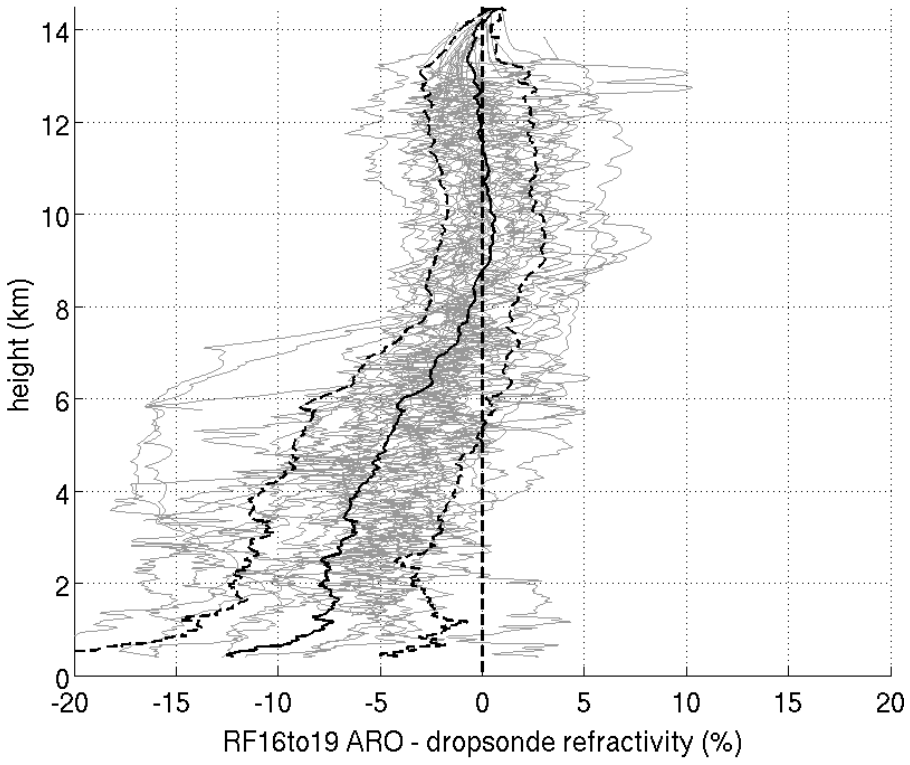

Figure 4.18 Difference of RF16 to19 ARO with co-located dropsondes (cases with location of dropsonde less than 275km from ARO occultation point).

For the purpose of only this section, the rising and setting ARO profiles were corrected for the mean bias as a function of height relative to ERAI refractivity shown in the top left and right of figure 4.16. The mean bias of setting ARO was subtracted from each setting profile and similarly rising ARO and the mean rising bias. Overall there is a

general correlation between ARO profiles and ERAI as expected (Figure 4.20 - 23). The agreement is clearest in RF16, with similar trend with height for profiles that are respectively higher or lower than the mean. RF16 prn03, setting, and prn04, rising, show the greatest difference from the background for both ERAI and for ARO profiles. In the RF17 case, the low level moisture for ARO observations of prn11 shows the greatest discrepancy with ERAI, unable to capture the high near-surface moisture. In RF18, prn30 shows much lower near surface moisture than the ERAI.

Table 4-8 Mean difference and standard deviation of ARO with co-located dropsonde refractivity.

Height (km)	Mean (%)	Std (%)
1	-7.8	6.1
2	-7.8	4.3
3	-6.5	4.1
4	-6.0	4.7
5	-4.7	4.5
6	-3.9	4.1
7	-1.8	3.2
8	-0.56	2,1
9	0.39	2.7
10	0.54	2.3
11	0.33	2.4
12	-0.10	2.5
13	-0.30	2.6
14	-0.32	0.75

In general, it appears that ARO captures large negative moisture variations, but is less reliable for large positive moisture variations. This might be an early onset of multipath given the strong vertical refractivity gradients seen between 6 and 8 km height calculated from dropsonde data when moisture is high. This investigation, while still inconclusive, merits further investigation by future researchers when implementation of

the radio holographic retrieval technique should further enhance the ability of ARO to accurately represent moisture fields at low levels.

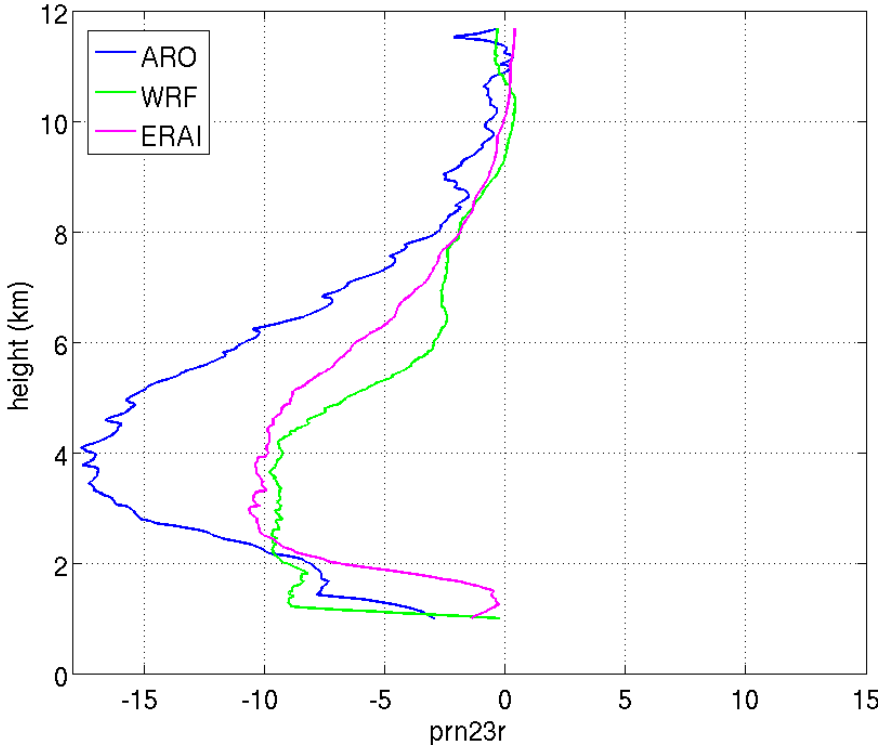

Figure 4.19 Comparison of the differences of RF18 rising prn23 occultation , ERAI and WRF with pre-Karl mean refractivity.

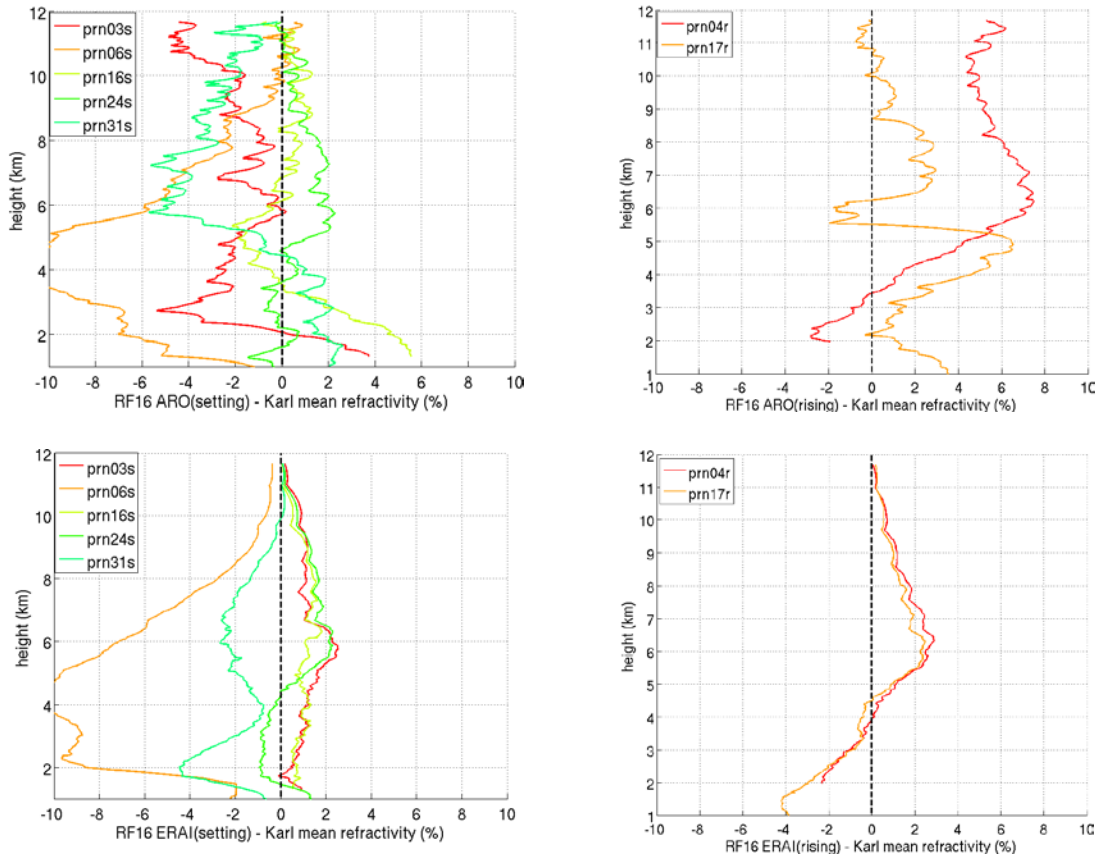

Figure 4.20 TOP: Difference of RF16 setting ARO profiles after ad hoc bias correction with Karl mean refractivity on left. Difference of rising ARO profiles is shown on right. BOTTOM: Difference of ERAI refractivity profiles following setting ARO tangent points with Karl mean refractivity are shown on the left. Difference of ERAI for rising RF16 ARO with Karl mean is shown on right.

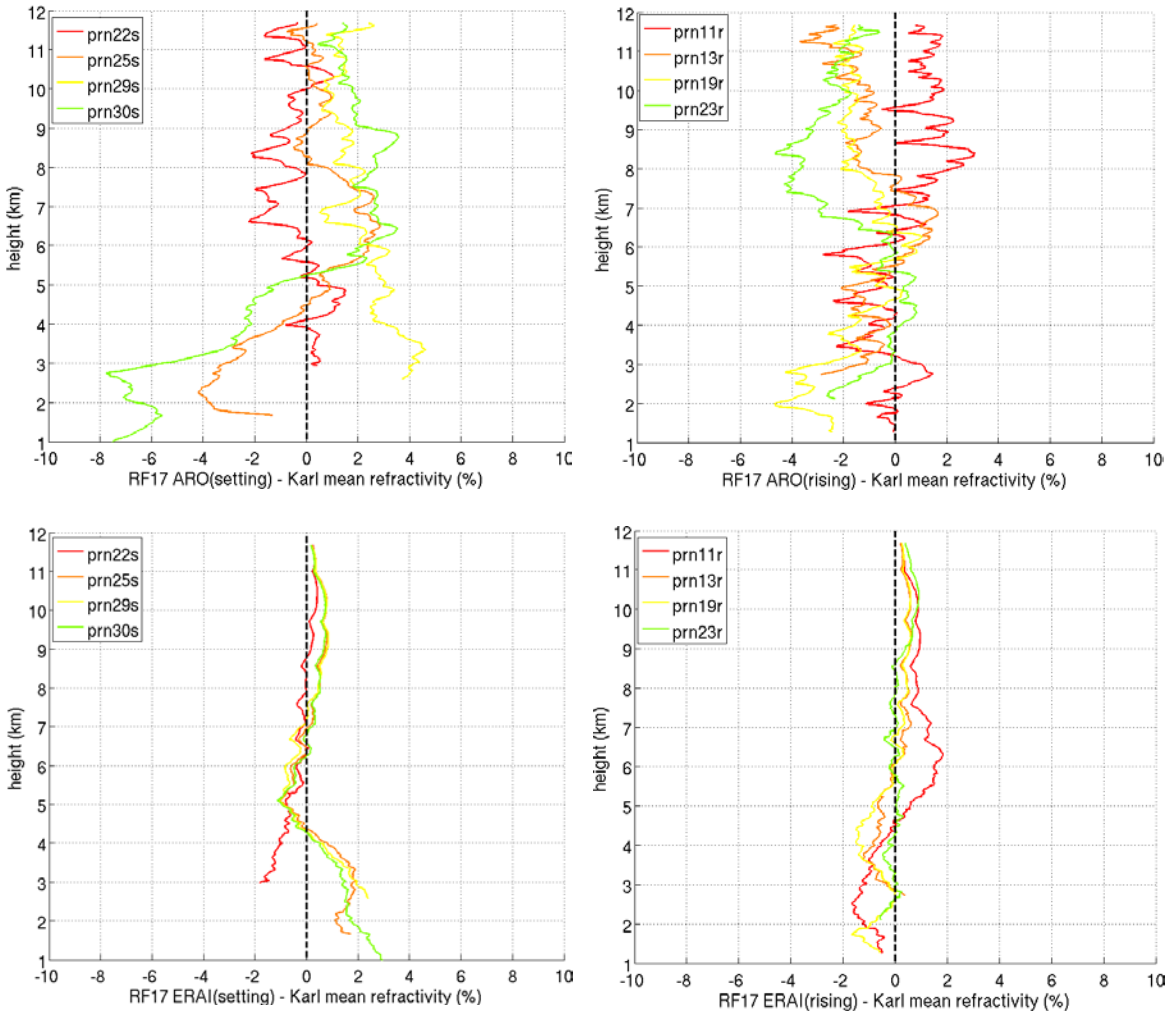

Figure 4.21 TOP: Difference of RF17 setting ARO profiles after ad hoc bias correction with Karl mean refractivity on left. Difference of rising ARO profiles is shown on right. BOTTOM: Difference of ERAI refractivity profiles following setting ARO tangent points with Karl mean refractivity are shown on the left. Difference of ERAI for rising RF17 ARO with Karl mean is shown on right.

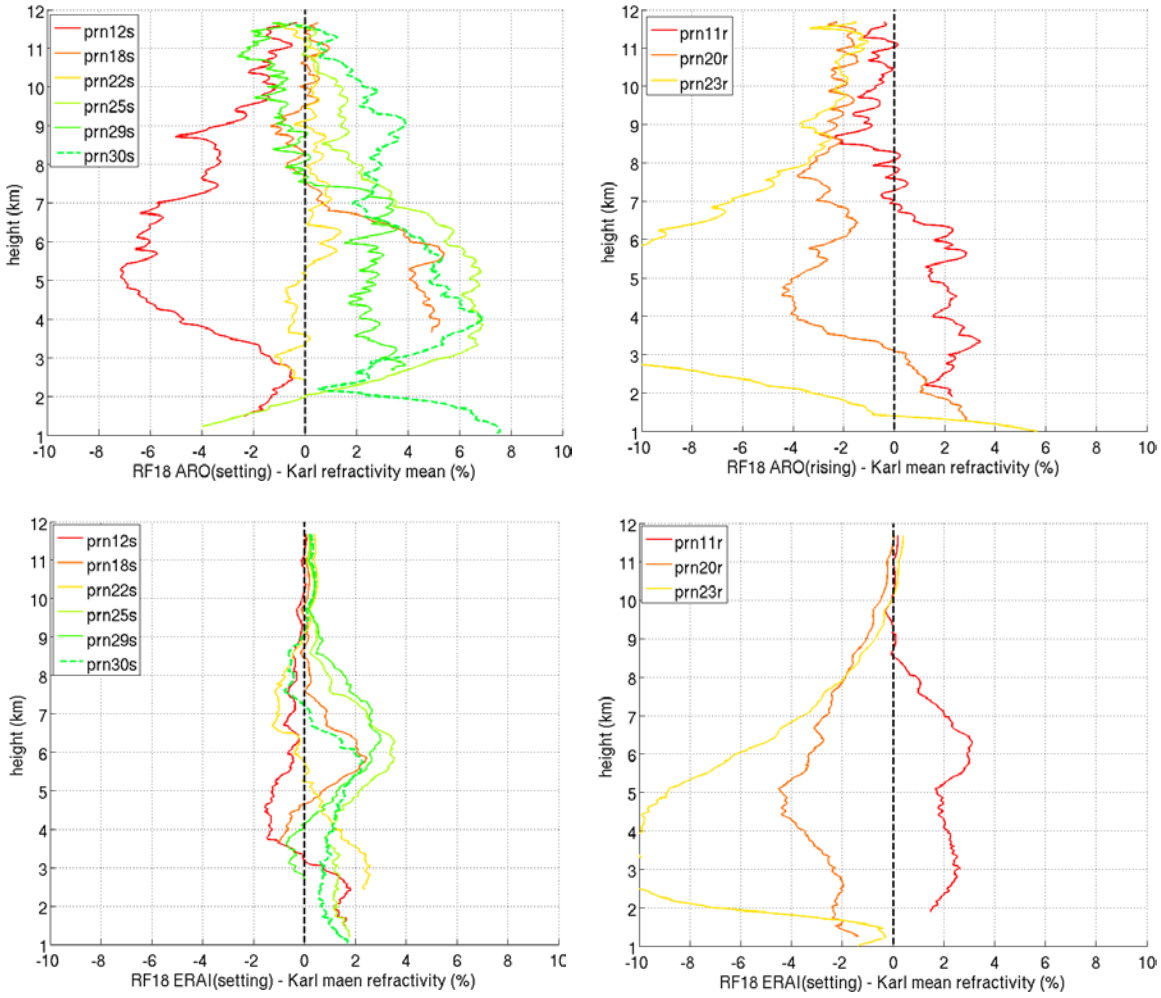

Figure 4.22 TOP: Difference of RF18 setting ARO profiles after ad hoc bias correction with Karl mean refractivity on left. Difference of rising ARO profiles is shown on right. BOTTOM: Difference of ERAI refractivity profiles following setting ARO tangent points with Karl mean refractivity are shown on the left. Difference of ERAI for rising RF18 ARO with Karl mean is shown on right.

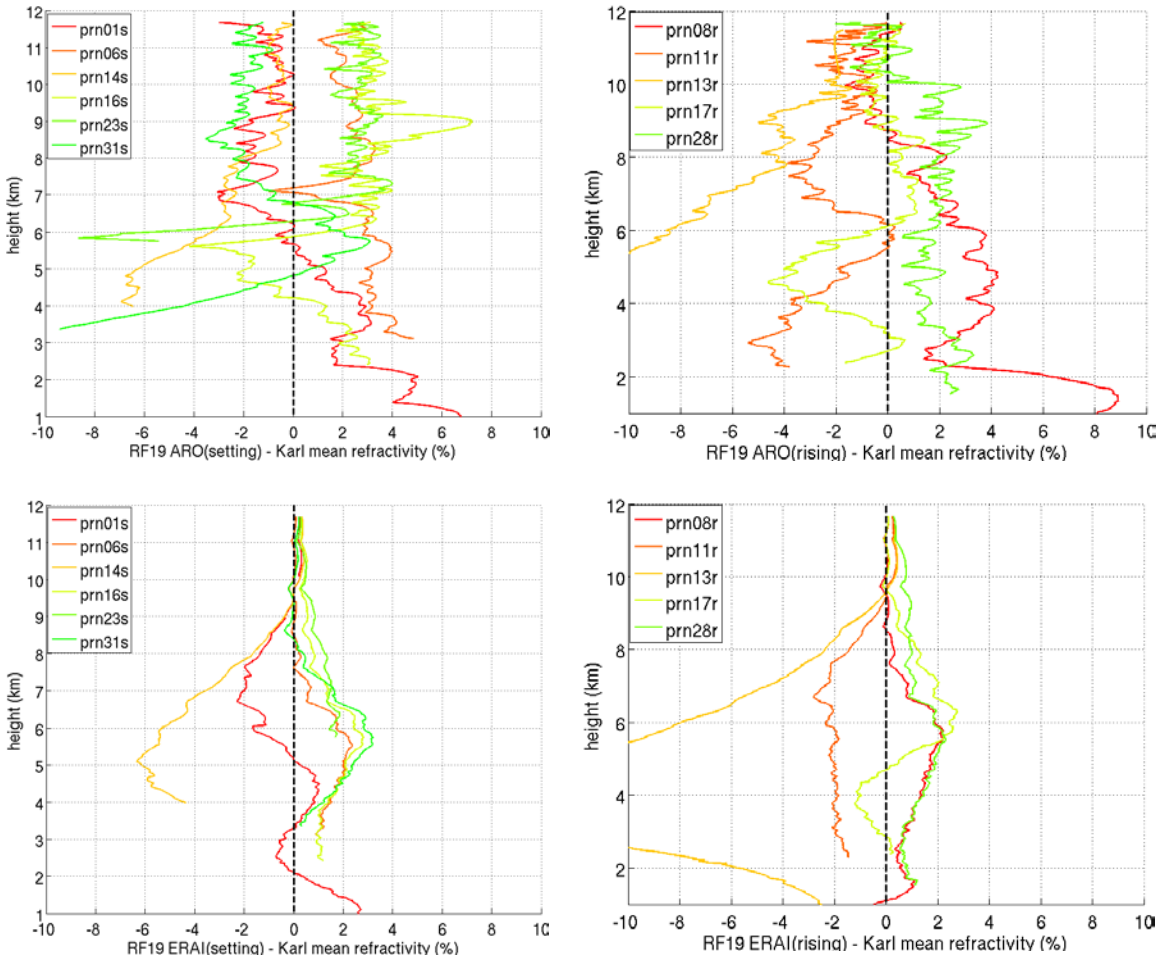

Figure 4.23 TOP: Difference of RF19 setting ARO profiles after ad hoc bias correction with Karl mean refractivity on left. Difference of rising ARO profiles is shown on right. BOTTOM: Difference of ERAI refractivity profiles following setting ARO tangent points with Karl mean refractivity are shown on the left. Difference of ERAI for rising RF19 ARO with Karl mean is shown on right.

4.8 Temporal Variability from RF16 through RF19

In section 2.4.3, the near storm refractivity environment of Karl was examined using the small subset of ARO profiles retrieved from the GISMOS geodetic receivers over the five flights, RF14 – RF18, preceding genesis to tropical storm strength. It was found the change in refractivity over the five flights was consistent with mid-level

moistening in a 6 x 6° meso-α region around the storm center. The near storm refractivity is now investigated with the current set of open loop profiles from RF16 on 11 September 2010 to RF19 on 14 September. While the OL data set is not completely coincident with the Karl subset from the geodetic receivers, the much larger data set should be useful in further expanding on the results from the geodetic receiver study.

Table 4-9 Storm locations for RF16 to19 and ARO occultation points and dropsondes within meso-α box surrounding best track position of pre-Karl system

Research flight	Date	Storm center	prns & dropsondes
RF16	18:00 UT 11 September	14.6N 65.7W	prn3,4,8,17,24 drop1-5; 15-22
RF17	12:00 UT 12 September	15.7N 70.7W	prn11,13,19,23,25, 30 drop3-16
RF18	12:00 UT 13 September	16N 77.1W	prn7,11,22,25,30 drop2-19
RF19	12:00 UT 14 September	17.6N 82.3W	prn6,8,16,17,26,28 drop5-17; 20-21

The methodology was the same as for the investigation of pre-Karl refractivity with the geodetic receiver results. A meso-α 6 x 6° box [*Wang*, 2012] was selected surrounding the National Hurricane center best track positions (www.nhc.noaa.gov). For each flight, all occultations occurring within the meso-α region were averaged (table 4-9 and figures 4-24-27) together over the 6 – 12 km altitude range as a representation of the near storm refractivity from the mid to upper troposphere. The pre-Karl environmental mean was then subtracted from each flight's averaged near storm refractivity profile to compare flights relative to the mean background. It was again found that the ARO results show an increasing refractivity over 6 – 9 km which is consistent with a general

moistening of the midlevel troposphere as the pre-Karl system evolved (figure 4.28). The RF16 mean refractivity was an outlier showing a profile with generally greater refractivity or equal refractivity to later flights. The RF16 prn24 profile from the geodetic receiver Karl subset also was close to highest refractivity relative to background (figure 2.11). The ARO results indicate a moist atmosphere in the vicinity of the system location. The relative humidity of the dropsondes deployed in the meso-α regions are consistent with ARO. The mean relative humidity measured for RF16 is consistently higher then later flights as shown in figure 4.29.

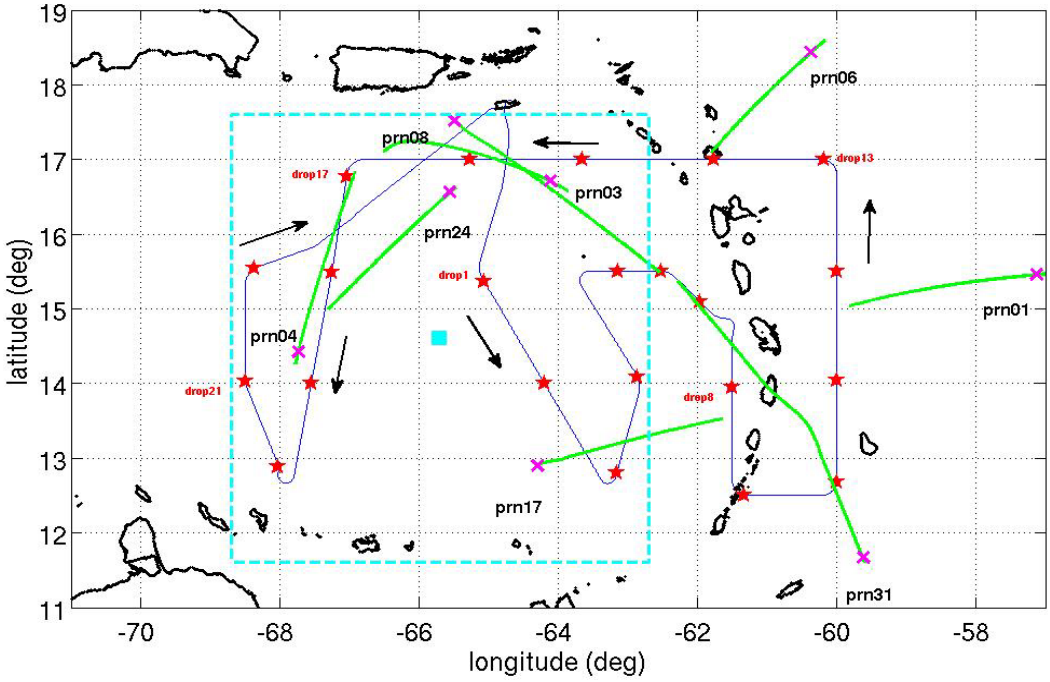

Figure 4.24 The RF16 ARO tangent point profiles are shown in green with occultation points labeled by magenta crosses. Dropsonde locations are marked by the red stars. The meso-α 6 x 6° area around the 18Z best track location is outlined by the dashed cyan box. RF16 prn 3,4,8,17 and 24 were used for the calculation of mean refractivity in the meso-α area.

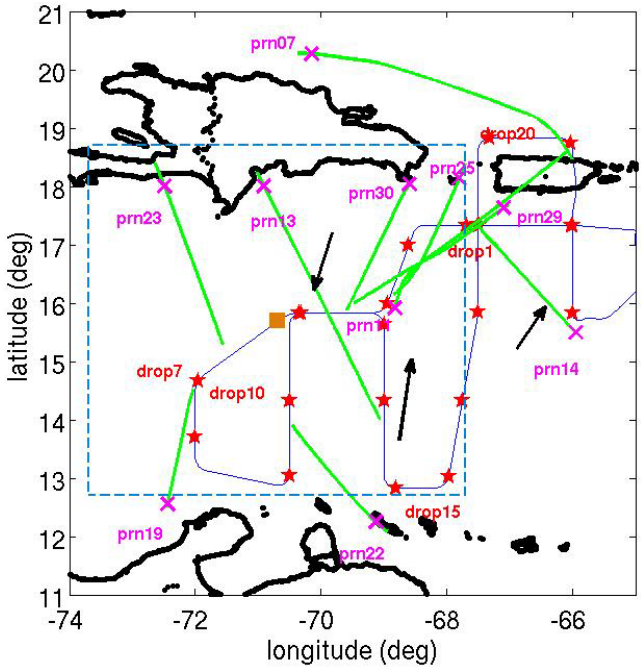

Figure 4.25 The RF17 ARO tangent point profiles are shown in green with occultation points labeled by magenta crosses. Dropsonde locations are marked by the red stars. The meso-α 6 x 6° area around the 12Z best track location is outlined by the dashed blue box. RF17 prn 11, 13, 19, 23, 25 and 30 were used for the calculation of mean refractivity in the meso-α area.

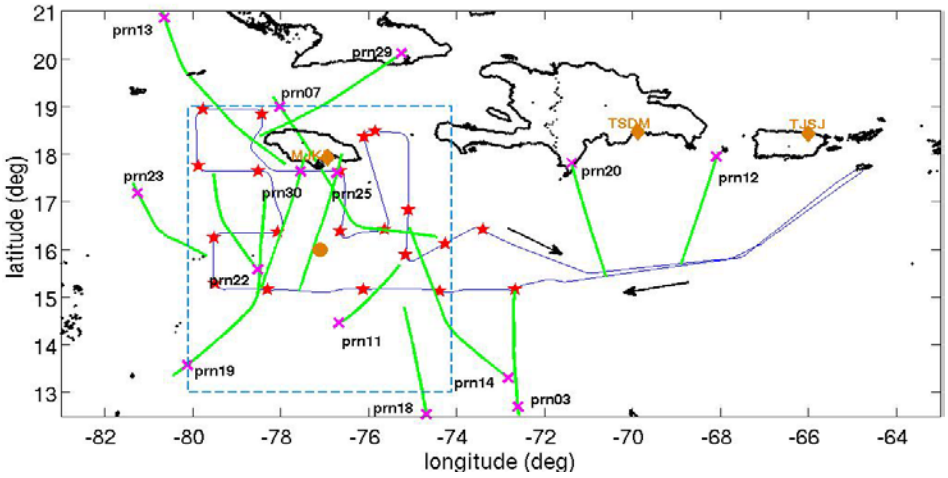

Figure 4.26 The RF18 ARO tangent point profiles are shown in green with occultation points labeled by magenta crosses. Dropsonde locations are marked by the red stars. The meso-α 6 x 6° area around the 12Z best track location is outlined by the dashed blue box. RF18 prn 7, 11, 22, 25, and 30 were used for the calculation of mean refractivity in the meso-α area.

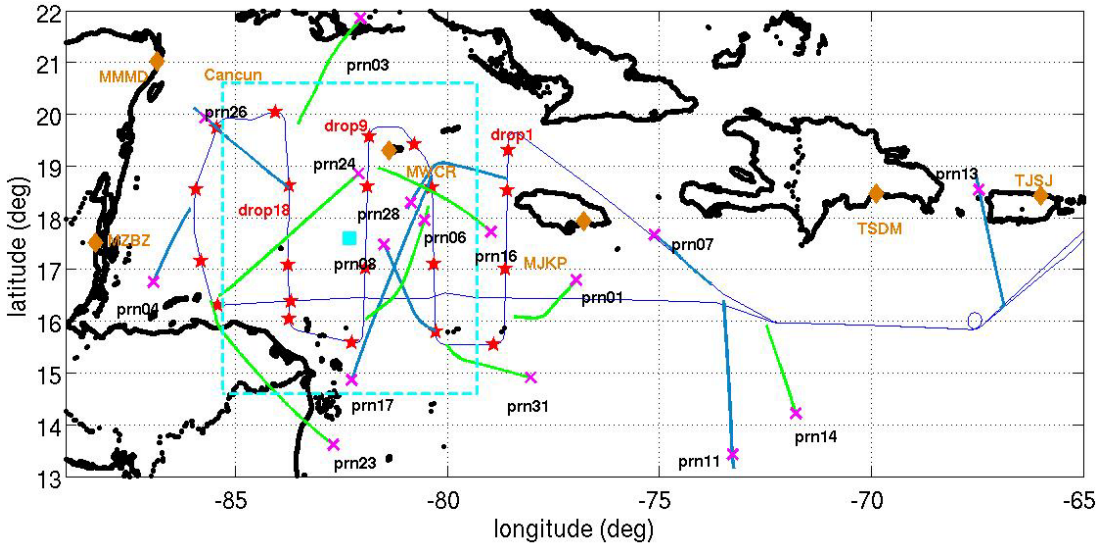

Figure 4.27 The RF19 ARO tangent point profiles are shown in green with occultation points labeled by magenta crosses. Dropsonde locations are marked by the red stars. The meso-α 6 x 6° area around the 12Z best track location is outlined by the dashed blue box. RF19 prn 6, 8, 16, 17, 26 and 28 were used for the calculation of mean refractivity in the meso-α area.

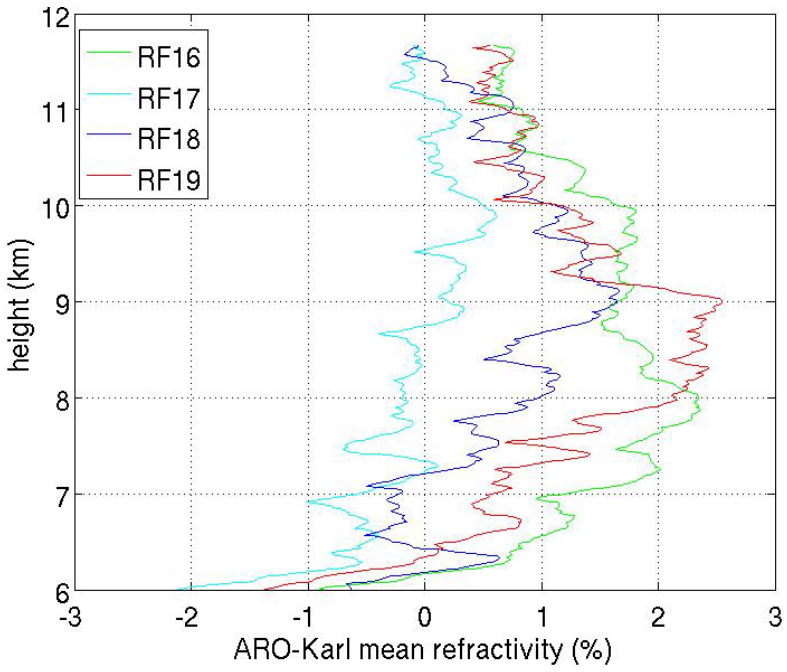

Figure 4.28 RF16 to19 ARO average refractivity in meso-α 6 x 6° area centered on best track storm location minus Karl mean refractivity.

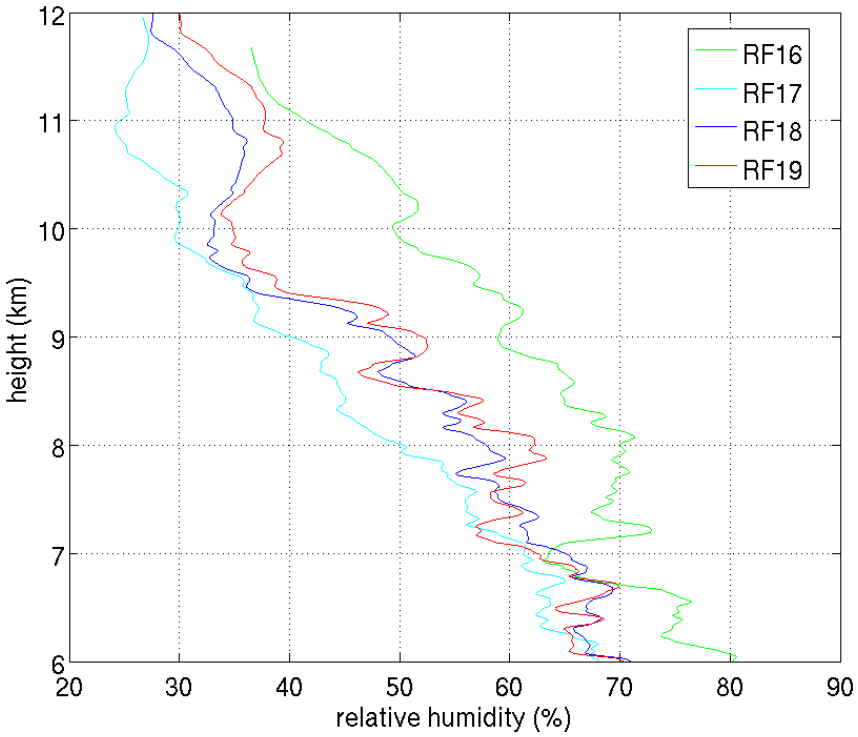

Figure 4.29 RF16 to19 average relative humidity calculated from dropsondes in a meso-α 6 x 6° box centered on best track storm.

4.9 Spatial Variation of Refractivity Shown by ARO Profiles at the Occultation Point

In section 4.5, it was shown that on average with a small error, ARO profiles are representative of the atmosphere when the vertical profile is assigned to the occultation point. Therefore, ARO profiles can be a useful complement to dropsondes when mapping the spatial variations in moisture as ARO can sample well outside or inside the flight path. The ability of ARO to map moisture variations when profiles are assigned to the occultation point is tested using refractivity again as a proxy for moisture.

For each flight, RF16 to 19, the occultation points were sorted according to the WRF simulation column precipitable water (pw) above 500 hPa (~ 6 km) averaged over a 9 grid point square centered on the occultation point. The above 6 km range was chosen

as comparisons with model and dropsondes have shown this is the region where the geometric optics retrievals are most reliable on average. A 3 x 3 grid point average was done to smooth out potential sharp variations in the high resolution WRF model output. Three bins for sorting were chosen: 1 – 3mm, 3 – 5 mm, 5 – 7 mm, which covers the average extent of pw seen in the vicinity of the flight. Once the sorting for a flight was complete, the refractivity profiles were averaged for each bin.

Each bin average was plotted relative to background by subtracting the pre-Karl environmental mean refractivity. For each flight, the comparison of ARO mean refractivity below 9 km was consistent with the magnitude of the pw (figure 4-30-37). Higher mean refractivity corresponded with a bin of higher pw and vice vesa with a lower mean refractivity. In figure 4-30-37, the ARO occultation points are color coded to their bin assignment and plotted overlaid on the WRF pw to demonstrate how the spatial variations in moisture can be represented by ARO profiles at the occultation point. ARO can then be combined with dropsondes observations, which do not sample outside the flight track, to provide a more comprehensive representation of the moisture field.

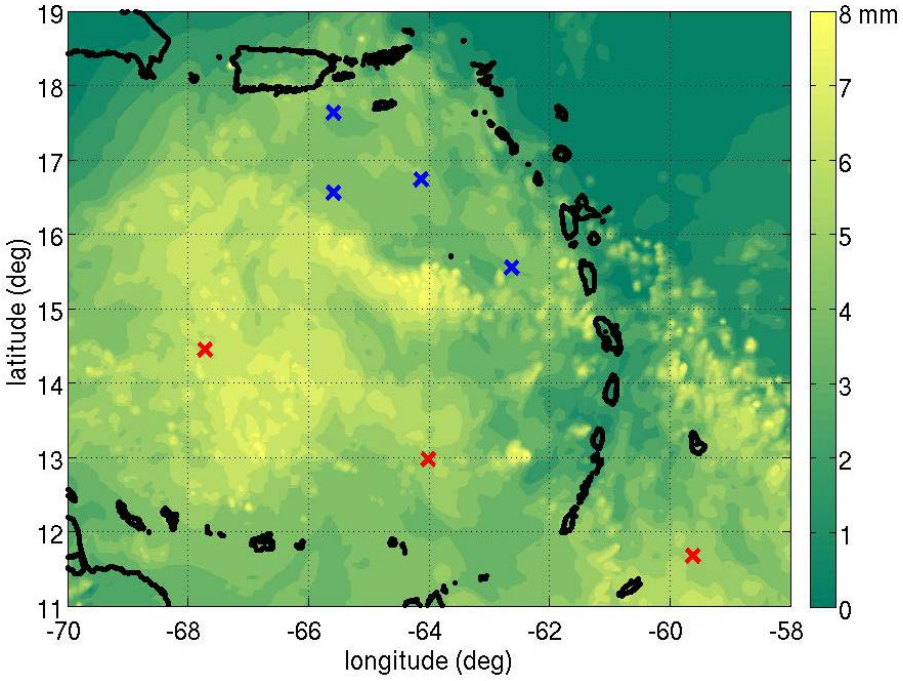

Figure 4.30 RF16 ARO refractivity color coded according to WRF total precipitable water above 500hPa at the location of the occultation point. Blue crosses indicate precipitable water levels of 3 to 5 mm and red indicates 5 to 7 mm.

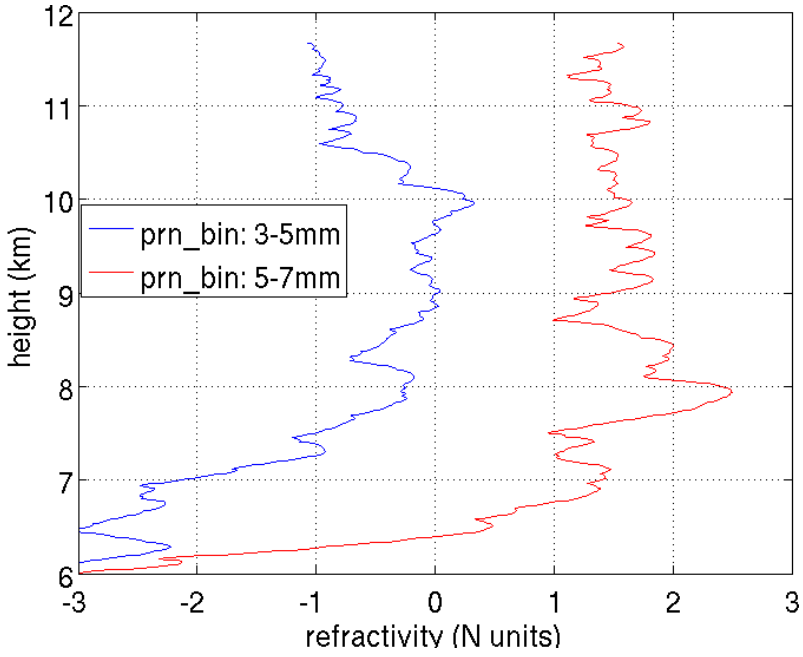

Figure 4.31 Difference of RF16 mean ARO refractivity profile with the Karl mean for the 3 – 5 mm and 5 – 7 mm bins.

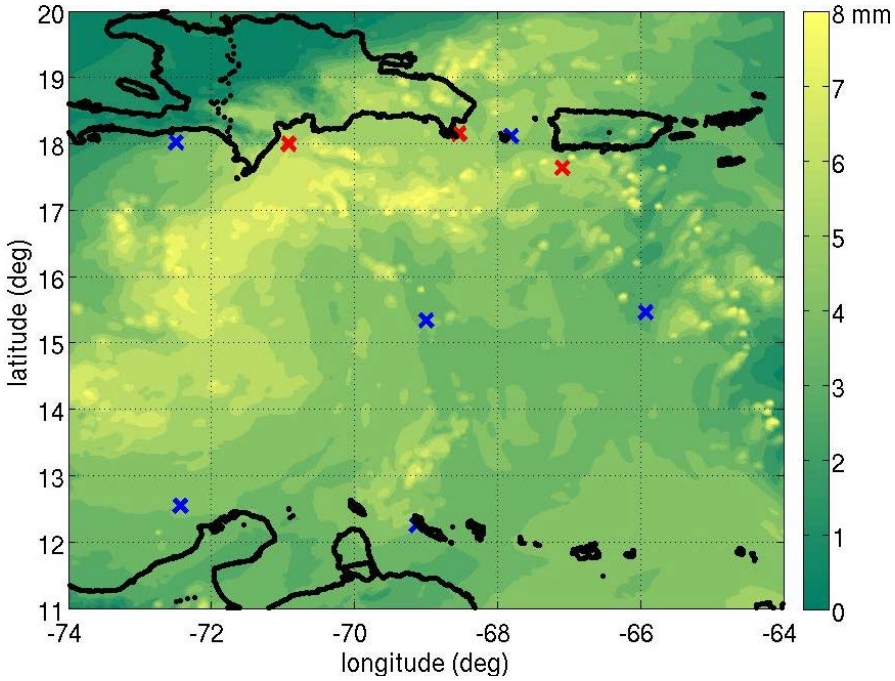

Figure 4.32 RF17 ARO refractivity color coded according to WRF total precipitable water above 500hPa at the location of the occultation point. Blue crosses indicate precipitable water levels of 3 to 5 mm and red indicates 5 to 7 mm.

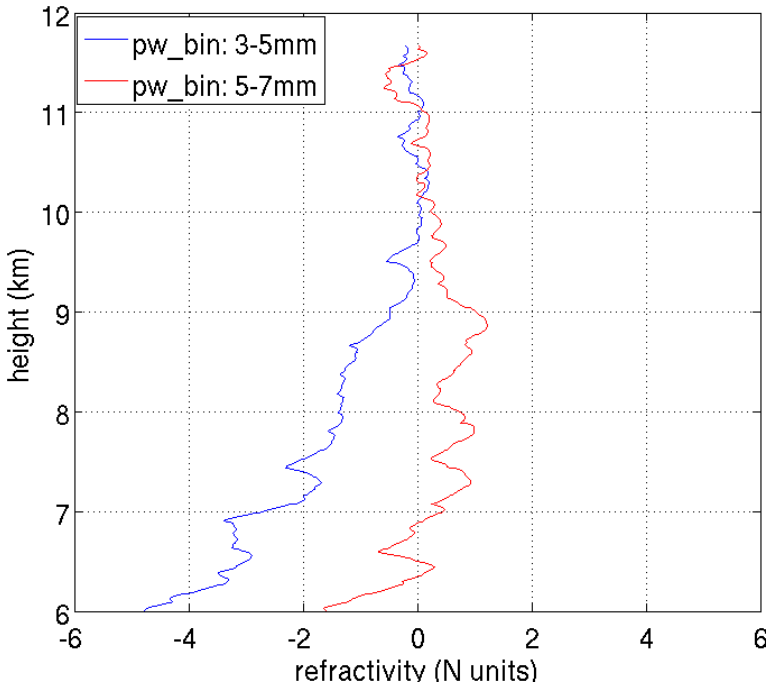

Figure 4.33 Difference of RF17 mean ARO refractivity profile with the Karl mean for the 3 – 5 mm and 5 – 7 mm bins.

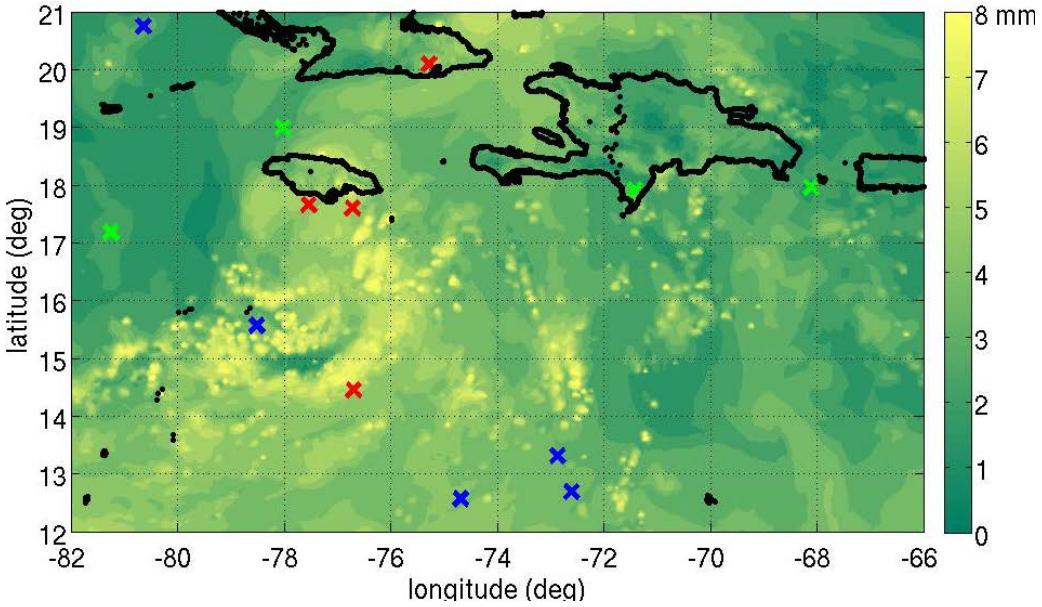

Figure 4.34 RF18 ARO refractivity color coded according to WRF total precipitable water above 500hPa at the location of the occultation point. Green crosses indicate precipitable water levels of 1 to 3 mm, blue crosses indicate 3 to 5 mm and red indicates 5 to 7 mm

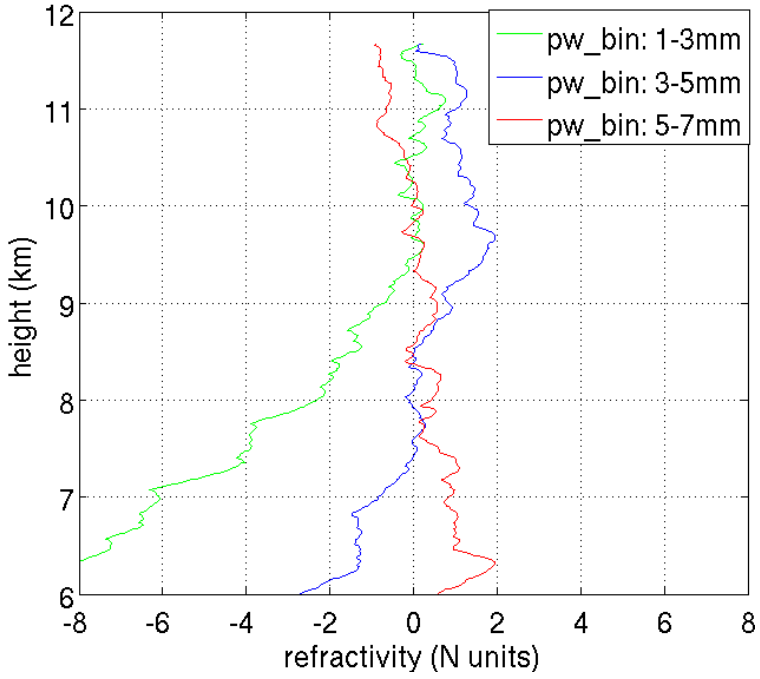

Figure 4.35 Difference of RF18 mean ARO refractivity profile with the Karl mean for the 1 – 3 mm, 3 – 5 mm and 5 – 7 mm bins.

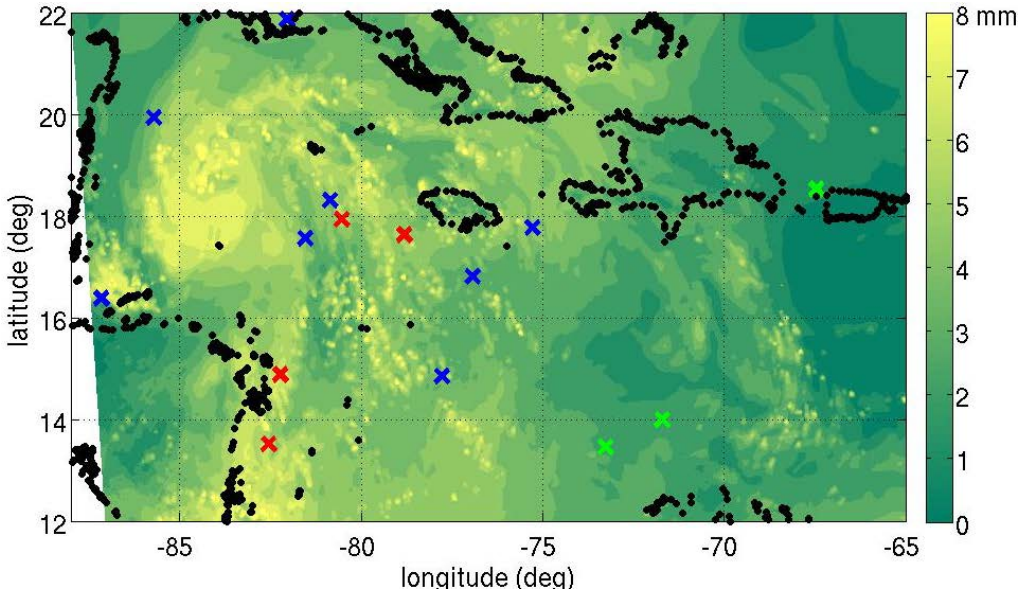

Figure 4.36 RF19 ARO refractivity color coded according to WRF total precipitable water above 500hPa at the location of the occultation point. Green crosses indicate precipitable water levels of 1 to 3 mm, blue crosses indicate 3 to 5 mm and red indicates 5 to 7 mm

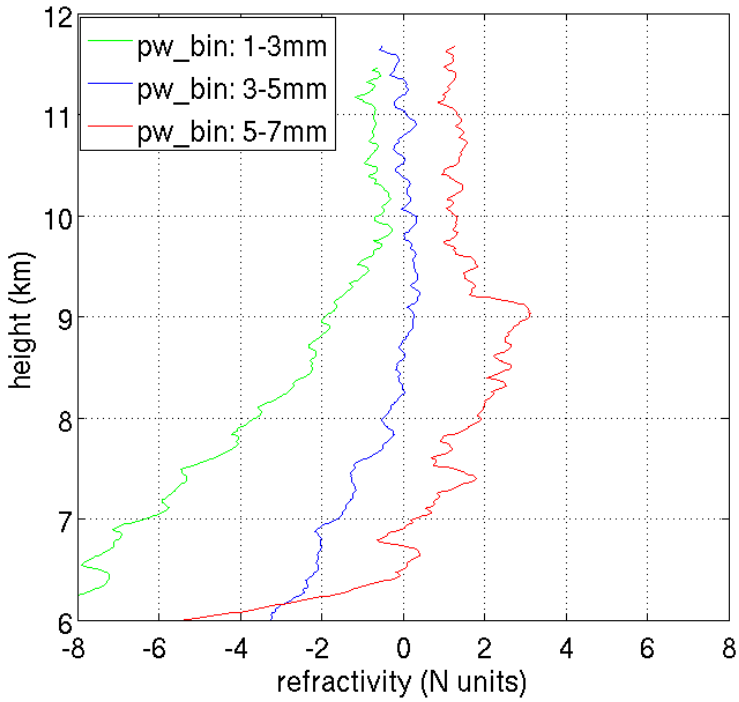

Figure 4.37 Difference of RF19 mean ARO refractivity profile with the Karl mean for the 1 – 3 mm, 3 – 5 mm and 5 – 7 mm bins.

4.10 Radial Sampling of the Tropical Storm Environment with ARO

A critical element in the improvement of hurricane forecasts has been the assimilation of meteorological satellite data into the NWP models [*Folmer et al.*, 2015; *McNally et al.*, 2013; *Vergados et al.*, 2013]. Satellite borne sensors such as the Advanced Microwave Sounding Unit (AMSU) and Advanced Microwave Sounding Radiometer (AMSR) can provide important data on hurricane structure such as temperature, moisture and surface winds [*Weng et al.*, 2007]. Geostationary infrared (IR) observations have been used to estimate the low level wind fields of hurricanes [*Mueller et al.*, 2006] and the three dimensional cloud structure of southern hemisphere cyclones has been mapped using CloudSat and Cloud Aerosol Lidar and Pathfinder Infrared Satellite Observations (CALIPSO) platforms [*Govekar et al.*, 2011]. Recently, it has been shown that spaceborne RO can be useful in describing the radial thermodynamic structure of hurricanes [*Vergados et al.*, 2013].

Vergados et al. [2013] attempted to capture this variation in a composite image of radial structure from serendipitously located spaceborne RO measurements from 42 tropical storms occurring from 2002 to 2010. The GPS RO profiles were used up 600 km from the storms' centers. The composite data was sorted and displayed as 25 km binned averages (figure 4.38). It was found the composite data revealed interesting TC structures such as a 8 km height peak of water vapor near the approximate location expected for the eyewall.

Data from GPS dropsondes can also provide a robust data set to investigate the dynamic and thermodynamic structure surrounding a tropical cyclone [*Franklin et al.*,

2003]. An extensive dropsonde data set was collected for many of the developing systems studied by PREDICT. Davis and Ahijevych [2013] captured this thermodynamic evolution with time using dropsonde profiles from several individual storms that were well sampled during the PREDICT campaign. Variables such as virtual temperature, moist static energy and relative humidity were profiled based on radial distance and also differentiated as a function of cloud top temperature using Geostationary Operational Environmental Satellite (GOES) data.

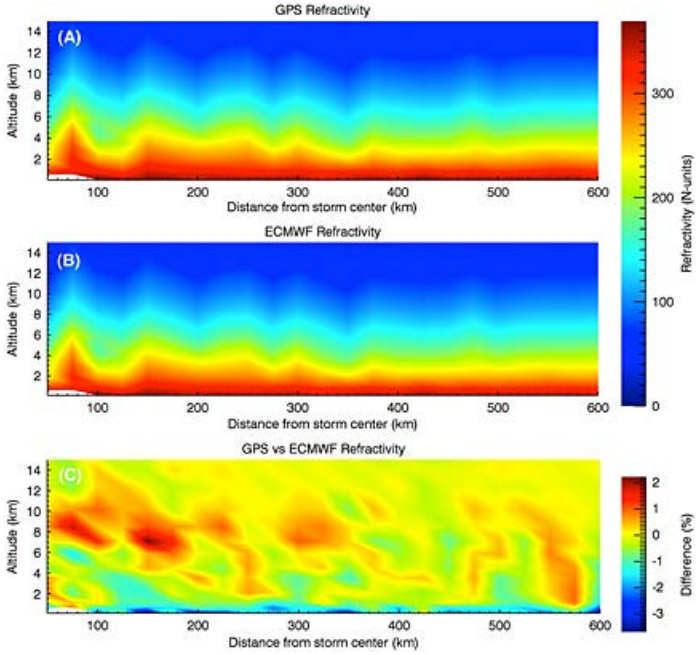

Figure 2. The tropical cyclone refractivity variability. Twenty-five kilometer binned averages of North Atlantic tropical cyclones from (a) GPSRO and (b) ECMWF as functions of altitude and distance from the storms' center between 2002 and 2010 expressed in refractivity units. (c) The difference between the GPSRO and ECMWF refractivity is measured in percentage difference.

Figure 4.38 (from Vergados et al, *J. Geophys. Res. Atmos.* , A validation study for GPS radio occultation data with moist thermodynamic structure of tropical cyclones, **118**, 16,2013) Composite radial plot of refractivity from the storms' center using spaceborne RO and ECMWF.

ARO provides additional complementary data to capture the radial structure with RO for individual storms using composites of data collected over several missions or on a daily basis during storm evolution. During PREDICT, the density of ARO observations during a mission that can be retrieved with OL tracking was usually sufficient to map the radial refractivity from the storm center (figure 4.39). When combined with dropsonde soundings, it extends the radial distance and coverage for a more complete description of the system structure.

Using the ARO profiles from the RF16 – 19 flights, a radial area of 875 km was sampled over a height range of 1 -12 km. Following a similar approach to Vergados et al, the ARO data were averaged within 175 km bins of radial distance from the NHC best track storm positions (Figure 4.40). The values below the dashed line (6 km) are low reliability without the radio-holographic retrieval. Above that level, the dense ARO sampling is sufficient for one flight to characterize the radial structure of the mesoscale system (figure 4.39). We constructed the same analysis assuming the 900 hPa circulation center used by Davis and Ahijevych [2012]. These were interpreted based on dropsonde winds, and showed significant differences to the NHC track. The alignment of the circulation centers at 500 and 900 hPa were believed to be a key stage in evolution leading to cyclogenesis. The choice of reference makes a significant difference in the mapping of high level dropsondes humidity from 5-9 km (figure 4-42). The work is at too preliminary a stage to draw inferences, but the radial-cross-sections are clearly densely enough sampled compared to spaceborne RO soundings, to pursue this area of research in the future.

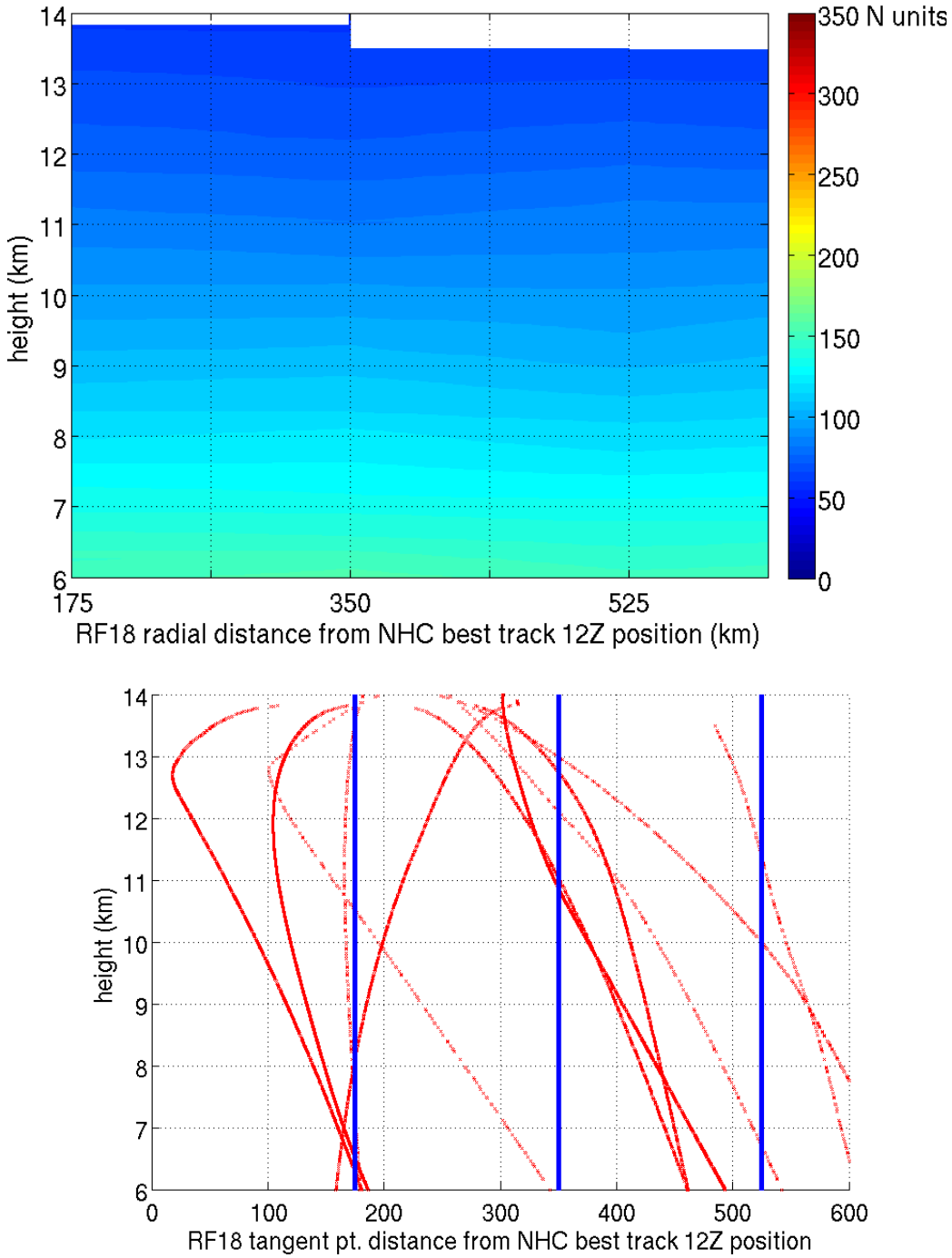

Figure 4.39 TOP: Radial refractivity field surrounding the 12Z NHC best track position of the pre-Karl system on 13 September 2010 as sampled by RF18 ARO profiles averaged by height over 175 km bins. BOTTOM: The RF18 ARO tangent point positions by height and radial distance from the best track 12Z position. Bins of 175 km are marked by blue lines to show concentration of profiles in each bin.

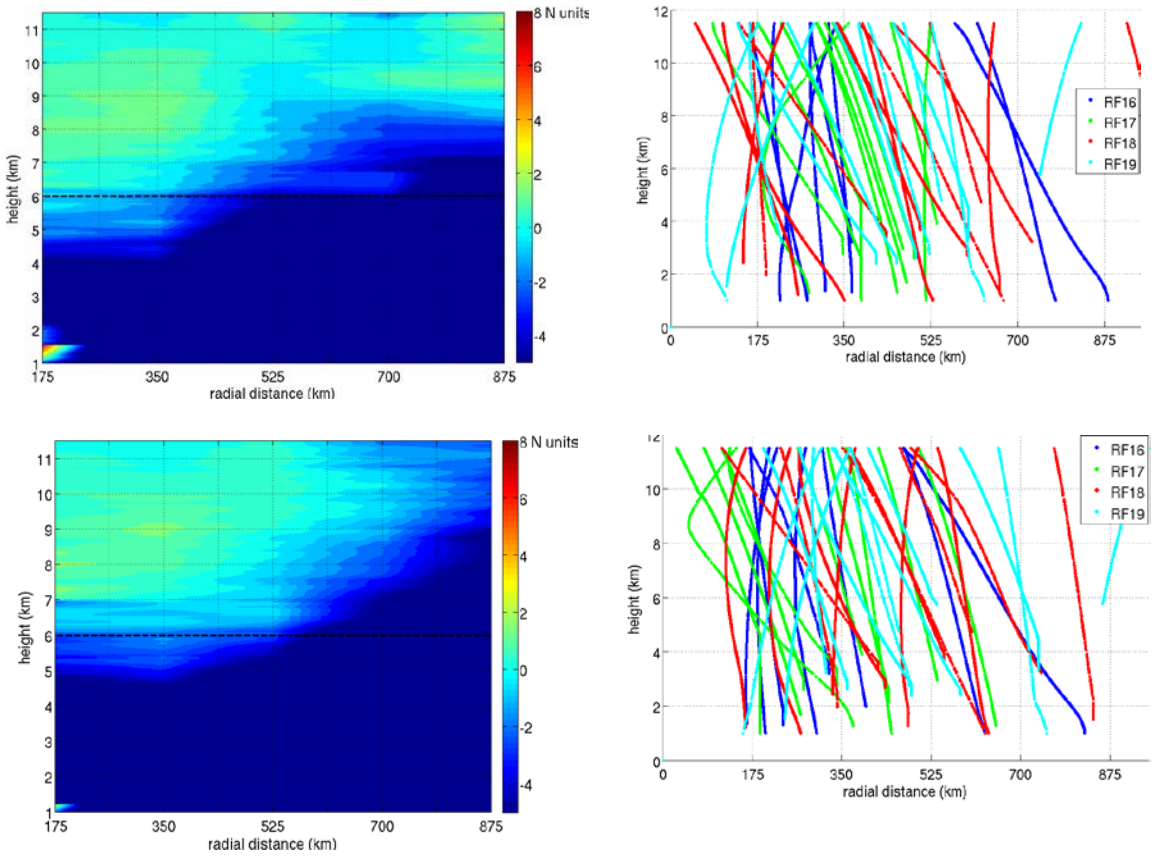

Figure 4.40 TOP RF16-19 ARO averaged over 175 km bins from NHC best track positions on left with ARO tangent points by radial distance and height on right. BOTTOM: ARO averaged over 175 km bins from 900mb circulation center on left with ARO tangent points on right.

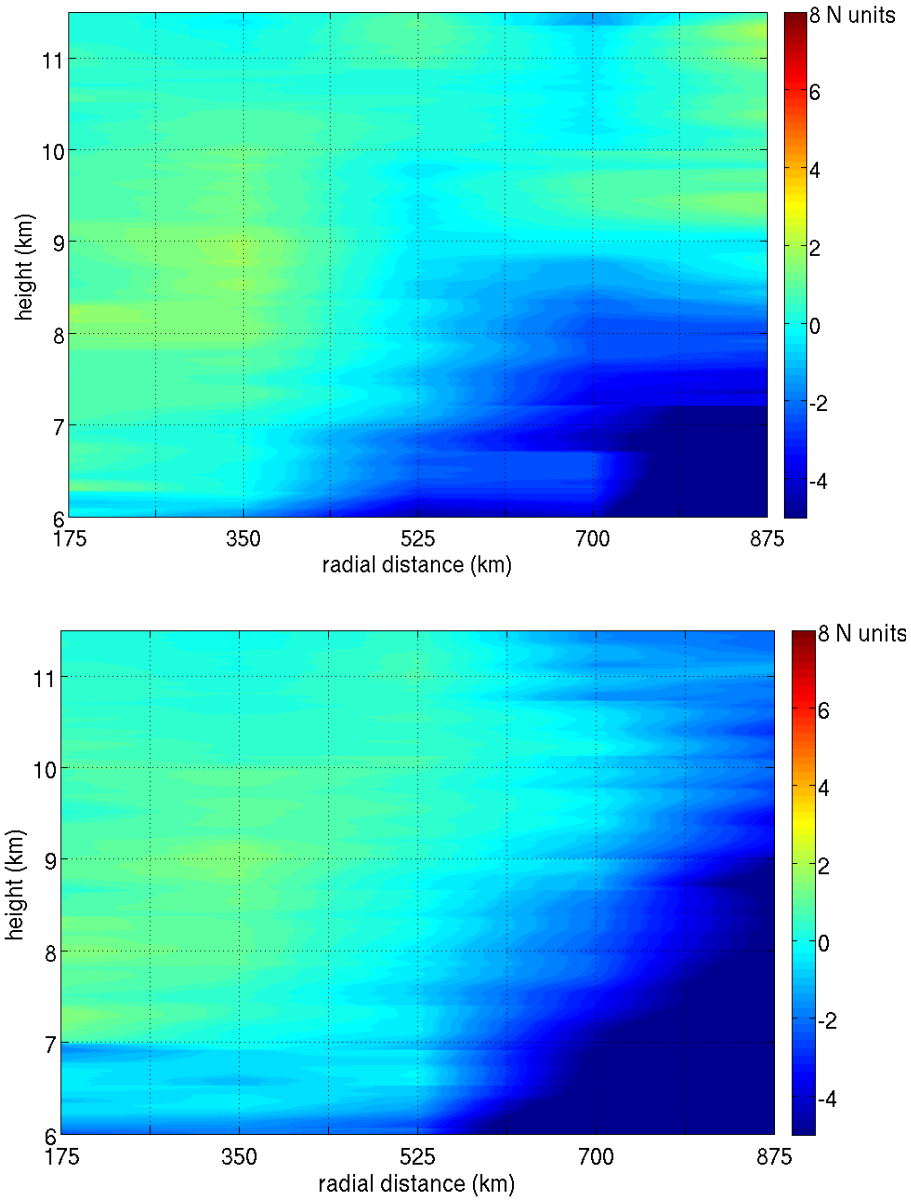

Figure 4.41 TOP: RF16-19 ARO averaged over 175 km bins from NHC best track positions shown only above 6 km height. BOTTOM: RF16-18 ARO averaged over 175 km bins from 900 hPa circulation center positions only above 6 km.

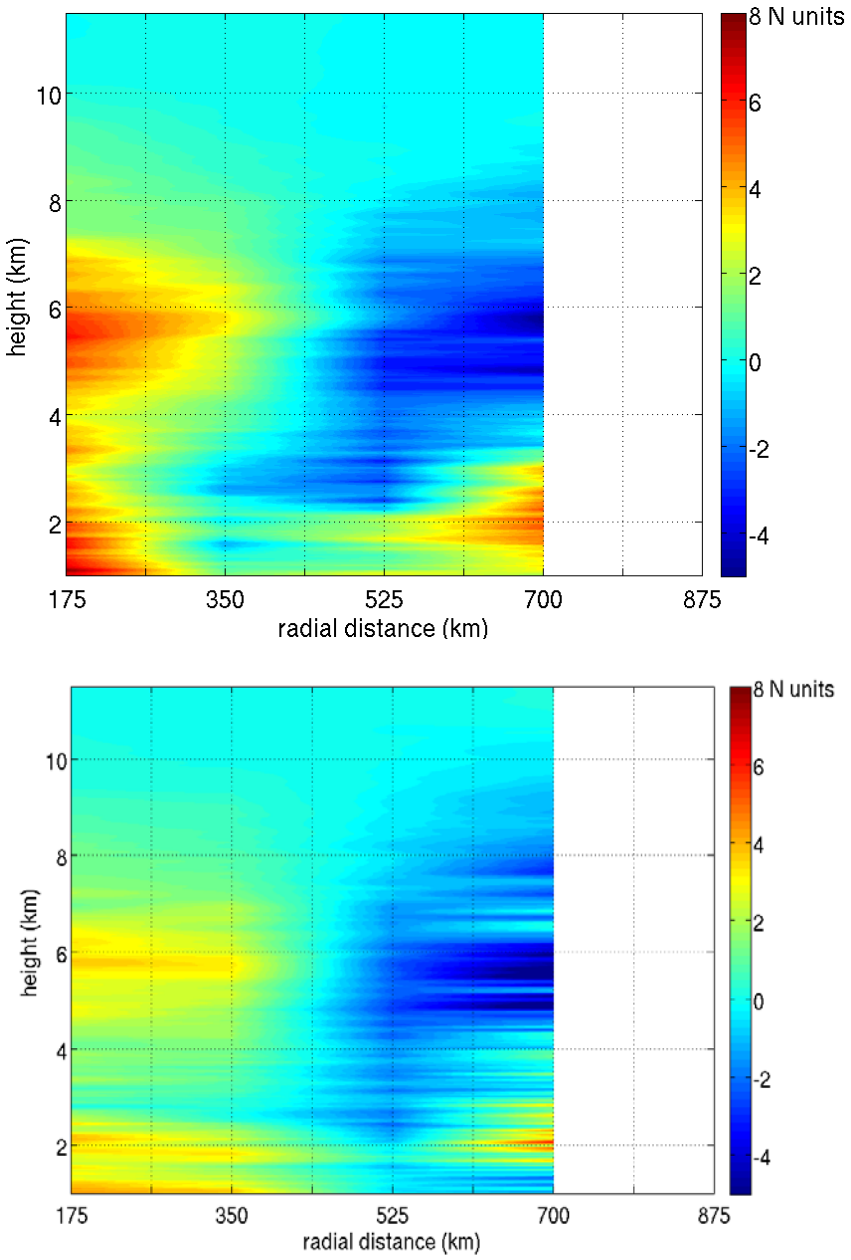

Figure 4.42 TOP: RF16-19 dropsondes averaged over 175 km bins from NHC best track positions. BOTTOM: RF16-19 dropsondes averaged over 175 km bins from 900mb circulation center positions on bottom.

4.11 Conclusions

The introduction of open loop tracking for ARO has made it possible to retrieve nearly all occultations that occurred during the PREDICT research flights. The 10 – 15 ARO profiles obtained for Karl flights within an approximate 900 by 1000 sq. km area around the storm is comparable to the roughly 20 dropsonde profiles available per flight. The ARO data is also able to complement the dropsondes by extending the area sampled beyond the flight path.

One caveat with ARO observations, compared to spaceborne RO, is that they have the added complexity of a larger tangent point drift, on the order of 400-600 km. The use of an occultation point to locate the vertical ARO refractivity profile following the convention of spaceborne RO was compared to treating the ARO profile as point measurements at each tangent point location. The differences with ERAI for the two approaches were comparable when using the geometric optics retrievals from PREDICT. The greatest horizontal fluctuations in refractivity are in the lower troposphere where the geometric optics retrievals are not reliable. The useful approximation of the 500 hPa occultation point for the location of the slated profile may not hold up when a full OL data set is retrieved using a radio holographic retrieval, which is more reliable in the lower troposphere,

ARO can provide spatially and temporally dense data sets which can be potentially useful for model validation. For the PREDICT flights, dropsondes were more comparable to ERAI and the difference of the Karl ARO data with ERAI showed smaller standard deviation in the 2 – 8 km range than with WRF. This spatially and temporally

dense set of observations will be used by the larger community for future NWP assimilation tests of the impact of ARO data because they capture the moisture variations associated with dry environmental air at distances greater than 500 km from the storm center and the location of large scale mid-level moisture variations along the axis of the tropical wave (figure 4.36).

Below 9 km, the moisture contribution to the refractivity variation dominates in the tropical environment because the profiles have relatively homogenous temperature profiles. Therefore, refractivity serves as useful proxy for moisture in this environment. The similarity in refractivity fluctuations of AR0, ERAI and WRF profiles with moisture variations shown by the models can be seen in figure 4.11 for the RF18 prn23 case. The variation in averaged refractivity is also seen to be consistent with variation of precipitable water derived from the WRF simulation as seen in figures 4.30 through 4.37.

A study of spaceborne RO profiles [*Vergados et al.*, 2013] has shown the ability of RO data to map the radial thermodynamic structure of hurricanes. However, since spaceborne RO profiles are relatively sparse the study used a RO data set in the vicinity of hurricanes composited from profiles sampled over 42 cyclones and 8 years. ARO has an advantage of being able to obtain a data set of sufficient density from one flight to map radial structure surrounding a storm (figure 4.39).

CHAPTER 5. CONCLUSIONS

The PREDICT campaign used dropsondes to investigate how moisture is exchanged between a protected environment associated with African easterly waves and the external environment, which could be affected by a drier air Saharan air layer, and the subsequent impact of this moisture exchange on tropical cyclone genesis [*Dunkerton et al.*, 2009; *Montgomery et al.*, 2012]. The objective of deploying the airborne radio occultation capability during PREDICT was to determine the average moisture structure within the region of enhanced convection, and of the external environment outside the tropical wave. The ability of ARO to sample the environment on both sides of the flight track, obtaining a high vertical resolution integrated picture of the surrounding air masses, is complementary to dropsonde observations beneath the flight track, and to high spatial but low vertical resolution satellite soundings. Data assimilation is planned to determine how well mesoscale features can be improved over using dropsondes alone by incorporating the dense sampling of crossing rays of the airborne RO dataset, using the nonlocal assimilation operators that account for the effect of integrating over a long horizontal path length. The ARO system continually measures during the dropsonde releases and thus provides a means to link the point measurements to the 4D moisture evolution. In order to provide a data set for assimilation, we need to assess the error

characteristics and accuracy of ARO soundings as well as determine the sensitivity of ARO to important spatial and temporal moisture variations.

The ARO measurements made during PREDICT mark the first full scale deployment of an ARO system for a science mission, and the first time occultation measurements have ever been made with the density capable of achieving these objectives, either from satellite or aircraft. In addition, this is the first time that a large set of occultation measurements have been made within an environment that has been well sampled by independent observations. This thesis lays the groundwork to carry out assimilation tests for forecasting tropical storms by developing the optimal methodology for analyzing the GPS data, determining the practical capabilities of the system, and providing a first look at horizontal and temporal variations in atmospheric properties over the early stages of tropical cyclone development as determined by these observations. It seeks to answer the following questions:

1) Given the flight paths and instrument capabilities, what are the sampling characteristics of ARO, how do the commercial conventional components compare to research instrumentation, what techniques can be used to increase performance in the tropical enviroment, and what are the implications for improvements and ease of use in future research deployments and a future operational system?
2) Given the challenges of observing from an aircraft platform, what new techniques are required to increase performance of the system in the presence of noise? What was the resulting improvement in sampling?

3) For the purpose of establishing reasonable description of observation errors required for future data assimilation, what is the accuracy of the retrieved profiles? Are these measures consistent, taking into consideration the different scales of independent measurements and models used for comparison? Are there limitations and what are the prospects for how accuracy can be improved?
4) Using observations from the system that would eventually become hurricane Karl, what are the expected and observed scales of temporal and spatial moisture variability evident directly in the refractivity profiles prior to any data assimilation and how is that evident in comparisons with high-versus low-resolution model fields over the course of tropical storm development? What is the observed contrast in refractivity in the larger scale environment compared with that near the storm center at different stages of development? What limitations are imposed on the interpretation because of biases and how might those change in the future with implementation of the radio holographic techniques?

The sampling characteristics of ARO were initially evaluated using data collected by the conventional geodetic GPS receivers for a preliminary assessment of feasibility. Raw GPS signal data was also recorded by a high speed 10 Mhz GPS recording system (GRS). Results from high gain narrow aperture antennas and lower gain isotropic antennas from the top and sides of the aircraft have also been compared. The ARO data is used to obtain atmospheric refractivity profiles as a function of height. Initial analysis of data from the geodetic receivers produced a set of 21 upper tropospheric profiles. The profiles extended from receiver height to on average to 6 km altitude and some to as low

as 4 km. This set of profiles typically did not extend further because of the loss of signal lock. In general, the ARO profiles did agree to within 2 % of refractivity calculated from dropsonde data and ERAI reanalysis which demonstrated the validity of the ARO technique. The tropical environment is more challenging for the radio occultation technique because of the very humid conditions. The high moisture can result in sharply changing atmospheric refractivity gradients through which the GPS signal must travel and is likely the cause of loss of signal lock by the geodetic receivers. The geodetic receivers also can only track setting occultations.

In order to achieve the necessary increase in performance, raw GPS signals were analyzed with an open loop (OL) tracking technique, which is not susceptible to the loss of signal lock in the moist tropical atmosphere that was seen in the geodetic receivers. Rising occultations can also be tracked with OL. Muradyan [2012] established during a validation campaign in winter subtropical to mid latitudes that a much greater number of ARO retrievals can be made using the OL technique, up to 3 per hour of flight time for straight line flights, and that OL retrievals can consistently reach to below 1 km altitude. The first goal of OL analysis in this work was to obtain comparable sized data sets in the tropics with profiles extending to near the surface. A data set was compiled comprising 46 profiles from four research missions out of a possible 55 occultations. Over the 4 flights, about 2 occultations were recorded per hour of flight time. However, the PREDICT flight paths were typically square spirals or lawnmower patterns and not straight line level flight. During the straight line ferry flight, FF04, 18 occultations were seen in the recorded GRS data over about 5.5 hours of flight time. While the PREDICT flights were not optimal for side looking antennas because of turns, most occultations

could be retrieved because of the unexpected strong performance of the top mounted avionics antenna. While this antenna does have less gain the specialized high gain side mounted antennas also used the GRS, its isotropic view allowed tracking of most occultations through aircraft turns. In the case of RF17, only 3 profiles were retrieved using from the side antenna data, but 10 were retrieved from the top antenna data.

Because ARO profiles samples along their tangent path out away from the flight track on the order of 400 km, the ARO measurements will complement dropsondes observations which are constrained near their launch point along the flight track. In the case of the PREDICT, areas of severe weather or convection which the GV had to avoid could still potentially be sampled by ARO.

New analysis methodology was also required to increase the performance in the presence of noise. Noise in the ARO data was evident, especially in conditions of lowered SNR. It was found that smoothed the receiver velocity components, needed in the calculation of bending angle, mitigated noise associated with the less stable airborne platform. Smoothing of the excess Doppler and the replacement of remaining outlier points with an averaged value was also effective in reducing noise in the bending angle profile. However, even with these steps , the region of the bending angle profile near zero elevation was typically still quite noisy, as well as in the positive elevation region which is expected to be more smooth because of the very small refractivity at heights above the GV. These sections of bending angle were replaced with a smooth simulated bending angle profiles based on an initial retrieval of refractivity. The inverse Abel retrieval was then repeated with the new bending profile. This iterative approach was effective in preventing the noise from propagating further into the final ARO refractivity.

For this data set, an estimate of the excess phase due to the atmosphere was used in the calculation of the Doppler model for OL tracking as well as the geometric phase. The estimate of excess phase was derived using the 1D ROSAP ray tracing with climatology data. Including the climatology in the Doppler model increases SNR which allows the signal to be tracked to lower altitudes, When only geometric phase is used for the Doppler model, OL profiles extended only to 4 km on average for these flights. The resulting improvement in sampling when climatology was the extension of OL profiles to on average 2 km altitude with some extending below 1 km. One half of the profiles reached below 2 km (table 5.1). The lower altitudes reached by the OL retrievals also represent a large improvement over those of the geodetic receiver data set.

While the OL tracking technique is robust in the tropical environment and will not lose signal lock as a conventional geodetic receiver will, the signal is attenuated through defocusing because of the increased fluctuation in the refractivity gradients of the atmosphere [*Kursinski et al.*, 1997]. Often, the signal to noise ratio (SNR) became too low for a reliable retrieval at heights of 2 – 4 km. This ARO dataset is unique in that independent observations of atmospheric properties are available to begin to look at attribution of multipath. No other spaceborne dataset has such a resource available. The critical parameter is a negative vertical gradient of refractivity, which creates the potential for multipath. By analyzing the gradients observed in dropsondes and SNR fluctuation in the ARO observations, the onset of sharply increasing fluctuations in the vertical refractivity gradient typically coincides with an increased variance in the SNR.

Table 5-1 Minimum heights above the surface for RF16 to RF19 ARO profiles

Mission	Minimum : 0 – 2 km	Minimum: 2 – 4 km	Minimum: 4 – 6 km
RF16	7	1	0
RF17	5	5	0
RF18	7	5	1
RF19	4	8	3
RF16 – RF19	23	19	4

Understanding observation errors is required for future data assimilation. This was investigated using comparisons with refractivity profiles calculated using dropsondes and NWP models. First, however, it is necessary to explain the unique characteristics of the ARO data and how point vertical profiles can be compared to ARO limb sounding measurements. The inverse Abel transform retrieves refractivity as a function of tangent point height assuming spherical symmetry, which is clearly not true in the highly variable environment of developing tropical storms. When assimilating ARO into the WRF model, different options are available to represent the refractivity profile. The ARO sounding could be assimilated as a vertical profile of refractivity as a function of tangent point height at the occultation point. In that case, the tangent point drift is neglected and spherical symmetry is assumed. The sounding can also be assimilated as a slanted profile where the refractivity at each tangent point height is assigned to the tangent point location. This approach accounts for the tangent point drift but still assumes spherical symmetry.

In order to account deviations from spherical symmetry due to horizontal inhomogeneity in refractivity, a nonlocal operator has been implemented for model assimilation of spaceborne radio occultation data which calculates the integrated amount of model refractivity along the ray path centered at the tangent point [*Chen et al.*, 2009;

Ma et al., 2009; *Sokolovskiy et al.*, 2005b; c]. A non-local operator method is also being developed for assimilation of ARO data [*Chen et al.*, 2014a] allowing increments of model integrated refractivity to be distributed along a horizontal ray path to fit the observed refractive delay. Colleagues at UC Davis will test the three methods to assimilate ARO measurements: vertical refractivity profile at the occultation point, a slanted profile of refractivity at each tangent point location, and the full 3D assimilation using a nonlocal operator.

By comparing ARO to dropsondes, we estimate observational errors appropriate for simple assimilation of ARO soundings represented by vertical profiles. This comparison also allows us to investigate any potential biases that may be found beyond the range of variation expected relative to the mean. Through a comparison of ARO to model refractivity at tangent point locations, we can account for the tangent point drift and estimate observation quality (combined model and observation error) that describes errors appropriate for assimilation of tangent point locations. In the limit of a lower resolution ERAI output at more widely separated grid points, the assimilation of ARO at the tangent point locations approaches the full 3D nonlocal operator assimilation. These descriptions of observation errors place an upper bound on the error characteristics to be used in the full 3D nonlocal operator assimilation, with no assumption of spherical symmetry, that will ultimately provide the best use of ARO measurements in near developing tropical storms

The agreement of OL profiles with dropsonde and model output was comparable to geodetic receiver results in the 6 – 14 km height range. The mean difference of OL with dropsondes was less than 0.5 % from 8 – 14 km, increasing to 4 % by 6 km and up

to about 8% at 2 km height. The difference of OL with ERAI reanalysis was similar, less than 0.5% in the 8 – 14 km altitude range and increasing to about 2.5 % by 6 km altitude and up to about 6.5% at 2 km height. A bias was discovered between the rising and setting OL profiles. The mean difference of the setting profiles with ERAI was -1 to -1.5% and the mean difference of the rising profiles with ERAI was +1 to +1.5% over the 8 – 14 km altitude. The bias was not attributed to the retrieval process because a rising/setting bias was also seen in the OL excess Doppler. The source of the bias is still undetermined. Testing the PSR OL tracking has been inconclusive to date and an error in the OL tracking process has not been ruled out. Another possible explanation is a mis-modeling of the estimated Doppler used for constructing the replica signal used in OL tracking and used in the retrieval of bending angle. Navigation and GPS clock data at higher sample rates were adopted into the OL tracking and retrieval analysis to mitigate modeling errors, though the impact of the higher rate data has been inconclusive to date.

A significant negative bias for both rising and setting occultations was discovered for most profiles below 6 km altitude. The bias increased from -3 to -4 % at 6 km altitude to about -10 % at 1 km altitude with respect to dropsondes and ERAI. Most of the bias below 6 km likely results from the limitations of geometric optics retrievals of the bending angle in a very moist tropical environment. A noticeable improvement has been seen in an ARO test case when radio holographic methods recently adapted for ARO were implemented to retrieve refractivity. These results imply that significant improvement is possible that would merit taking the entire ARO open loop data excess phase results through the new retrieval method in future work. While further refinements in ARO the refractivity retrieval will be needed to correct the biases seen in the current

data, it is important to note that the majority of occultations observed during a flight provided reliable OL excess phase results to altitudes near the surface. Therefore, the dense ARO data are available to furnish profiles that are appropriate for assimilation into regional NWP models or for validation studies of model output.

Observation errors from tangent point drift were evaluated through comparison to NWP model output. The ROSAP 1-D ray tracing program was used to estimate the tangent point locations of the ARO data set. The tangent point drift of the ARO was found to be typically 200 to 600 km, sometimes longer and about 400 km on average (table 5.2). Because of the horizontal drift, presenting ARO profiles as point measurements at the tangent points would be a more physically accurate representation. The OL ARO data set was compared to ERAI reanalysis both at the occultation point and along the tangent point locations. The mean difference and standard deviation for both cases was not significantly different. However, the ERAI is not a high resolution model (about 80 km grid spacing) and over the horizontal scale of a typical ARO tangent point drift, 200 – 600 km, the ERAI refractivity does not resolve small scale variations. The mean difference between ERAI profiles following the ARO tangent points and those at ARO occultation points is less than 0.1% with standard deviations differing by 0.15 - 0.8 %. The same comparisons using the WRF model output yielded similar results although the WRF simulation is much higher resolution. The mean difference between WRF profiles following the ARO tangent points and those at ARO occultation points is 0.1 to 0.5 % with standard deviations differing by about 0.2 %. At high altitudes (greater than 8 km), the variation in refractivity is expected to be small because of the homogeneous temperature field and the very small moisture levels and variations at these

altitudes. At lower altitudes, where refractivity variations are primarily due to moisture, greater variation is expected between model refractivity calculated the occultation point vs refractivity calculated at tangent point locations. Differences are expected between comparisons of model output at the occultation point and model output along the tangent point locations when compared to ARO at lower altitudes. The large negative bias of ARO in both profiles may influence the results at lower altitudes and further investigation is needed to assess this possibility.

Table 5-2 The number of occultatios for each flight with tangent point drifts in a given range. The mean tangent point drift for each flight is also given in the final column.

Mission	100 – 200 (km)	200 – 300 (km)	300 – 400 (km)	400 – 500 (km)	500 - 600 (km)	600 – 700 (km)	Mean (km)
RF16	0	2	4	1	0	1	396
RF17	0	2	5	0	2	1	411
RF18	0	2	6	1	4	0	402
RF19	1	4	6	3	1	0	354
RF16 to RF19	1	10	21	5	7	2	387

Atmospheric refractivity is directly related to both moisture and temperature. Moisture is a particularly important thermodynamic field in the study of developing tropical storms. This work quantifies the relative sensitivity of refractivity to temperature and moisture through analysis of dropsonde data and determines that as high as 9 km altitude, refractivity variations are dominated by moisture, a fact not previously appreciated. This is used as justification for using refractivity as a proxy for moisture, in this first order analysis of moisture variations.

The spatial and temporal variability in moisture was examined in the ARO refractivity observations. This provides confidence that ARO is sensitive to important moisture characteristics that were observed during the evolution if the pre-Karl system so that future assimilation of observations made in regions not sampled by dropsondes will be expected to improve the forecasts. For the OL and geodetic receiver data sets it was seen that increases in atmospheric refractivity measured by ARO over the days preceding the genesis of the pre-Karl system was consistent with a general mid-level to 10 km moistening in the vicinity of the National Hurricane Center best track storm location, consistent with dropsonde observations [*Smith and Montgomery*, 2012]. ARO refractivity was also consistently higher in regions of high mid to upper level precipitable water levels obtained in high resolution WRF simulation output. The general consistency of the dense ARO data set with dropsonde moisture observations and model output show the data is sensitive to the large scale moisture variations seen in these products, and merit further impact tests to determine whether they will improve NWP forecasts when assimilated. Given that the ARO data can measure properties far outside a flight track, they are likely to provide complementary information to the model to that provided by dropsonde data sets, which are constrained as point measurements along the flight track.

GPS ARO has proven to be a promising new application of the radio occultation technique. Dense ARO data sets have been obtained in the challenging environments of developing tropical storms which compare within 2% of independent dropsonde data and model output in the mid to upper troposphere. Preliminary results testing radio holographic methods indicate the potential to significantly reduce the large negative biases discovered in the lower troposphere. The ARO data sets are appropriate for

assimilation into NWP and provide a complementary source of data to current dropsonde, radiosonde and satellite observing systems. Surprisingly good results from an isotropic gain standard avionics antenna on the top of the aircraft provide additional indications that the development of a compact ARO system installed on commercial aircraft could lead to the availability of daily sets dense ARO soundings over worldwide locations [*Lesne et al.*, 2002].

REFERENCES

REFERENCES

Acikoz, U. (2011), Open-loop tracking of rising GPS radio occultation signals, Masters thesis, 149 pp, Purdue University, West Lafayette, IN.

Anthes, R. A. (2011a), Exploring Earth's atmosphere with radio occultation: contributions to weather, climate and space weather, *Atmos. Meas. Tech.*, *4*(6), 1077-1103.

Anthes, R. A. (2011b), Exploring Earth's atmosphere with radio occultation: contributions to weather, climate and space weather, *Atmos. Meas. Tech.*, *4*(6), 1077-1103, doi:10.5194/amt-4-1077-2011.

Anthes, R. A., P. A. Bernhardt, Y. Chen, L. Cucurull, K. F. Dymond, D. Ector, S. B. Healy, S. P. Ho, D. C. Hunt, Y. H. Kuo, H. Liu, K. Manning, C. McCormick, T. K. Meehan, W. J. Randel, C. Rocken, W. S. Schreiner, S. V. Sokolovskiy, S. Syndergaard, D. C. Thompson, K. E. Trenberth, T. K. Wee, N. L. Yen, and Z. Zeng (2008), The COSMIC/FORMOSAT-3 Mission: Early results, *Bull. Am. Meteorol. Soc.*, *89*(3), 313-333, doi:10.1175/bams-89-3-313.

Ao, C. O., T. K. Meehan, G. A. Hajj, A. J. Mannucci, and G. Beyerle (2003), Lower troposphere refractivity bias in GPS occultation retrievals, *J. Geophys. Res.: Atmos.*, *108*(D18).

Asgarimehr, M., and M. Hossainali (2015), GPS radio occultation constellation design with the optimal performance in Asia Pacific region, *J. Geodesy*, *89*(6), 519-536, doi:10.1007/s00190-015-0795-3.

Barker, D. M., W. Huang, Y. R. Guo, A. J. Bourgeois, and Q. N. Xiao (2004), A Three-Dimensional Variational Data Assimilation System for MM5: Implementation and Initial Results, *Mon. Weather Rev.*, *132*(4), 897-914, doi:10.1175/1520-0493(2004)132<0897:ATVDAS>2.0.CO

Beutler, G., A. Moore, and I. Mueller (2009), The international global navigation satellite systems service (IGS): development and achievements, *J. Geodesy*, *83*(3-4), 297-307, doi:10.1007/s00190-008-0268-z.

Beutler, G., M. Rothacher, S. Schaer, T. A. Springer, J. Kouba, and R. E. Neilan (1999), The International GPS Service (IGS): An interdisciplinary service in support of Earth sciences, *Adv. Space Res.*, *23*(4), 631-653, doi:http://dx.doi.org/10.1016/S0273-1177(99)00160-X.

Bevis, M., S. Businger, S. Chiswell, T. A. Herring, R. A. Anthes, C. Rocken, and R. H. Ware (1994), GPS meteorology: mapping zenith wet delays onto precipitable water, *J. Appl. Meteorol.*, *33*(3), 379-386.

Beyerle, G., T. Schmidt, J. Wickert, S. Heise, M. Rothacher, G. Konig-Langlo, and K. B. Lauritsen (2006), Observations and simulations of receiver-induced refractivity biases in GPS radio occultation, *J. Geophys. Res.: Atmos.*, *111*(D12).

Biondi, R., S.-P. Ho, W. Randel, S. Syndergaard, and T. Neubert (2013), Tropical cyclone cloud-top height and vertical temperature structure detection using GPS radio occultation measurements, *J. Geophys. Res.: Atmos*, *118*(11), 5247-5259, doi:10.1002/jgrd.50448.

Biondi, R., T. Neubert, S. Syndergaard, and J. K. Nielsen (2011), Radio occultation bending angle anomalies during tropical cyclones, *Atmos. Meas. Tech.*, *4*(6), 1053-1060, doi:10.5194/amt-4-1053-2011.

Born, M., and E. Wolf (1999), *Principles of optics: electromagnetic theory of propagation, interference and diffraction of light*, 7th (expanded) ed., xxxiii, 952 p. pp., Cambridge University Press, Cambridge England ; New York.

Braun, S. A., R. Kakar, E. Zipser, G. Heymsfield, C. Albers, S. Brown, S. L. Durden, S. Guimond, J. Halverson, A. Heymsfield, S. Ismail, B. Lambrigtsen, T. Miller, S. Tanelli, J. Thomas, and J. Zawislak (2013), NASA's Genesis and Rapid Intensification Processes (GRIP) Field Experiment, *Bull. Am. Meteorol. Soc.*, *March*, 345-363.

Chen, S.-Y., C.-Y. Huang, Y.-H. Kuo, Y.-R. Guo, and S. Sokolovskiy (2009), Assimilation of GPS refractivity from FORMOSAT-3/COSMIC using a nonlocal operator with WR 3DVAR and its impact on the prediction of a typhoon event, *Terr. Atmos. Ocean Sci.*, *20*, 133-154.

Chen, S. Y., C. Y. Huang, Y. H. Kuo, and S. Sokolovskiy (2011), Observational error estimation of FORMOSAT-3/COSMIC GPS radio occultation data, *Mon. Weather Rev.*, *139*(3), 853-865.

Chen, X.-M., S.-H. Chen, J. S. Haase, S.-Y. Chen, and C. Y. Huang (2014a), Airborne Radio Occultation: a Set of Observing System Simulation Experiments (OSSE), in *Eigth FORMOSAT-3/COSMIC Data Users' Workshop*, edited, Boulder, CO.

Chen, X. M., S.-H. Chen, S.-Y. Chen, and C. Y. Huang (2014b), Assimilation of Non-Local Radio Occultation Measurements and its Impact on WRF Model Prediction of Hurricane Earl in 2010, in *31st Conference on Hurricanes and Tropical Meteorology*, edited, San Diego, CA.

Chou, M. D., and M. J. Suarez (1999), A Solar Radiation Parameterization for Atmospheric Studies*Rep. NASA/TM-1999-104606*, 51 pp, Goddard Space Flight Center, Greenbelt, Maryland.

Cleveland, W. S. (1979), Robust Locally Weighted Regression and Smoothing Sactterplots, *J. Am. Stat. Assoc.*, *74*(368).

Cucurull, L., J. C. Derber, R. Treadon, and R. J. Purser (2008), Preliminary impact studies using global positioning system radio occultation profiles at NCEP, *Mon. Weather Rev.*, *136*, 1865-1877.

Davis, C. A., and D. A. Ahijevych (2012), Mesoscale structural evolution of three tropical weather systems observed during PREDICT, *J. Atmos. Sci.*, *69*(4), 1284-1305, doi:10.1175/jas-d-11-0225.1.

Davis, C. A., and D. A. Ahijevych (2013), Thermodynamic Environments of Deep Convection in Atlantic Tropical Disturbances, *J. Atmos. Sci.*, *70*(7), 1912-1928, doi:10.1175/JAS-D-12-0278.1.

Davis, C. A., D. A. Ahijevych, J. A. Haggerty, and M. J. Mahoney (2014), Observations of temperature in the upper troposphere and lower stratosphere of tropical weather disturbances, *J. Atmos. Sci.*, *71*(5), 1593-1608, doi:Doi 10.1175/Jas-D-13-0278.1.

Dee, D. P., S. M. Uppala, A. J. Simmons, P. Berrisford, P. Poli, S. Kobayashi, U. Andrae, M. A. Balmaseda, G. Balsamo, P. Bauer, P. Bechtold, A. C. M. Beljaars, L. van de Berg, J. Bidlot, N. Bormann, C. Delsol, R. Dragani, M. Fuentes, A. J. Geer, L. Haimberger, S. B. Healy, H. Hersbach, E. V. Holm, L. Isaksen, P. Kallberg, M. Kohler, M. Matricardi, A. P. McNally, B. M. Monge-Sanz, J. J. Morcrette, B. K. Park, C. Peubey, P. de Rosnay, C. Tavolato, J. N. Thepaut, and F. Vitart (2011), The ERA-Interim reanalysis: configuration and performance of the data assimilation system, *Q. J. Roy. Meteorol. Soc.*, *137*(656), 553-597, doi:10.1002/qj.828.

Dunkerton, T. J., M. T. Montgomery, and Z. Wang (2009), Tropical cyclogenesis in a tropical wave critical layer: Easterly waves, *Atmos. Chem. Phys.*, *9*(15), 5587-5646.

Durre, I., T. Reale, D. Carlson, J. Christy, M. Uddstrom, M. Gelman, and P. Thorne (2005), Improving the usefulness of operational radiosonde data, *Bull. Am. Meteorol. Soc.*, *86*(3), 411-416, doi:10.1175/BAMS-86-3-411.

Durre, I., R. S. Vose, and D. B. Wuertz (2006), Overview of the Integrated Global Radiosonde Archive, *J. Clim.*, *19*(1), 53-68, doi:10.1175/JCLI3594.1.

Evans, C., H. R. M. Archambault, J. M. Cordeira, C. Fritz, T. J. Galarneau, S. Gjorgjievska, K. S. Griffin, A. Johnson, W. A. Komaromi, S. Monette, P. Muradyan, B. Murphy, M. Riemer, J. Sears, D. Stern, B. Tang, and S. Thompson (2012), The PRE-Depression Investigation of Cloud-Systems in the Tropics (PREDICT) field campaign Perspectives of early career scientists, *Bull. Am. Meteorol. Soc.*, *93*(2), 173-187.

Fjeldbo, G., A. J. Kliore, and V. R. Eshleman (1971), The neutral atmosphere of Venus as studied with the Mariner V radio occultation experiments, *Astron. J.*, *76*(2), 123-140.

Folmer, M. J., M. DeMaria, R. Ferraro, J. Beven, M. Brennan, J. Daniels, R. Kuligowski, H. Meng, S. Rudlosky, L. Zhao, J. Knaff, S. Kusselson, S. D. Miller, T. J. Schmit, C. Velden, and B. Zavodsky (2015), Satellite Tools to Monitor and Predict Hurricane Sandy (2012): Current And Emerging Products, *Atmos. Res.*(0), doi:http://dx.doi.org/10.1016/j.atmosres.2015.06.005.

Frank, W. M., and P. E. Roundy (2006), The role of tropical waves in tropical cyclogenesis, *Mon. Weather Rev.*, *134*(9), 2397-2417, doi:10.1175/mwr3204.1.

Franklin, J. L., M. L. Black, and K. Valde (2003), GPS Dropwindsonde Wind Profiles in Hurricanes and Their Operational Implications, *Weather and Forecasting*, *18*(1), 32-44, doi:10.1175/1520-0434(2003)018<0032:GDWPIH>2.0.CO;2.

Fritz, C., and Z. Wang (2013), A numerical study of the impacts of dry air on tropical cyclone formation: A development case and a nondevelopment case, *J. Atmos. Sci.*, *70*(1), 91-111, doi:Doi 10.1175/Jas-D-12-018.1.

Garrison, J. L., M. Walker, J. S. Haase, T. Lulich, F. Xie, B. D. Ventre, M. H. Boehme, B. Wilmhoff, and S. J. Katzberg (2007), Development and testing of the GISMOS instrument, paper presented at IEEE International Geoscience and Remote Sensing Symposium, Barcelona, Spain, 23-27 July 2007.

Gold, R. (1967), Optimal binary sequences for spread spectrum multiplexing (Corresp.), *Information Theory, IEEE Transactions on*, *13*(4), 619-621, doi:10.1109/TIT.1967.1054048.

Gorbunov, M. (2002), Canonical transform method for processing radio occultation data in the lower troposphere *Radio Sci.*, *37*(5), 1076, doi:1010.10292000RS10002592.

Gorbunov, M. E., H. H. Benzon, A. S. Jensen, M. S. Lohmann, and A. S. Nielsen (2004), Comparative analysis of radio occultation processing approaches based on Fourier integral operators, *Radio Sci.*, *39*(6).

Gorbunov, M. E., and K. B. Lauritsen (2004), Canonical transform methods for radio occultation data, in *Occultations for Probing Atmosphere and Climate*, edited by G. Kirchengast, U. Foelsche and A. Steiner, pp. 61-68, Springer Berlin Heidelberg, doi:10.1007/978-3-662-09041-1_6.

Govekar, P. D., C. Jakob, M. J. Reeder, and J. Haynes (2011), The three-dimensional distribution of clouds around Southern Hemisphere extratropical cyclones, *Geophys. Res. Lett.*, *38*(21), L21805, doi:10.1029/2011GL049091.

Haase, J. S., B. Murphy, X.-M. Chen, S.-H. Chen, P. Muradyan, F. G. Nievinski, K. M. Larson, J. L. Garrison, K.-N. Wang, and S.-Y. Chen (2012), Preliminary results from the retrieval and assimilation of GPS radio occultation refractivity observations during tropical storm development, paper presented at American Geophysical Union, San Francisco, CA, 3-7 Dec 2012.

Haase, J. S., B. J. Murphy, P. Muradyan, F. Nievinski, K. M. Larson, J. L. Garrison, and K.-N. Wang (2014), First results from an airborne GPS radio occultation system for atmospheric profiling, *Geophys. Res. Lett.*, *40*, doi:10.1002/2013GL058681.

Hajj, G. A., C. O. Ao, B. A. Iijima, D. Kuang, E. R. Kursinski, A. J. Mannucci, T. K. Meehan, L. J. Romans, M. D. Juarez, and T. P. Yunck (2004), CHAMP and SAC-C atmospheric occultation results and intercomparisons, *J. Geophys. Res.: Atmos.*, *109*(D6), doi:D06109, doi:10.1029/2003JD003909.

Hajj, G. A., E. R. Kursinski, L. J. Romans, W. I. Bertiger, and S. S. Leroy (2002), A technical description of atmospheric sounding by GPS occultation, *J. Atmos. Sol. Terr. Phys.*, *64*(4), 451-469.

Healy, S. B. (2011), Refractivity coefficients used in the assimilation of GPS radio occultation measurements, *J. Geophys. Res.*, *116*(D1), D01106.

Healy, S. B., and J. R. Eyre (2000), Retrieving temperature, water vapour and surface pressure information from refractive-index profiles derived by radio occultation: A simulation study, *Q. J. R. Meteorol. Soc.*, *126*, 1661-1683.

Healy, S. B., J. S. Haase, and O. Lesne (2002), Abel transform inversion of radio occultation measurements made with a receiver inside the Earth's atmosphere, *Ann. Geophys.*, *20*(8), 1253-1256.

Heckler, G., and J. L. Garrison (2004), Architecture of a Reconfigurable Software Receiver, paper presented at 17th International Technical Meeting of the Satellite Division of the Institute of Navigation(ION GNSS 2004), Institute of Navigation, Long Beach Convention Center, Long Beach, CA, September 21-24.

Ho, S.-p., X. Yue, Z. Zeng, C. O. Ao, C.-Y. Huang, E. R. Kursinski, and Y.-H. Kuo (2013), Applications of COSMIC Radio Occultation Data from the Troposphere to Ionosphere and Potential Impacts of COSMIC-2 Data, *Bull. Am. Meteorol. Soc.*, *95*(1), ES18-ES22, doi:10.1175/BAMS-D-13-00035.1.

Hoeg, P., A. Hauchecorne, G. Kirchengast, S. Syndergaard, B. Belloul, R. Leitinger, and W. Rothleitner (1996), Derivation of Atmospheric Properties using a Radio Occultation Technique, *ESA Contract Report (ESTEC/C. No. 11024/94/NL/CN) Rep. DMI Scientific Report 95-4*, 208 pp, Danish Met. Institute, Copenhagen, Denmark.

Hofmann-Wellenhof, B., and H. Moritz (2006), *Physical Geodesy*, 403 pp., Springer, New York.

Hong, S. Y., Y. Noh, and J. Dudhia (2006), A new vertical diffusion package with explicit treatment of entrainment processes, *Mon. Weather Rev.*, *134*, 2318-2341, doi:10.1175/MWR3199.1.

Houze, R. A., W.-C. Lee, and M. M. Bell (2009), Convective contribution to the genesis of hurricane Ophelia (2005), *Mon. Weather Rev.*, *137*(9), 2778-2800, doi:10.1175/2009MWR2727.1.

Huang, C.-Y., Y.-H. Kuo, S.-Y. Chen, M.-T. Kueh, P.-L. Lin, C.-T. Terng, F.-C. Chien, M.-J. Yang, S.-C. Lin, K.-Y. Wang, S.-H. Chen, C.-J. Wang, and A. S. K. A. V. Prasad Rao (2008), Impact of GPS radio occultation measurements on severe weather prediction in Asia., paper presented at GRAS SAF Workshop on Applications of GPSRO measurements, 16-18 June 2008.

Huang, C. Y., Y. H. Kuo, S. Y. Chen, C. T. Terng, F. C. Chien, P. L. Lin, M. T. Kueh, S. H. Chen, M. J. Yang, C. J. Wang, and A. S. K. A. V. P. Rao (2010), Impact of GPS radio occultation data assimilation on regional weather predictions, *Gps Solutions*, *14*(1), 35-49.

Huang, G., Q. Zhang, H. Li, and W. Fu (2013), Quality variation of GPS satellite clocks on-orbit using IGS clock products, *Adv. Space Res.*, *51*(6), 978-987, doi:http://dx.doi.org/10.1016/j.asr.2012.09.041.

Jensen, A. S., H. H. Benzon, A. S. Nielsen, and M. S. Lohmann (2006), Processing radio occultation data by full spectrum inversion techniques: An overview and recent developments, in *Atmosphere and Climate*, edited by U. Foelsche, G. Kirchengast and A. Steiner, pp. 95-112, Springer Berlin Heidelberg, doi:10.1007/3-540-34121-8_9.

Jensen, A. S., M. S. Lohmann, H. H. Benzon, and A. S. Nielsen (2003), Full spectrum inversion of radio occultation signals, *Radio Sci.*, *38*(3).

Jensen, A. S., M. S. Lohmann, A. S. Nielsen, and H. H. Benzon (2004), Geometrical optics phase matching of radio occultation signals, *Radio Sci.*, *39*(3), doi: 10.1029/2003rs002899.

Jiménez, P. A., J. Dudhia, J. F. González-Rouco, J. Navarro, J. P. Montávez, and E. García-Bustamante (2011), A Revised Scheme for the WRF Surface Layer Formulation, *Mon. Weather Rev.*, *140*(3), 898-918, doi:10.1175/MWR-D-11-00056.1.

Jin, S. (2013), *GNSS remote sensing: theory, methods and applications*, 276 pp., Springer, Dordrecht, Netherlands.

Kain, J. S. (2004), The Kain-Fritsch convective parameterization: An update, *J. Appl. Meteorol.*, *43*, 170-181, doi:10.1175/1520-0450(2004)043<0170:TKCPAU>2.0.CO;2.

Kidder, S. Q., M. D. Goldberg, R. M. Zehr, M. DeMaria, J. F. W. Purdom, C. S. Velden, N. C. Grody, and S. J. Kusselson (2000), Satellite analysis of tropical cyclones using the Advanced Microwave Sounding Unit (AMSU), *Bull. Am. Meteorol. Soc.*, *81*(6), 1241-1259, doi:10.1175/1520-0477(2000)081.

Kirchengast, G., J. Hafner, and W. Poetzi (1999), The CIRA86aQ_UoG model: An extension of the CIRA-86 monthly tables including humidity tables and a Fortran95 global moist air climatology model, *ESA Technical Report No.8/1999, ESA Contract no. 13327/98/NL/GD Rep. ESA Technical Report No.8/1999, ESA Contract no. 13327/98/NL/GD*, 18 pp, IGAM, University of Graz, Graz, Austria.

Komaromi, W. A. (2013), An investigation of composite dropsonde profiles for developing and nondeveloping tropical waves during the 2010 PREDICT field campaign, *J. Atmos. Sci.*, *70*(2), 542-558.

Kueh, M.-T., C.-Y. Huang, S.-Y. Chen, S.-H. Chen, and C.-J. Wang (2009), Impact of GPS radio occultation refractivity soundings on a simulation of Typhoon Bilis (2006) upon landfall, *Terr. Atmos. Ocean Sci.*, *20*(1), 115-131.

Kunii, M., H. Seko, M. Ueno, Y. Shoji, and T. Tsuda (2012), Impact of Assimilation of GPS Radio Occultation Refractivity on the Forecast of Typhoon Usagi in 2007, *Journal of the Meteorological Society of Japan. Ser. II*, *90*(2), 255-273, doi:10.2151/jmsj.2012-207.

Kuo, Y. H., W. S. Schreiner, J. Wang, D. L. Rossiter, and Y. Zhang (2005), Comparison of GPS radio occultation soundings with radiosondes, *Geophys. Res. Lett.*, *32*(5).

Kuo, Y. H., T. K. Wee, S. Sokolovskiy, C. Rocken, W. Schreiner, D. Hunt, and R. A. Anthes (2004), Inversion and error estimation of GPS radio occultation data, *J. Meteorol. Soc. Jpn.*, *82*(1B), 507-531.

Kursinski, E. R., G. A. Hajj, K. R. Hardy, J. T. Schofield, and R. Linfield (1997), Observing Earth's atmosphere with radio occultation measurements, *J. Geoph. Res.*, *102*(23), 23.429 - 423.465.

Landsea, C. W. (1993), A climatology of intense (or major) Atlantic hurricanes, *Mon. Weather Rev.*, *121*, 1703-1713.

Lesne, O., J. S. Haase, G. Kirchengast, J. Ramsauer, and W. Poetzi (2002), Sensitivity analysis of GNSS radio occultation for airborne sounding of the troposphere, *Phys. and Chem. of the Earth*, *27*(4-5), 291-299.

Liu, H. (2009), Initialization of the environment of tropical cyclogenesis by assimilating radio occultation refractivity with an ensemble filter, paper presented at 4th FORMOSAT-3/COSMIC Data Users Workshop, Boulder, CO, 27-29 October 2009.

Liu, H., J. Anderson, Y.-H. Kuo, C. Snyder, and A. Caya (2008), Evaluation of a nonlocal quasi-phase observation operator in assimilation of CHAMP radio occultation refractivity with WRF, *Mon. Weather Rev.*, *136*(1), 242-256, doi:10.1175/2007MWR2042.1.

Liu, H., J. Anderson, and Y. H. Kuo (2012), Improved analyses and forecasts of hurricane Ernesto's genesis using radio occultation data in an ensemble filter assimilation system, *Mon. Weather Rev.*, *140*(1), 151-166.

Lulich, T. (2010), Open loop tracking of radio occultation signals from an airborne platform, 216 pp, Purdue University, West Lafayette, IN.

Lulich, T. D., J. L. Garrison, J. S. Haase, Y.-M. Yang, J. Voo, F. Xie, and P. Muradyan (2010), Open loop tracking of radio occultation signals from an airborne platform, paper presented at Proceedings of the 23rd International Technical Meeting of the Satellite Division of the Institute of Navigation (ION GNSS 2010), Portland, Oregon, September 21-24, 2010.

Ma, Z., Y.-H. Kuo, B. Wang, W.-S. Wu, and S. Sokolovskiy (2009), Comparison of local and nonlocal observation operators for the assimilation of GPS RO data with the NCEP GSI system: An OSSE study, *Mon. Weather Rev.*, *137*(10), 3575-3587, doi:10.1175/2009MWR2809.1.

Mannucci, A. J., C. O. Ao, L. E. Young, and T. K. Meehan (2014), Studying the Atmosphere Using Global Navigation Satellites, *Eos, Transactions American Geophysical Union*, *95*(43), 389-391, doi:10.1002/2014EO430001.

McNally, T., M. Bonavita, and J.-N. Thépaut (2013), The Role of Satellite Data in the Forecasting of Hurricane Sandy, *Mon. Weather Rev.*, *142*(2), 634-646, doi:10.1175/MWR-D-13-00170.1.

Melbourne, W. G. (2005), *Radio occultations using earth satellites: a wave theory treatment*, xxiv, 647 p. pp., Wiley-Interscience, Hoboken, N.J.

Merrill, R. T. (1991), Physical retrieval of typhoon structure using passive microwave observations, in *Preprints, 19th Conf. on Hurricanes and tropical meteorology*, edited, pp. 405 - 408, American Meteorology Society, Miami, Fl.

Misra, P., and P. Enge (2006), *Global positioning system: signals, measurements, and performance*, 2nd ed., 569 p. pp., Ganga-Jamuna Press, Lincoln, Mass.

Montgomery, M. T., C. Davis, T. J. Dunkerton, Z. Wang, C. Velden, R. Torn, S. Majumdar, F. Zhang, R. K. Smith, L. Bosart, M. M. Bell, J. S. Haase, A. Heymsfield, J. Jensen, T. Campos, and M. A. Boothe (2012), The PRE-Depression Investigation of Cloud systems in the Tropics (PREDICT) experiment: Scientific basis, new analysis tools and some first results, *Bull. Am. Meteorol. Soc.*, *92*(9), 153-172, doi:10.1175/BAMS-D-11-00046.1.

Montgomery, M. T., M. E. Nicholls, T. A. Cram, and A. B. Saunders (2006), A Vortical Hot Tower Route to Tropical Cyclogenesis, *J. Atmos. Sci.*, *63*(1), 355-386, doi:10.1175/JAS3604.1.

Moradi, I., B. Soden, R. Ferraro, P. Arkin, and H. Vömel (2013), Assessing the quality of humidity measurements from global operational radiosonde sensors, *J. Geophys. Res.: Atmos*, *118*(14), 8040-8053, doi:10.1002/jgrd.50589.

Morrison, H., G. Thompson, and V. Tatarskii (2009), Impact of Cloud Microphysics on the Development of Trailing Stratiform Precipitation in a Simulated Squall Line: Comparison of One- and Two-Moment Schemes, *Mon. Weather Rev.*, *137*(3), 991-1007, doi:10.1175/2008MWR2556.1.

Mostafa, M., J. Hutton, and B. Reid (2001), GPS/IMU products- the Applanix approach, paper presented at Photogrammetric Week, University of Stuttgart, Institute for Photgrammetry, Stuttgart, 24-28 September 2001.

Mueller, K. J., M. DeMaria, J. Knaff, J. P. Kossin, and T. H. Vonder Haar (2006), Objective Estimation of Tropical Cyclone Wind Structure from Infrared Satellite Data, *Weather and Forecasting*, *21*(6), 990-1005, doi:10.1175/WAF955.1.

Muradyan, P. (2009), GPS/INS navigation precision and its effect on airborne radio occultation, MS thesis, 93 pp, Purdue University, West Lafayette, IN, USA.

Muradyan, P. (2012), Profiling the atmosphere with the airborne GPS radio occultation technique using open-loop tracking, PhD thesis, 196 pp, Purdue University, West Lafayette, IN, U.S.A.

Muradyan, P., J. S. Haase, F. Xie, J. L. Garrison, T. Lulich, and J. Voo (2010), GPS/INS navigation precision and its effect on airborne radio occultation retrieval accuracy, *GPS Solutions*, *10.1007/s10291-010-0183-7*.

Murphy, B. J., J. S. Haase, P. Muradyan, J. L. Garrison, and K. N. Wang (2015), Airborne GPS radio occultation refractivity profiles observed in tropical storm environments, *J. Geophys. Res.: Atmos*, *120*(5), 2014JD022931, doi:10.1002/2014JD022931.

Niu, G.-Y., Z.-L. Yang, K. E. Mitchell, F. Chen, M. B. Ek, M. Barlage, A. Kumar, K. Manning, D. Niyogi, E. Rosero, M. Tewari, and Y. Xia (2011), The community Noah land surface model with multiparameterization options (Noah-MP): 1. Model description and evaluation with local-scale measurements, *J. Geophys. Res.: Atmos*, *116*(D12), D12109, doi:10.1029/2010JD015139.

Nolan, D. S. (2007), What is the trigger for tropical cyclogenesis?, *Aust. Meteorol. Mag.*, *56*(4), 241-266.

Pavlis, N. K., S. A. Holmes, S. C. Kenyon, and J. K. Factor (2012), The development and evaluation of the Earth Gravitational Model 2008 (EGM2008), *J. Geophys. Res.: Solid Earth*, *117*(B4), B04406, doi:10.1029/2011JB008916.

Poli, P., S. B. Healy, and D. P. Dee (2010), Assimilation of global positioning system radio occultation data in the ECMWF ERA-Interim reanalysis, *Q. J. Roy. Meteorol. Soc.*, *136*(653), 1972-1990, doi:10.1002/qj.722.

Poli, P., S. B. Healy, F. Rabier, and J. Pailleux (2008), Preliminary assessment of the scalability of GPS radio occultations impact in numerical weather prediction, *Geophys. Res. Lett.*, *35*(23), L23811, doi:10.1029/2008gl035873.

Reale, T., B. Sun, F. H. Tilley, and M. Pettey (2012), The NOAA Products Validation System (NPROVS), *J. Atmos. Oceanic Technol.*, *29*(5), 629-645, doi:10.1175/JTECH-D-11-00072.1.

Rocken, C., R. Anthes, M. Exner, D. Hunt, S. Sokolovskiy, R. Ware, M. Gorbunov, W. Schreiner, D. Feng, B. Herman, Y.-H. Kuo, and X. Zou (1997), Analysis and validation of GPS/MET data in the neutral atmosphere, *J. Geophys. Res.*, *102*, 29849-29866.

Rodgers, C. D. (1976), Retrieval of atmospheric temperature and composition from remote measurements of thermal radiation, *Rev. of Geophys. and Space Phys.*, *14*(4), 609-624.

Schafer, R. W. (2011), What Is a Savitzky-Golay Filter?, *IEEE Signal Process Mag.*, *28*(4), 111-117.

Schreiner, W., C. Rocken, S. Sokolovskiy, S. Syndergaard, and D. Hunt (2007), Estimates of the precision of GPS radio occultations from the COSMIC/FORMOSAT-3 mission, *Geophys. Res. Lett.*, *34*(4).

Skamarock, W. C., J. Klemp, J. Dudhia, D. Gill, D. Barker, M. Duda, X. Huang, W. Wang, and J. G. Powers (2008), A description of the Advanced Research WRF Version 3, *NCAR Technical Note*.

Smith, E. K., and S. Weintraub (1953), The constants in the equation for atmospheric refractive index at radio frequencies, *Proc. IRE*, *41*(8), 1035-1037.

Smith, R. K., and M. T. Montgomery (2012), Observations of the convective environment in developing and non-developing tropical disturbances, *Q. J. Roy. Meteorol. Soc.*, *138*(668), 1721-1739.

Sokolovskiy, S. (2001), Tracking tropospheric radio occultation signals from low Earth orbit, *Radio Sci.*, *36*(3), 483-498.

Sokolovskiy, S., Y.-H. Kuo, and W. Wang (2005a), Assessing the accuracy of a linearized observation operator for assimilation of radio occultation data: case simulations with a high-resolution weather model, *Mon. Weather Rev.*, *133*(8), 2200-2212, doi:10.1175/MWR2948.1.

Sokolovskiy, S., Y. H. Kuo, and W. Wang (2005b), Assessing the accuracy of a linearized observation operator for assimilation of radio occultation data: Case simulations with a high-resolution weather model, *Mon. Weather Rev.*, *133*(8), 2200-2212.

Sokolovskiy, S., Y. H. Kuo, and W. Wang (2005c), Evaluation of a linear phase observation operator with CHAMP radio occultation data and high-resolution regional analysis, *Mon. Weather Rev.*, *133*(10), 3053-3059.

Stauffer, D. R., and N. L. Seaman (1990), Use of Four-Dimensional Data Assimilation in a Limited-Area Mesoscale Model. Part I: Experiments with Synoptic-Scale Data, *Mon. Weather Rev.*, *118*(6), 1250-1277, doi:10.1175/1520-0493(1990)118<1250:UOFDDA>2.0.CO;2.

Sun, B., A. Reale, S. Schroeder, D. J. Seidel, and B. Ballish (2013), Toward improved corrections for radiation-induced biases in radiosonde temperature observations, *J. Geophys. Res.: Atmos*, *118*(10), 4231-4243, doi:10.1002/jgrd.50369.

Sun, B. M., A. Reale, D. J. Seidel, and D. C. Hunt (2010), Comparing radiosonde and COSMIC atmospheric profile data to quantify differences among radiosonde types and the effects of imperfect collocation on comparison statistics, *J. Geophys. Res.: Atmos.*, *115*.

Syndergaard, S. (1998), Modeling the impact of the Earth's oblateness on the retrieval of temperature and pressure profiles from limb sounding, *J. Atmos. and Solar-Terrestrial Phys.*, *60*(2), 171-180.

Syndergaard, S. (1999), Retrieval Analysis and methodologies in Atmospheric Limb Using the GNSS Radio Occultation Technique*Rep. 6*, Danish Meteorological Institute, Copenhagen, Denmark.

Tory, K. J., and W. M. Frank (2010), Tropical cyclone formation, *Global Perspectives on Tropical Cyclones: From Science to Mitigation*, *4*, 55.

Tsuda, T., X. Lin, H. Hayashi, and Noersomadi (2011), Analysis of vertical wave number spectrum of atmospheric gravity waves in the stratosphere using COSMIC GPS radio occultation data, *Atmos. Meas. Tech.*, *4*(8), 1627-1636, doi:DOI 10.5194/amt-4-1627-2011.

Ventre, B. D. (2006), Open-loop Tracking of an Occulting GNSS Signal, 227 pp, Purdue University, West Lafayette, IN.

Vergados, P., Z. J. Luo, K. Emanuel, and A. J. Mannucci (2014), Observational tests of hurricane intensity estimations using GPS radio occultations, *J. Geophys. Res.: Atmos*, *119*(4), 2013JD020934, doi:10.1002/2013JD020934.

Vergados, P., A. J. Mannucci, and H. Su (2013), A validation study for GPS radio occultation data with moist thermodynamic structure of tropical cyclones, *J. Geophys. Res.: Atmos*, *118*(16), 9401-9413, doi:10.1002/jgrd.50698.

von Engeln, A., Y. Andres, C. Marquardt, and F. Sancho (2011), GRAS radio occultation on-board of Metop, *Adv. Space Res.*, *47*(2), 336-347.

Voo, J. K., J. L. Garrison, J. S. Haase, and T. D. Lulich (2009), Recent experiments in ocean remote sensing with bistatic radar using global navigation satellite signals, in *2009 IEEE Radar Conference*, edited, p. 5, Pasadena, CA, doi:10.1109/RADAR.2009.4977115.

Vorob'ev, V. V., and T. G. Krasil'nikova (1994), Estimation of the accuracy of the atmospheric refractive index recovery from Doppler shift measurements at frequencies used in the NAVSTAR system, *Phys. Atmos. Ocean (English Translation)*, *29*(5), 602-609.

Wang, J. H. (2005), Evaluation of the dropsonde humidity sensor using data from DYCOMS-II and IHOP_2002, *J. Atmos. Oceanic Technol.*, *22*(3), 247-257, doi:Doi 10.1175/Jtech1698.1.

Wang, J. H., J. C. Bian, W. O. Brown, H. Cole, V. Grubisic, and K. Young (2009a), Vertical Air Motion from T-REX Radiosonde and Dropsonde Data, *J. Atmos. Oceanic Technol.*, *26*(5), 928-942, doi:10.1175/2008jtecha1240.1.

Wang, K.-N., J. L. Garrison, U. Acikoz, J. S. Haase, B. Murphy, P. Muradyan, T. Lulich, and B. Ventre (2015a), Open Loop Tracking of rising and setting GNSS radio-occultation signals from an airborne platform: signal model and error analysis, *Trans. IEEE Geosci. and Remote Sens. (submitted)*.

Wang, K. N., J. L. Garrison, J. Haase, B. Murphy, and C. O. Ao (2015b), Implementation of the phase matching(pm) method for the GPS airborne radio occultation (ARO) system, in *IGARSS 2015*, edited, IEEE, Milan, Italy.

Wang, Z. (2012), Thermodynamic aspects of tropical cyclone formation, *J. Atmos. Sci.*, *69*(8), 2433-2451, doi:10.1175/jas-d-11-0298.1.

Wang, Z., M. T. Montgomery, and T. J. Dunkerton (2009b), A dynamically-based method for forecasting tropical cyclogenesis location in the Atlantic sector using global model products, *Geophys. Res. Lett.*, *36*(3), L03801, doi:10.1029/2008GL035586.

Ware, R., M. Exner, D. Feng, M. Gorbunov, K. R. Hardy, B. M. Herman, Y. Kuo, T. K. Meehan, W. G. Melbourne, C. Rocken, W. Schreiner, S. Sokolovskiy, F. Solheim, X. Zou, A. Anthes, S. Businger, and K. Trenberth (1996), GPS Sounding of the atmosphere from low Earth orbit: preliminary results, *Bull. Am. Meteor. Soc.*, *77*(1), 19-40.

Weng, F., T. Zhu, and B. Yan (2007), Satellite Data Assimilation in Numerical Weather Prediction Models. Part II: Uses of Rain-Affected Radiances from Microwave Observations for Hurricane Vortex Analysis, *J. Atmos. Sci.*, *64*(11), 3910-3925, doi:10.1175/2006JAS2051.1.

Wickert, J., G. Michalak, T. Schmidt, G. Beyerle, C. Z. Cheng, S. B. Healy, S. Heise, C. Y. Huang, N. Jakowski, W. Kohler, C. Mayer, D. Offiler, E. Ozawa, A. G. Pavelyev, M. Rothacher, B. Tapley, and C. Arras (2009), GPS radio occultation: Results from CHAMP, GRACE and FORMOSAT-3/COSMIC, *Terr. Atmos. Ocean Sci.*, *20*(1), 35-50.

Wickert, J., C. Reigber, G. Beyerle, R. Konig, C. Marquardt, T. Schmidt, L. Grunwaldt, R. Galas, T. K. Meehan, W. G. Melbourne, and K. Hocke (2001), Atmosphere sounding by GPS radio occultation: First results from CHAMP, *Geophys. Res. Let*, *28*(17), 3263-3266.

Wickert, J., T. Schmidt, G. Beyerle, R. Konig, and C. Reigber (2004), The radio occultation experiment aboard CHAMP: Operational data analysis and validation of vertical atmospheric profiles, *J. Meteorol. Soc. Jpn.*, *82*(1B), 381-395.

Xie, F., J. S. Haase, and S. Syndergaard (2008), Profiling the Atmosphere Using the Airborne GPS Radio Occultation Technique: A Sensitivity Study, *Trans. IEEE Geosci. and Remote Sens.*, *46*(11), 3424-3435.

Xu, X., J. Luo, and C. Shi (2009), Comparison of COSMIC radio occultation refractivity profiles with radiosonde measurements, *Adv. Atmos. Sci.*, *26*(6), 1137-1145, doi:10.1007/s00376-009-8066-y.

Yue, X., W. S. Schreiner, N. Pedatella, R. A. Anthes, A. J. Mannucci, P. R. Straus, and J.-Y. Liu (2014), Space Weather Observations by GNSS Radio Occultation: From FORMOSAT-3/COSMIC to FORMOSAT-7/COSMIC-2, *Space Weather*, *12*(11), 616-621, doi:10.1002/2014SW001133.

Zou, X., F. Vandenberghe, B. Wang, M. E. Gorbunov, Y. H. Kuo, S. Sokolovskiy, J. C. Chang, J. G. Sela, and R. A. Anthes (1999), A ray-tracing operator and its adjoint for the use of GPS/MET refraction angle measurements, *J. Geophys. Res.: Atmos.*, *104*(D18), 22301-22318.

Zuffada, C., G. Hajj, and E. R. Kursinski (1999), A novel approach to atmospheric profiling with a mountain-based or airborne GPS receiver, *J. Geoph. Res.*, *104*(D20), 24435-24447.

Zus, F., G. Beyerle, S. Heise, T. Schmidt, J. Wickert, and C. Marquardt (2011), Validation of refractivity profiles derived from GRAS raw-sampling data, *Atmos. Meas. Tech. Discuss.*, *4*(2), 1825-1852, doi:10.5194/amtd-4-1825-2011.

APPENDIX

APPENDIX

ARO data is presented in multi-panel plots. In the left top panel, the differences of ARO, ERAI and WRF refractivity profiles with the pre-Karl mean are shown. In the top right panel, the SNR of the received GPS signal is shown in blue with the 10 second moving average shown in red. The cyan line indicates the plane heading in degrees. The occulting prn azimuth relative to the plane heading is given by the magenta plot in degrees. The plane heading (cyan) and azimuth (magenta) are both plotted using the same ordinate scale on the y-axis as SNR. If a dropsonde is co-located with the ARO occultation point, the vertical gradient of refractivity calculated from the dropsonde data and is shown on the left in the middle panel as a scatter plot overlaid on the mean gradient and standard deviation of all dropsondes deployed during the flight shown in red. The SNR as a function of tangent point height is shown on the right with the moving average in yellow and flight mean SNR and standard deviation shown in red. If there is no co-located dropsonde, only the SNR as a function of tangent point height is shown in the middle panel The left bottom panel shows a cross-section of difference of ERAI model specific humidity along the tangent point path with the pre-Karl mean. The tangent point path as a function of height is plotted in black. The vertical error bars indicate the distance variation over the ± 5s vertical resolution. The horizontal error

bars represent the expected horizontal resolution based on the interval over which 70% of ray path bending takes place at each tangent point height.

RF16:

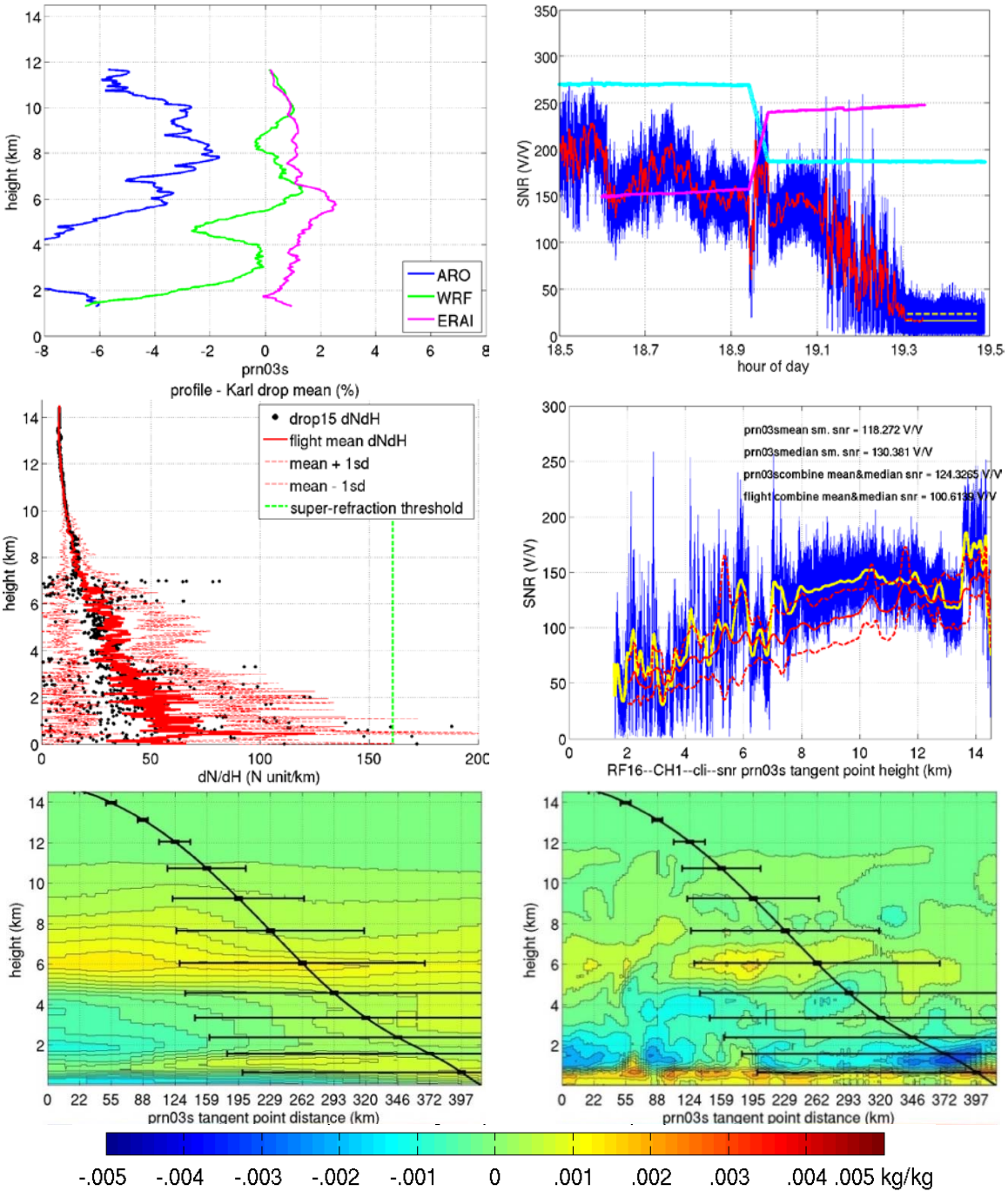

Figure A. 1 RF16 OL CH1_cli prn03s. In the middle left panel, dropsonde 15 was located 58 km from the prn03s occultation point.

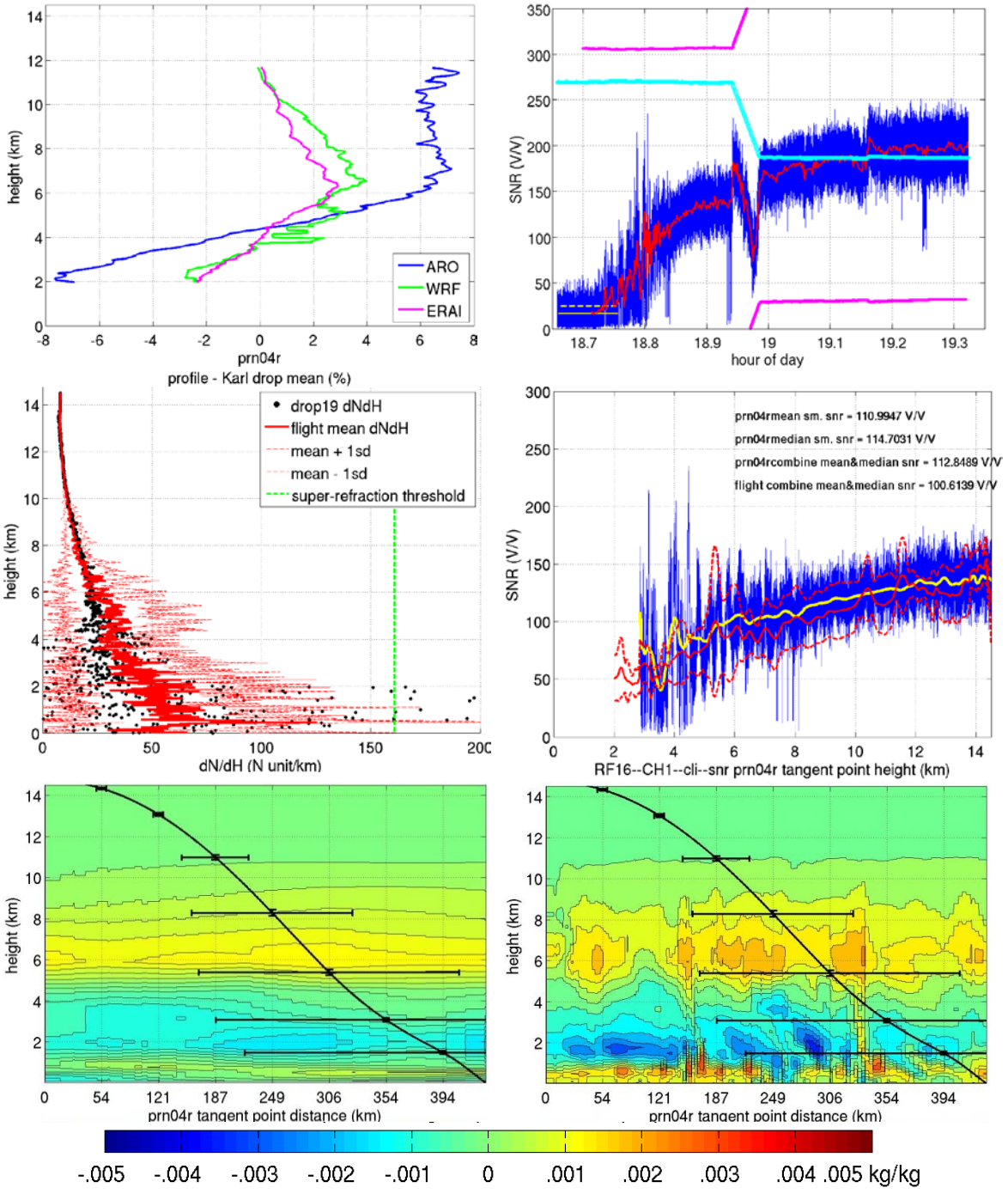

Figure A. 2 RF16 OL CH1_cli prn04r. In the middle left panel, dropsonde 19 was located 129 km from the prn04r occultation point.

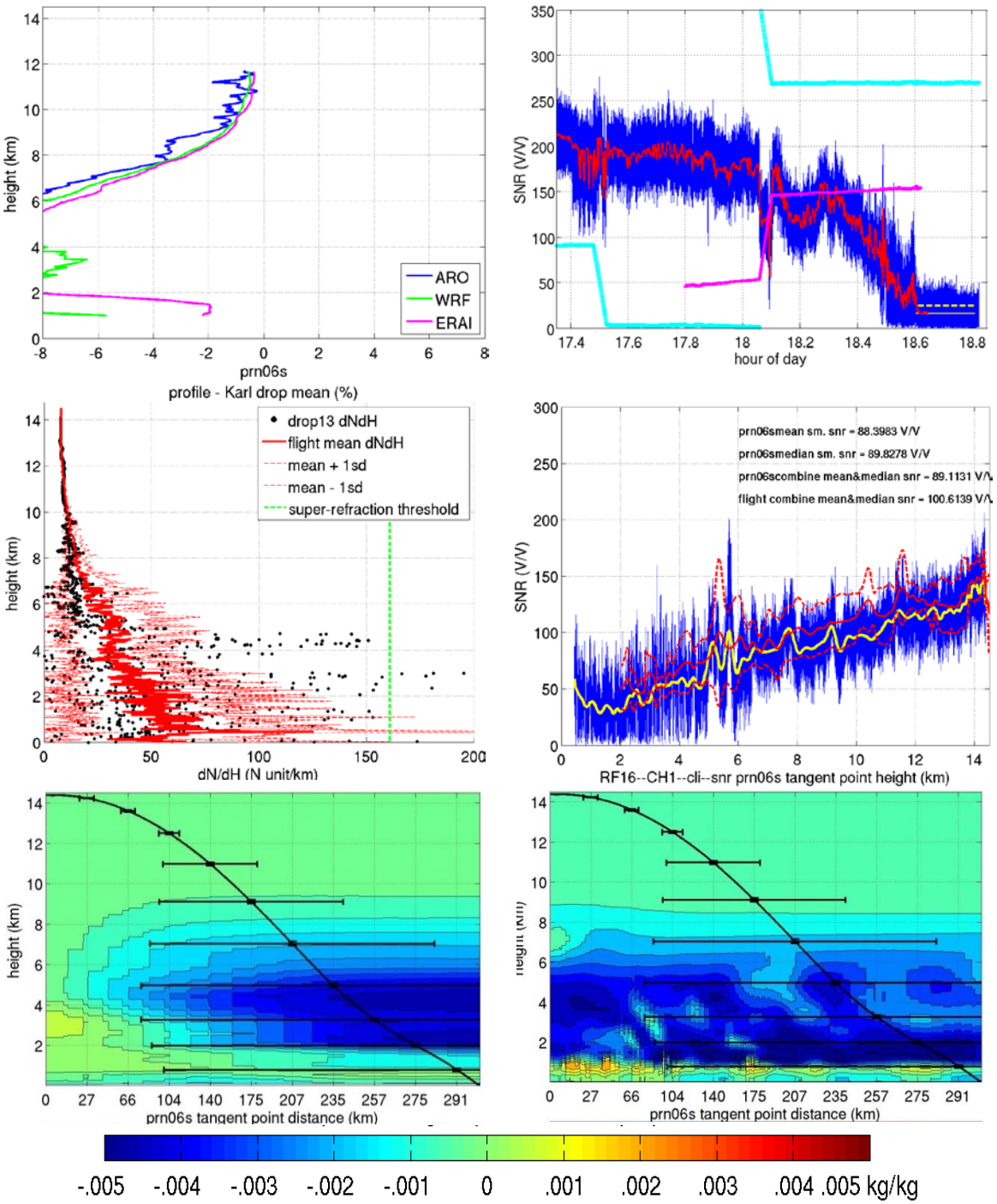

Figure A. 3 RF16 OL CH1_cli prn06s. In the middle left panel, dropsonde 13 was located 161 km from the prn06s occultation point.

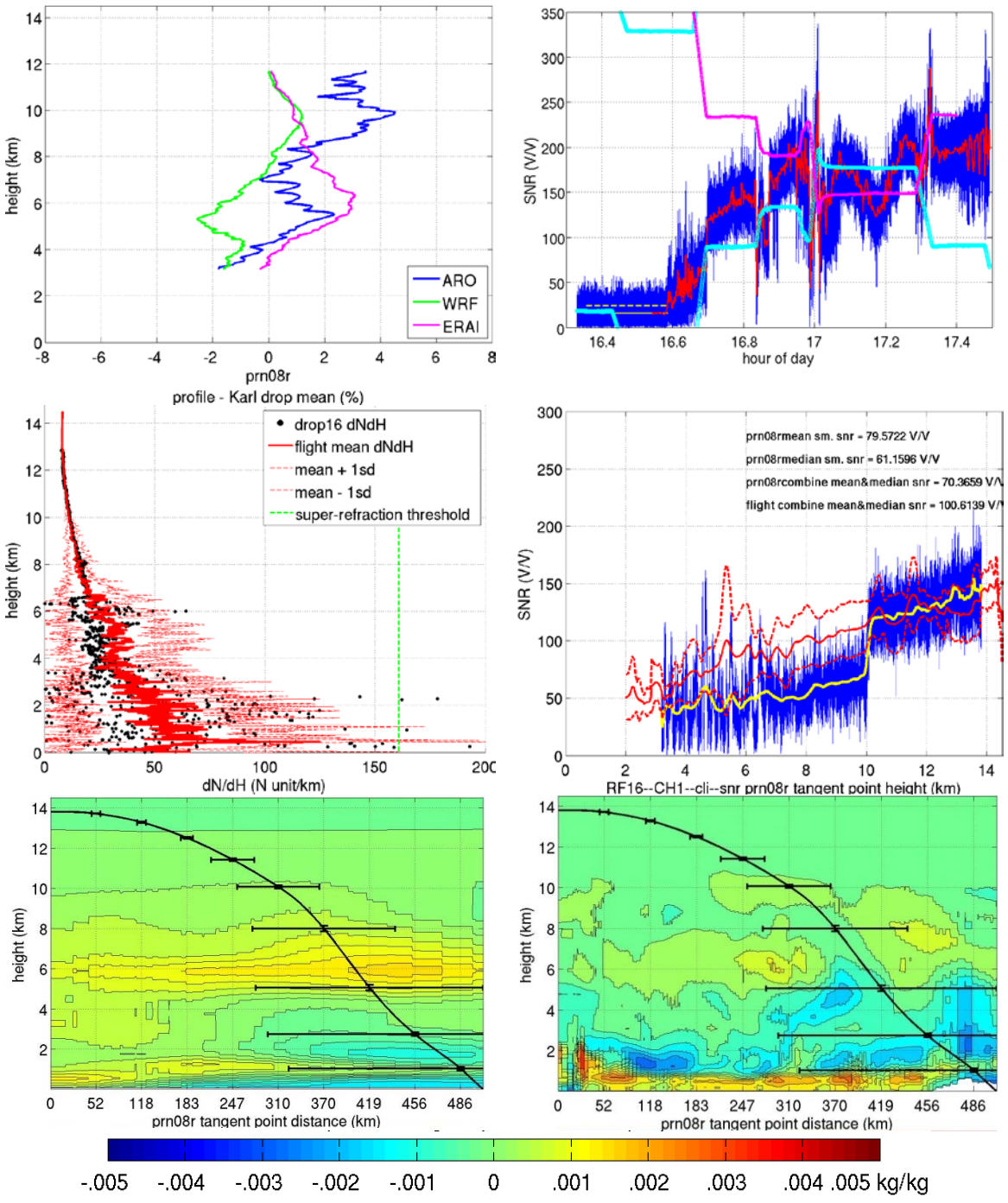

Figure A. 4 RF16 OL CH1_cli prn08r. In the middle left panel, dropsonde 16 was located 63 km from the prn06s occultation point.

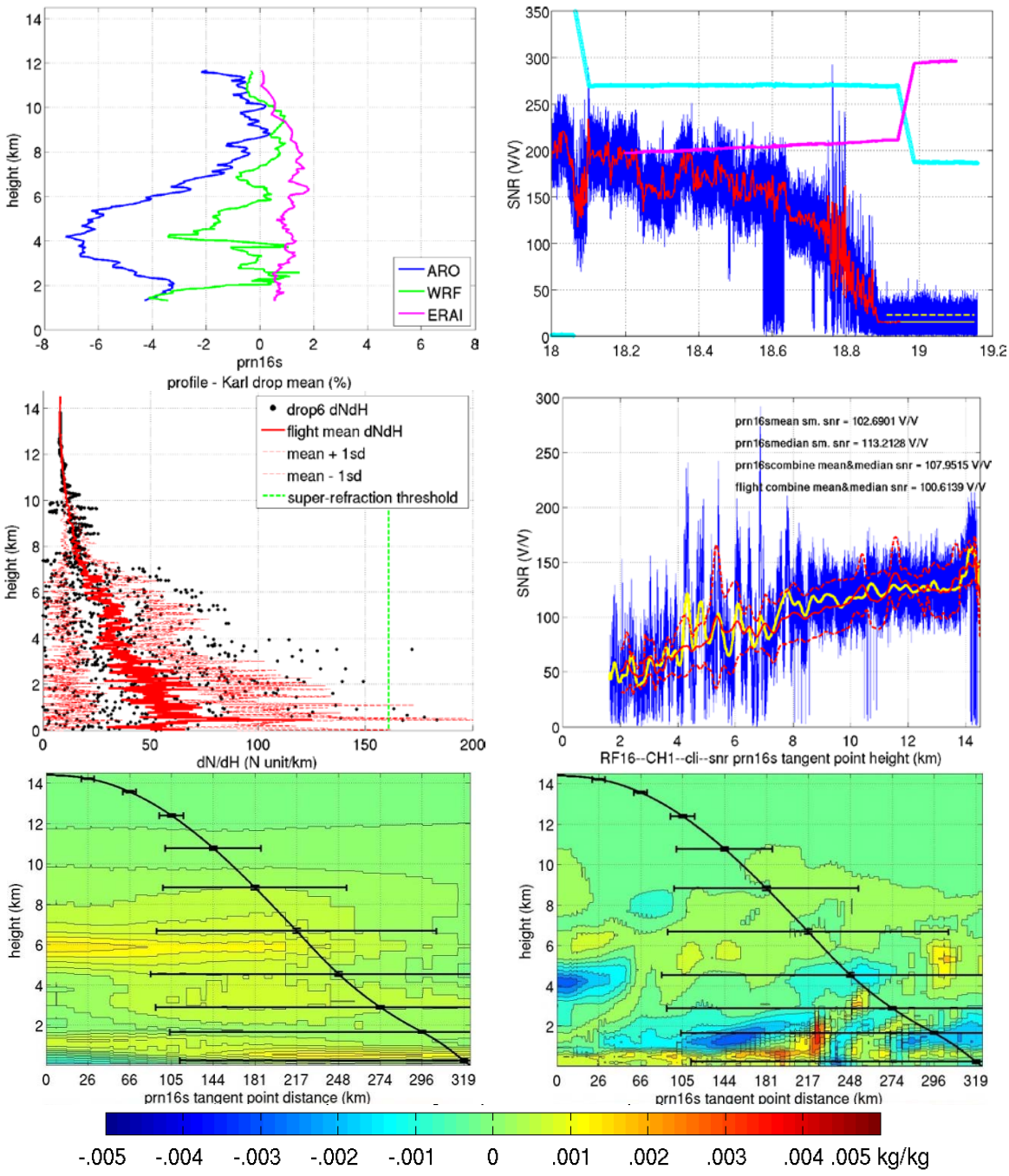

Figure A. 5 RF16 OL CH1_cli prn16s. In the middle left panel, dropsonde 6 was located 11 km from the prn16s occultation point.

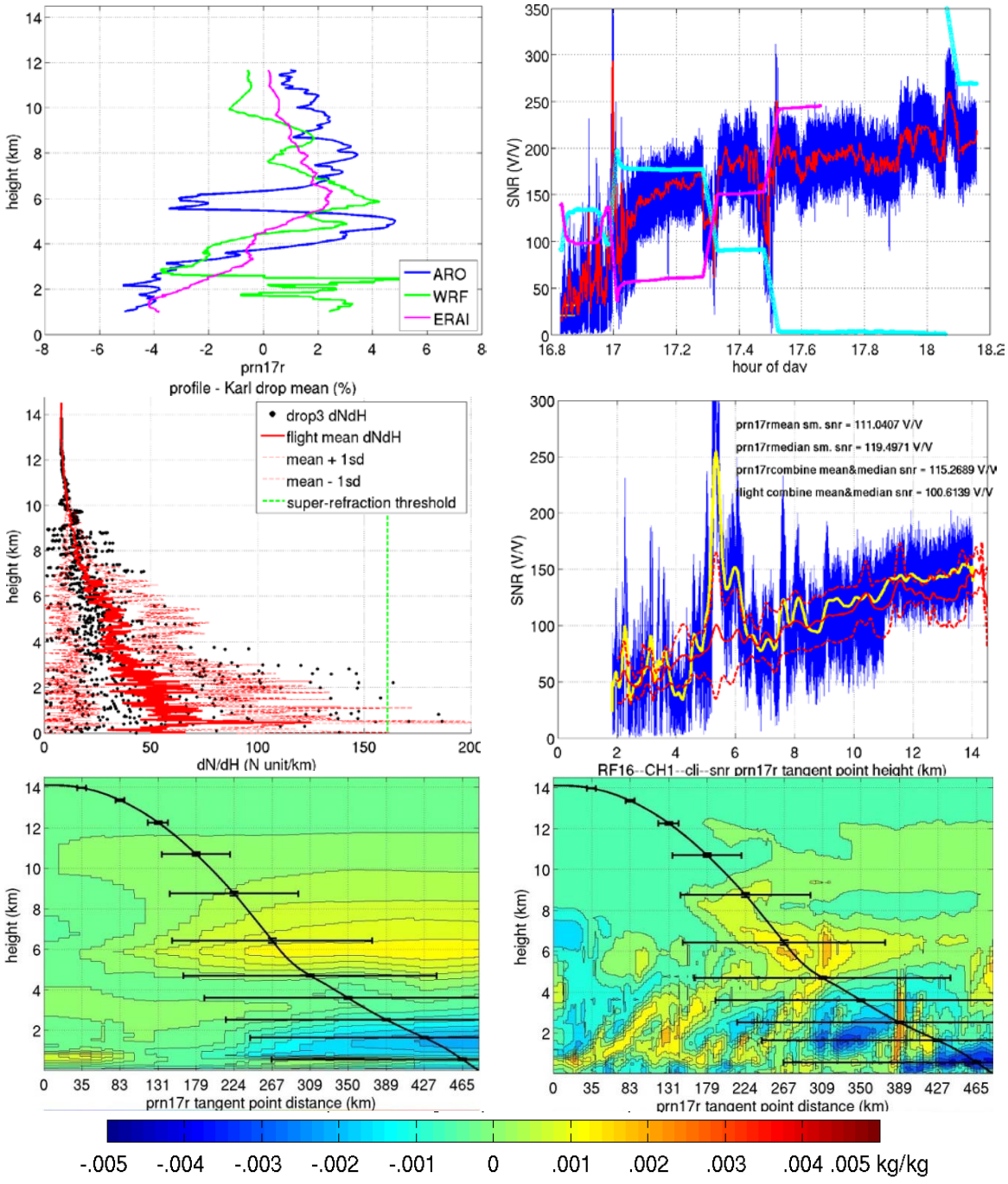

Figure A. 6 RF16 OL CH1_cli prn17r. In the middle left panel, dropsonde 3 was located 124km from the prn17r occultation point.

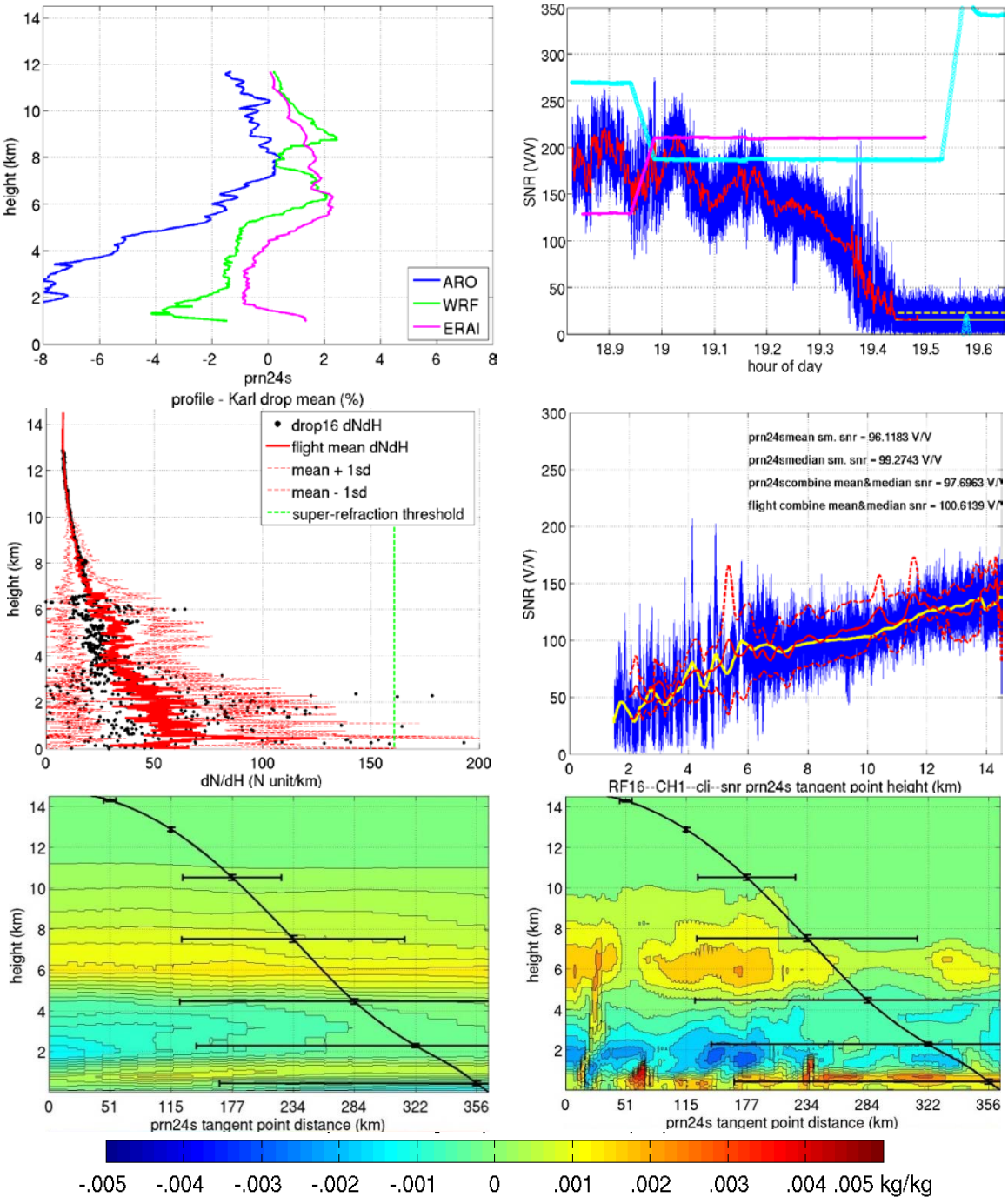

Figure A. 7 RF16 OL CH1_cli prn24s. In the middle left panel, dropsonde 16 was located 57 km from the prn24s occultation point.

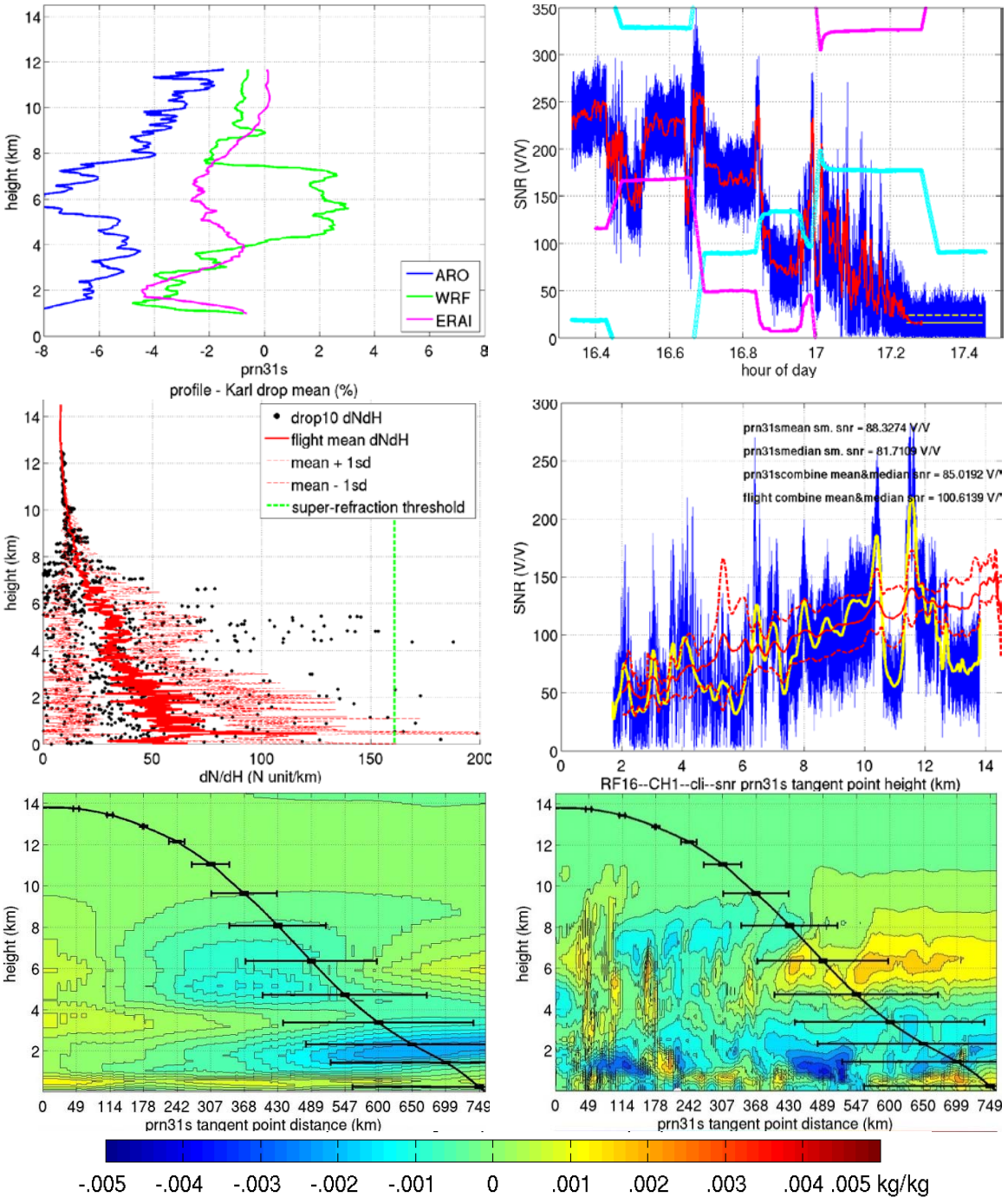

Figure A. 8 RF16 OL CH1_cli prn31s. In the middle left panel, dropsonde 10 was located 120 km from the prn31s occultation point.

RF17:

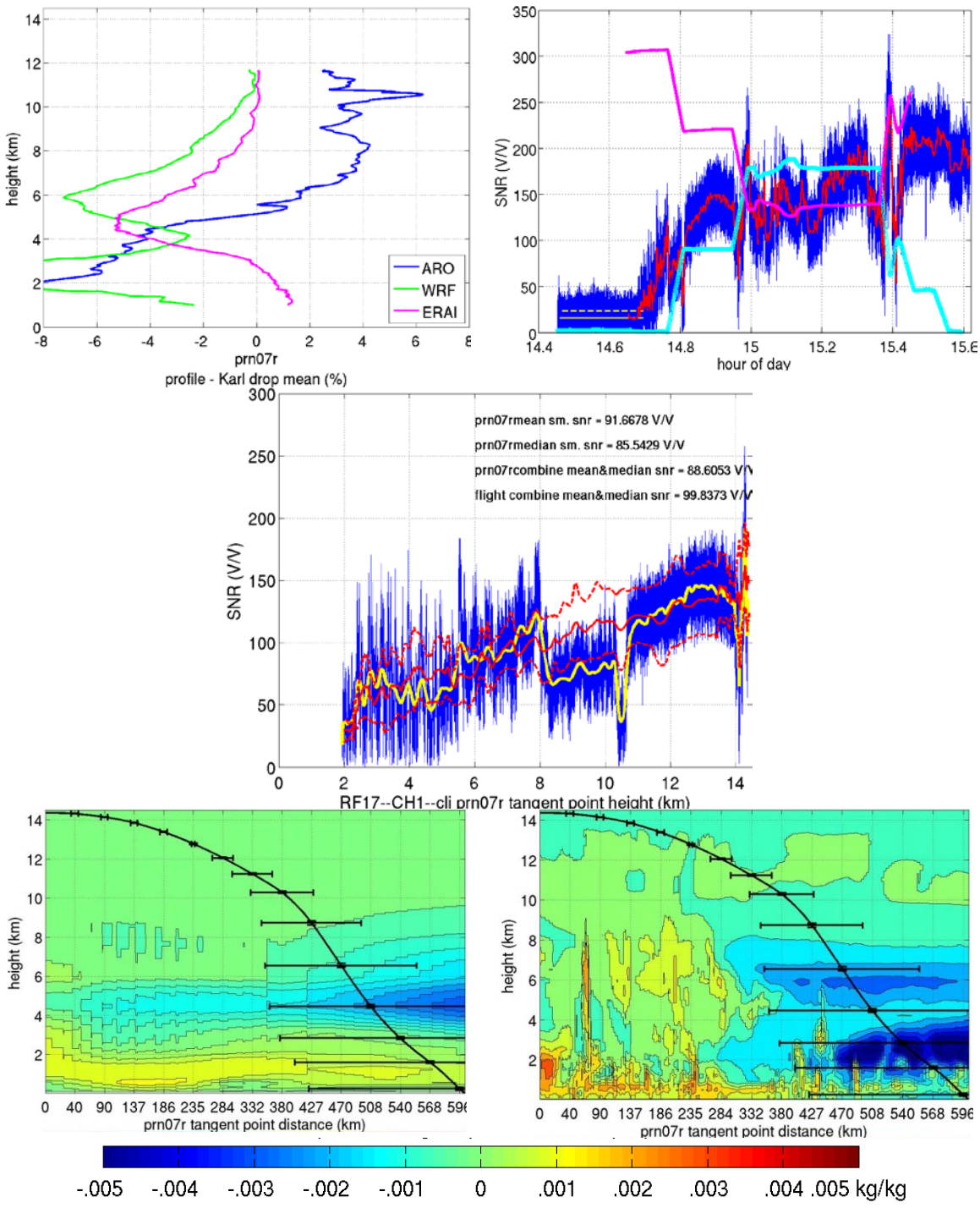

Figure A. 9 RF18 OL CH1_cli prn07r.

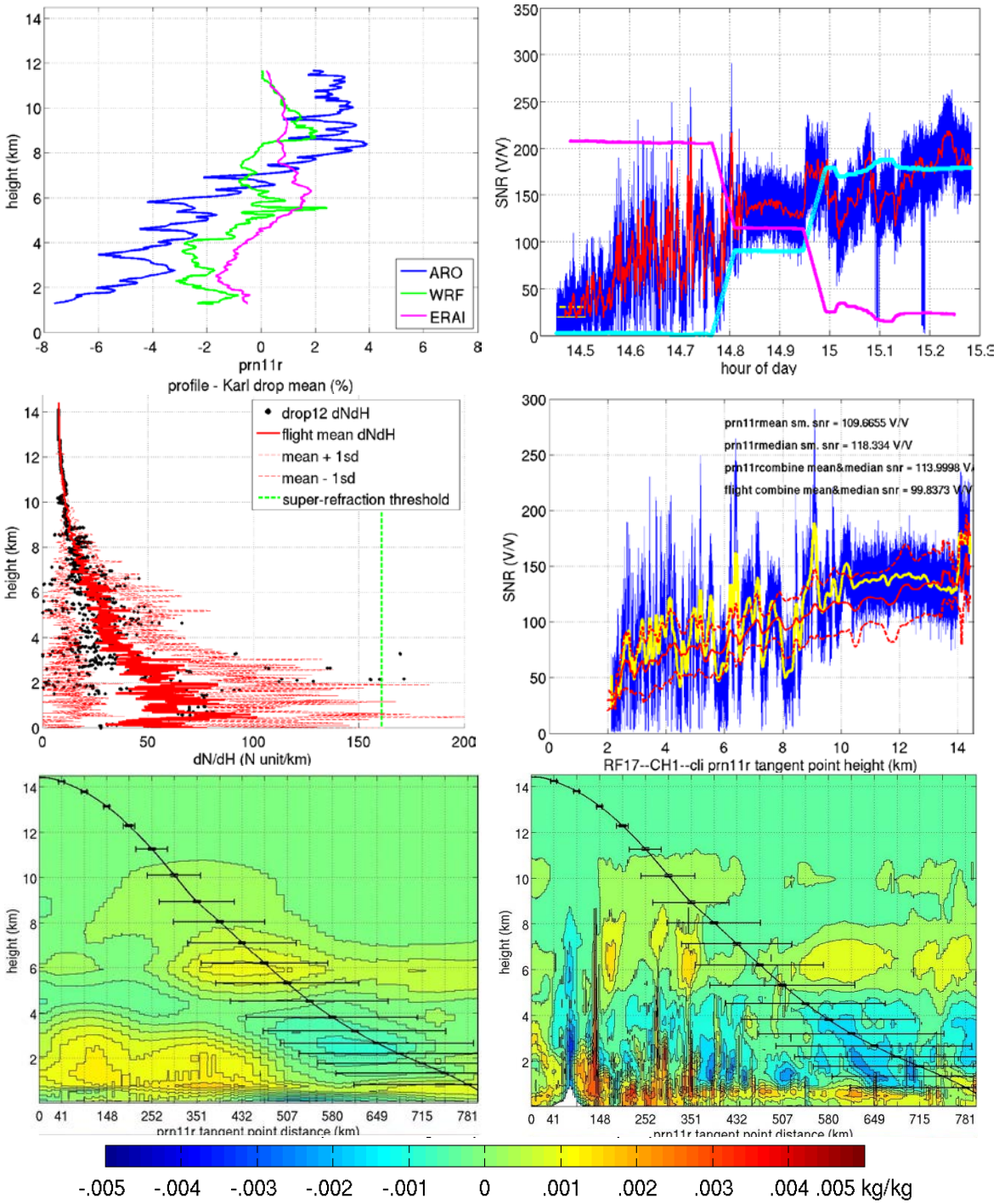

Figure A. 10 RF17 OL CH1_cli prn11r. In the middle left panel, dropsonde 12 was located 37km from the prn11r occultation point.

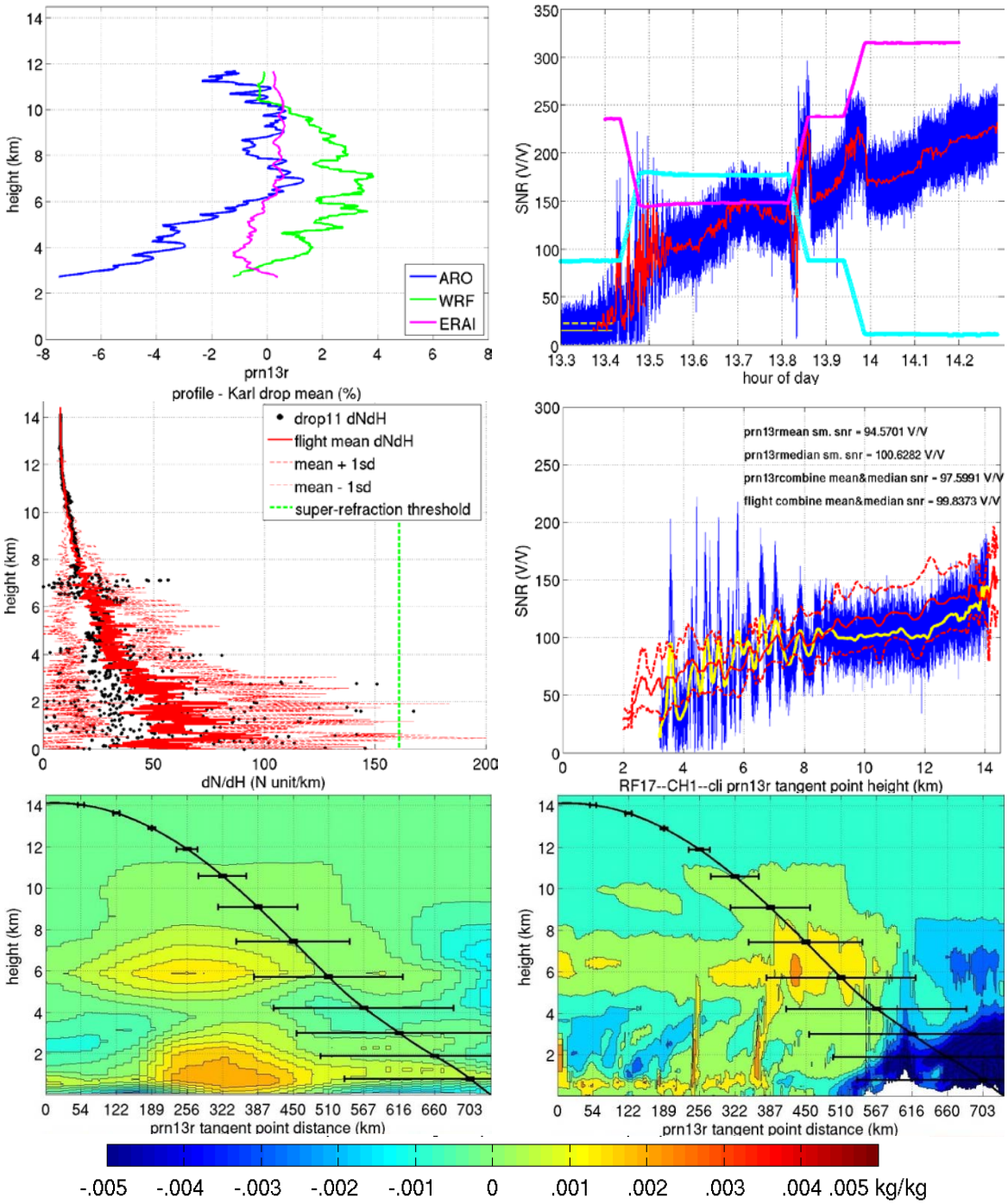

Figure A. 11 RF17 OL CH1_cli prn13r. In the middle left panel, dropsonde 11 was located 250km from the prn13r occultation point.

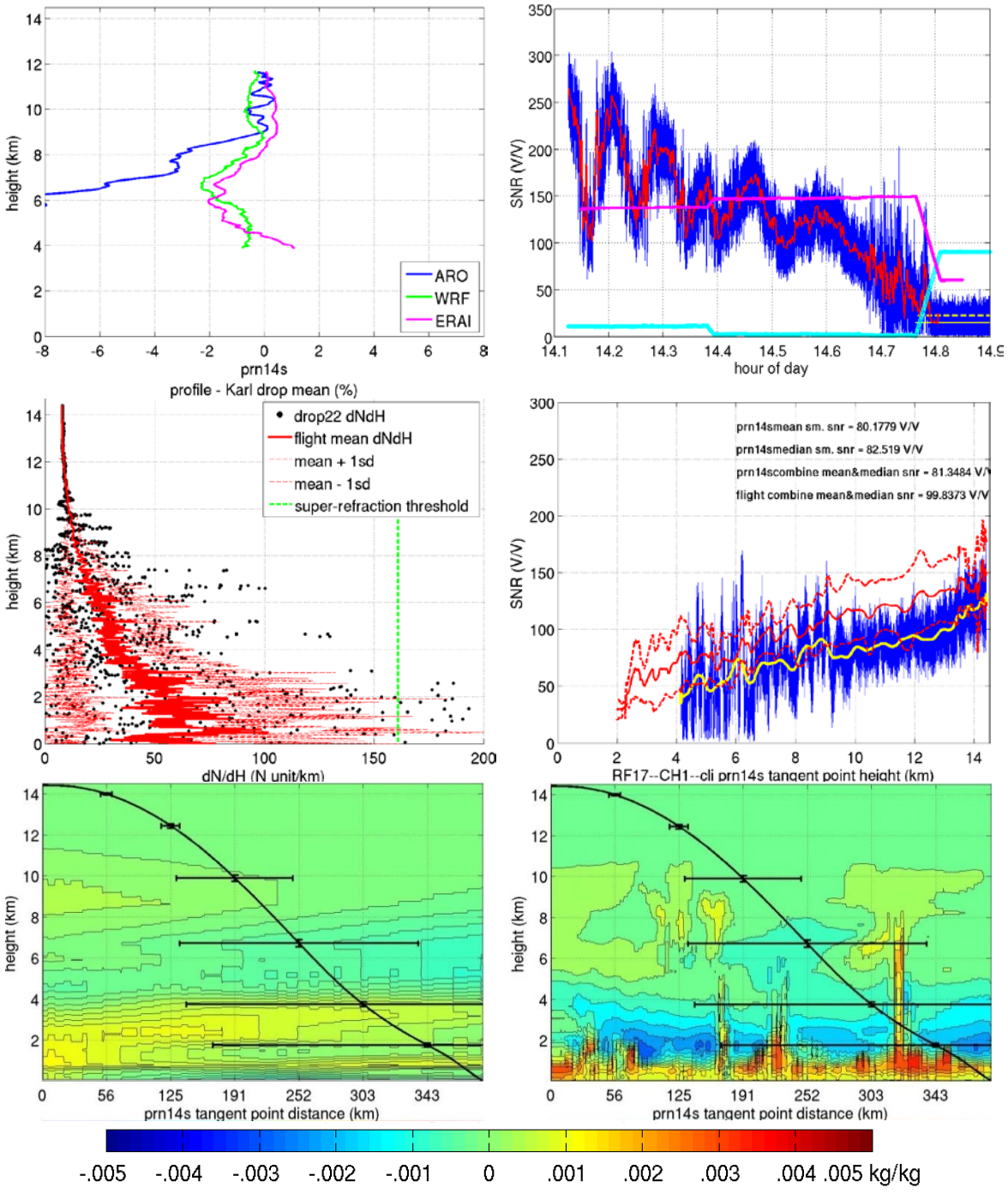

Figure A. 12 RF17 OL CH1_cli prn14s. In the middle left panel, dropsonde 22 was located 37km from the prn14s occultation point.

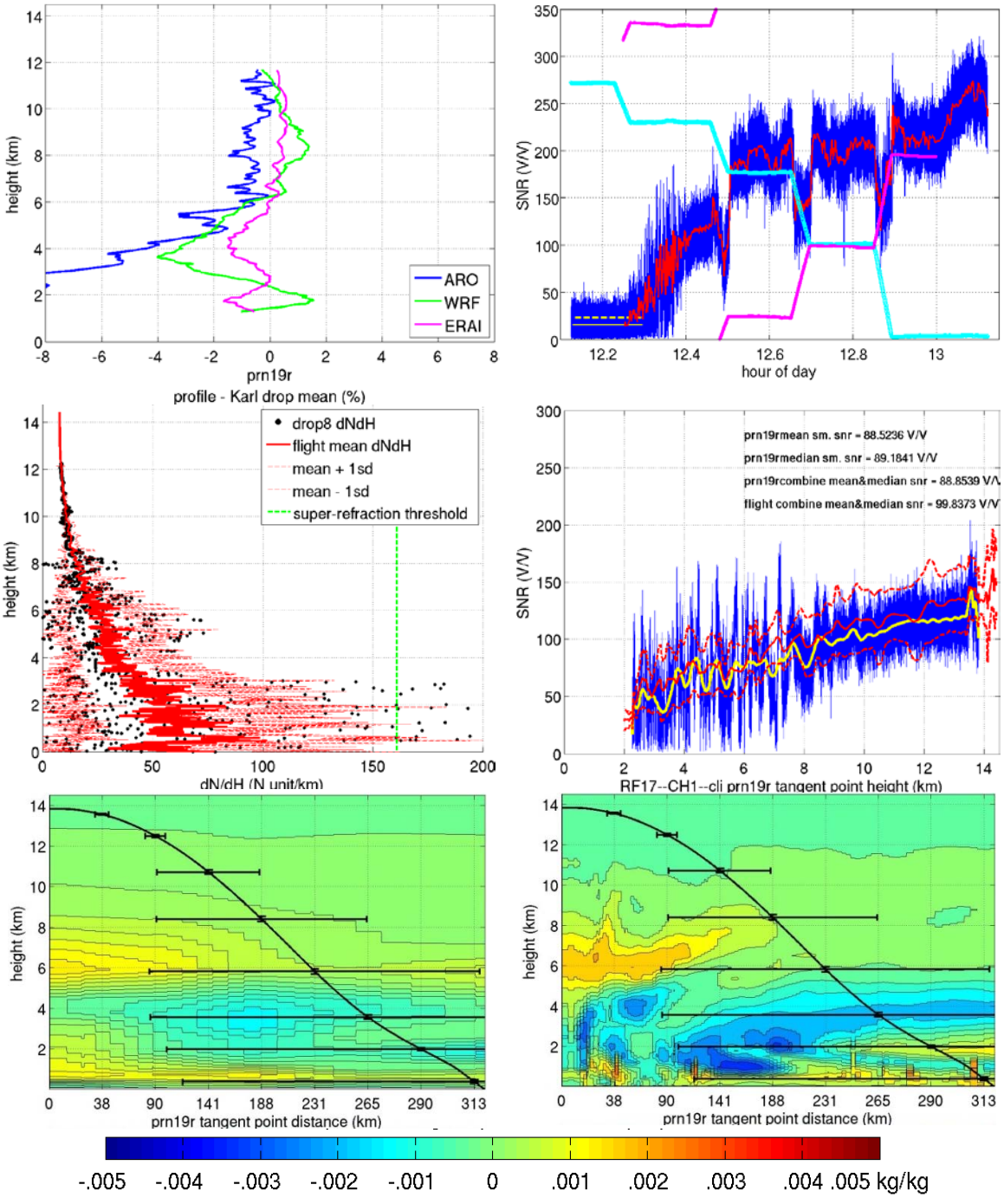

Figure A. 13 RF17 OL CH1_cli prn19r. In the middle left panel, dropsonde 08 was located 137km from the prn19r occultation point.

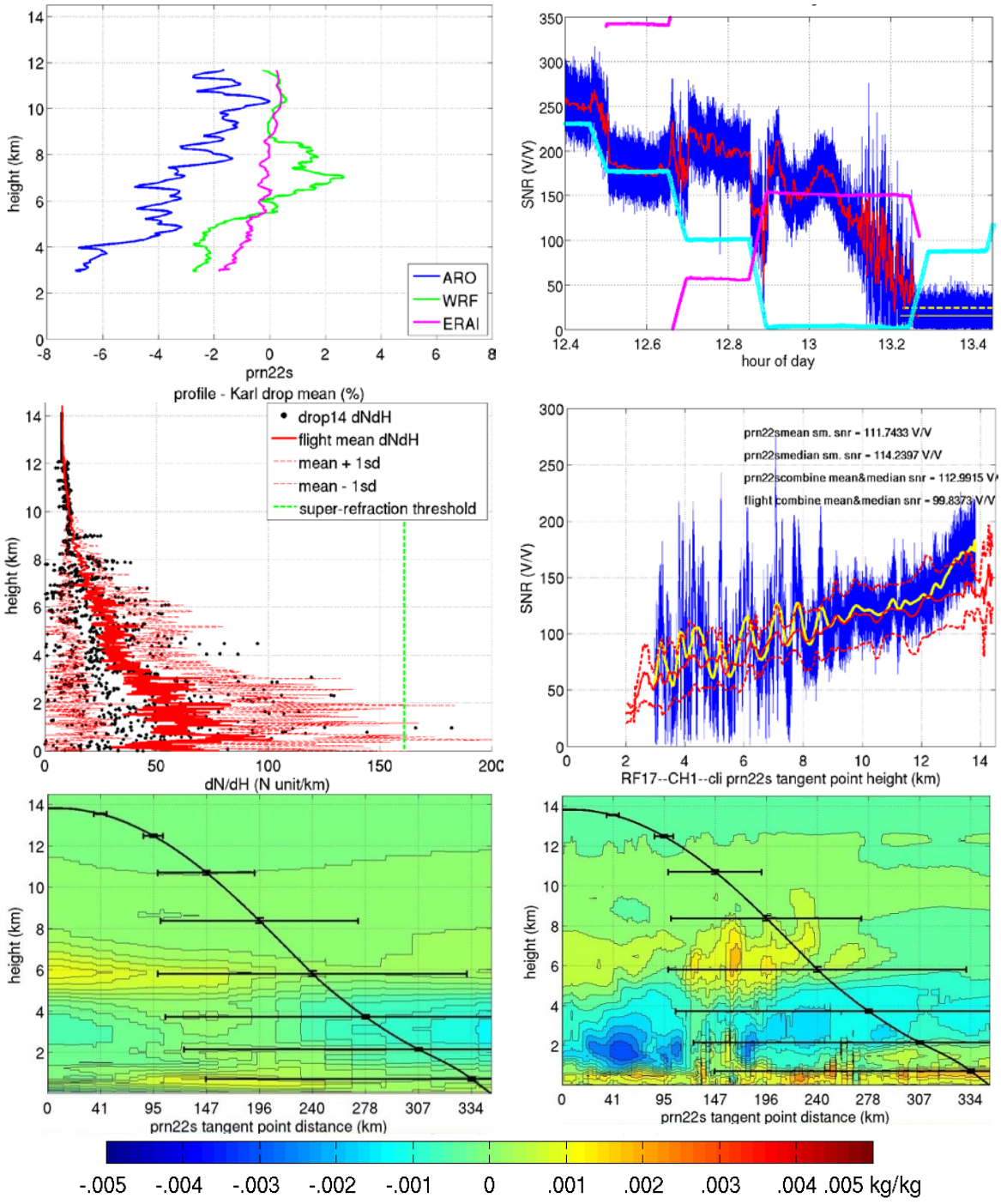

Figure A. 14 RF17 OL CH1_cli prn22s. In the middle left panel, dropsonde 14 was located 72km from the prn22s occultation point.

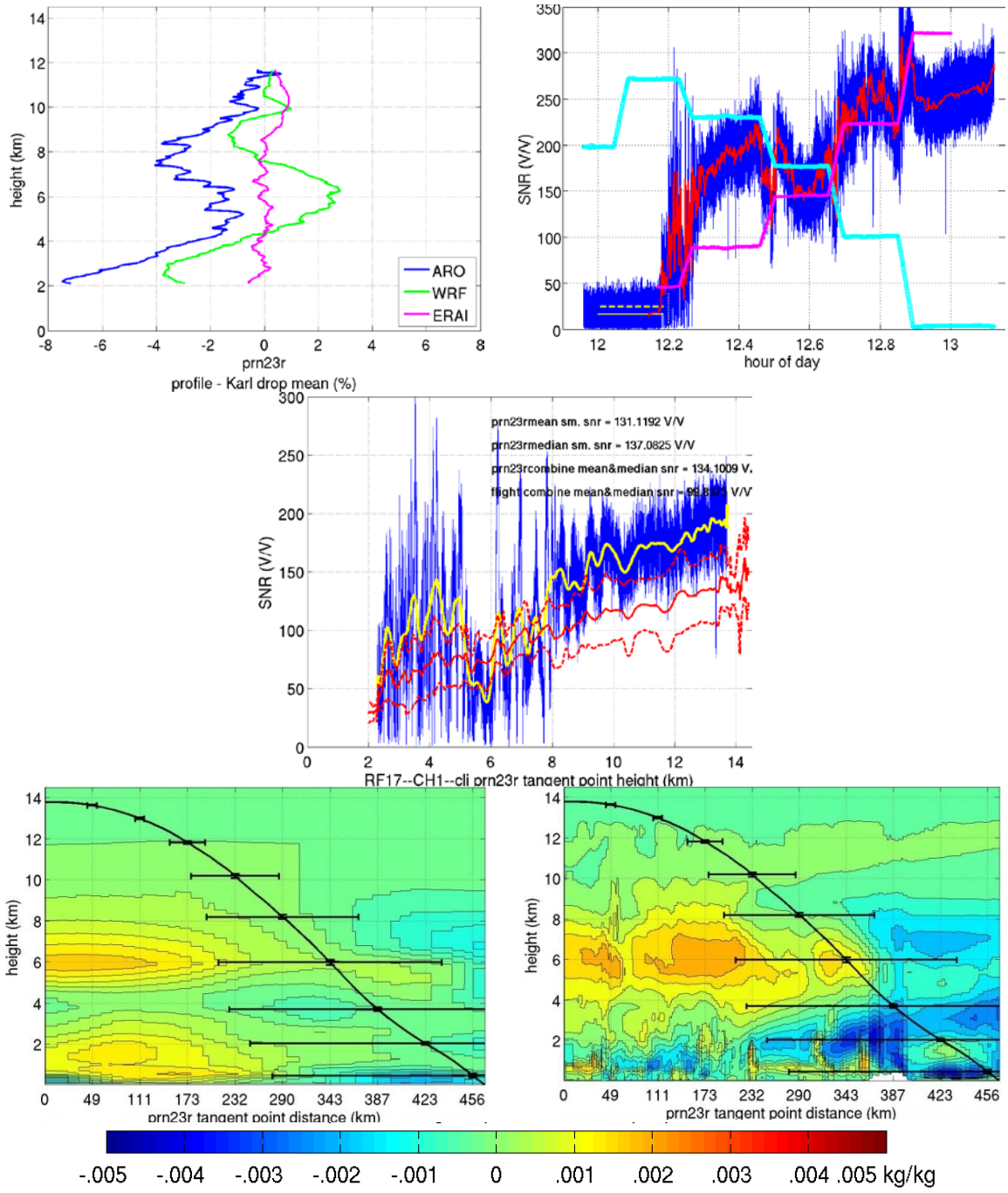

Figure A. 15 RF17 OL CH1_cli prn23r.

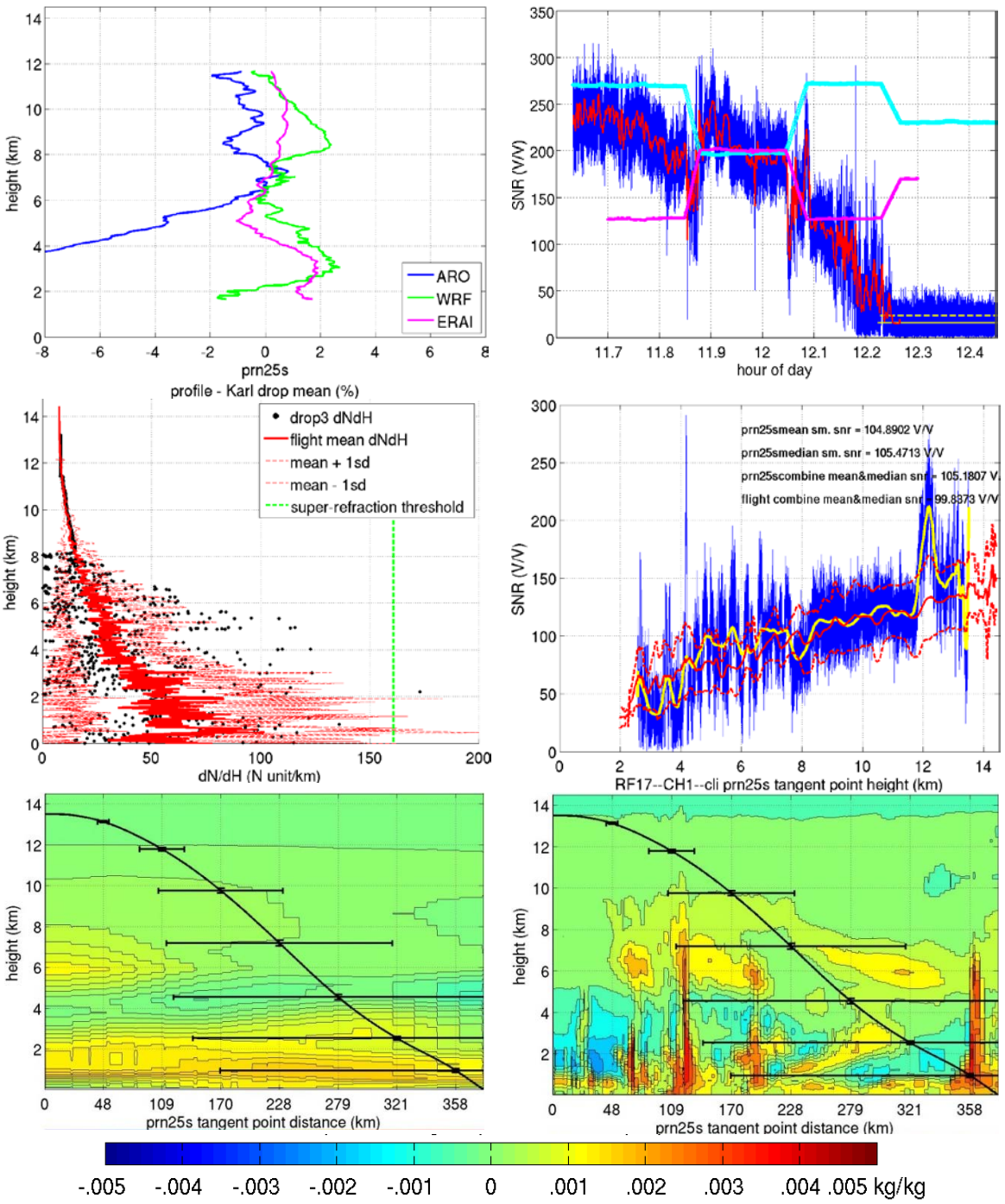

Figure A. 16 RF17 OL CH1_cli prn25s. In the middle left panel, dropsonde 03 was located 90km from the prn25s occultation point.

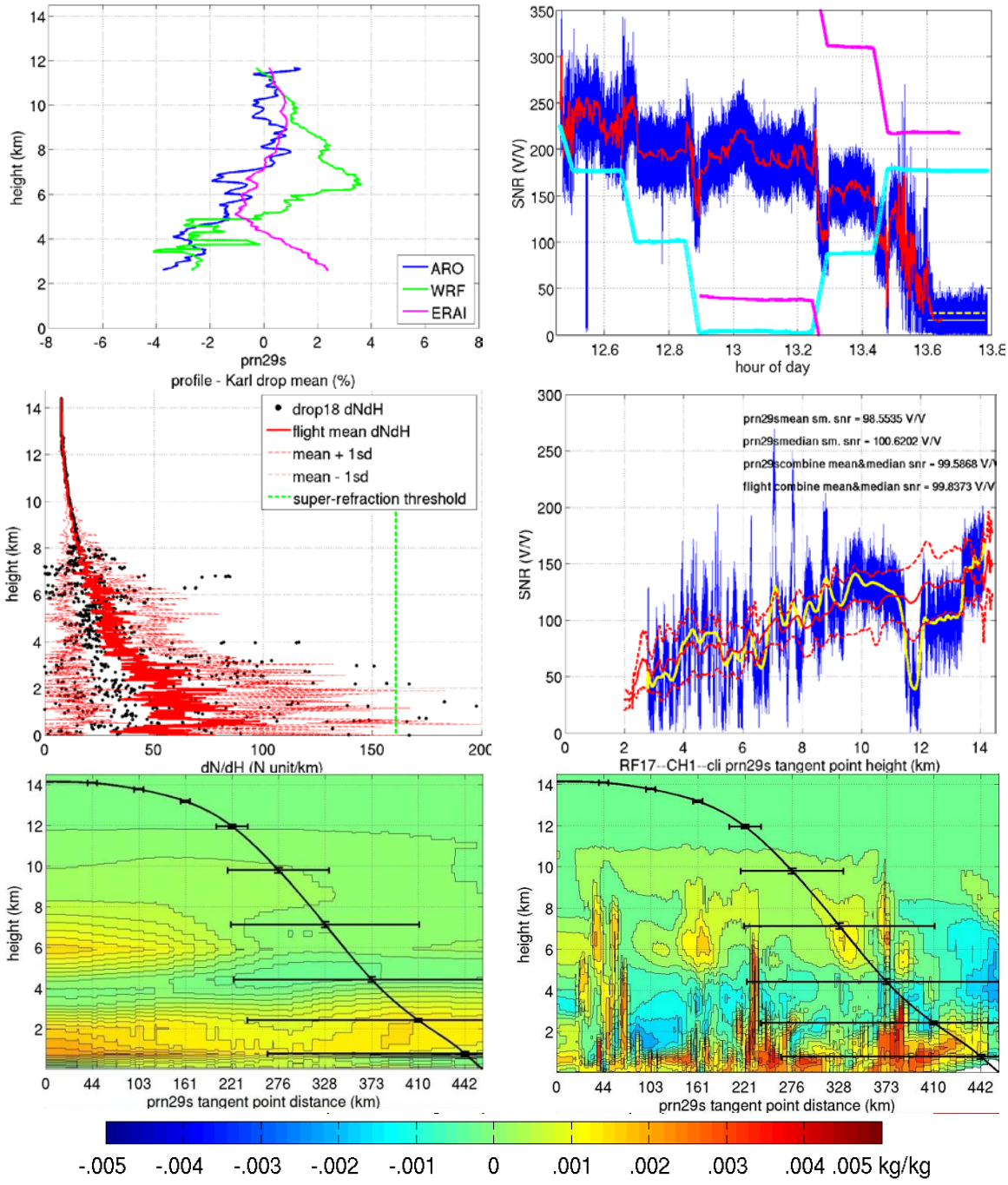

Figure A. 17 RF17 OL CH1_cli prn29s. In the middle left panel, dropsonde 18 was located 54km from the prn29s occultation point.

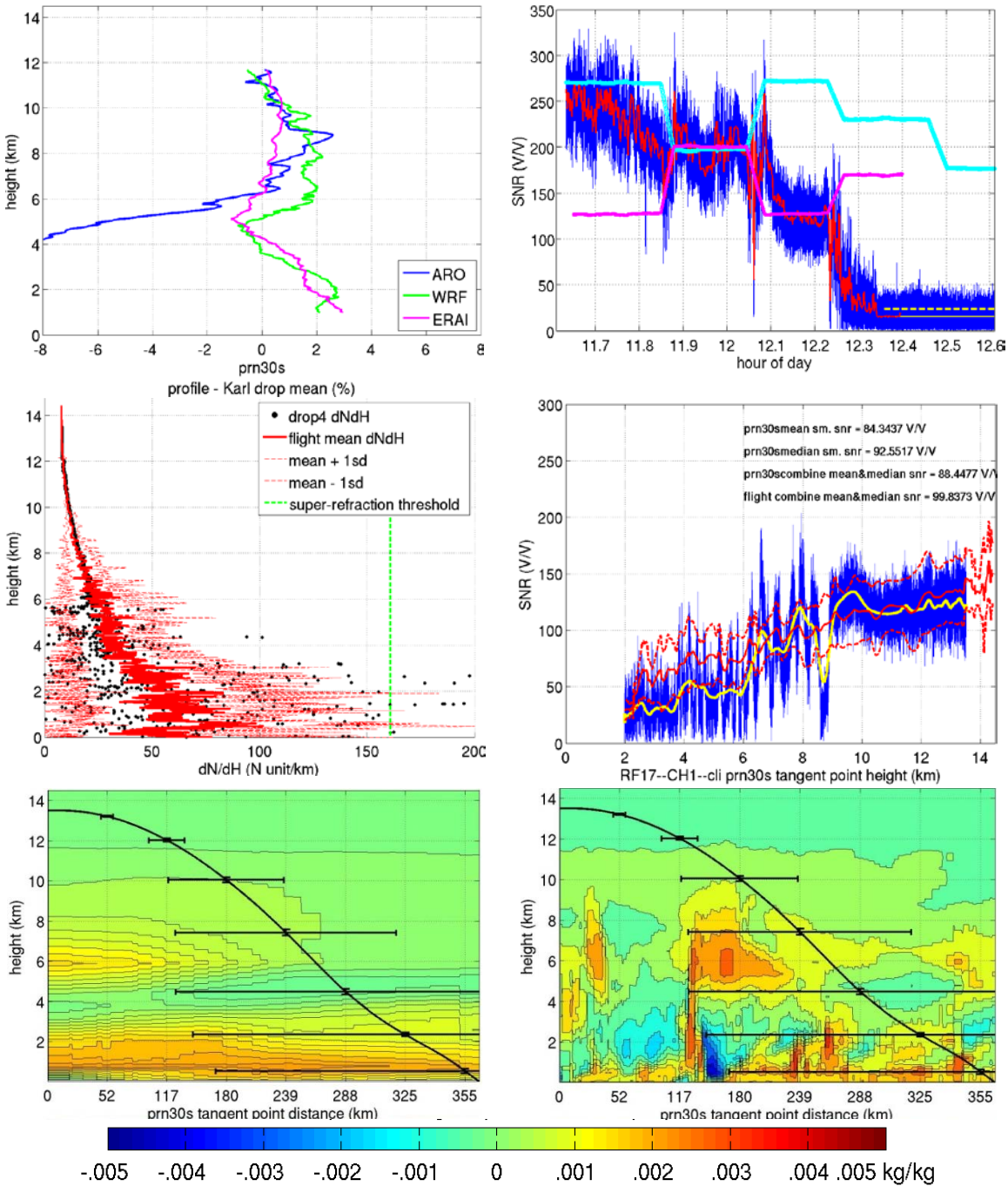

Figure A. 18 RF17 OL CH1_cli prn30s. In the middle left panel, dropsonde 04 was located 117km from the prn30s occultation point.

RF18

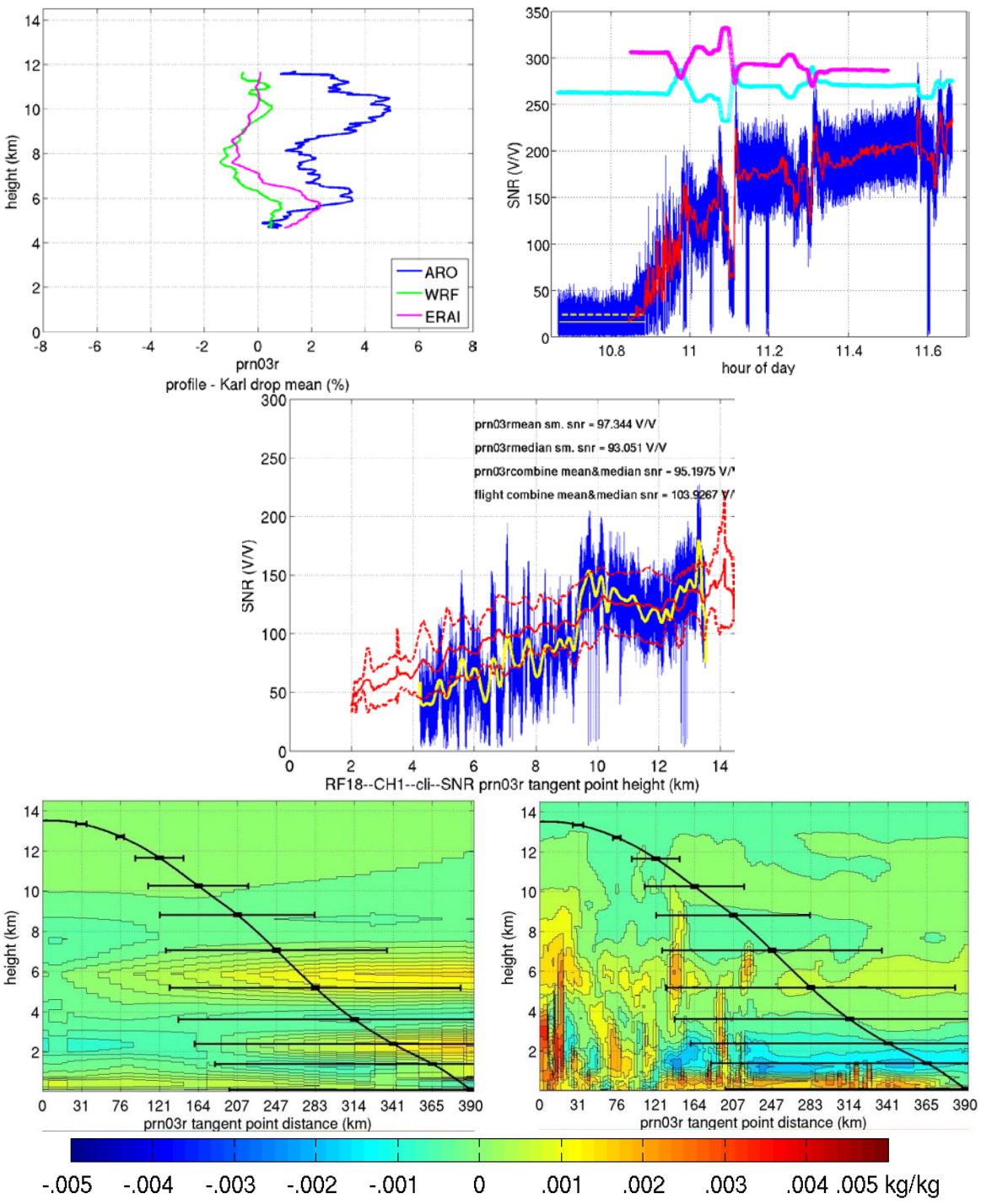

Figure A. 19 RF18 OL CH1_cli prn03r

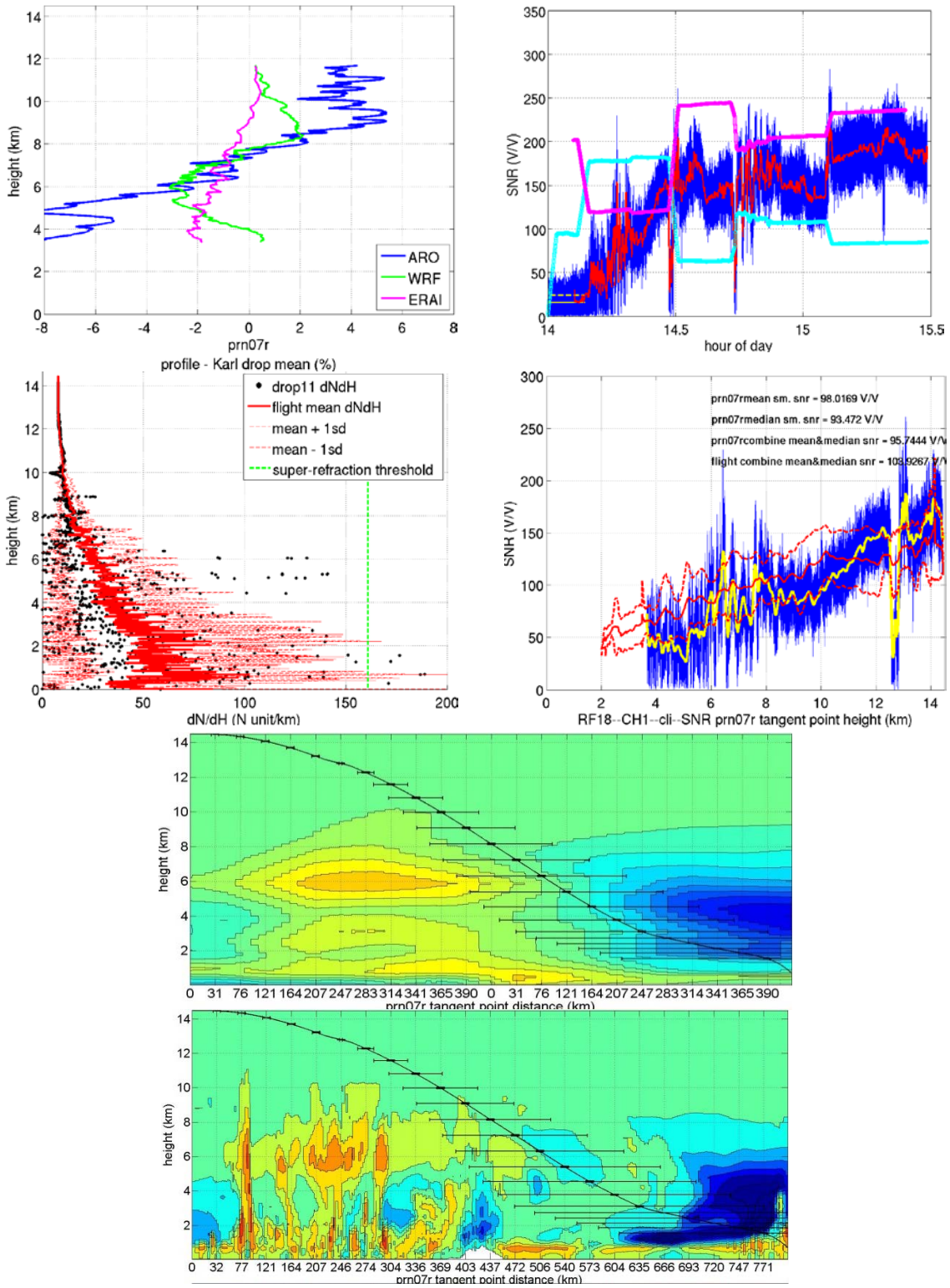

Figure A. 20 RF18OL CH1_cli prn07r. In the middle left panel, the co-located dropsonde 11 is 46 km from occultation point.

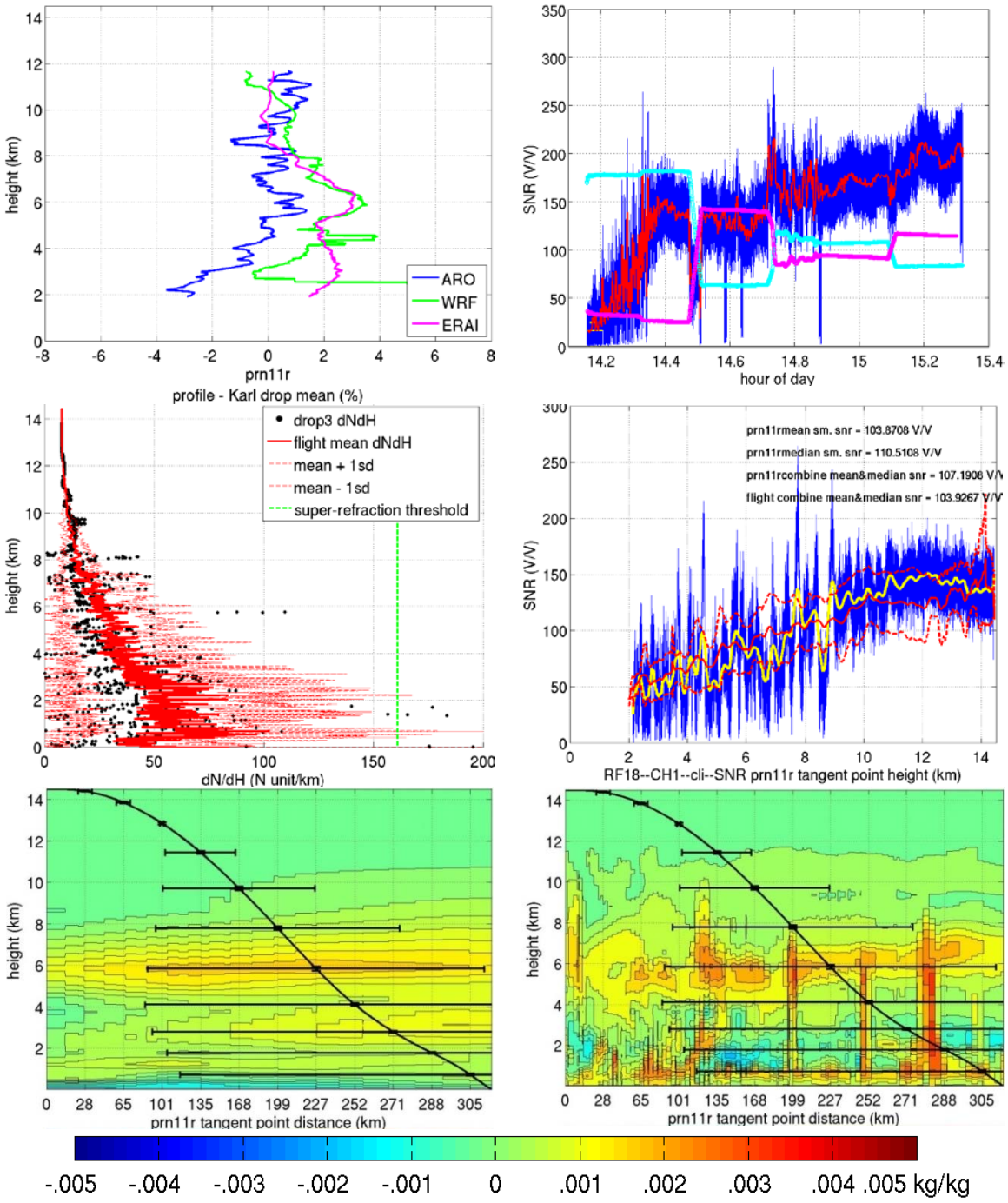

Figure A. 21 RF18 OL CH1_cli prn11r. In the middle left panel, the co-located drop3 was 99 km from prn11r occultation point.

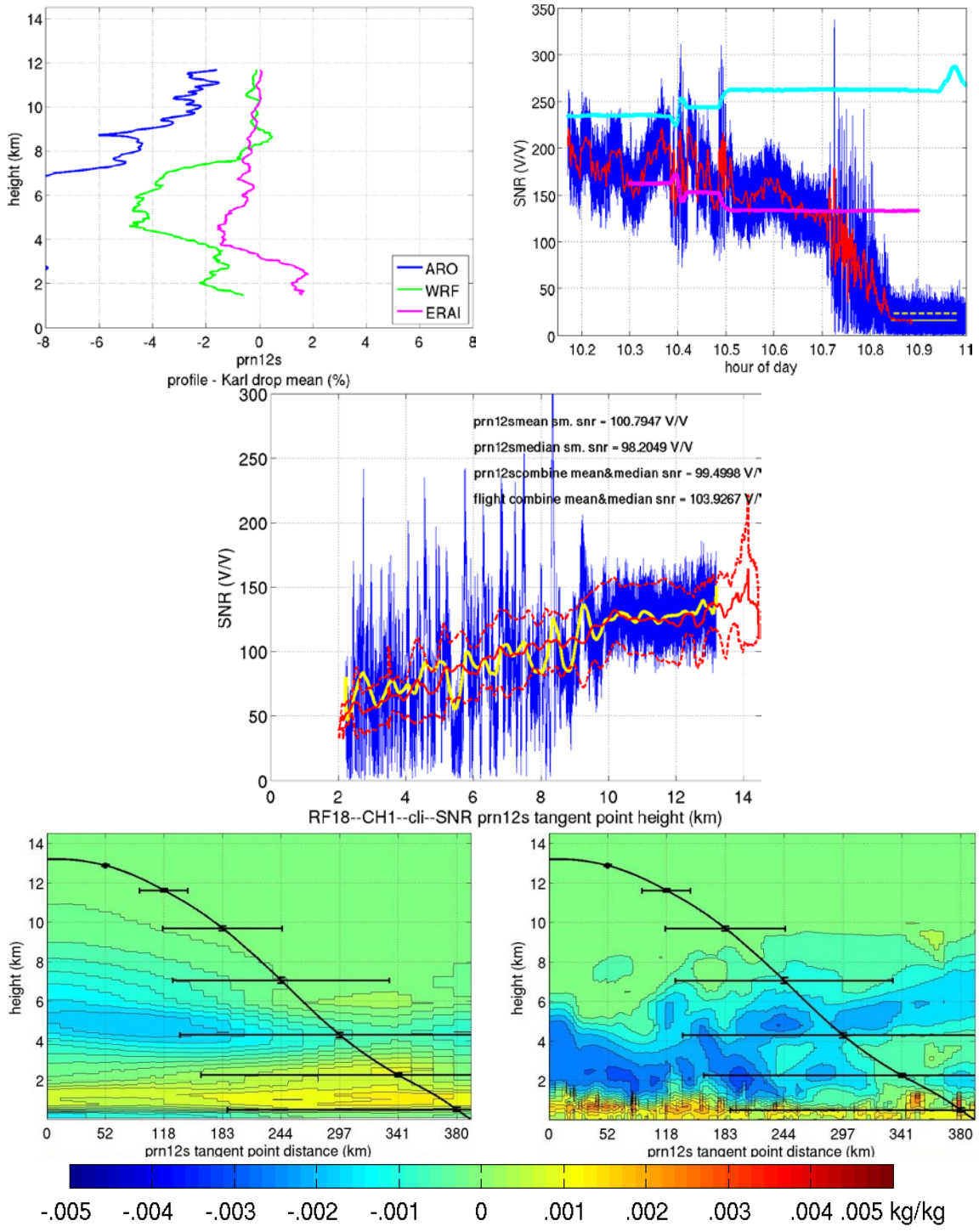

Figure A. 22 RF18 OL CH1_cli prn12s.

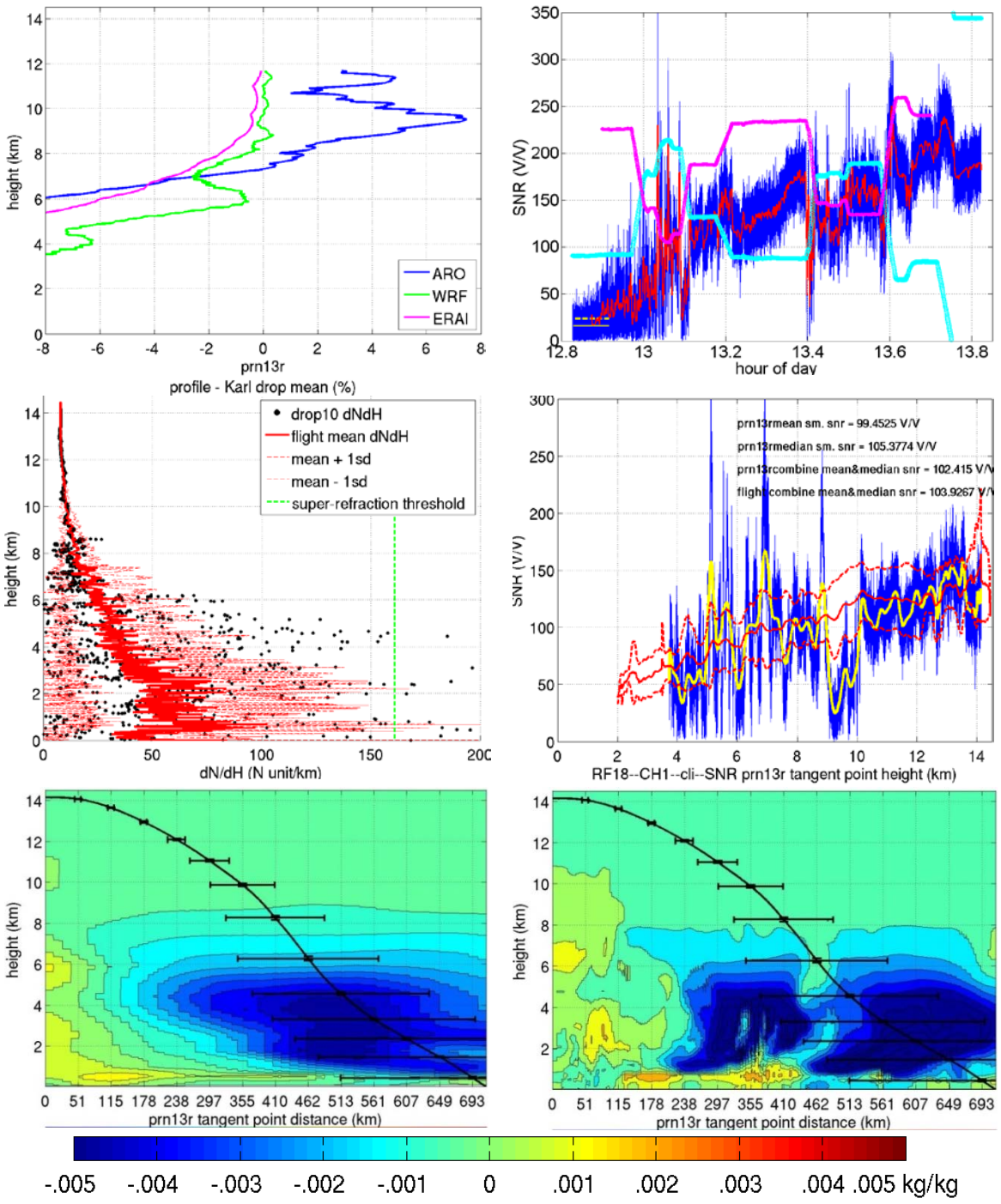

Figure A. 23 RF18 OL CH1_cli prn13r. In the middle left panel, the co-located drop10 was 232 km from prn13r occultation point.

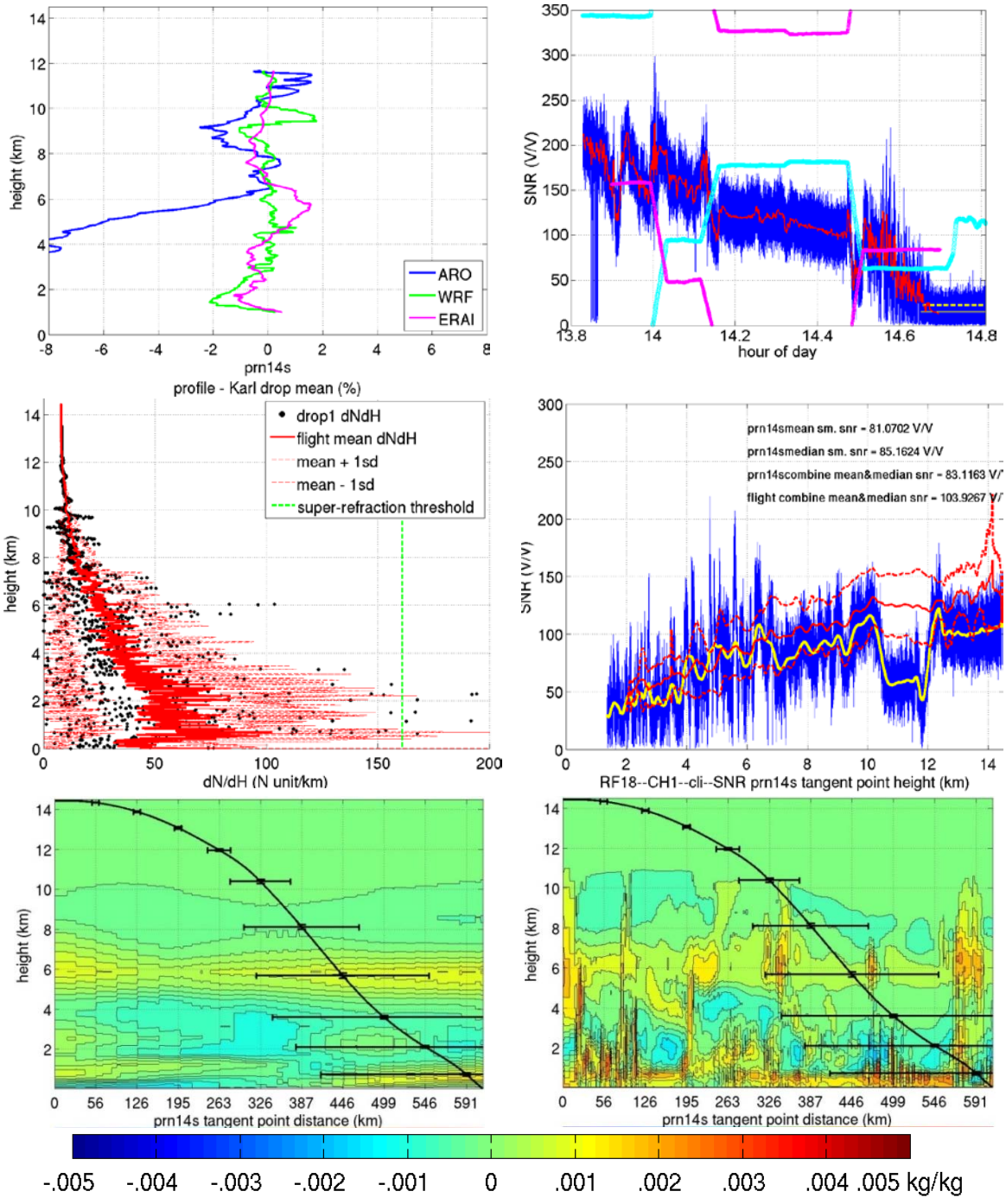

Figure A. 24 RF18 OL CH1_cli prn14s. In the middle left panel, the co-located drop01 was 207 km from occultation point.

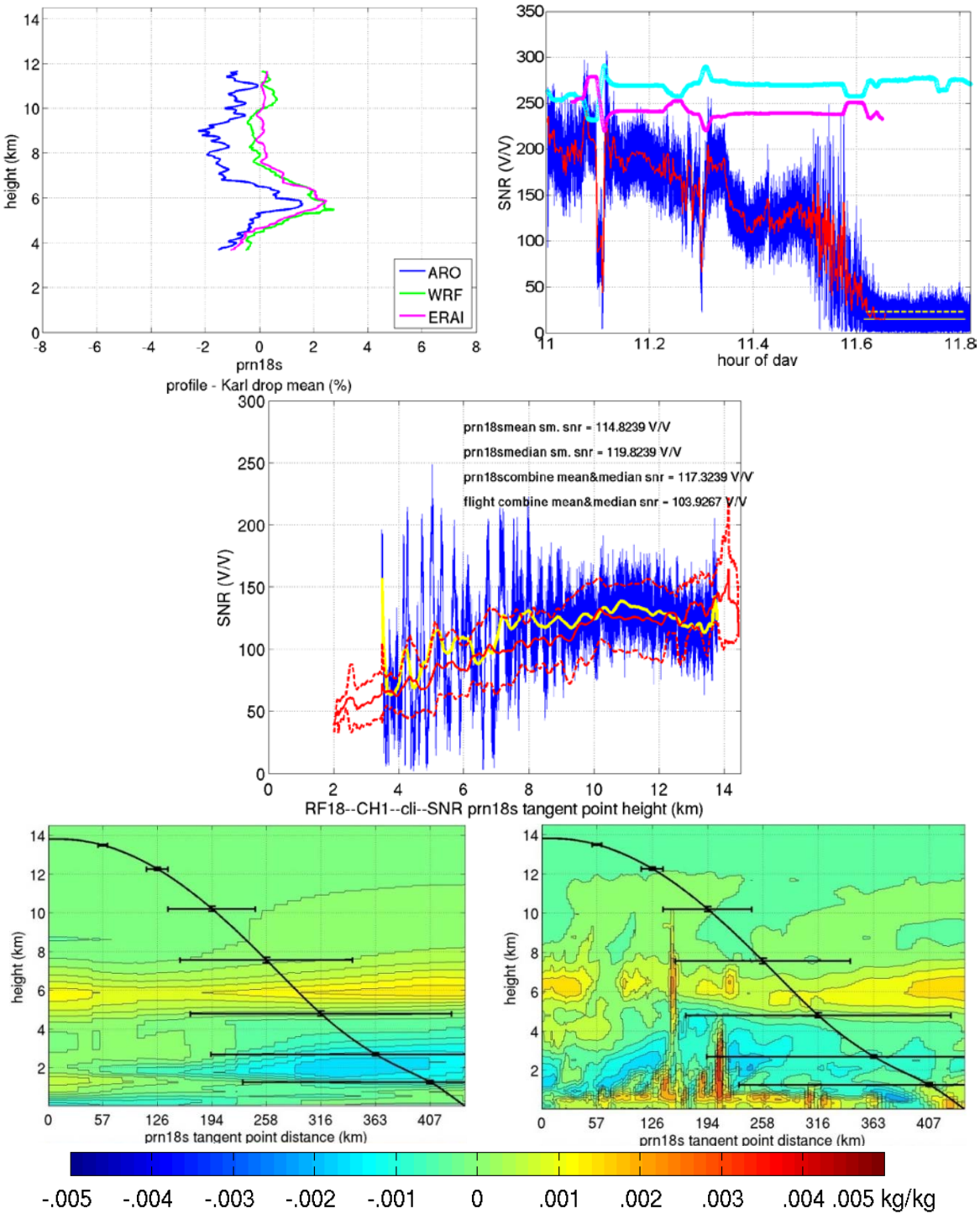

Figure A. 25 RF18 OL CH1_cli prn18s.

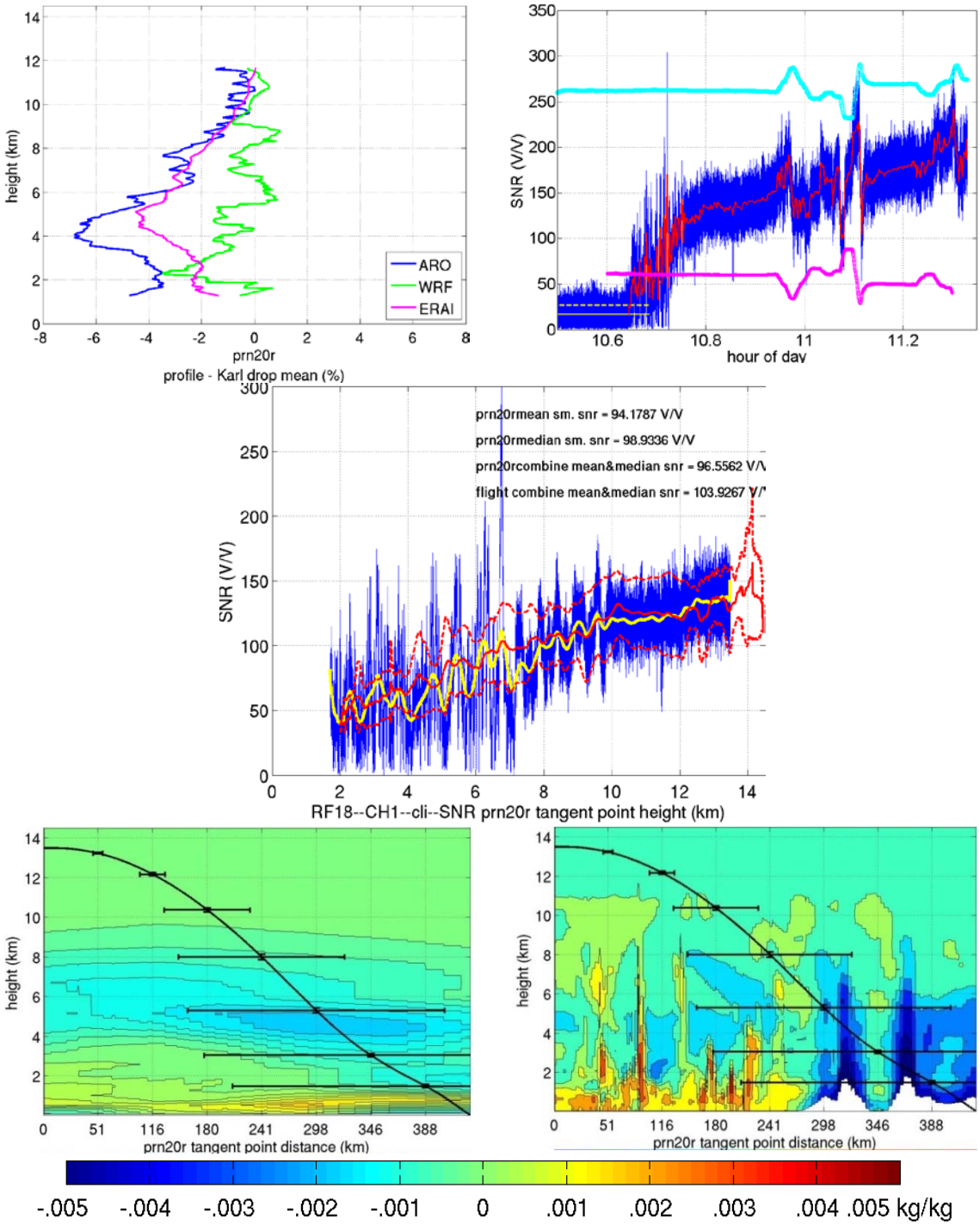

Figure A. 26 RF18 OL CH1_cli prn20r.

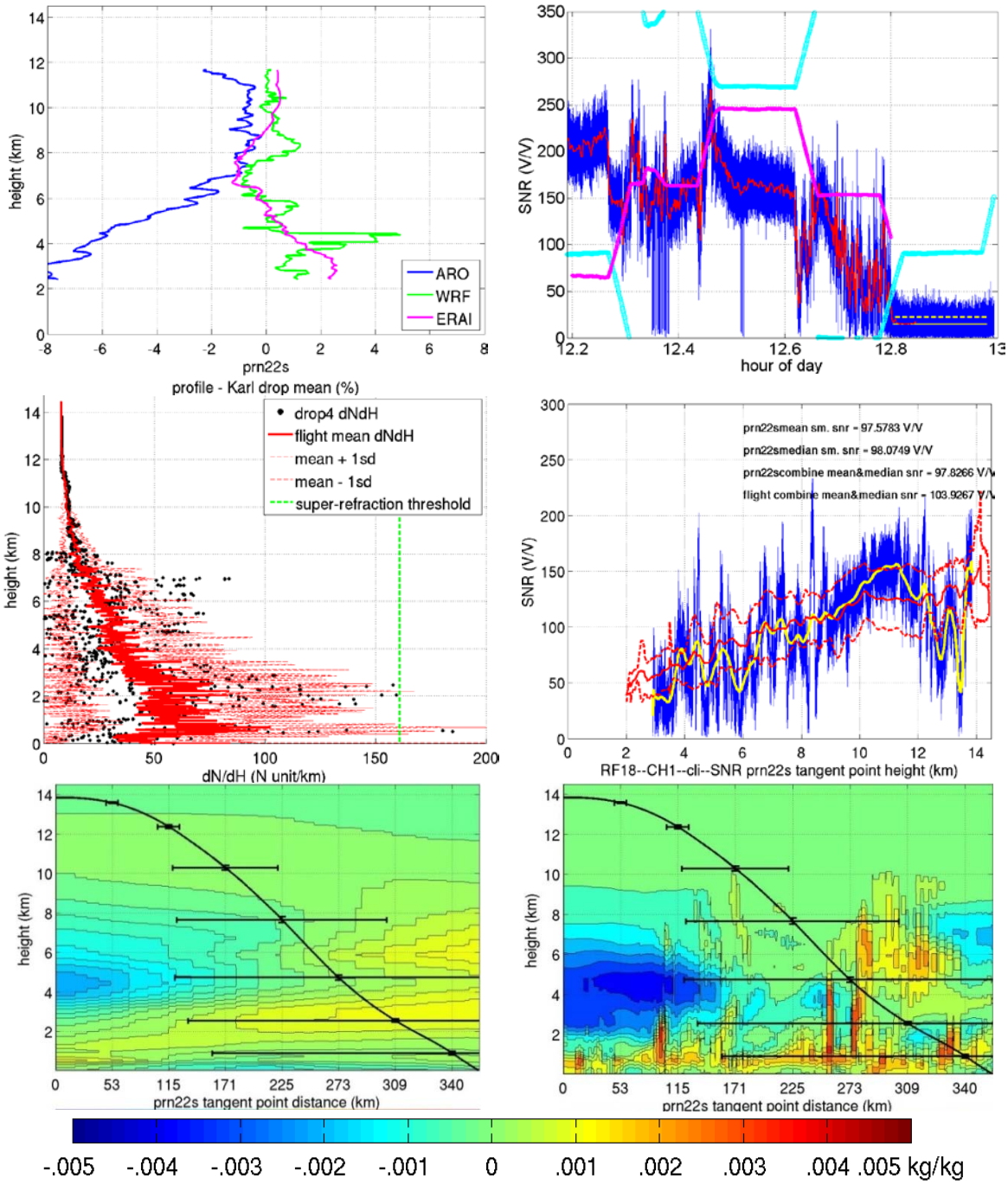

Figure A. 27 RF18 OL CH1_cli prn22s. In middle left plot, the co-located drop4 was 55 km from prn22s occultation point.

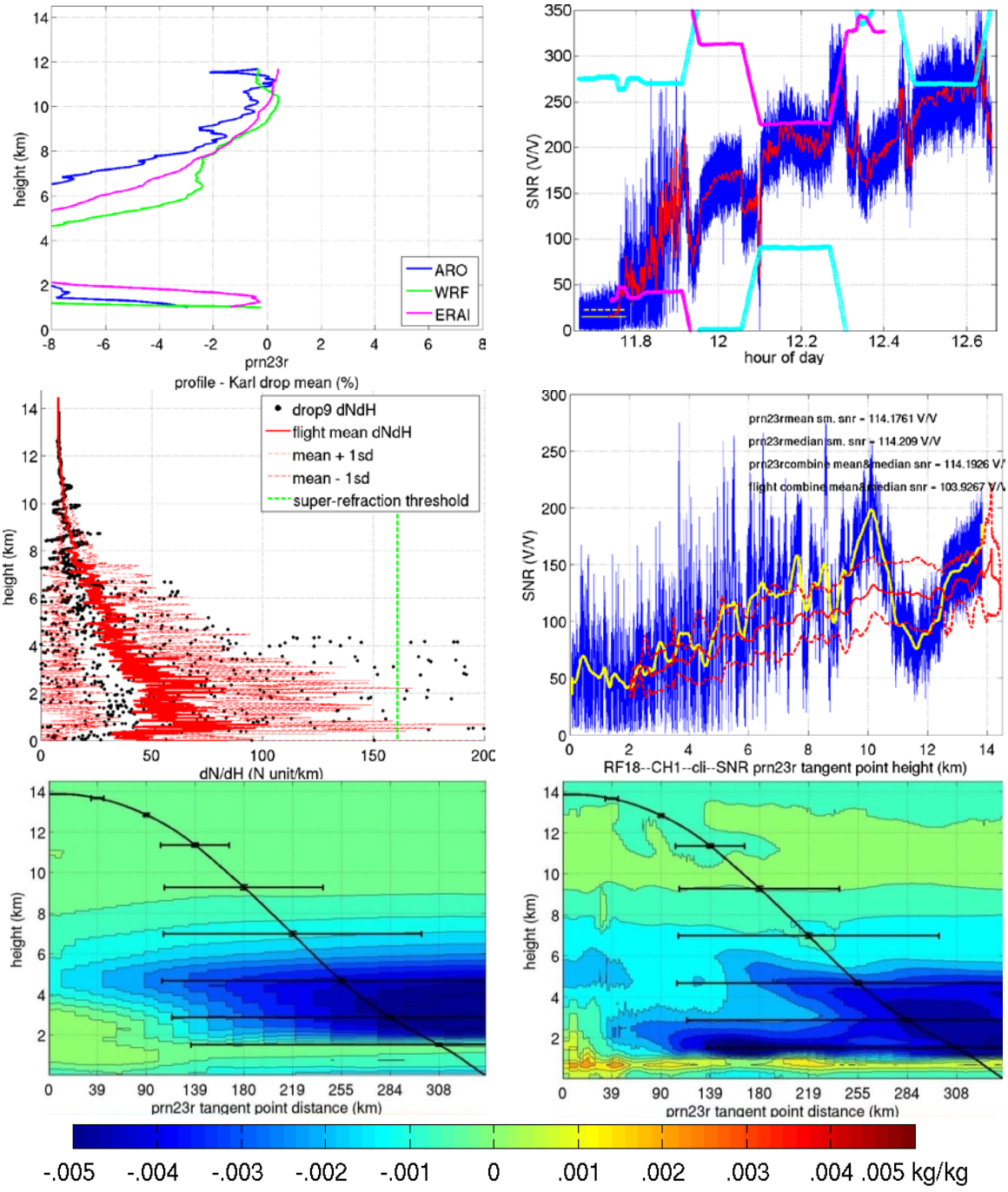

Figure A. 28 RF18 OL CH1_cli prn23r. In the middle left panel, the co-located drop09 was 160 km from prn23r occultation point.

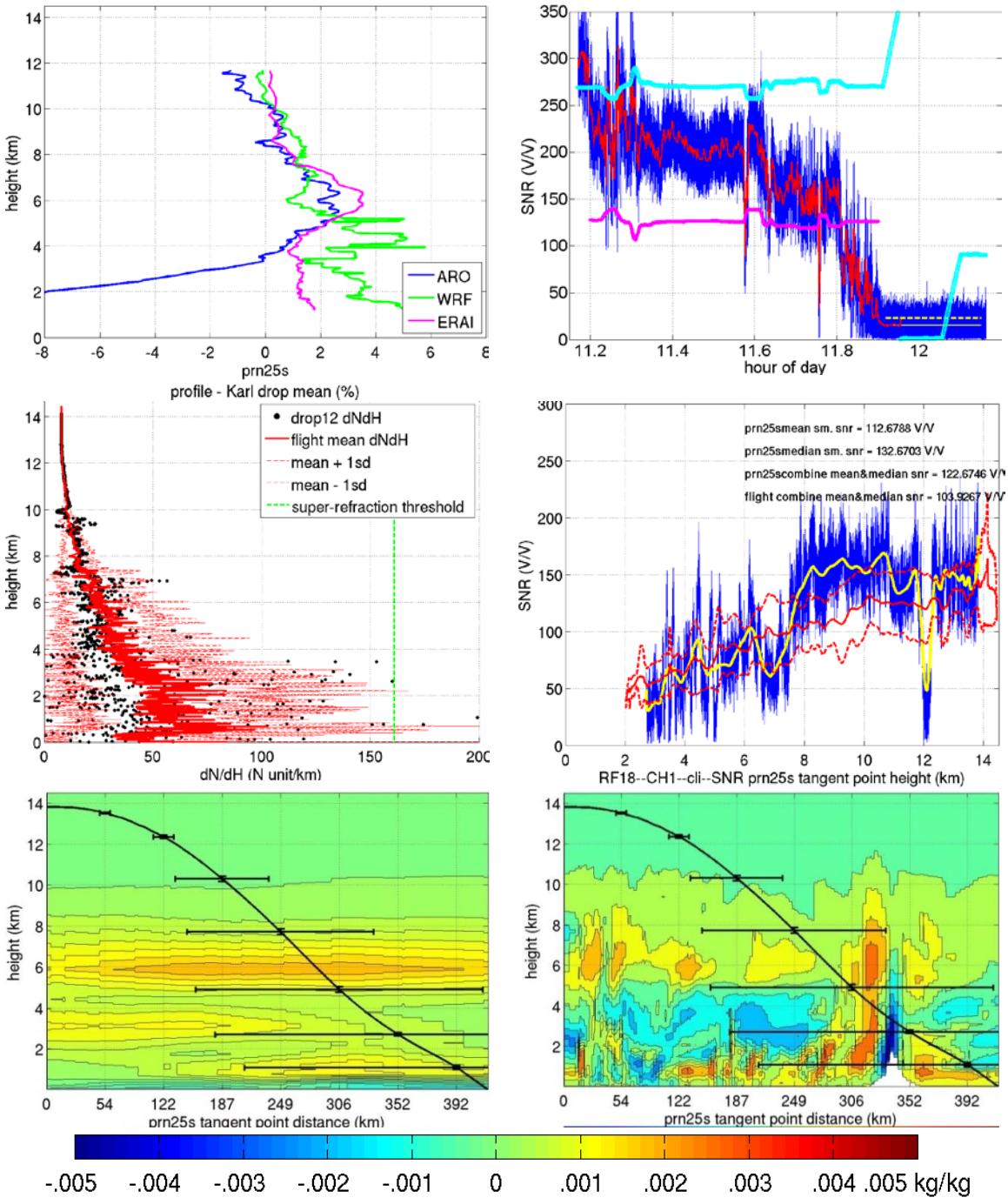

Figure A. 29 RF18 OL CH1_cli prn25s. In the middle left panel, the co-located drop12 was 9 km from prn25s occultation point.

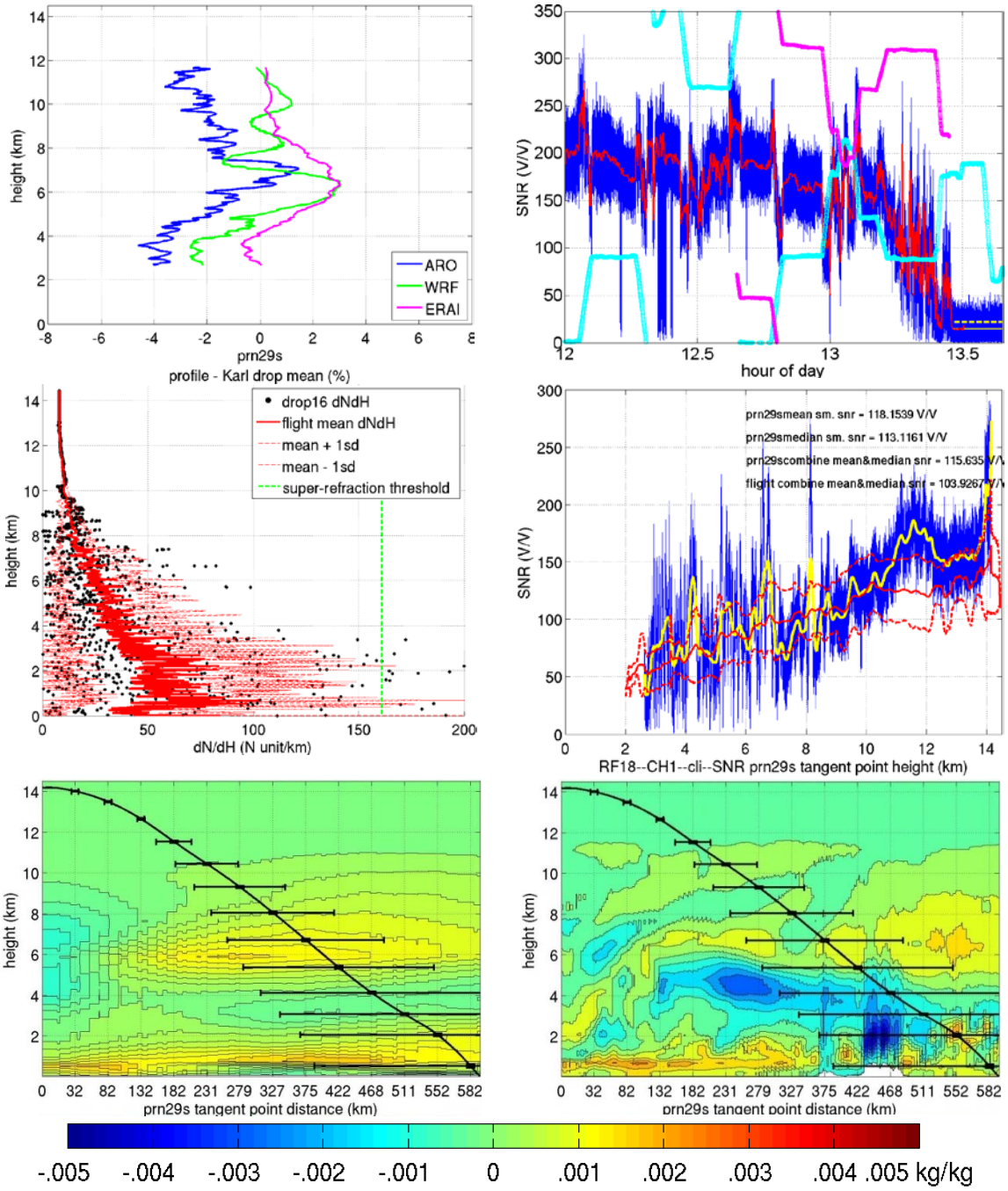

Figure A. 30 RF18 OL CH1_cli prn29s. In the middle panel, the co-located drop16 was 192 km from prn29s occultation point.

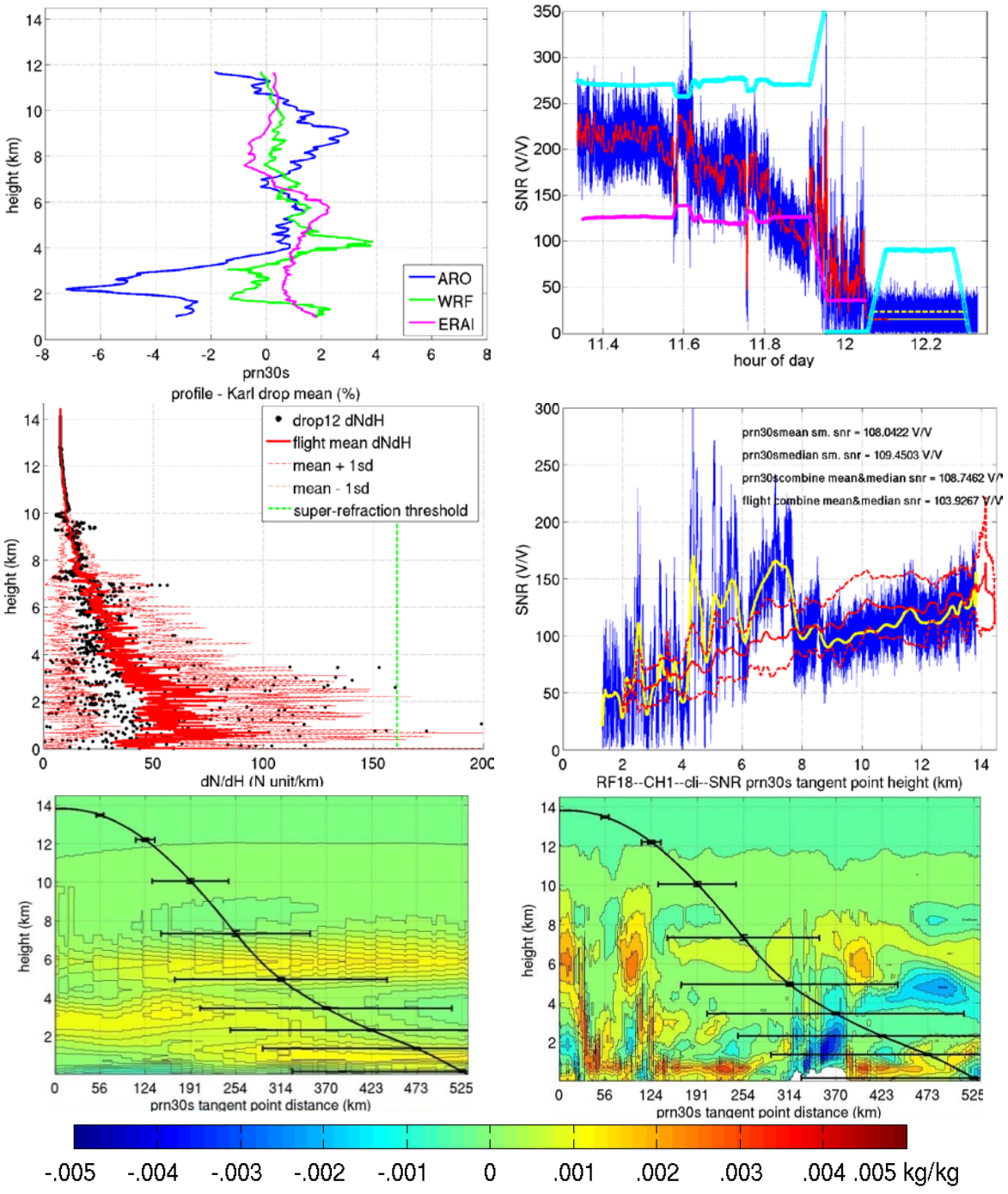

Figure A. 31 RF18 OL CH1_cli prn30s. In the middle panel, the co-located drop12 was 92 km from prn30s occultation point.

RF19:

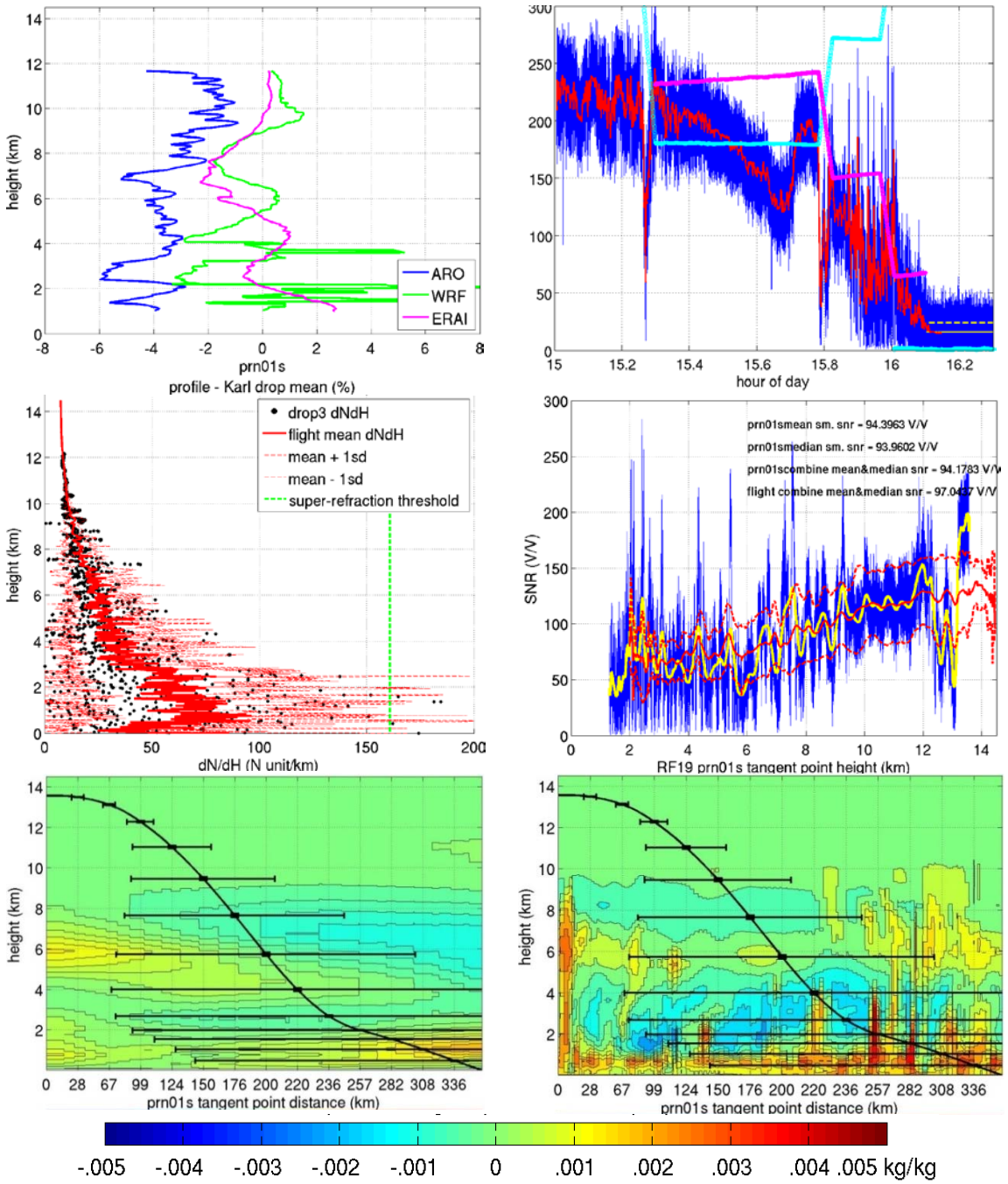

Figure A. 32 RF19 OL CH1_cli prn01s. In the middle panel, dropsonde 3 was located 177 km from the prn01s occultation point.

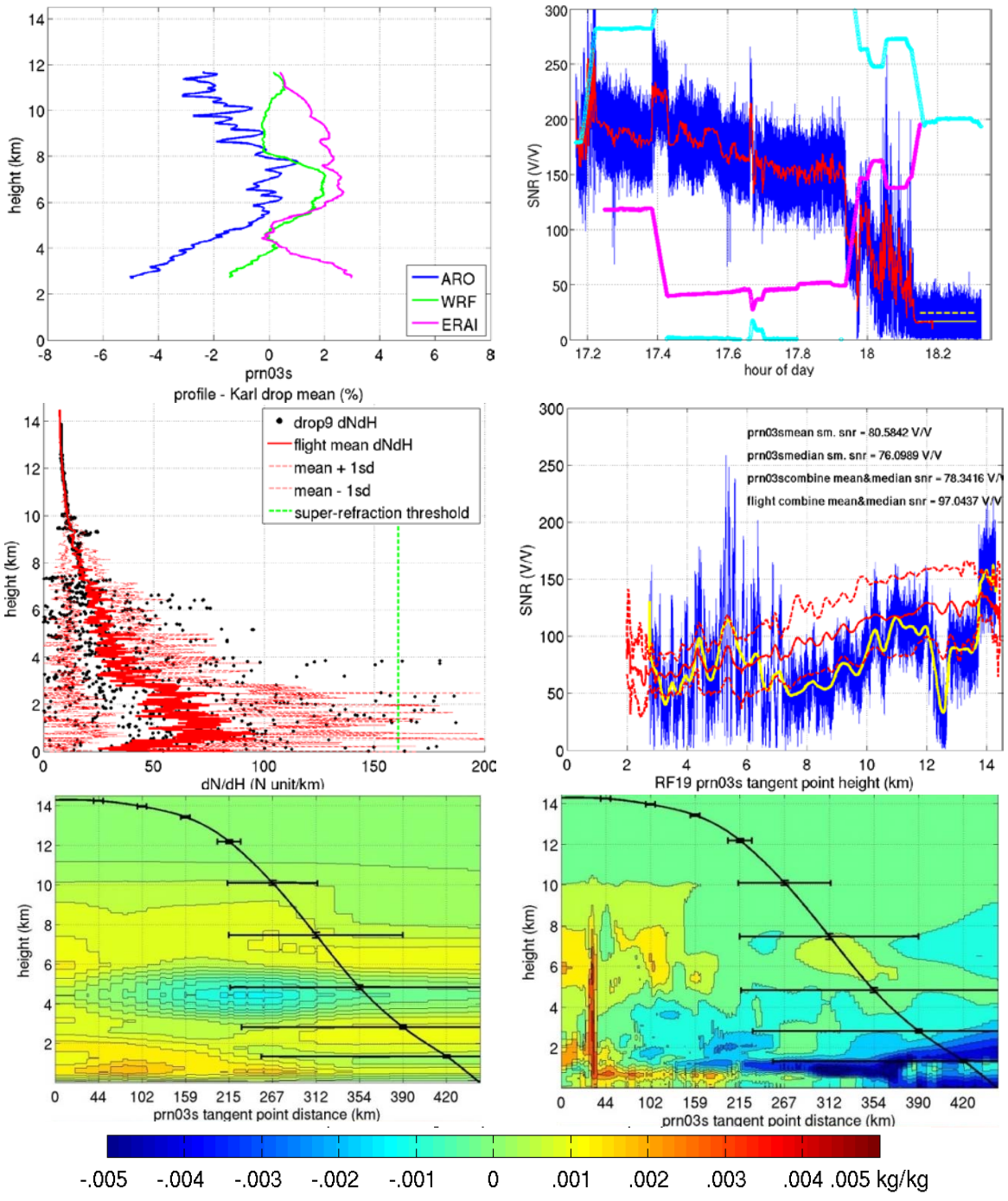

Figure A. 33 RF19 OL CH1_cli prn03s. In the middle left panel, dropsonde 9 was located 255 km from the prn01s occultation point.

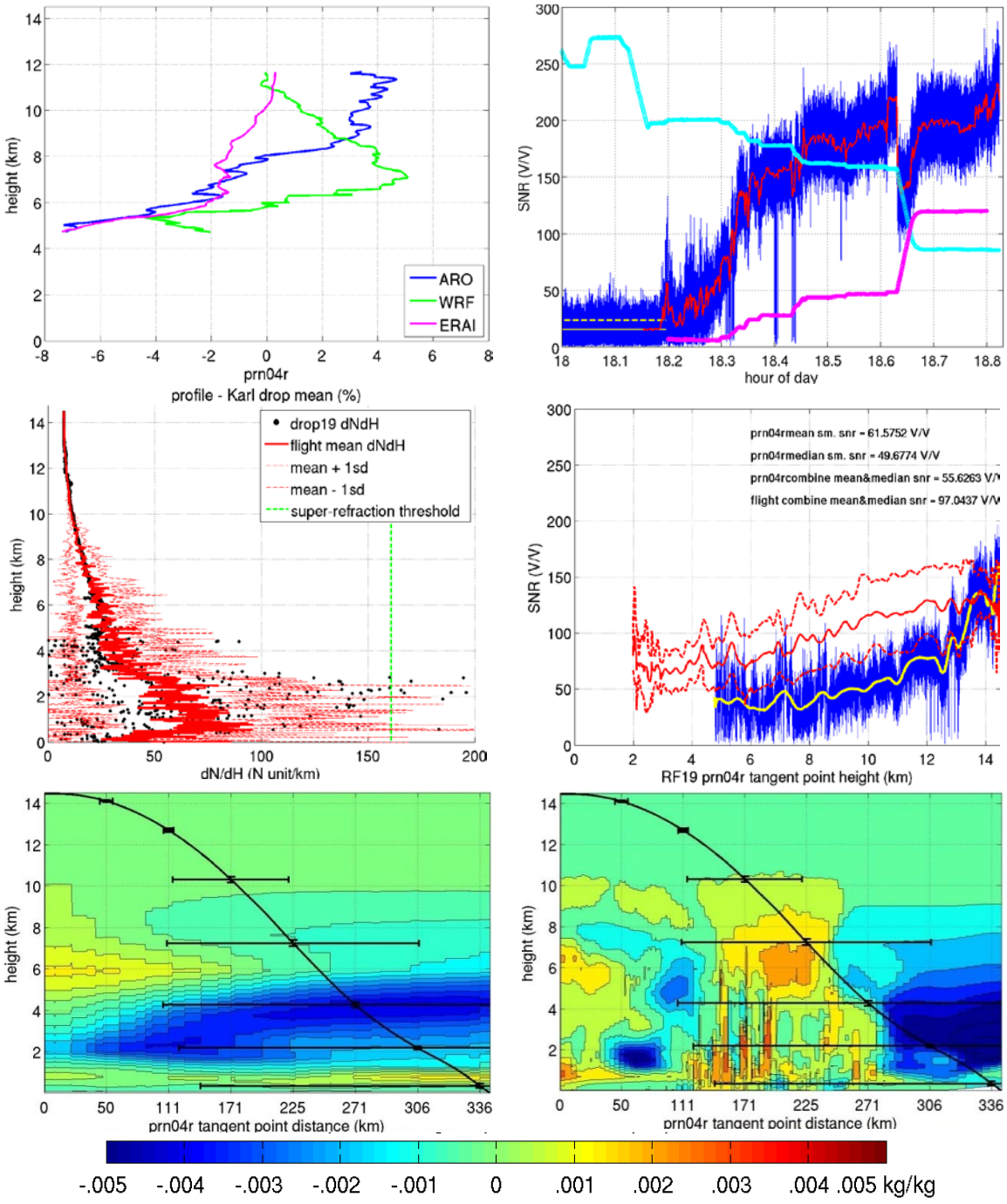

Figure A. 34 RF19 OL CH1_cli prn04. In the middle left panel, dropsonde 19 was located 128 km from the prn01s occultation point.

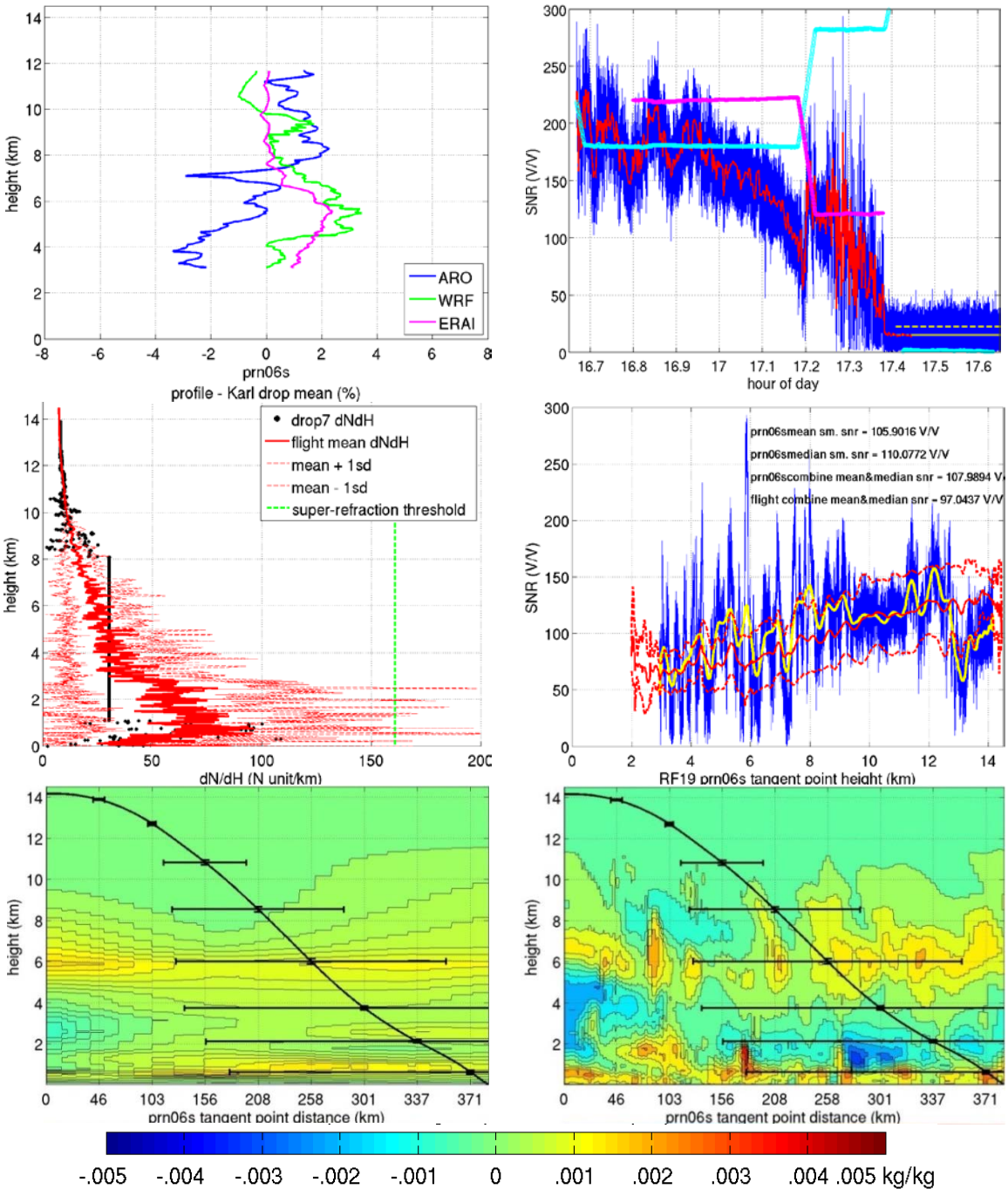

Figure A. 35 RF19 OL CH1_cli prn06s. In the middle left panel, dropsonde 7 was located 73 km from the prn01s occultation point.

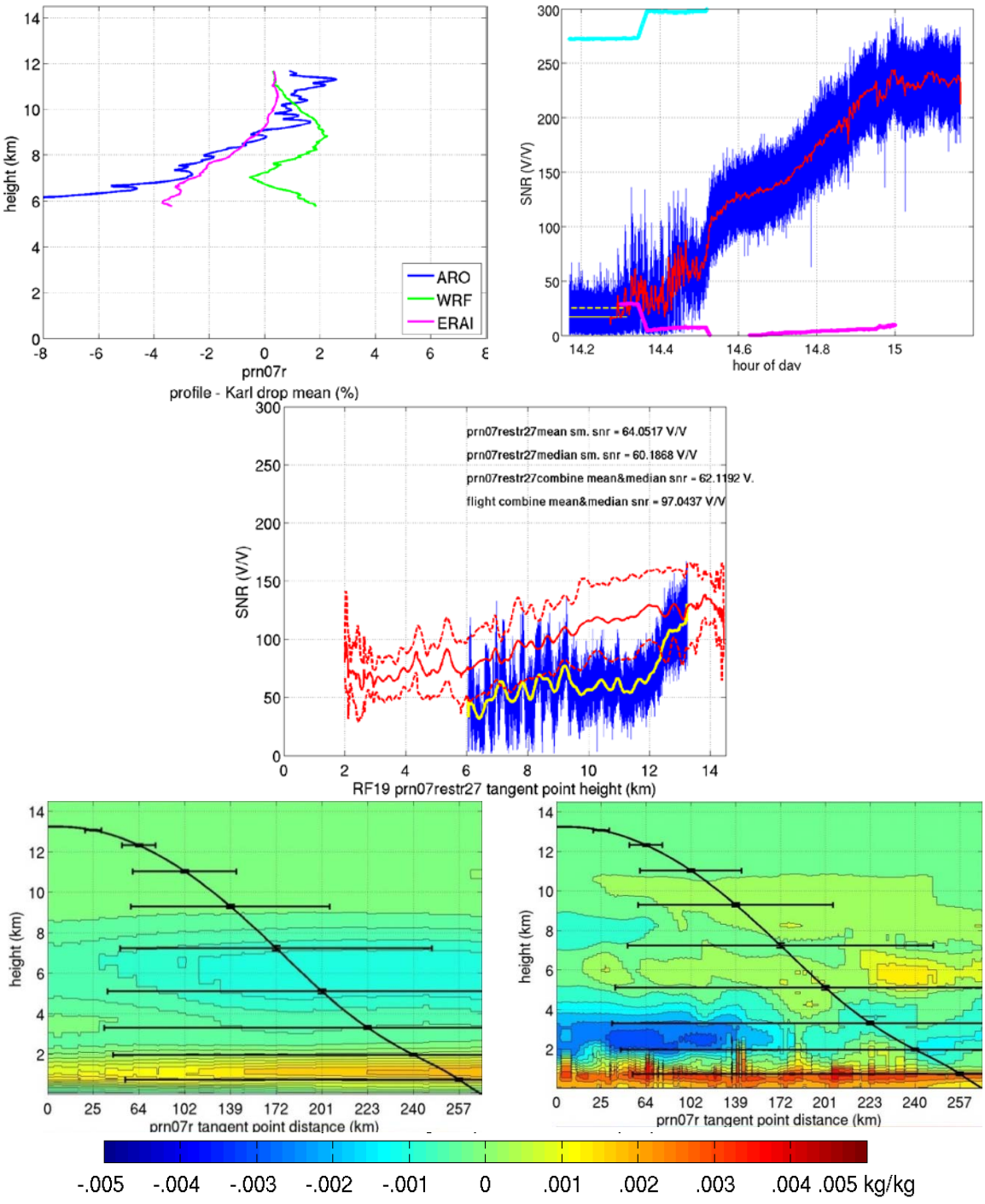

Figure A. 36: RF19 OL CH1_cli prn07r

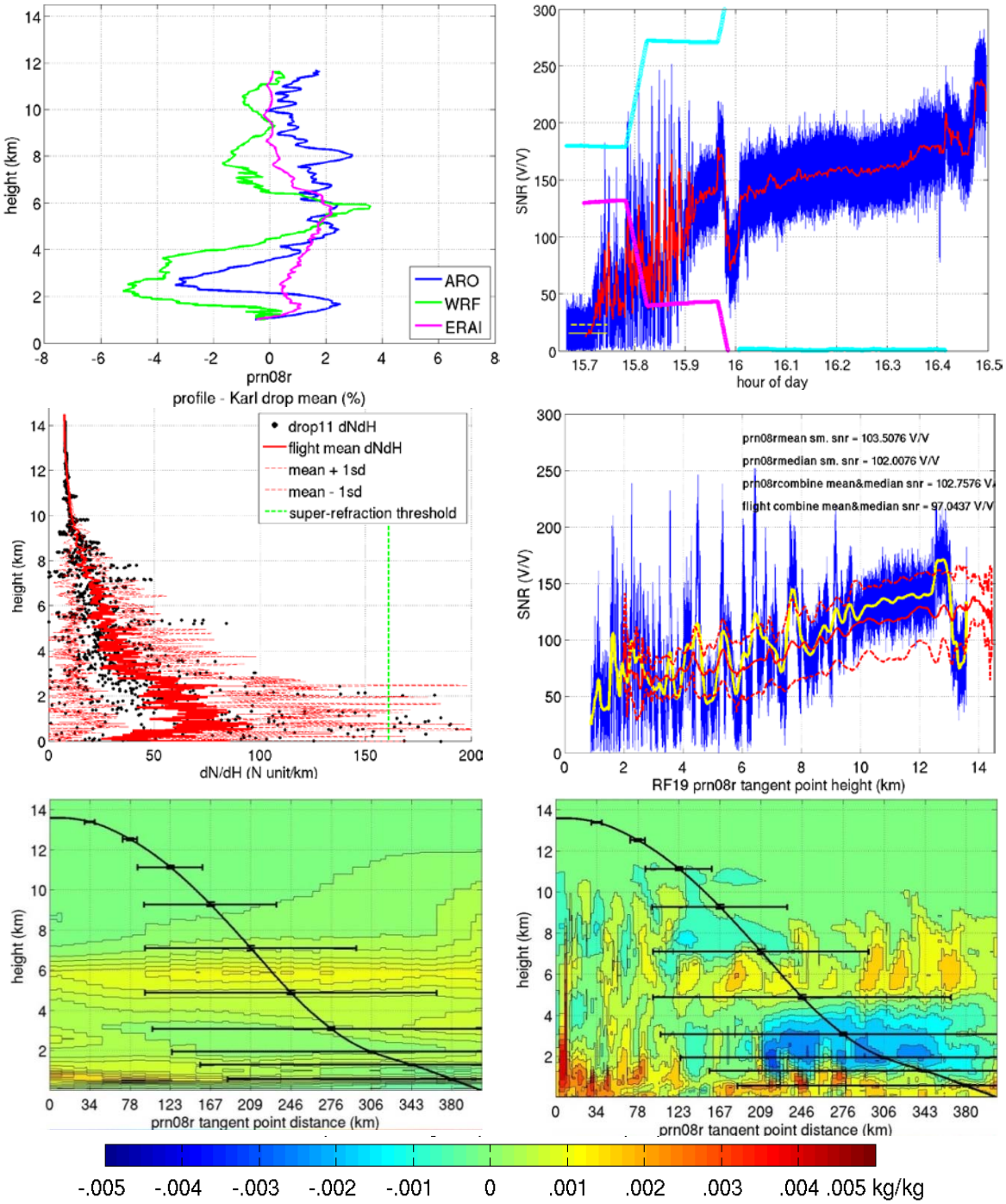

Figure A. 37 RF19 OL CH1_cli prn08r. In the middle left panel, dropsonde 11 was located 69 km from the prn01s occultation point.

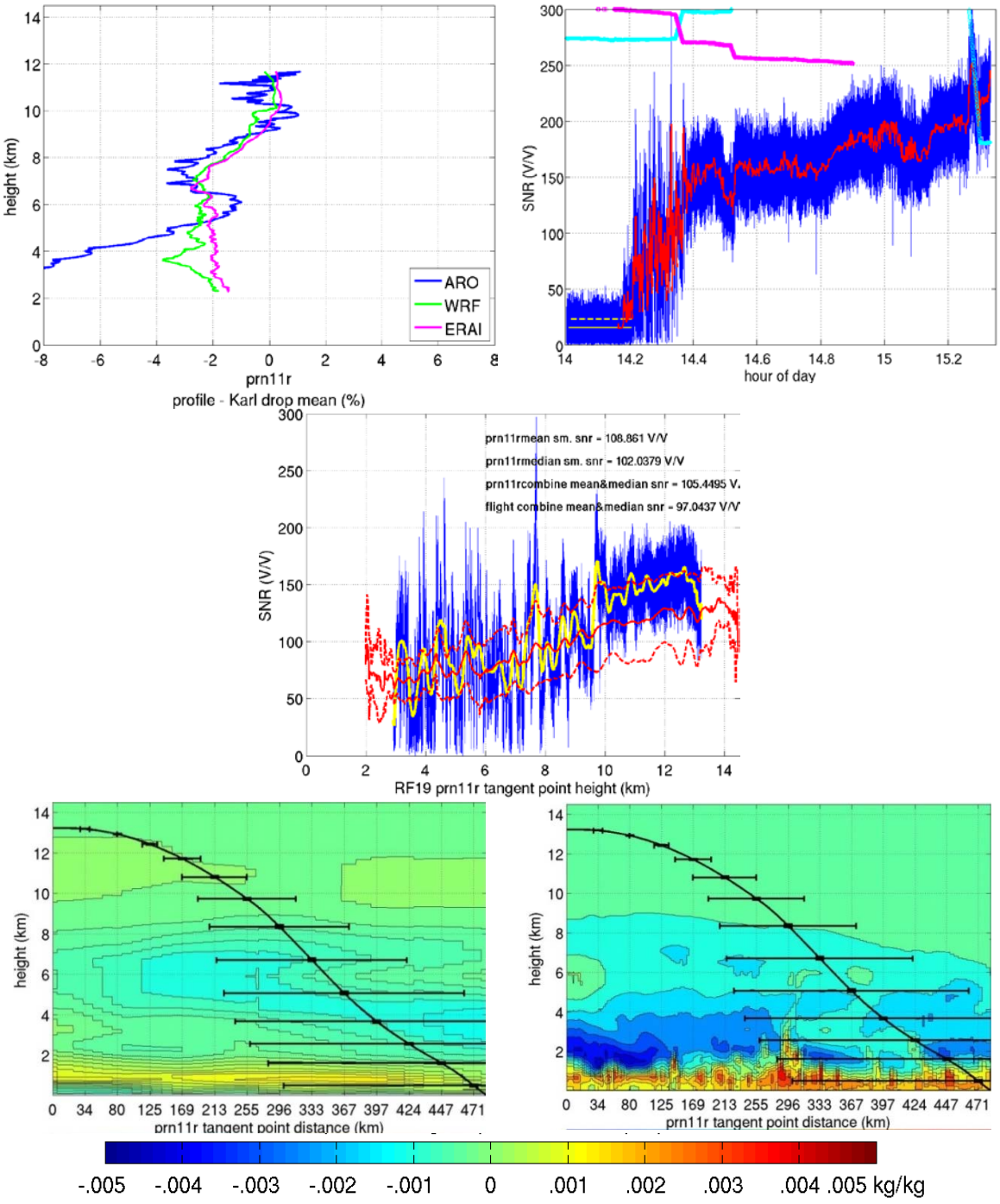

Figure A. 38 RF19 OL CH1_cli prn11r.

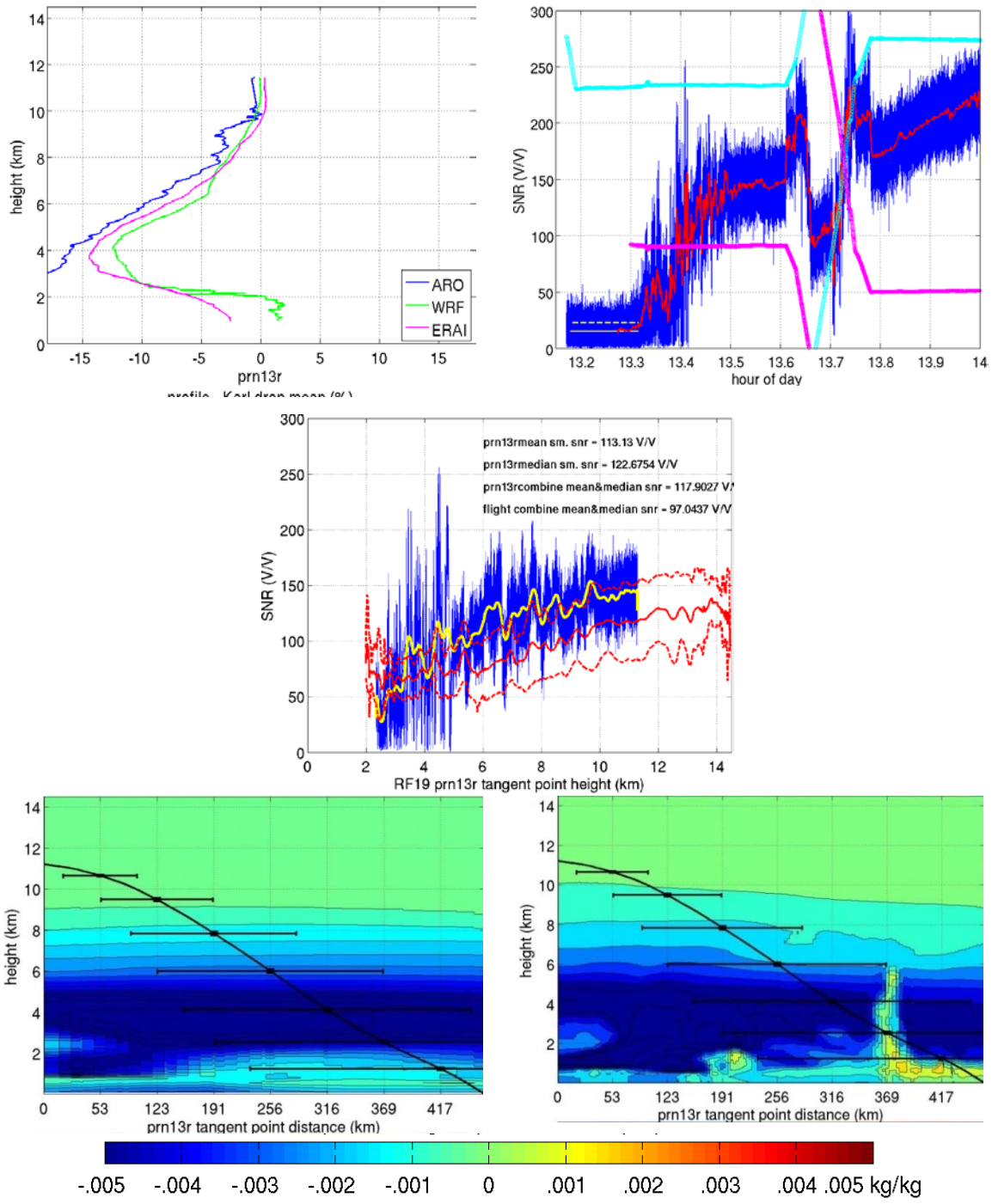

Figure A. 39 RF19 OL CH1_cli prn13r.

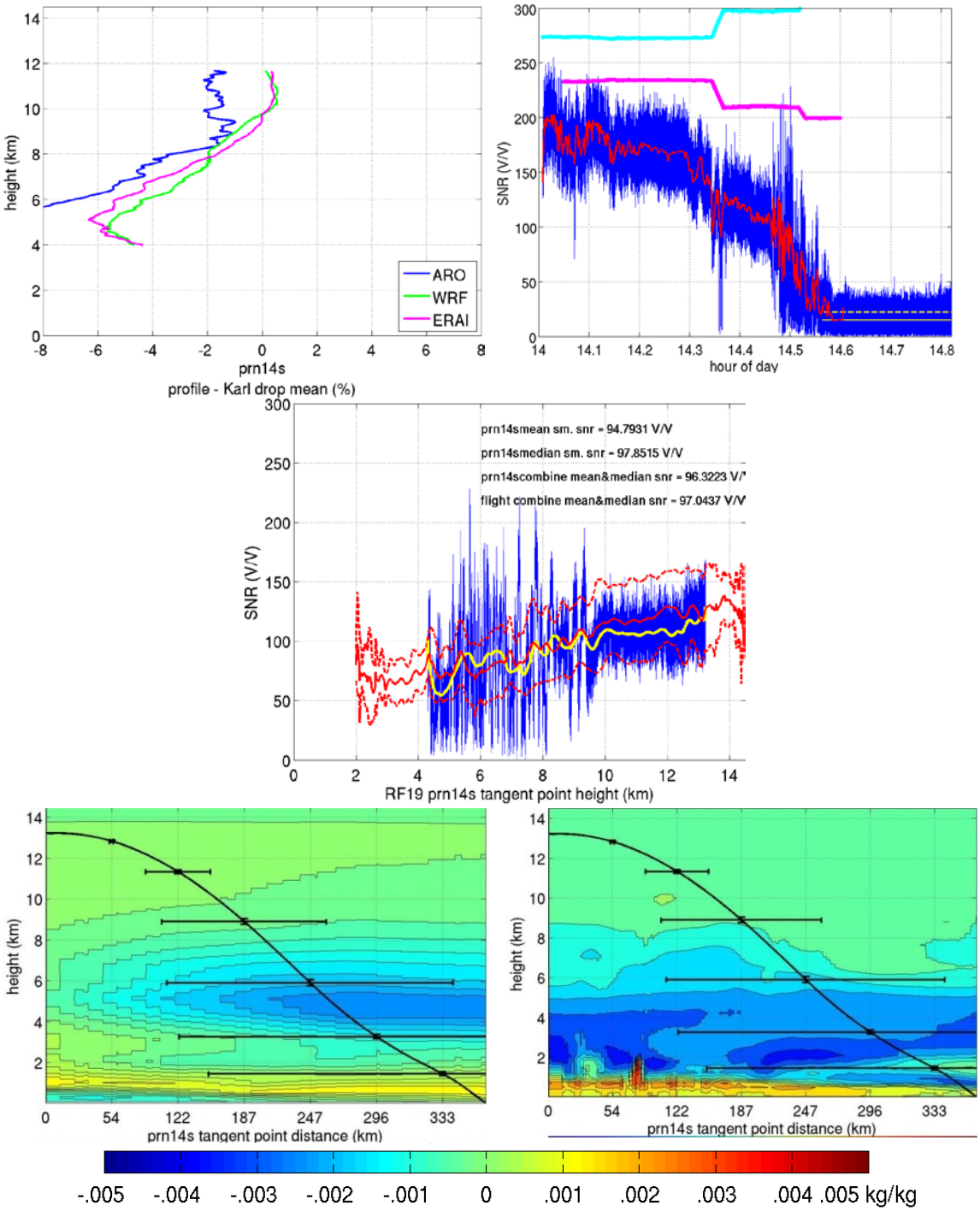

Figure A. 40 RF19 OL CH1_cli prn14s.

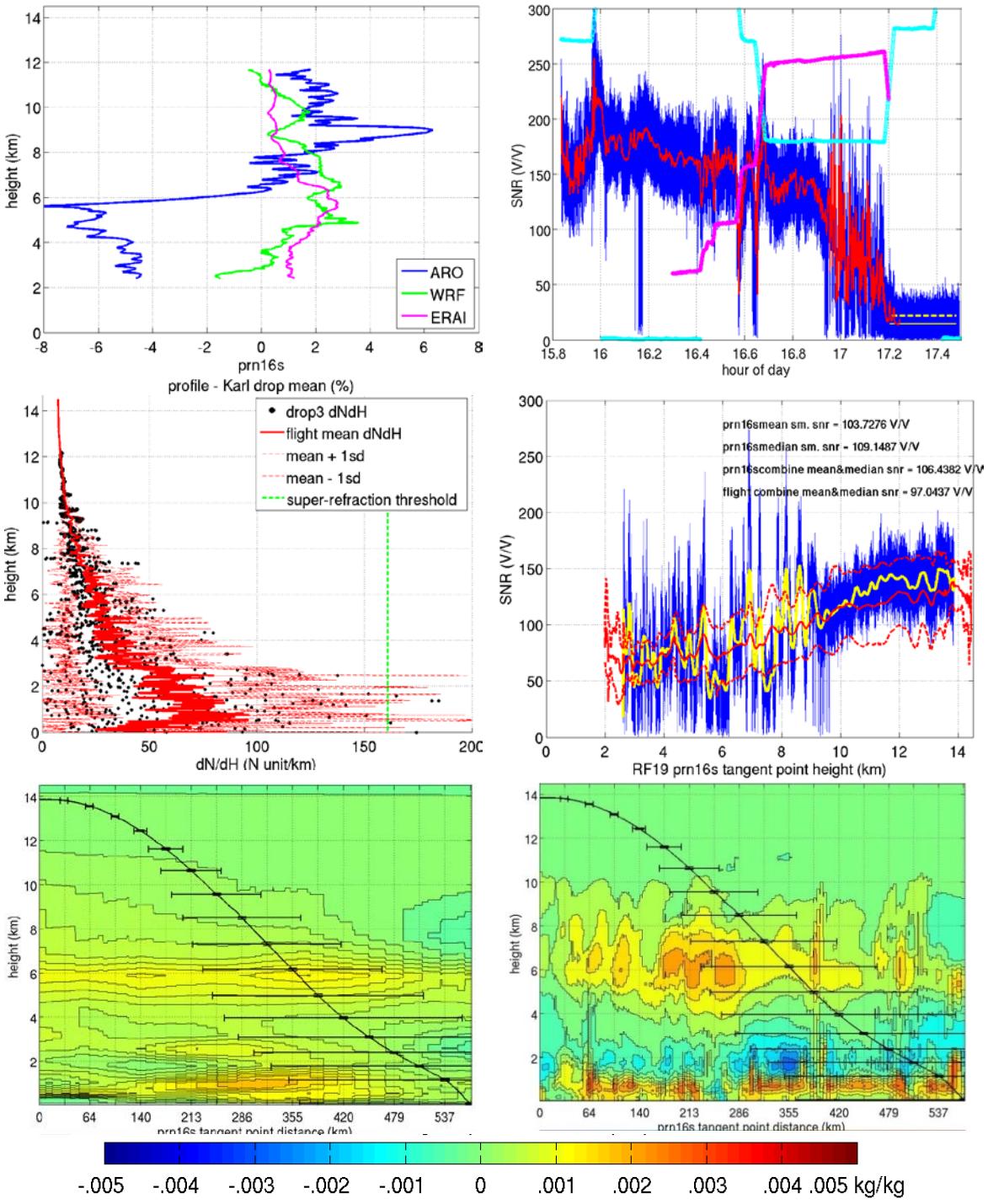

Figure A. 41 RF19 OL CH1_cli prn16s. In the middle panel, dropsonde 3 was located 88 km from the prn01s occultation point.

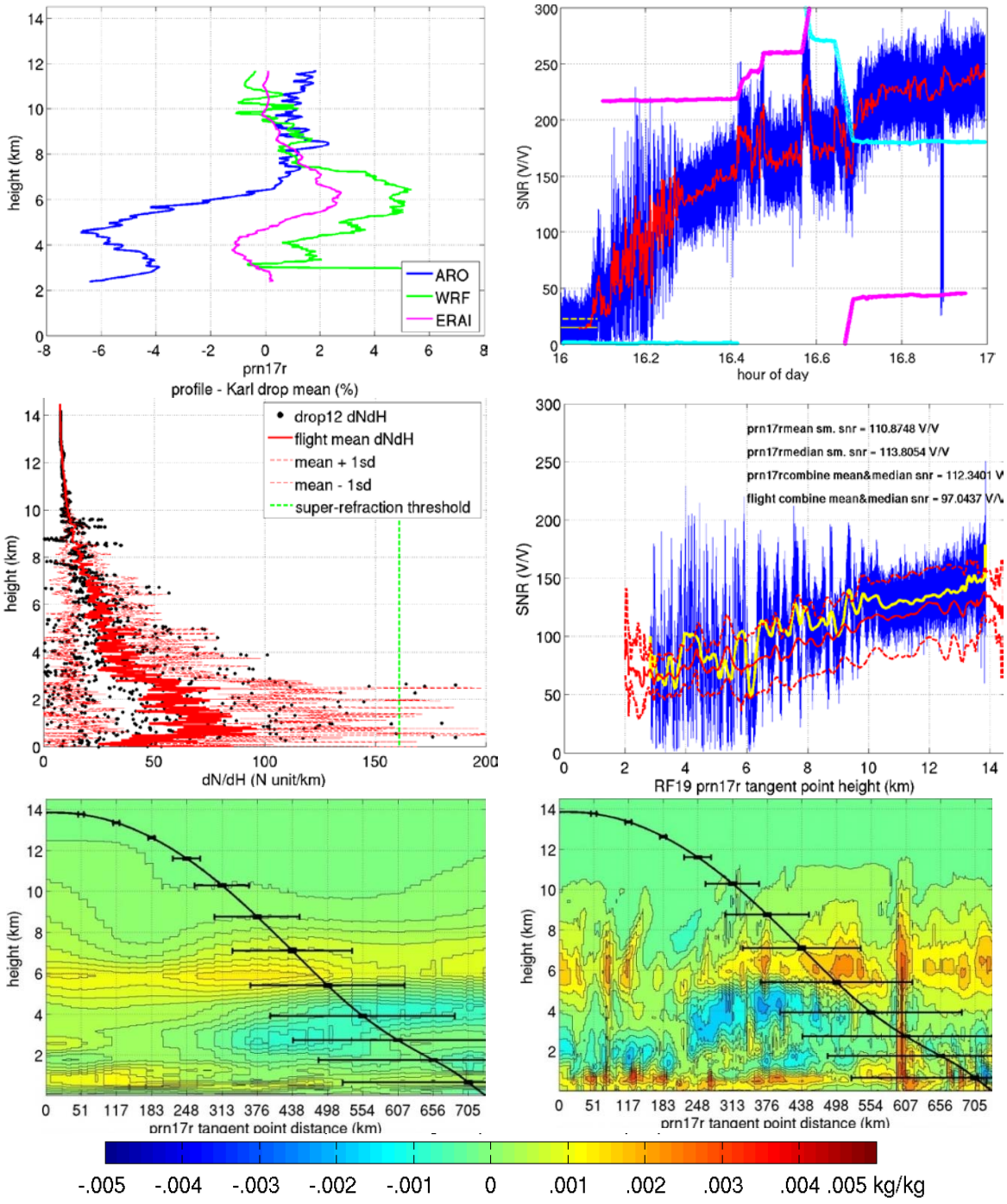

Figure A. 42 RF19 OL CH1_cli prn17r. In the middle panel, dropsonde 12 was located 81 km from the prn01s occultation point.

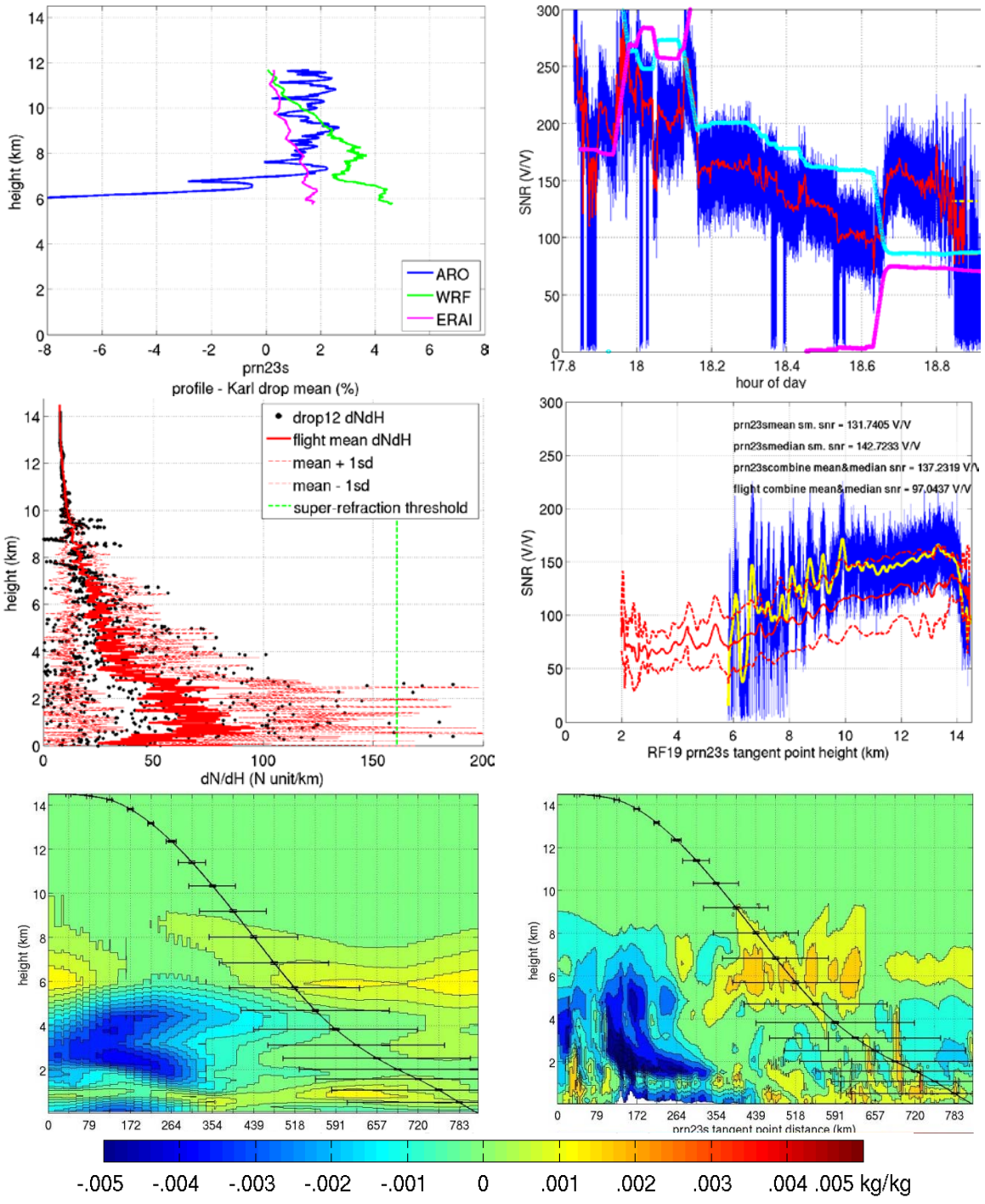

Figure A. 43 RF19 OL CH1_cli prn23s. In the middle left panel, dropsonde 12 was located 225 km from the prn01s occultation point.

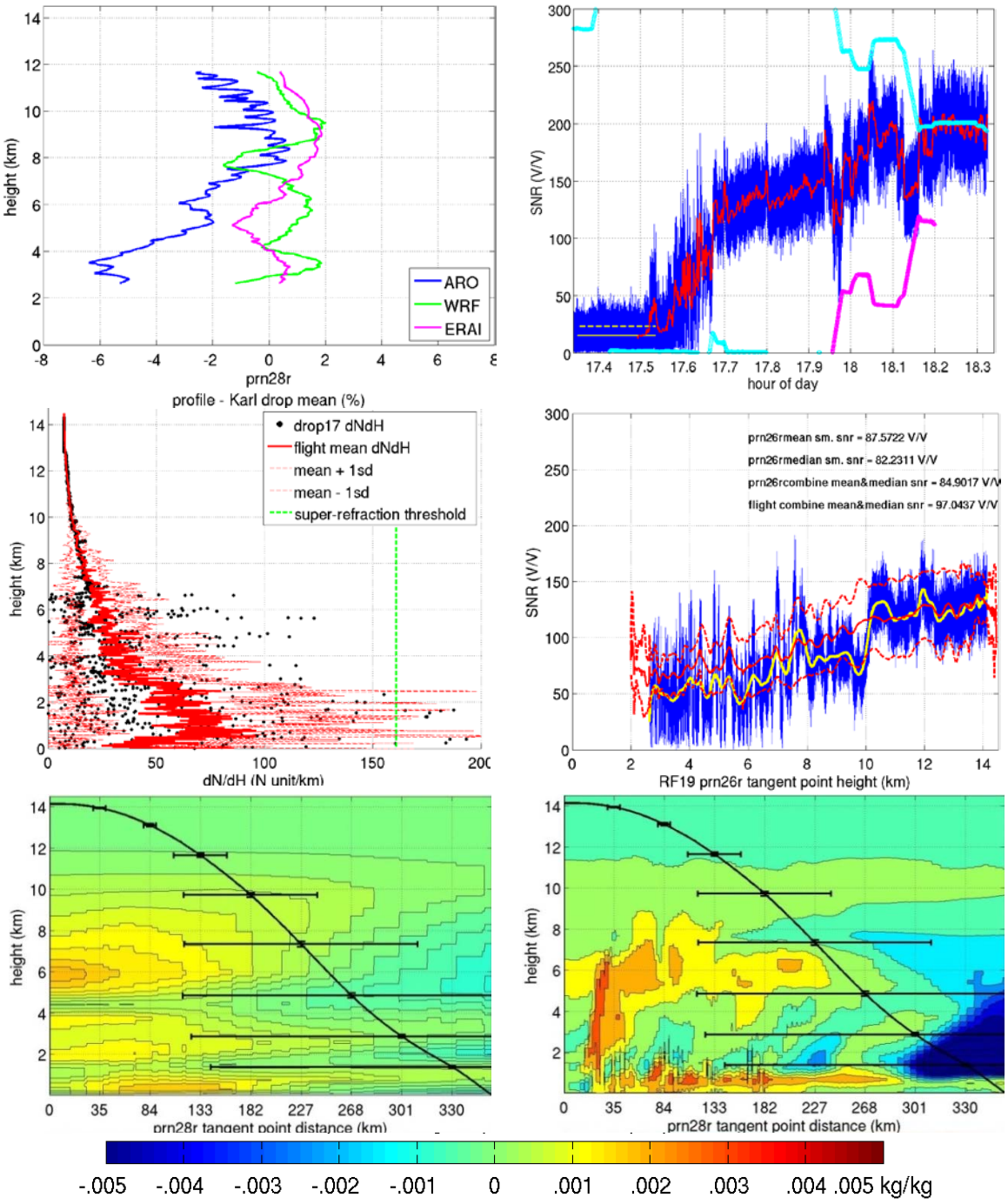

Figure A. 44 RF19 OL CH1_cli prn26r I had a labeling issue so some figs say prn28. In the middle panel, dropsonde 17 was located 36 km from the prn01s occultation point.

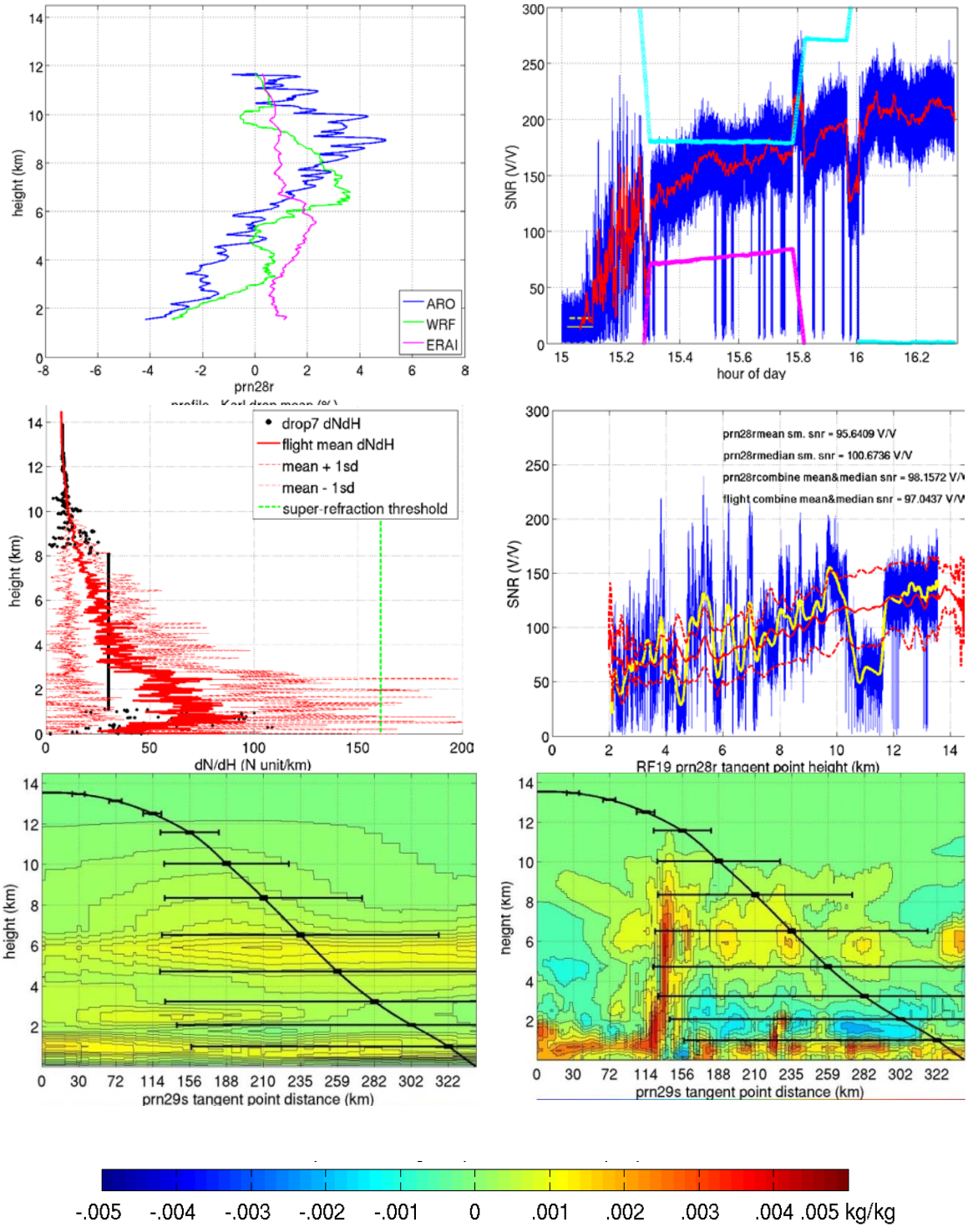

Figure A. 45 RF19 OL CH1_cli prn28r. Some lbeling issues again. In the middle panel, dropsonde 7 was located 62 km from the prn01s occultation point.

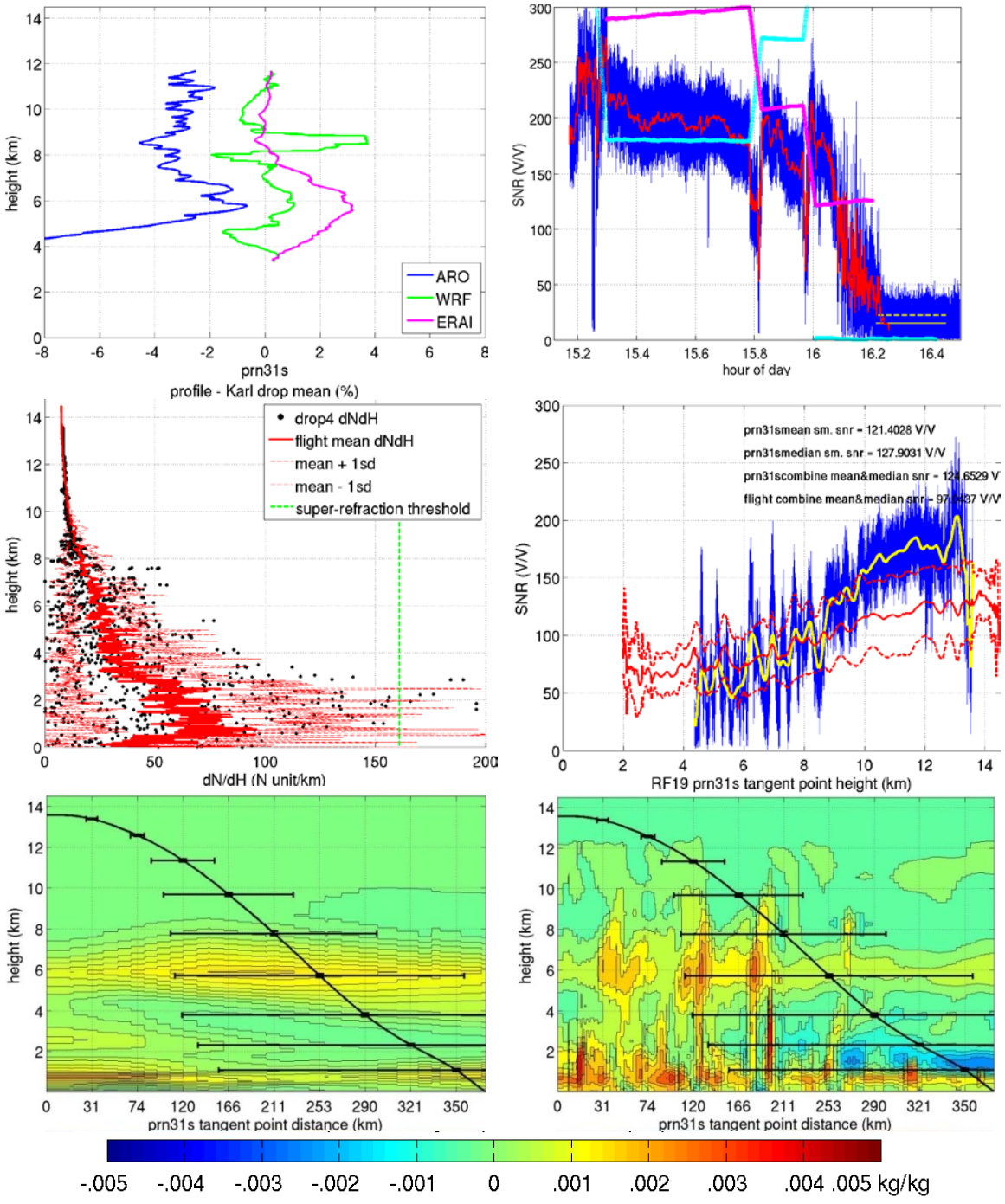

Figure A. 46 RF19 OL CH1_cli prn31s. In the middle panel, dropsonde 4 was located 117 km from the prn01s occultation point.

VITA

VITA

Brian Murphy was born in Evanston, Illinois. He grew up in Fort Wayne, IN and attended Bishop Dwenger High School. He attended Hanover College and received a B.A. degree in physics and earned a M.S. in physics from Purdue University.

After teaching math and physics for several years at Ivy Tech Community College and Purdue in West Lafayette, he began as a doctoral student in the Department of Earth, Atmospheric and Planetary Sciences in the fall of 2010, working under the supervision of his major professor, Dr. Jennifer S. Haase. His dissertation defense was in the summer of 2015 and he anticipates receiving a Ph.D. in August, 2015.